Nearfield Shielding and Green Shielding
(Passive and Active Electromagnetic Shielding Approaches)

Amirashkan Darvish

A Dissertation

In the Department of

Electrical and Computer Engineering

Presented in Partial Fulfillment of the Requirements

For the Degree of

Doctor of Philosophy (Electrical and Computer Engineering)

Concordia University

Montreal, Quebec, Canada

August 2023

CONCORDIA UNIVERSITY

SCHOOL OF GRADUATE STUDIES

This is to certify that the dissertation prepared

By: Amirashkan Darvish

Entitled: Nearfield Shielding and Green Shielding (Passive and Active Electromagnetic Shielding Approaches)

and submitted in partial fulfillment of the requirements for the degree of

DOCTOR OF PHILOSOPHY (Electrical and Computer Engineering)

complies with the regulations of the University and meets the accepted standards with respect to originality and quality.

Signed by the final examining committee:

---------- Chair
Chair's name: Dr. Yousef R. Shayan

---------- External Examiner
Examiner's name: Dr. George V. Eleftheriades

---------- Examiner
Examiner's name: Dr. Abdelrazik Sebak

---------- Examiner
Examiner's name: Dr. Robert Paknys

---------- Examiner
Examiner's name: Dr. Farjad Shadmehri

---------- Dissertation Supervisor
Supervisor's name: Dr. Ahmed Kishk

Approved by -----Dr. Yousef R. Shayan----------
Chair of Department or Graduate Program Director:

Month/day/year -----2023-10-24----------
Dean's name: Dr. Mourad Debbabi
Gina Cody School of Engineering and Computer Science

ABSTRACT

Nearfield Shielding and Green Shielding
(Passive and Active Electromagnetic Shielding Approaches)

Amirashkan Darvish, PhD
Concordia University, 2023

Nothing comes without costs. Electromagnetic interference (EMI) has been one of the first costs humans started identifying after initial achievements on how electromagnetic waves interact with different substances. *Shielding* against EMI emissions became one of the prominent challenges for the Electromagnetic Compatibility (EMC) community. The extent of the benefits of EMI shielding ranges from healthcare applications to commercial/industrial ones. The dissertation aims to solve two major shielding problems in the context of passive and active methods. The first problem is the nearfield shielding characterization of Frequency Selective Surfaces (FSSs), where the near-field performance of FSS structures is analyzed and differentiated from far-field performance. After introducing sufficient analytical models and techniques to characterize shields' near-field responses, an analysis is provided to reveal the fundamental failure of conventional FSS-based shields in providing NF shielding. Then, a new flexible bandstop FSS is introduced that provides stable near-field (NF) characteristics in the X-band. Thorough analyses are carried out to monitor the effects of incident angle, edge diffraction, bending, and wave polarization on shielding. The dissertation investigates further the active techniques that enable the user to harness the incident signal while providing the required shielding. This part of the study investigates reconfigurable intelligent surfaces for shielding or amplification, where a space-time-modulated (STM) medium is designed as a potential solution for green shielding purposes. Then, the green shielding possibilities are investigated through four different mechanisms. It turns out that STM media can be influential for other similar purposes, encouraging future attempts to realize the media.

ACKNOWLEDGEMENTS

I would like to thank my supervisor, Dr. Ahmed Kishk, for guiding me through this journey, my family, and friends for their unwavering support.

Thank you.

DEDICATION

With a heart weighed down by sorrow, this dissertation is devoted to

Sarina Esmaelzadeh, 16

Nika Shakarami, 16

Hadis Najafi, 20

Hananeh Kia, 23

Yalda Aghafazli, 19

Aylar Haghi, 23

Ghazaleh Chelavi, 32

Setareh Tajik, 17

Asra Panahi, 15

Mahsa Amini, 22

Negin Abdulmaleki, 21

Donya Farhadi, 22

Mahsa Mogouyi, 18

Bahar Khorshidi, 22

and to all the other courageous women in Iran who were mercilessly arrested, tortured, and murdered in *Woman, Life, Freedom* uprising while speaking up, protesting, and fighting for their rights.

Their legacy will be honored by continuing to amplify their voices and standing in solidarity with those who persistently advocate for their rights worldwide.

Table of Contents

List of Figures

List of Tables

List of Acronyms

ADS	Advanced Design Systems
CSL	Convoluted Square Loop
ECM	Equivalent Circuit Model
EM	Electromagnetic
EMC	Electromagnetic Compatibility
EMI	Electromagnetic Interference
EMR	Electromagnetic Radiations
FCC	Federal Communications Commission
FEM	Finite Element Method
FF	Far-field
FSS	Frequency Selective Surfaces
HECR	High energy concentration region
IC	Industry Canada
JR	Jerusalem Resonator
LECR	Low energy concentration region
MOM	Method of moment
NF	Near-field
PSO	Particle Swarm Optimization
RCS	Radar Cross Section
SE	Shielding Effectiveness
SL	Square loop
SPM	Small Perturbation Method
SRR	Split-Ring Resonator
TEM	Transverse Electromagnetic

Chapter 1: Contextualizing the Problem

1.1 Introduction

Protection against harmful electromagnetic (EM) radiation and interferences is crucial in the RF and microwave industry, as well as in EMC laboratories [1], biomedical imaging facilities [2], and radiotherapy [3]. This is because many sensitive electronic devices and circuits are vulnerable to EM waves, which can cause malfunctions by exciting additional induction currents. Therefore, there is a need to design lightweight, flexible, and practical EM shields to protect these vulnerable objects. On the other hand, the desire for ultra-compact shielded products has increased interest in flexible shields that can be used near susceptible substances. Additionally, the negative thermal effects of high-power X-band Electromagnetic Radiations (EMR) on living organisms' systems, including the nervous, reproductive, cardiovascular, immune, hematopoietic, and endocrine systems, emphasizes the importance of wearable/reconfigurable EM shields. These shields could effectively protect exposed organisms in electromagnetically polluted environments.

Passive and active meta-surfaces have emerged as effective options for electromagnetic shielding due to their ability to filter desired and undesired frequency components [4]. This filtering characteristic becomes even more appealing when combined with actively disturbed media. One significant challenge in electromagnetic shielding is uncertainty about the shield's performance in near-field (NF) zones [5, 6]. In compact or wearable applications, shields must prevent specific frequency components from passing through susceptible circuits or living organisms (such as skin, enzymes, or brain cells) by reflecting or absorbing the undesired spectrum. They must eliminate any interfering field within a small fraction of a wavelength from the susceptible object. For the X-Band spectrum, this fraction of wavelength falls within a range of approximately 1-50mm and is crucial for wearable biomedical applications. Designing an ultra-thin, wearable shield that can protect a susceptible object within this NF range requires careful consideration of both near-field and far-field (FF) characteristics. Designers of flexible shields often avoid dealing with NF areas due to the present NF uncertainty of Frequency Selective Surface (FSS) structures [7, 8]. As a result, a lack of reliable NF attenuation often leads to bulky products as manufacturers must increase the distance between the shield and the susceptible circuit to stabilize the attenuation level of the embedded shield. Therefore, a stable NF performance is essential for the feasibility of compactly shielded products.

Another shielding trend that utilizes meta-surfaces aims to minimize secondary reflections from shields to create electromagnetically clean environments [9, 10]. It is referred to as "green shielding." In this context, the term "green" can refer to the use of environmentally friendly materials and the goal of creating a safer and healthier environment for people and

electronic equipment by reducing electromagnetic interference. Green shielding is commonly used in various industries, including aerospace, defense, telecommunications, and medical, where electromagnetic interference can have serious consequences. The unique green properties are achieved through specialized materials that absorb electromagnetic radiation, reducing reflections and transmissions. When it comes to achieving filtering or tunability characteristics, active disturbance can result in green shields with advanced extended features that open many doors to designers with more complicated problems. For instance, active shields realized by space-time-modulated (STM) materials show features that enable them to act as green shields while representing functions similar to mixers. This special advantage shields one frequency band while transferring data to another band without producing high reflections. However, identifying various characteristics of green shields using such actively disturbed media requires extensive analytical insight into wave interaction, attenuation, and amplification in STM environments.

This work addresses the two shielding challenges mentioned above through the context of passive and active media, respectively.

1. To overcome the first challenge, the specific behavior of passive FSS shields in NF zones needs to be identified, analyzed, and comprehensively characterized. Additionally, promising techniques need to be established to estimate and measure NF anomalies in a way that provides future designers with sufficient knowledge and tools to design flexible shields capable of absorbing or reflecting high-power incident waves within a fraction of the wavelength. The performance of NF-compatible shields does not rely solely on the cell's NF performance, as it may be affected by various conditions, such as changes in the geometrical configuration of the shield, edge diffractions, polarization, and incident angle [5]. Therefore, the same shield might exhibit different efficiency when the mentioned conditions change. Aside from trying to understand, model, and estimate NF abnormalities, the current research focuses on decoupling the NF shielding concept from the mentioned disruptive factors by introducing a novel method for designing FSS shields.

2. The shielding behavior of lossy space-time modulated (STM) media needs to be investigated to propose solutions for the second challenge. The presence of losses in such a disturbed medium might come with advantages and drawbacks that need to be distinguished and leveraged for green shielding purposes. Developing an analytical model that considers the effect of dispersion may be a useful approach to dealing with the problem and enabling it for various frequency ranges and materials [11]. Green shielding would be impossible without developing a numerical method to analyze complicated modes, configurations, and applications. Therefore, a verified numerical technique is necessary for parametrically analyzing the functions and monitoring the resulting behaviors that STM media provide for green shielding.

Tackling the abovementioned procedures requires thorough expertise in electromagnetics and microwaves. Estimating the shields' performances in terms of shielding effectiveness (SE) level, verifying their compliance with regulatory organizations such as the Federal Communications Commission (FCC) or Innovation, Science and Economic Development Canada (ISED), extracting equivalent circuit models (ECM) for miniaturized meta-surfaces, and analyzing crosstalk effects in adjacent circuits requires a solid understanding of Electromagnetic Compatibility (EMC). Proposing an analytical solution for the nearfield performance of passive meta-surfaces requires theoretical knowledge of nearfield transmission and reflection problems. Fabricating the proposed structures and measuring their farfield and nearfield performances through different scenarios require experimental knowledge and the ability to work with a Vector Network Analyzer (VNA) and calibration techniques.

On the other hand, to develop methods for green shielding using actively disturbed media, knowledge about the fundamental aspects of space-time modulated (STM) media will be useful. Part of this work uses computational methods to investigate the media's shielding performance. Knowing about the Method of Moments (MoM) technique and the Finite Difference Time Domain (FDTD) method simplifies the grasp of green shielding simulations. However, those familiar with numerical methods can still benefit from the analyses, achievements, and conclusions regarding green shielding techniques. Lastly, optimization techniques using nature-inspired evolutionary algorithms (EA) are used sporadically throughout the literature. Taking courses such as "Advanced Electromagnetics," "Electromagnetic Compatibility," "Active Microwave Circuits," "Microwave Engineering," and "Antenna Engineering" are highly recommended for an efficient understanding of the concepts.

1.2 Problem Statement

The shielding problems addressed in this work follow two mainstreams with two distinct solution approaches: passive and active. A passive approach focuses on FSS designs to address NF shielding, while the active approach incorporates STM media for green shielding purposes.

1.2.1 An Overview of Passive NF shielding problem

The diagram in Figure 1.1(a) provides a conceptual overview of the passive radiation susceptibility problem being studied. The distance between the shield and the protected object (the susceptible object) is denoted as "r." In compact packages and wearable technology applications, this distance typically falls within the near-field (NF) zone, which ranges from zero

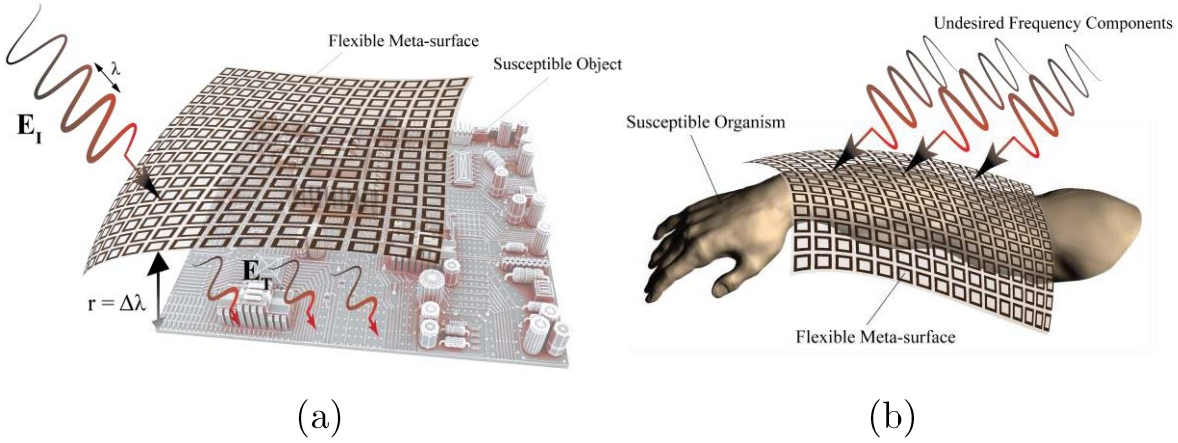

Figure 1.1. NF radiation susceptibility problem [5,6]. The distance between the flexible shield and the susceptible objects (r) may be referred to as observation distance and could be a fraction of wavelength in compact shields. (a) NF Shielding susceptible products, (b) NF Shielding of living organisms such as human body

to a fraction of the wavelength. Figure 1.1(b) demonstrates the potential use of a flexible shield to protect the human body or a living organism. For example, in the case of a smart-watch or receptor chip operating at 2.5 GHz, the shield should prevent the harmful X-band components while allowing lower frequency components that need to be transmitted toward the body for specific purposes. Several examples of electromagnetic shielding methods, specifically designed for the nearfield zone exist. These methods lack a frequency selective characteristic, leading to increasing interference or susceptibility.

Conductive Enclosures: Enclosures made of conductive materials isolate and protect devices from close-range electromagnetic interference.

Metamaterial Cloaks: Specially crafted metamaterials can manipulate electromagnetic waves, creating cloaks that divert or absorb nearby electromagnetic radiation.

Magnetic Shields for Small Devices: Compact shields, crafted from high-permeability materials, are designed to shield small electronic components from nearby magnetic interference.

Nearfield Absorbers: The strategic placement of absorptive materials absorbs and dissipates electromagnetic energy in the nearfield, minimizing reflections and resonances.

Resonant Absorbers: Specially designed structures resonate at specific frequencies, absorbing and dissipating electromagnetic energy in the nearfield, suitable for scenarios requiring targeted frequency absorption.

Electrically Conductive Coatings: Coatings that contain conductive particles or materials, when applied to surfaces, establish a conductive layer, effectively shielding electronic devices or enclosures from nearby electromagnetic interference.

Isolation Transformers: Transformers designed for electrical isolation between circuits, commonly used in power distribution to prevent electrical noise from interfering with sensitive equipment nearby.

However, a slight shift in the resonant frequency of the Frequency Selective Surface (FSS) used in the shield could result in degradation of the NF shielding performance, leading to undesired radiation leakage into the cover towards susceptible circuits or living tissues [5]. It is crucial to accurately address any variations in the resonant frequency to maintain the practicality of the shield. Additionally, the use of flexible FSSs in rough configurations can lead to near-field (NF) and far-field (FF) malfunction [12-16]. Moreover, the finite non-spherical dimensions of shields can cause edge diffraction as another source of degradation in the NF shield performance.

In order to be able to estimate the capability of a shield in these applications, the following questions may be answered:

- What are the differences between the NF and FF shielding response of the FSS shield?
- What is the relation between the NF and FF responses in a shield?
- What is the physical interpretation for shielding discrepancies in NF and FF?
- What are the criteria for measuring the NF performance of shields?
- Is there a theoretical approach to estimate/model the NF behavior of a shield?
- How would the NF shielding response be affected in conformal structures?
- How does edge diffraction affect conformable shields, specifically in the NF zone?
- What disadvantages of conventional FSSs make them unsuitable for NF shielding?
- How is a flexible shield designed to simultaneously provide the desired FF and NF response?

The shielding problem addressed in this work involves a hypothetical susceptible object and an interfering or hazardous signal. The susceptible object is only sensitive to a certain frequency band (X-band), while communication through other frequency bands is permitted. Therefore, two desired and undesired frequency components need to be defined. The shield is expected to block the undesired component while allowing the desired component to pass. It will be shown that this cannot be achieved through conventional structures as they exhibit unstable near-field (NF) shielding behavior. As a result, there will still be some interference (such as biological hazards or component malfunctions) when conventional unit cells are used in a wearable shield. The NF response of conventional structures experiences predictable instability, leading to a degradation in the expected attenuation level of the shield. A model will be proposed to predict this abnormality in single-layer, one-sided structures. Then, a structural solution to overcome these NF instabilities will be developed and verified at different stages of cell performance, geometrical effects, and incidence effects.

1.2.2 An Overview of Active Green Shielding Problem

Advancing wireless communication technologies and devices has filled our environment with meandering electromagnetic pollution. Electromagnetic pollution, also known as electromagnetic radiation (EMR), refers to the presence of electromagnetic waves in the environment that can negatively affect human health and the environment [17]. Electromagnetic radiation comes from various sources, including power lines, cell phones, Wi-Fi, radio and television broadcasting, and many other electronic devices. While electromagnetic radiation is a natural part of the environment, the increasing use of technology has significantly increased electromagnetic pollution. Cell phones and Radar radiation are becoming the main sources of high-frequency radiation, while power lines and electrical wiring can emit low-frequency electromagnetic radiation, which can also negatively affect human health or create interference. In nature, these waves are absorbed by natural substances such as forests, oceans, snow-covered mountains, etc. However, in civilized municipal areas, indoor environments, and workplaces, numerous causes reduce absorption while increasing the secondary reflections. These secondary reflections highly increase electromagnetic pollution and interference (e.g., in the interferences in RF laboratories), as shown in Figure 1.2.

Limiting exposure to electromagnetic radiation is important to reduce the negative effects of electromagnetic pollution. This can include using wired rather than wireless devices, limiting the time spent on electronic devices, and avoiding areas with high levels of electromagnetic radiation, such as near power lines or electrical transformers. Recently, new passive materials have been invented in order to provide high absorption of electromagnetic waves [9, 17]. These materials highly reduce the secondary reflections, leaving the environment free of EM pollution. However, they dampen the whole frequency bands, leading to data loss, which might not be desirable for many wireless communication systems [10]. We will show that incorporating periodic disturbance using the space-time modulation concept can satisfy this need with unprecedented features. The following essential questions need to be answered in order to address this problem:

- How can actively disturbed media behave as a shield?
- Is there any possibility of providing shielding for one frequency component (band) while preserving the data?
- How is tunability achieved for such a disturbed medium?
- What is the relation between amplification and shielding in such a medium?
- How far is the current technology from fabricating such active components?
- What are the future applications for such a technology?

Through this study, the questions above will be answered thoroughly. Since the available analytical methods for analyzing STM media behavior are for lossless cases, the first step for

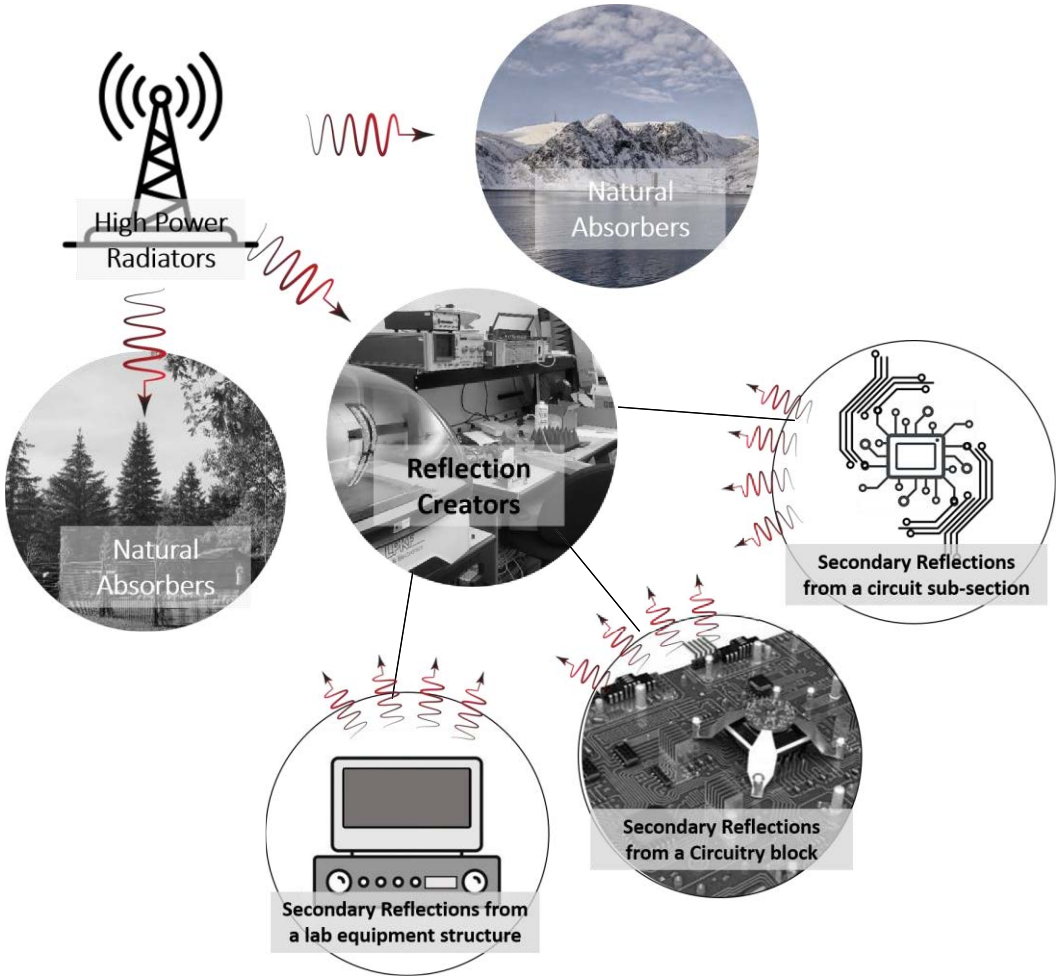

Figure 1.2. A conceptual illustration of secondary reflections and electromagnetic pollutions in workplaces versus nature.

analyzing the shielding properties of STM media is to develop the analytical approach to account for losses and dispersion where applicable. Thus, the theoretical representation of space-time modulated media, where the effect of losses will be added to the formulations, will be considered. Then, a numerical model will be developed based on the theoretical analysis. After validation, green shielding methods will be investigated in sinusoidally disturbed media.

1.3 Literature Review

Shielding against electromagnetic (EM) emissions has been around since the early 1960s when the skin depth of different conductors was examined [18]. The theory of shielding stems from the fundamental phenomenon of wave attenuation (i.e., the shallow skin depth) in conductors and the dependency of this attenuation on the operation frequency, medium conductivity, or the dispersive characteristic of the dielectric. Shielding might have biological or industrial motives. According to Federal Communications Commission (FCC) codes, the thermal effect is the main regulated hazard known for EM emissions. Aside from the heating problems, the exposure to high-power radiations might cause growing concerns about EMI

biological hazards, specifically X-Band radiations [19-21] (the reader is also referred to [19-28] for more information). From an industrial point of view, shield designers need to protect their susceptible circuit/device/component by making the coupling path as inefficient as possible.

The biological and industrial concerns led to extensive efforts toward EM shielding, where various materials have been analyzed regarding EMI shielding effectiveness, skin depth, and dissipated power, assuming being exposed to high-power emissions [29-33]. Traditional shielding methods involve using conductive filler composites and conductive fabrics produced by metals and their alloys. The commercially available EMI shields include but are not limited to metal-coated carbon fiber, metalized cloths, sprayed coating on substrates, and shielding tents (specifically for military applications) [1, 34]. Polymers and Nanocomposites [35, 36], porous composites [37], and Graphene-based foams [38] are some of the popular materials used for EMI reduction. Other special materials used for these purposes are featured in [1]. MXenes (Maxenes) are newly investigated materials that provide lightweight EMI shielding [39]. The readers may be referred to [40-44] for more information about passive EMI materials.

While the aforementioned materials and methods have widely been investigated and employed by companies, they are mainly designed to suppress the whole spectrum of the incident signal. That is to say, if the main signal contains two desired and undesired frequency spectrums, the shields are not capable of separating these two. These shields may be called "all-band shields," where the performance is usually measured based on the amount of attenuation the lowest applicable frequency experiences within a specific thickness/depth of the shield.

The emergence of frequency selective surfaces (FSSs) initiated a new trend in designing passive shields with a filtering characteristic. This way, the desired frequencies could pass the shield toward the shielded target while the undesired frequency components are filtered out (being reflected). Low pass [45], band pass [46, 47], band stop [7], high pass, and multi-band [48-50] filters have been realized using single- or multi-layer FSS. Shielding against radiated electromagnetic (EM) emissions [5, 8, 51-54], filtration [46], polarizing [55], and beam alteration [56] are some of the other ever-growing FSS applications. It has been shown that properly cascading such surfaces can realize any desired multipole response or non-commensurate multiband filter [57, 58]. From a shielding perspective, FSSs have noticeably been used to provide protection against radio waves of different spectrums [12-15, 59]. For instance, a 2.5-dimensional structure was proposed in [12] that provides dual-band shielding for GSM band waves with the minimum applicable distance of 1.5 m and 41-49 dB effectiveness. Room shielding against X-band emissions was investigated in [59] where an engineered band-stop FSS with an elaborate equivalent circuit model (ECM) was incorporated efficiently. WiMAX, WLAN, and ISM/WiMAX emissions can be shielded using a mechanically tunable FSS introduced in [54]. Ultra-wideband shielding was another attempt to reduce the negative X-band hazards of radar measurement systems' emissions [53]. This has been achieved by two layers of cladding, each of which operates in a different sub-band. There has been a surge toward reconfigurable shields, but the designs usually lead to inflexible structures with unattended

complexities that make them unsuitable for wearable applications. A reconfigurable polarization-insensitive varactor-based FSS was introduced in [60] to provide tunable shielding for 0.5-3 GHz. As stated, the shields involve tens of varactor diodes that might alter the performance of the shield through the malfunction of a single element. Readers are also referred to [52, 61] for more information about FSS shields.

FSS Shield Designers usually avoid dealing with near-field (NF) areas as they are not confident about the NF performance of FSS structures. Therefore, the lack of reliable NF attenuation leads to inevitable bulky fabricated products as the manufacturers have to increase the distance between the shield and the susceptible circuit on the orders of multiples of wavelength to maintain the securely stable attenuation level of the embedded shield. Therefore, a stable NF performance guarantees the feasibility of compactly shielded products. For the cases of wearable applications, where the goal is to prevent passing particular frequency components toward a living organism (skin, enzymes, or brain cells), the wearable surfaces are expected to reflect the undesired spectrum. At the same time, they are located within a small fraction of wavelength away from the susceptible object. This fraction of wavelength for the X-Band spectrum is roughly within a range of 1-50 mm, which is of great importance for such wearable biomedical applications.

To the author's knowledge, almost all the available shields have been designed to provide farfield characterization, which may be considered an indispensable gap [12-16]. On the other hand, designing wearable/flexible shields for compact shielded products necessitates a solid knowledge of the shield's nearfield (NF) properties. Meanwhile, the NF point of view critically lacks the required investigations. Only a few studies provide limited analyses of curved structures without giving clear nearfield information [7, 62]. For instance, in [62], the proposed split-ring resonators (SRRs) meta-skin showed unstable FF scattering suppression over different incident angles when wrapped around a dielectric rod. A limited number of investigations have tried to reduce the distance between the shield and the susceptible object without pinpointing the NF properties of the shield. A 10 dB X-band attenuation is reported when a flexible FSS is wrapped around an antenna in a conformal structure with a curvature radius of 77 mm [63]. The shielding effectiveness of conformal structures was investigated in [7] and [64], where the receiving probes have maximally been placed at a distance of 50 cm and 20 cm from the structure, respectively. In addition, the curvature radius used is about $4\lambda - 8\lambda$ in [7], which is considered large and inapplicable for NF wearable applications. While the curvature radius considered in [64] is $2\lambda - 4\lambda$ which may be acceptable. When the requirement of polarization independency in NF zone is added to the specifications, almost no research can be found that targets the issue.

The other shielding challenge that has been drawing much attention recently is the rising questions about the green shielding concept. The investigations of green EMI shielding are carried out to reduce the secondary reflections from shields to the environment [17]. The reduced reflected emissions prevent the workspace from being electromagnetically polluted [9]. Reducing reflections is fundamentally possible by increasing absorption or transmission (the latter is not

the case for shielding purposes). As stated earlier, passive materials have been conventionally used for this purpose. The passive WS2−rGO-based green architecture investigated in [10] provides a minimum shielding effectiveness of 20 dB in 2-18 GHz, while the green index has been reported to be almost one. While the materials mentioned above are aligned with the green EMI shielding goals, they mainly suppress the whole spectrum of the incident signal [9]. Frequency-selective surfaces cannot be good candidates for green shielding as the main mechanism in FSS shields is the reflection in resonant frequency. Therefore, there are at least two problems with the passive shields mentioned above. The conventional green shields are reliable in reducing reflection but cannot be designed for a specific frequency range, leading to data loss.

On the other hand, FSSs can shield a specific frequency while not considered green shields as they reflect the undesired frequencies. In addition, all the mentioned shields practically waste the shielded data (either in the form of reflection or absorption). Consequently, drawing attention to a new class of shielding methods where active materials are used to *harness* the undesired energy in a way that the requirements for green shielding are met, will be a useful attempt. Active components allow the shield to be actively reconfigured for different shielding specifications and frequencies.

1.4 The Necessity Statements

Although we believe that the necessity was implicitly expressed, here, it is further elaborated in terms of the practical and scientific niches that need to be filled regarding NF shielding and Green Shielding.

The passive NF shielding methodology that will be proposed leads to the production of an ultra-thin wearable radiation shield from which many companies and engineers could take advantage. Not only can it provide more compact shielded products, but it can also utilize the shield in electromagnetically polluted environments, resulting in more secure working places. Microwave device producers and wireless sensor manufacturers require such efficient shields to cover their susceptible products. When the shield supports the nearfield feature, it may be placed closer to the susceptible circuits, resulting in a compact shielded product. In high-power laboratories, technicians can use lightweight, ultra-thin wearable shields to protect their bodies from harmful radiation. Companies can develop the designed shield for other NF applications to cover various radiations and frequency bands. Residential areas that are located in the proximity of airport radars or military transmitters could be the other beneficiaries of the research program. There is always some leakage from microwave transmitters, even in academic laboratories, and the ultra-thin NF FSS shields could be designed to protect people from these radiation emissions. Finally, the study brings a new groundwork for future advancements in nearfield shielding with flexible materials.

Investigating green shielding using STM media is necessary and significant, at least for three reasons. First, there was no realization of STM media in 5G and millimeter-wave regions.

One reason is that there is no analytical approach to represent the wave behavior (attenuation or amplification) when the frequency increases. Without such a theory, how can the technology estimate the desired outcome? Thus, there were insufficient estimation tools for power consumption, energy distribution, propagation, and dispersion. Even recent STM developments have avoided exceeding 2 GHz as the loss effect was not predictable for higher frequencies [65]. A recent work investigated the oblique illumination of an STM slab in the sub-6 GHz 5G region without taking the loss into effect in the numerical and analytical calculation [66]. While the lossless methods (analytical and numerical) are in agreement, to realize STM slabs as shields, the loss factor must be incorporated into the calculations, resulting in the desired thickness for the shield. Without taking the loss into effect, estimating the thickness of the slab will be impossible unless one can ensure that the loss effect will be practically negligible (maybe due to the negligible thickness of the STM media). Evidently, these kinds of assumptions would not be the case regarding higher frequencies. Therefore, this concept is also a good fit for wave engineering applications that aim to control and utilize electromagnetic waves in different media [67-70]. This work enables the user to step into higher frequency ranges without missing the loss as a critical factor. Second, this investigation will provide the necessary and sufficient tools for more accurate analysis and reveal some specific interpretations about the behavior of STM harmonics when the wave attenuation is analyzed in the high-loss region. There will be some reports and observations that are unique and necessary. The unwanted/undesired phase shift resulting from the nonlinear dispersion curves of the lossy environment is one of them. Loss makes the dispersion traces curve rather than linear. It points out that each harmonic may experience a different propagation constant that nonlinearly changes versus frequency. Therefore, the phase shifts each harmonic experiences differ from the lossless counterpart (dispersion effect). Conceivably, there was no previous report regarding how dispersion affects STM harmonics. Third, the study utilizes the concept of "zero attenuation frequencies" to design unique shields that can achieve zero reflectivity and amplify desired frequencies.

1.5 The Novelty Statements

- From the passive NF shielding point of view, this work provides several novel contributions using frequency selective surfaces (FSS):

Firstly, this work fills a gap in the literature by providing a numerical representation of the FSS NF attenuation, followed by FF and NF analytical models, which gives a deep intuition of the ongoing problem. This is the first time that such a comparative analysis of four mostly reported FSSs, namely, Split Ring Resonator (SRR), Jerusalem Resonator (JR), Square loop (SL), and Convoluted Square Loop (CSL) has been conducted.

Secondly, this work comprehensively addresses the instability that arises from a gradual convergence in FSS near- to far- field, which is investigated as a special feature of the NF zone. After characterizing the near-field behavior, a novel model is introduced to predict these

instabilities. Based on the observations, the distance criterion for the FSS NF performance is introduced, which may be used in future flexible FSS designs.

Thirdly, this work introduces a new class of X-band flexible shields that provide a stable NF stopband suitable for wearable and compact shields. The proposed structure's reliability is validated through a curved configuration to ensure the stability of resonances of the shield in NF and FF regions, and through a parametric study to find a solution for the narrowband characteristics of the proposed structure.

In summary, the passive part provides several novel contributions to the area of passive nearfield shielding using frequency-selective surfaces, including a numerical representation of the FSS NF attenuation, an approximate theoretical model to estimate NF abnormalities in extreme areas, introducing a distance criterion for NF shielding, and proposing a new class of X-band flexible shields with NF protection capacity.

- From the active green shielding point of view, the proposed work using space-time modulated (STM) media provides several novel contributions.

Firstly, this work addresses a significant gap in theoretical and computational tools used for analyzing lossy STM media, particularly in millimeter-wave regimes. This is unique because, when looking back at recent works, we notice that most of them are limited to low-frequency microwave bands [65, 69, 71-76], and acoustic waves [77-79], where the effects of loss and dispersion are insignificant when it comes to fabricated products [65, 71, 80-84]. The investigation develops analytical and numerical methods and compares the upsides and downsides of each method to deal with the effect of loss in STM media. Despite its complexities, the loss and dispersion effects are added to the space-time modulation formulation, which is novel and significant.

Another novel contribution is the development of a new notion to deal with conductivity in Maxwell equations. The pump wave and signal wave frequencies differ, which means they must experience different losses. This is essential for millimeter-wave regions, and the study modifies the Floquet representation of waves in STM media to account for this effect. The work introduces the SPM method as a good estimation for a high-loss regime, considering the effect of modulation strength.

The work also presents interesting results, such as the effects the dispersion diagram goes through when the conductivity is taken into effect, the phenomenon of extra phase shift that the harmonics experience, the notion of propagation of a specific frequency component without loss in a lossy medium, and the notion of stability and shielding. Additionally, the work develops FDTD update equations for lossy STM media, making it the first work to do so. Before this work, the FDTD was applied to lossless cases only valid for low frequencies (up to 3GHz) [65].

Finally, the proposed work draws attention to a new class of shielding methods where space-time-modulated (STM) materials are used to harness undesired energy to meet the

requirements for green shielding. The shield can be actively reconfigured for different shielding specifications and frequencies, and the equations can be converted from wave theory to transmission line theory, addressing both conducted and radiated emission problems.

Ultimately, the dissertation's view about shielding goes beyond the usual shielding concepts, which opens the door to further novel ideas. We will shed light on the remaining topics related to active shielding. We will discuss the benefits that STM media can provide for the optics and electromagnetics community. The possibilities of making invisibility cloaks in optics and microwave regimes are explored, and the concepts of active cloaking and active shielding are merged to familiarize readers with different terminologies that serve similar purposes. We will emphasize that RCS reduction could be useful for achieving similar camouflage effects in microwave and millimeter wave regimes. Therefore, we will draw the reader's attention to the application of STM media in Radar Cross Section (RCS) reduction as a future method of shielding aircraft from being detected by radars.

Chapter 2: Background

This chapter introduces shielding effectiveness and highlights its significance in the electromagnetic compatibility (EMC) community. Specifically, we will delve into the accurate and approximate methods to derive theoretical formulas for farfield shielding effectiveness, which will provide readers with a deeper understanding of the interaction of shielded materials in the electromagnetic field. Additionally, useful relations for nearfield shielding effectiveness are presented, enabling readers to deal with essential parameters in nearfield shielding. It is important to note that there are fundamental differences between nearfield and farfield shielding effectiveness, which we will discuss in detail. By the end of these sections, readers will have gained a comprehensive understanding of shielding effectiveness and its crucial role in EMC design and implementation.

2.1 Shielding

In scientific terms, a "shield" is a metallic enclosure that can surround an object or product susceptible to electromagnetic contamination. The purpose of shielding is twofold. Firstly, it aims to prevent a product from emitting interference that could harm living organisms or interfere with other products. Secondly, it aims to protect a susceptible object from any damage or malfunctions caused by unwanted emissions. The Federal Communications Commission (FCC) and Industry Canada (IC) regulate all types of communications in the US and Canada. Therefore, products must be designed within the limits defined by these regulators. These limits are based on four electromagnetic compatibility problems: Radiated Emissions and Susceptibility, Conducted Emissions, and Susceptibility. Shielding helps companies keep their product emissions within authorized limits and protect them from unregulated radiations or conductions.

2.2 Shielding Effectiveness (SE)

Shielding effectiveness of a shield can be quantitatively defined as the ratio between the electric/magnetic field intensity impinging on the surface and the transmitted electric/magnetic field, expressed as

$$SE = 20\ log \left| \frac{\widehat{\boldsymbol{\chi}}_{\boldsymbol{I}}}{\widehat{\boldsymbol{\chi}}_{\boldsymbol{T}}} \right| \tag{2.1}$$

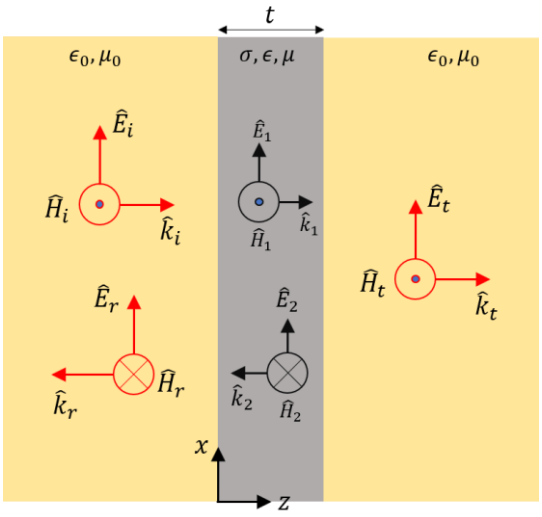

Figure 2.1. A shield exposed to a uniform plane wave that strikes it perpendicularly.

where the subscripts I and T refer to the incident and transmitted waves, respectively, and $\hat{\chi}$ denotes the electric or magnetic fields. The hat symbol denotes the use of complex quantities throughout the dissertation. Figure 2.1 illustrates this problem where a shield slab is surrounded by free space. When the media around the shield are identical, and a uniform plane wave impinges on the surface, the electric and magnetic fields will produce identical SE results due to their association with the intrinsic impedance of the medium. However, two distinct SE values may be defined for inhomogeneous media or NF zones, either electric-field- or magnetic-field-based. As implied by (2.1), since the incident field magnitude is always larger than the transmitted field magnitude, the dB value of SE is supposed to be a positive number.

Various phenomena reduce the incident field passing through a shield barrier. The first effect is a reflection at the left surface of the barrier, where a portion of the incident electric field is reflected according to the reflection coefficient for that surface. The second effect is absorption loss, where the amplitude of the wave crossing the barrier is attenuated exponentially due to the conductive medium it passes through, and the factor governing this attenuation is $e^{-\alpha z}$, where α is the attenuation constant of the material. The third effect is multiple reflections and transmissions that occur as the wave crosses the barrier, which is progressively attenuated by their travel through the conductive barrier. However, if the shield is designed to have a thickness much greater than the skin depth of the material ($\delta = 1/\alpha = 1/\sqrt{\pi f \mu \sigma}$, for good conductors) at the frequency of the anticipated incident field, the continued reflections and transmissions can be disregarded, and only the initial reflection and transmission at the left and right interfaces need to be considered. Nevertheless, for a slab surrounded by identical media and under the normal incidence of plane waves, the SE given in (2.1) can be represented by

$$SE = R_{dB} + A_{dB} + M_{dB} \tag{2.2}$$

where R refers to the reflection loss caused by reflections at the two interfaces of the shield layer, A is the absorption loss of the wave as it proceeds through the shield, and M represents the effect of multiple reflections and transmissions. Note that considering a positive value for SE

(the shield is passive, and the incident field is supposed to be stronger than the transmitted field), A and R are positive values, while M has a negative value in a way that

$$|R_{dB} + A_{dB}| > |M_{dB}| \tag{2.3}$$

If (2.3) is not satisfied, the shield will not operate properly. There are two types of shielding, FF and NF, which have different properties and require different analyses depending on the electrical position of the source or susceptible objects. In order to analyze any shield or create analytical models for farfield Shielding Effectiveness (FF SE) and Nearfield Shielding Effectiveness (NF SE) in meta-surfaces, we will utilize the separate notations of R, A, and M, as previously mentioned. The next section of this dissertation will delve further into FF and NF shielding and their significance.

2.3 Farfield Shielding Effectiveness (FF SE)

This section assumes that the shield slab is being illuminated by far-field sources, which means that the incident field can be approximated as a uniform plane wave. We will explore both precise and rough estimates for the shielding effectiveness.

2.3.1 Precise Estimates

To find the exact solution for how well a shield blocks electromagnetic waves, we must solve the problem depicted in Figure 2.1. The problem involves a shield slab with a thickness of t, with free space assumed to be present on both sides of the shield. A uniform plane wave is emitted towards the left surface of the shield. According to Maxwell's equations, forward and backward-traveling waves are present in the left medium and shield. However, only a forward-traveling wave is expected in the medium to the right of the shield since no additional barrier exists to create a reflected field. The electric fields with known and unknown coefficients are represented as follows,

$$\vec{\hat{E}}_i = \hat{E}_{i0} e^{-jB_0 z} \vec{a}_x \tag{2.4}$$
$$\vec{\hat{E}}_r = \hat{E}_{r0} e^{+jB_0 z} \vec{a}_x \tag{2.5}$$
$$\vec{\hat{E}}_1 = \hat{E}_{10} e^{-j\hat{\gamma} z} \vec{a}_x \tag{2.6}$$
$$\vec{\hat{E}}_2 = \hat{E}_{20} e^{+j\hat{\gamma} z} \vec{a}_x \tag{2.7}$$
$$\vec{\hat{E}}_t = \hat{E}_{t0} e^{-jB_0 z} \vec{a}_x \tag{2.8}$$

where $\hat{E}_{r0}, \hat{E}_{10}, \hat{E}_{20}, \hat{E}_{t0}$ are unknown. $B_0 = \omega\sqrt{\mu_0 \epsilon_0}$ is the phase constant in free space and $\hat{\gamma}$ is the complex propagation constant inside the shield, identified by

$$\hat{\gamma} = \sqrt{j\omega\mu(\sigma + j\omega\epsilon)} = \alpha + j\beta \tag{2.9}$$

The magnetic fields associated with (2.5) -(2.8) are calculated by $\vec{\hat{H}} = \frac{1}{\eta}\vec{k} \times \vec{\hat{E}}$, where η represents the intrinsic impedance of the medium where the conversion occurs. For free space $\eta = \sqrt{\mu_0/\epsilon_0}$. while for the shield,

$$\eta = \sqrt{\frac{j\omega\mu}{\sigma + j\omega\epsilon}} \tag{2.10}$$

To find the unknown coefficients, we require four equations obtained by applying the boundary conditions on the field vectors at the two shield boundaries, as depicted in Figure 2.1. The four equations are derived from ensuring the continuity of tangential electric and magnetic fields at the two interfaces (z=0 and z=t), assuming there is no electric or magnetic current source on the interface).

$$\hat{E}_{i0} + \hat{E}_{r0} = \hat{E}_{10} + \hat{E}_{20} \tag{2.11}$$

$$\hat{E}_{10}e^{-j\hat{\gamma}t} + \hat{E}_{20}e^{+j\hat{\gamma}t} = \hat{E}_{t0}e^{-jB_0t} \tag{2.12}$$

$$\frac{\hat{E}_{i0}}{\eta_0} - \frac{\hat{E}_{r0}}{\eta_0} = \frac{\hat{E}_{10}}{\eta} - \frac{\hat{E}_{20}}{\eta} \tag{2.13}$$

$$\frac{\hat{E}_{10}}{\eta}e^{-j\hat{\gamma}t} - \frac{\hat{E}_{20}}{\eta}e^{+j\hat{\gamma}t} = \frac{\hat{E}_{t0}}{\eta_0}e^{-jB_0t} \tag{2.14}$$

Solving the system of equations yields the following relation for $\widehat{\boldsymbol{E}}_{\boldsymbol{i}}/\widehat{\boldsymbol{E}}_{\boldsymbol{t}}$

$$\frac{\widehat{\boldsymbol{E}}_{\boldsymbol{i}}}{\widehat{\boldsymbol{E}}_{\boldsymbol{t}}} = \frac{(\eta_0 + \hat{\eta})^2}{4\eta_0\hat{\eta}}\left[1 - \left(\frac{\eta_0 - \hat{\eta}}{\eta_0 + \hat{\eta}}\right)^2 e^{-2\gamma t}\right]e^{\gamma t}e^{-jB_0t}, \tag{2.15}$$

which is the precise solution for the problem in Figure 2.1. The precise value for shielding effectiveness will be

$$\begin{aligned} SE_{dB} &= 20\,log\left|\frac{\widehat{\boldsymbol{E}}_{\boldsymbol{i}}}{\widehat{\boldsymbol{E}}_{\boldsymbol{t}}}\right| \\ &= 20\log\left(\left|\frac{(\eta_0 + \hat{\eta})^2}{4\eta_0\hat{\eta}}\left[1 - \left(\frac{\eta_0 - \hat{\eta}}{\eta_0 + \hat{\eta}}\right)^2 e^{-2\gamma t}\right]e^{\gamma t}\right|\right) \\ &= 20\log\left(\left|\frac{(\eta_0 + \hat{\eta})^2}{4\eta_0\hat{\eta}}\right|\right) + 20\log\left(\left|1 - \left(\frac{\eta_0 - \hat{\eta}}{\eta_0 + \hat{\eta}}\right)^2 e^{-2\gamma t}\right|\right) + 20\log(|e^{\gamma t}|) \\ &= 20\log\left(\left|\frac{(\eta_0 + \hat{\eta})^2}{4\eta_0\hat{\eta}}\right|\right) + 20\log\left(\left|1 - \left(\frac{\eta_0 - \hat{\eta}}{\eta_0 + \hat{\eta}}\right)^2 e^{-2\gamma t}\right|\right) + 20\log(e^{\alpha t}) \end{aligned} \tag{2.16}$$

For the cases where the shield is made up of a good conductor ($|\hat{\eta}| \ll \eta_0$) and the shield thickness is much greater than the skin depth of the conductor ($t \gg \delta = 1/\alpha$), the equation above can be simplified to

$$SE_{dB} = \underbrace{20\log\left(\left|\frac{\eta_0}{4\hat{\eta}}\right|\right)}_{R_{dB}} + \left(M_{dB}\Big|_{M_{dB} \cong 0}\right) \underbrace{+ 20\log\left(e^{\frac{t}{\delta}}\right)}_{A_{dB}} \tag{2.17}$$

Knowing that the first and third factors of (2.17) are reflection loss and absorption loss, the middle factor will be multiple transmission and reflection that converge to zero for this condition.

2.3.2 Rough Estimates

This section will demonstrate how to solve the problem shown in Figure. 2.1, the same result can be derived by approximate methods without any significant loss in accuracy. The reason we are interested in rough estimates lies in the fact that they have the potential to be extended or modified for different surfaces and configurations. This approach employs a technique comparable to the one utilized to determine the gain for cascaded amplifiers. Consequently, the reflection loss, absorption loss, and multiple transmissions and reflections are evaluated independently.

2.3.2.1 Reflection Loss

In order to estimate the reflection loss, we first need to eliminate the effect of absorption loss and multiple transmission and reflection loss. The effect of absorption loss is an exponential factor that can be added later. To remove the effect of multiple transmission and reflection, we assume the thickness of the barrier is much larger than the skin depth. Then, the transmitted part of the wave across the left interface (E_1) is significantly weakened by the time it reaches the right interface. As a result, the reflected wave (E_2) arriving at the left interface is insignificant and contributes minimally to the total reflected wave (E_r). Hence, the transmission from the left interface of Figure 2.1 can be approximated by transmission between two infinite media

$$\frac{\widehat{\boldsymbol{E}}_{\boldsymbol{1}}}{\widehat{\boldsymbol{E}}_{\boldsymbol{i}}} \cong \frac{2\hat{\eta}}{\eta_0 + \hat{\eta}} \tag{2.18}$$

Similarly, transmission from the right interface can be written as

$$\frac{\widehat{\boldsymbol{E}}_{\boldsymbol{t}}}{\widehat{\boldsymbol{E}}_{\boldsymbol{1}}} \cong \frac{2\eta_0}{\eta_0 + \hat{\eta}} \tag{2.19}$$

In the *absence of attenuation*, the total transmitted wave can be estimated when the following relation is used.

$$\begin{aligned} \frac{\widehat{\boldsymbol{E}}_{\boldsymbol{t}}}{\widehat{\boldsymbol{E}}_{\boldsymbol{i}}} &= \frac{\widehat{\boldsymbol{E}}_{\boldsymbol{t}}}{\widehat{\boldsymbol{E}}_{\boldsymbol{1}}} \times \frac{\widehat{\boldsymbol{E}}_{\boldsymbol{1}}}{\widehat{\boldsymbol{E}}_{\boldsymbol{i}}} \cong \frac{2\eta_0}{\eta_0 + \hat{\eta}} \frac{2\hat{\eta}}{\eta_0 + \hat{\eta}} \\ &\cong \frac{4\eta_0\hat{\eta}}{(\eta_0 + \hat{\eta})^2} \end{aligned} \tag{2.20}$$

The reflection loss will be

$$\boldsymbol{R_{dB}} = \boldsymbol{20log}\left|\frac{\widehat{\boldsymbol{E}}_{\boldsymbol{i}}}{\widehat{\boldsymbol{E}}_{\boldsymbol{t}}}\right| \cong \boldsymbol{20log}\left|\frac{(\eta_0 + \hat{\eta})^2}{4\eta_0\hat{\eta}}\right| \tag{2.21}$$

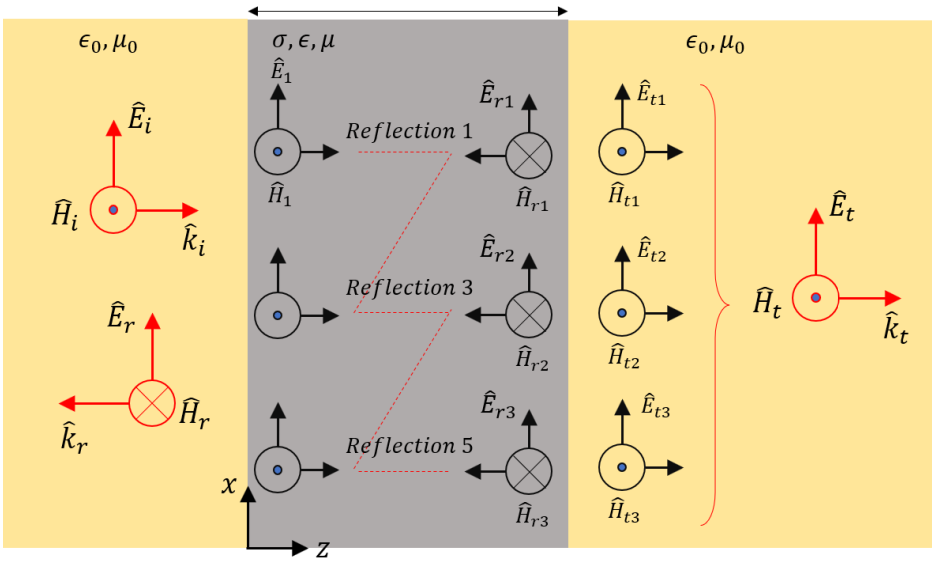

Figure 2.2. Multiple reflections and transmissions

2.3.2.2 Absorption Loss

So far, we have assumed that the thickness of the barrier was significantly larger than the skin depth, allowing for the separation of calculations of reflections and transmissions at the two interfaces. However, the calculation of the product of the two transmission coefficients in equation (2.20) assumes that the amplitude of $\widehat{\boldsymbol{E}}_{\boldsymbol{1}}$ is identical at both interfaces. In reality, the magnitude of $\widehat{\boldsymbol{E}}_{\boldsymbol{1}}$ at the right interface will be considerably decreased from its value at the left interface by a factor of $e^{-\alpha t}$. To include this attenuation, one can multiply equation (2.20) by $e^{-\frac{t}{\delta}}$ to obtain the absorption factor that accounts for attenuation. The absorption loss is introduced as

$$\boldsymbol{A_{dB} = 20 log e^{\frac{t}{\delta}}} \tag{2.22}$$

2.3.2.3 Multiple Transmission and Reflection Loss

If the thickness of the barrier is not significantly greater than the skin depth, as previously assumed, then "secondary reflections and transmissions" may be essential. In cases where multiple reflections are significant, they are included using a multiple-reflection factor provided in equation (2.16). Figure 2.2 illustrates this concept. The total transmitted electric field is the sum of the primary and secondary transmitted waves at the right interface.

$$\widehat{\boldsymbol{E}}_{\boldsymbol{t}} = \widehat{\boldsymbol{E}}_{\boldsymbol{t_1}} + \widehat{\boldsymbol{E}}_{\boldsymbol{t_2}} + \widehat{\boldsymbol{E}}_{\boldsymbol{t_3}} + \cdots \tag{2.23}$$

$$= \widehat{\boldsymbol{E}}_{\boldsymbol{t_1}}(1 + \Delta_1 + \Delta_2 + \cdots)$$

where $\widehat{\boldsymbol{E}}_{\boldsymbol{t_1}}$, $\widehat{\boldsymbol{E}}_{\boldsymbol{t_2}}$, $\widehat{\boldsymbol{E}}_{\boldsymbol{t_3}}$, etc., represent the multiple transmissions of the wave trapped inside the slab. According to Figure 2.2, every time the wave hits the two interface and exit the right interface, a reflection factor of $\hat{\Gamma}_{21}$ or $\hat{\Gamma}_{23}$ is multiplied by the initial wave expression, $\widehat{\boldsymbol{E}}_{\boldsymbol{1}}$, splitting it into a reflection part and a transmission part. In addition, each time it travels between the two interfaces, an attenuation factor of $e^{-2\gamma t}$ associated with medium conductivity is multiplied by the term. Thus $\widehat{\boldsymbol{E}}_{\boldsymbol{t_2}} = \Delta\widehat{\boldsymbol{E}}_{\boldsymbol{t_1}}$, $\widehat{\boldsymbol{E}}_{\boldsymbol{t_3}} = \Delta\widehat{\boldsymbol{E}}_{\boldsymbol{t_2}}$ with $\Delta = \hat{\Gamma}_{21}\hat{\Gamma}_{23}e^{-2\gamma t}$. Assuming $|\Delta| < 1$, the total transmitted field is

$$\widehat{\boldsymbol{E}}_{\boldsymbol{t}} = \widehat{\boldsymbol{E}}_{\boldsymbol{t_1}}(1 + \Delta + \Delta^2 + \cdots) = \frac{\widehat{\boldsymbol{E}}_{\boldsymbol{t_1}}}{1 - \Delta} \tag{2.24}$$

The SE can be estimated by

$$\begin{aligned} SE_{dB} &= 20\log\left(\left|\frac{\widehat{\boldsymbol{E}}_{\boldsymbol{i}}}{\widehat{\boldsymbol{E}}_{\boldsymbol{t}}}\right|\right) \\ &= 20\log\left(\left|\frac{\widehat{\boldsymbol{E}}_{\boldsymbol{i}}}{\widehat{\boldsymbol{E}}_{\boldsymbol{t_1}}}\right|\right) + 20\log(|1 - \Delta|) \end{aligned} \tag{3.25}$$

Knowing that the first term is $R_{dB} + A_{dB}$, multiple reflection and transmission loss are found as

$$M_{dB} = 20\log(|1 - \Delta|) = 20\log\left(\left|1 - \left(\frac{\eta_0 - \hat{\eta}}{\eta_0 + \hat{\eta}}\right)^2 e^{-2\hat{\gamma}t}\right|\right) \tag{2.26}$$

This methodology will be used in Chapter 3 to find the FF shielding effectiveness of single-layer, single-sided frequency selective surfaces.

2.4 Nearfield Shielding Effectiveness (NF SE)

Farfield analysis of a conductive wall Shielding Effectiveness (SE) assumes the incidence of a uniform plane wave normal to the interface of the shield. This section reviews the considerations adopted for nearfield sources. It will be explained that a difference between magnetic and electric sources needs to be considered when nearfield SE is calculated for each source. Similarly, different shielding techniques might be used for each source type. Readers are also referred to [18, 85-87] for more information about magnetic shielding. It must be highlighted that, unlike farfield formulas for SE, achieving high-accuracy estimations in the NF region is rare as the region's field distributions are complicated. Therefore, the available NF solutions are highly approximate. The core of the NF approximation is based on replacing the free space intrinsic impedance ($\eta_0 = \sqrt{\mu_0/\epsilon_0}$) in FF relations by the wave impedance ($\hat{z}_w$) of the electric or magnetic infinitesimal dipoles. This is due to the proven assumption that NF sources are either electric or magnetic, and the impedance of the impinging waves might have a major effect

on the shield's performance [18, 88]. It is a seemingly rough approximation, but the investigation in [88] proves the relatively precise results it will provide. To comprehend this phenomenon, consider that when a wave (not necessarily a plane wave) is emitted, normally, on a medium with the intrinsic impedance of $\hat{\eta}$, the reflection and transmission behavior is a function of the wave impedance as follows

$$\Gamma = \frac{\hat{\eta} - \hat{z}_w}{\hat{\eta} + \hat{z}_w} \tag{2.27}$$

$$\mathrm{T} = \frac{2\hat{\eta}}{\hat{\eta} + \hat{z}_w} \tag{2.28}$$

where Γ and T are the reflection and transmission coefficients of the interface. Two mechanisms exist based on the location of the source

1-If the source is in the FF region, then the components of E_θ and H_ϕ are orthogonal with a constant ratio equal to the intrinsic impedance of the medium ($\eta_0 = E_\theta / H_\phi$). Therefore, $\hat{z}_w = \eta_0$.

2-If the source is located in the NF region, the above condition is invalid. Different wave impedances may be defined based on the source type. In addition, the wave impedance is a strongly nonlinear function of this case's position vector (r). The latter is what will be discussed in this section in terms of electric and magnetic sources.

2.4.1 Electric and Magnetic Sources

Consider the electric field radiation pattern of a small electric source (i.e., z-directed Hertzian Dipole) as

$$\widehat{\mathrm{E}}_\mathrm{r} = \eta_0 \frac{I_0 l \cos\theta}{2\pi r^2}\left[1 + \frac{1}{jB_0 r}\right] e^{-jB_0 r} \tag{2.29}$$

$$\widehat{\mathrm{E}}_\theta = j\eta_0 \frac{B_0 I_0 l \sin\theta}{4\pi r}\left[1 + \frac{1}{jB_0 r} - \frac{1}{(B_0 r)^2}\right] e^{-jB_0 r} \tag{2.30}$$

$$\mathrm{E}_\phi = 0 \tag{2.31}$$

In the NF region, the field components vary with the factors of $1/r$, $1/r^2$ and $1/r^3$ so that the wave impedance is not identical to the intrinsic impedance ($\hat{E}_\theta / \hat{H}_\phi \neq \eta_0$). Using Maxwell's equation to calculate $\hat{H}_\phi$, the NF wave impedance for a Hertzian dipole is

$$\hat{Z}_{we} = \frac{\hat{E}_\theta}{\hat{H}_\phi} = \eta_0 \frac{\frac{j}{B_0 r} + \frac{1}{(B_0 r)^2} - \frac{j}{(B_0 r)^3}}{\frac{j}{B_0 r} + \frac{1}{(B_0 r)^2}} \tag{2.32}$$

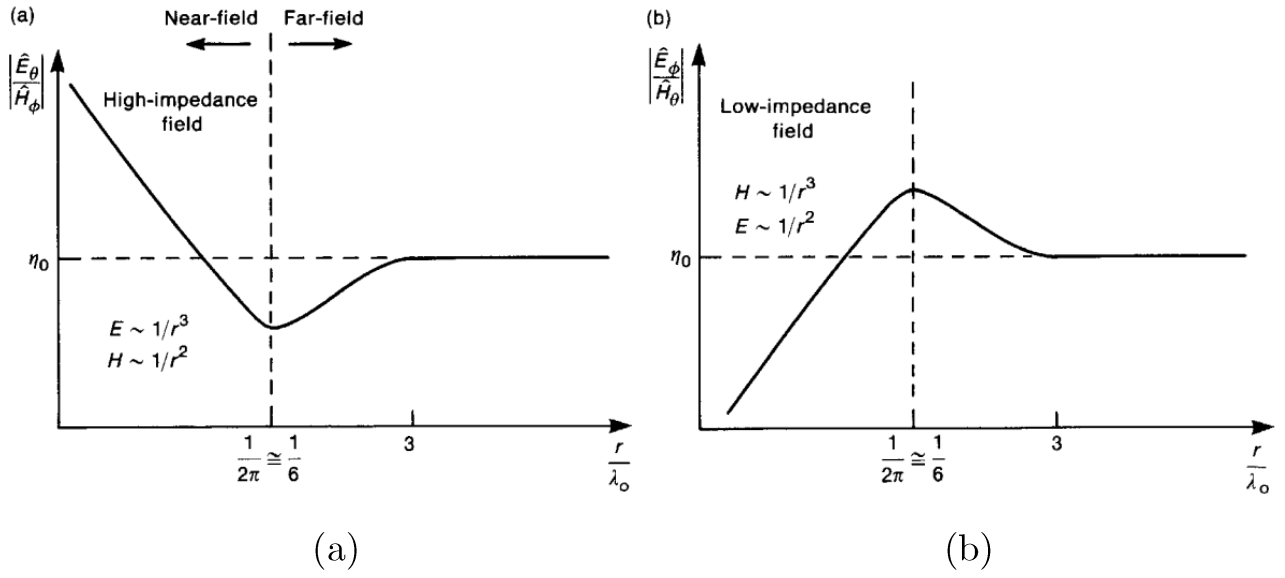

(a) (b)

Figure 2.3. Wave impedance of (a) Electric Dipole, (b) Magnetic Dipole (Image from [18] page 738).

In FF where $B_0 r \gg 1$, the impedance converges to $\hat{Z}_{we} = \eta_0$, while in NF ($B_0 r \ll 1$), it could be approximated by $\hat{Z}_{we} \cong \eta_0 \left(-\frac{j}{B_0 r}\right) = \frac{60\lambda_0}{r} \angle -90$. It is useful to know that in the FF zone, both $\hat{E}_\theta$ and $\hat{H}_\phi$ are a function of $1/r$. While in the NF zone $\hat{E}_\theta$ and $\hat{H}_\phi$ are related to r by the factors of $1/r^3$ and $1/r^2$, respectively. According to the duality theorem, the electric and magnetic fields of an elemental magnetic dipole (loop) could be derived by interchanging the electric and magnetic field relations for the electric dipole. Thus, the wave impedance for a magnetic dipole is obtained by

$$\hat{Z}_{wm} = \frac{\hat{E}_\phi}{\hat{H}_\theta} = -\eta_0 \frac{\frac{j}{B_0 r} + \frac{1}{(B_0 r)^2}}{\frac{j}{B_0 r} + \frac{1}{(B_0 r)^2} - \frac{j}{(B_0 r)^3}} \tag{2.33}$$

In FF, where $B_0 r \gg 1$, the $\frac{1}{B_0 r}$ terms dominate, and the impedance converges to $\hat{Z}_{wm} = \eta_0$, while in NF, $\frac{1}{(B_0 r)^2}$ and $\frac{j}{(B_0 r)^3}$ dominate, and it could be approximated by $\hat{Z}_{wm} \cong -j\eta_0 B_0 r = 2369 \frac{r}{\lambda_0} \angle -90$.

The wave impedances of (2.30) and (2.31) are plotted in Figure 2.3. It is shown that the impedance goes through a substantial change when the observer moves from the NF region to the FF region. Both sources represent a transition from NF to FF regions (there is no abrupt change from NF to FF).

in Figure 2.3 (a), the wave impedance of an electric dipole drops when r increases from NF. However, the value converges to η_0 when r is large enough that the $\frac{1}{B_0 r}$ terms dominate.

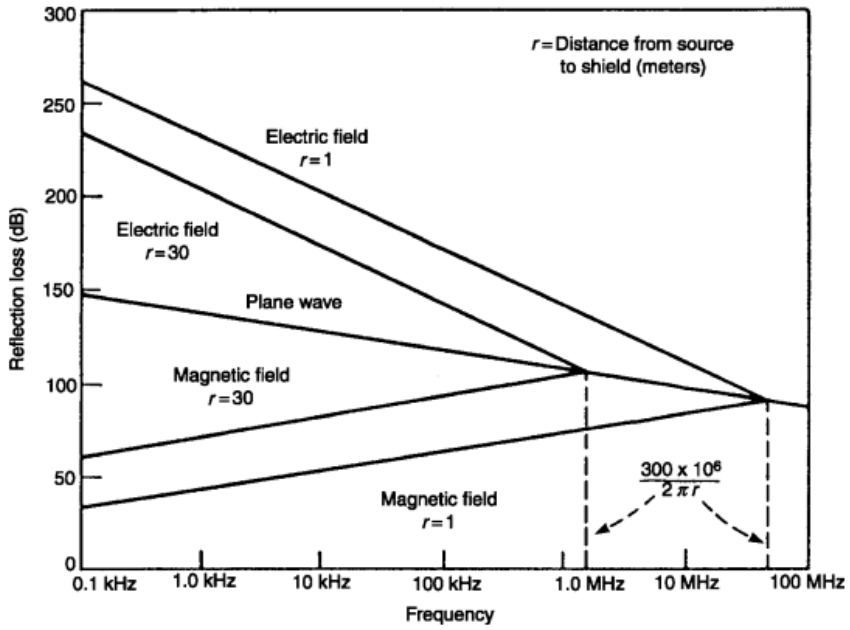

Figure 2.4. Reflection loss for electric dipole, magnetic dipole and plane wave (Image from [18] page 738).

Since the wave impedance has higher NF values, the electric dipole is a *high-impedance source*. On the other hand, the magnetic source wave impedance starts from lower values and converges to the constant η_0 value. Magnetic dipoles are referred to as *low-impedance sources*. In addition, it is useful to point out that an electric dipole represents a strong capacitive characteristic, while a magnetic dipole shows a weak capacitive effect in the NF zone. The capacitive effects may be found in the following relations

$$\hat{Z}_{we} \cong \eta_0 \left(-\frac{j}{B_0 r}\right) = \frac{1}{j\omega C_e} \tag{2.34}$$

$$\hat{Z}_{wm} \cong -j\eta_0 B_0 r = \frac{1}{j\omega C_m} \tag{2.35}$$

where C_e and C_m signify the NF capacitive effects of an electric and magnetic dipole, respectively. In some cases, the problem might also be considered in a cylindrical coordinate where two different SE in the radial and z-direction are defined to simplify the problem [89].

2.4.2 Estimating NF SE

As pointed out before, the NF SE of a shielding wall is based mainly upon the FF SE relations. However, the source type changes how the shield interacts with the impinging wave. Since the shield's FF SE is comprised of three factors: *reflection loss* (R), *absorption loss* (A), and *multiple reflections* (M), the only modification required is substituting the free space intrinsic impedance by the NF wave impedance in all obtained farfield relations. This yields an approximate solution with reasonable accuracy in terms of the extreme conditions of NF and FF regions. However, since the absorption loss is not a function of wave impedance and the

effect of multiple reflections might add to the complexity of the problem, the modification only applies to the reflection loss as follows.

$$R_{dB} = 20\log\left|\frac{\left(\hat{Z}_w + \hat{\eta}\right)^2}{4\hat{Z}_w\hat{\eta}}\right| \cong 20\log\left|\frac{\hat{Z}_w}{4\hat{\eta}}\right| \tag{2.36}$$

Substituting the electric source wave impedance from (2.30) and using good conductor approximation yields the NF reflection loss of a shield for a Hertzian dipole as

$$R_{dB,e} = 322 + 10\log\left(\frac{\sigma_r}{\mu_r f^3 r^2}\right), \tag{2.37}$$

while the same substitution for a magnetic field source yields

$$R_{dB,m} = 14.57 + 10\log(\frac{f^1 r^2 \sigma_r}{\mu_r}) \tag{2.38}$$

Plotting the two factors may provide a very useful comparison of the two sources. The reflection loss of a copper shield for an electric source, magnetic source, and plane wave excitation are compared in Figure 2.4. The position (r) is changed from 1 to 30 meters while the frequency is sweeping from 0.1 kHz to 1 MHz. Both the $R_{dB,m}$ and $R_{dB,e}$ terms asymptotically converge to the plane wave loss when the position or frequency increases ($B_0 r$ increases). However, the amount of attenuation for electric sources is much higher than for magnetic sources. In addition, as r increases, the $R_{dB,m}$ increases while the $R_{dB,e}$ decreases.

The next chapter will use similar fundamental observations and methodology to interpret shields' NF responses. In other words, knowing the NF and FF responses of the shield for each source will help us develop a new model to estimate the NF SE for complex structures, such as frequency selective surfaces.

Chapter 3: X-Band Nearfield Shielding

This chapter will examine the advantages, disadvantages, and performance gaps of traditional single-layer stopband flexible metasurface shields. This analysis is vital to identify novel performance improvements that can be made in the field of shielding. The study begins with far-field (FF) and near-field (NF) comparisons for four common 10 GHz Stopband Frequency Selective Surfaces (FSS) to evaluate their effectiveness in electromagnetic shielding applications. Then, analytical derivations of the FF and NF shielding effectiveness (SE), which are useful for predicting the extreme responses of single-layer structures, are presented. The study also examines the effects of edge diffraction due to finite structures in one- and two-dimensional (1D and 2D) diffractions. The NF performance of conformal structures is analyzed based on the radii of curvature, and datasets are extracted to introduce two useful measures for determining the efficiency of a conformal shield. The investigation uses Finite Element Method (FEM) to evaluate the FSSs' shielding performance in both the far-field (FF) and near-field (NF) zones. The FEM results are compared to the Method of Moment (MOM) results to verify the findings. The study creates reliable insight for further developments of flexible shielding surfaces from a near-field perspective.

3.1 The Importance of Nearfield Shielding

The popularity of ultra-compact shielded products has generated interest in flexible Frequency Selective Surfaces (FSS), which can be used near susceptible substances. However, designers of flexible shields have typically avoided dealing with near-field (NF) areas due to uncertainty about the NF performance of FSS structures. This lack of reliable NF attenuation in FSS shields leads to bulky shielded products because manufacturers must increase the distance between the shield and the susceptible circuit to stabilize attenuation levels.

A stable NF performance guarantees the feasibility of compactly shielded products, especially for wearable applications that aim to prevent the passing of particular frequency components toward a living organism. It has been discovered that X-band electromagnetic radiation (EMR) has harmful effects on various living systems, such as the nervous, reproductive, cardiovascular, immune, hematopoietic, and endocrine systems (see [25, 28, 90-97] for review). This emphasizes the need for wearable and reconfigurable shields to protect organisms in environments polluted with electromagnetic radiation. When designing X-Band frequency selective shields for wearable applications, it is essential to remove specific frequency components within a small fraction of the spectrum wavelength, ranging from 1-60 mm ($d<2\lambda$). This is especially important for biomedical imaging applications, where the shield needs to be close to the susceptible organism.

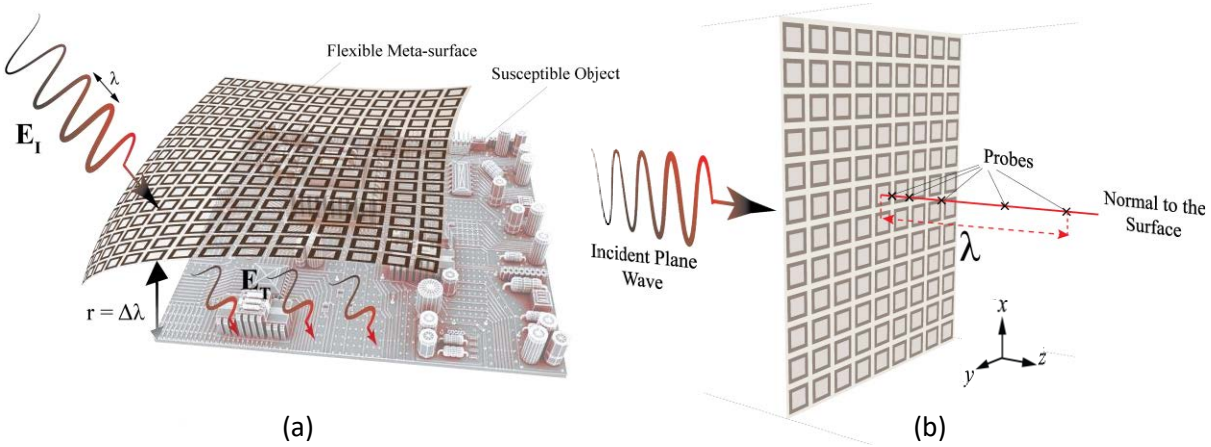

Figure 3.1. NF radiation susceptibility problem [5]. (a) Compact shielding concept for a susceptible circuit. The distance between the flexible shield and the susceptible objects (r) may be referred to as observation distance and could be a fraction of wavelength in compact shields. (b) A perspective view of the probe locations and the direction of incidences in an infinite surface.

Small changes in the resonant frequency of FSSs can negatively impact their ability to shield against radiation, potentially allowing undesired radiation to leak into covered areas. Even minor variations in the resonant frequency can lead to significant decreases in stopband attenuation levels, which must be accurately addressed to maintain the shield's effectiveness. Furthermore, using flexible FSSs in rough configurations can cause near-field and far-field malfunctions, while edge diffraction can also degrade the performance of finite, nonspherical shields. Unfortunately, there is a lack of research on the near-field effects of flexible FSSs, with only a few useful studies providing far-field analysis of curved structures [7, 62]. For instance, one study [62] found that a split-ring resonator meta-skin displayed unstable scattering suppression when wrapped around a dielectric rod at different angles. Despite the availability of flexible, reconfigurable, and wearable structures, there is no useful criterion for their efficient use in practical projects due to the lack of such investigations.

After reading this chapter, the reader will learn about assessing near-field (NF) shielding concerns through four frequently reported frequency-selective surfaces (FSSs) and their comparative analysis. Split Ring Resonator (SRR) [62], Jerusalem Resonator (JR) [98], Square loop (SL) [99], and Convoluted Square Loop (CSL) [7, 100] are considered. A numerical representation of the NF attenuation of FSSs and analytical models for both far-field (FF) and NF regions are provided. The chapter also comprehensively addresses the effects of NF transmission zero variations, edge diffraction, and bending on rigid and flexible FSS structures. The instability arising from gradual convergence in FSS near-to-far-field is shown and a distance criterion for FSS's NF assessment is introduced. The chapter discusses the effect of edge diffraction of finite structures on the NF-SE, the intrinsic behavior of structures against NF-SE changes, and the concept of NF transition from transmission to reflection. Finally, the chapter presents the bending effect on flexible models and defines the "essential radius" as another

parameter for NF assessment of curved structures. The chapter concludes that near-field monitoring provides a complementary contribution to the characterization of flexible microwave shields for practical compact applications.

3.2 NF & FF SE Analysis Using Numerical Methods

Figure. 3.1 (a) illustrates a conceptual view of the radiation susceptibility problem addressed in this study, where r is the distance between the shield and the susceptible object. This distance is within a zero to a fraction of wavelength (NF zone) in compact packages and wearable applications. The next section illustrates how the unit cell's SE is calculated for such a shield. Then, different analyses are provided.

3.2.1 Unit Cell NF Analysis

3.2.1.1 NF-SE in Local Regions (Normal Illuminations)

The analysis of unit cells provides a reliable view of infinite planar frequency selective surfaces, but it does not consider edge diffraction. In this section, the local near-field characteristics of meta-surfaces are investigated and confirmed using two numerical methods. The structures analyzed are the Square Loop (SL), Convoluted Square Loop (CSL), Jerusalem Resonator (JR), and Split Ring Resonator (SRR), shown in Figures 3.2(a)-(d). To create flexible and wearable shields, the structures can be printed on a single-sided flexible laminate made of Rogers/Duroid 5880 with a thickness of 0.127mm, a relative permittivity of 2.2, and a loss tangent of 0.0009. This laminate can be embedded in textiles for wearable applications. The structures undergo a full-wave analysis illuminated by a modulated Gaussian wave containing X-band components in the normal direction. The electric field intensities of the transmitted and reflected waves are measured within the near-field range by placing electric field probes in the appropriate locations, shown in Figure 3.1(b). The following equation can be used to calculate the reflected wave in the area where reflection occurs.

$$\vec{E}_R = \vec{E}_{TOT} - \vec{E}_I \tag{3.1}$$

where $\vec{E}_R$, $\vec{E}_{TOT}$, and $\vec{E}_I$ are the reflected electric field vector, total electric field vector, and the incident electric field vector. In the transmission zone, the following relation exists.

$$\vec{E}_{TOT} = \vec{E}_T \tag{3.2}$$

Table 3.1. Optimized Dimensions of the Unit Cells Under Test in Millimeters (Case 1)

Resonant Frequency 10 GHz							
SL		CSL		JR		SRR	
Dim.	Value	Dim.	Value	Dim.	Value	Dim.	Value
x_1	5.508	y_1	6.565	z_1	4.140	t_1	0.850
x_2	0.408	y_2	0.505	z_2	0.966	t_2	0.680
P	5.610	y_3	1.010	z_3	3.243	P	11.15
D	0.102	P	6.868	z_4	1.242	D	0.850
		D	0.303	P	11.04		
				D	1.380		

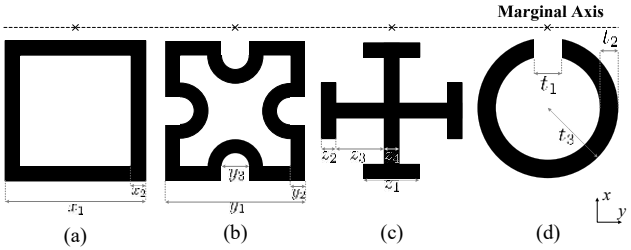

Figure 3.2. The structures under test [5]. (a) Square Loop, (b) Convoluted Square Loop, (c) Jerusalem Cross Dipole, (d) Split-Ring Resonator

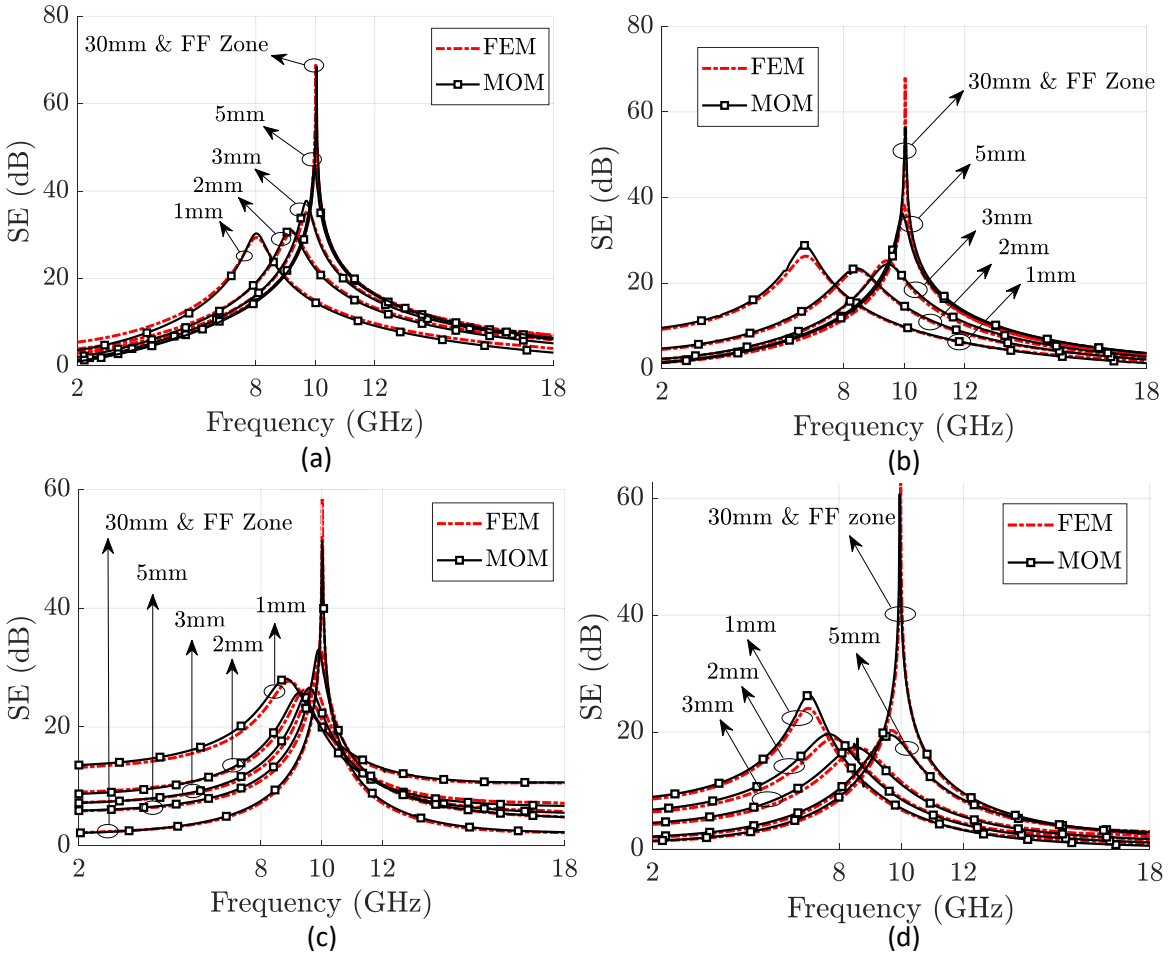

Figure 3.3. SE versus frequency on central axis and different observation distances (NF and FF zones) [5] for (a) SL FSS, (b) CSL FSS, (c) JR FSS, (d) SRR FSS

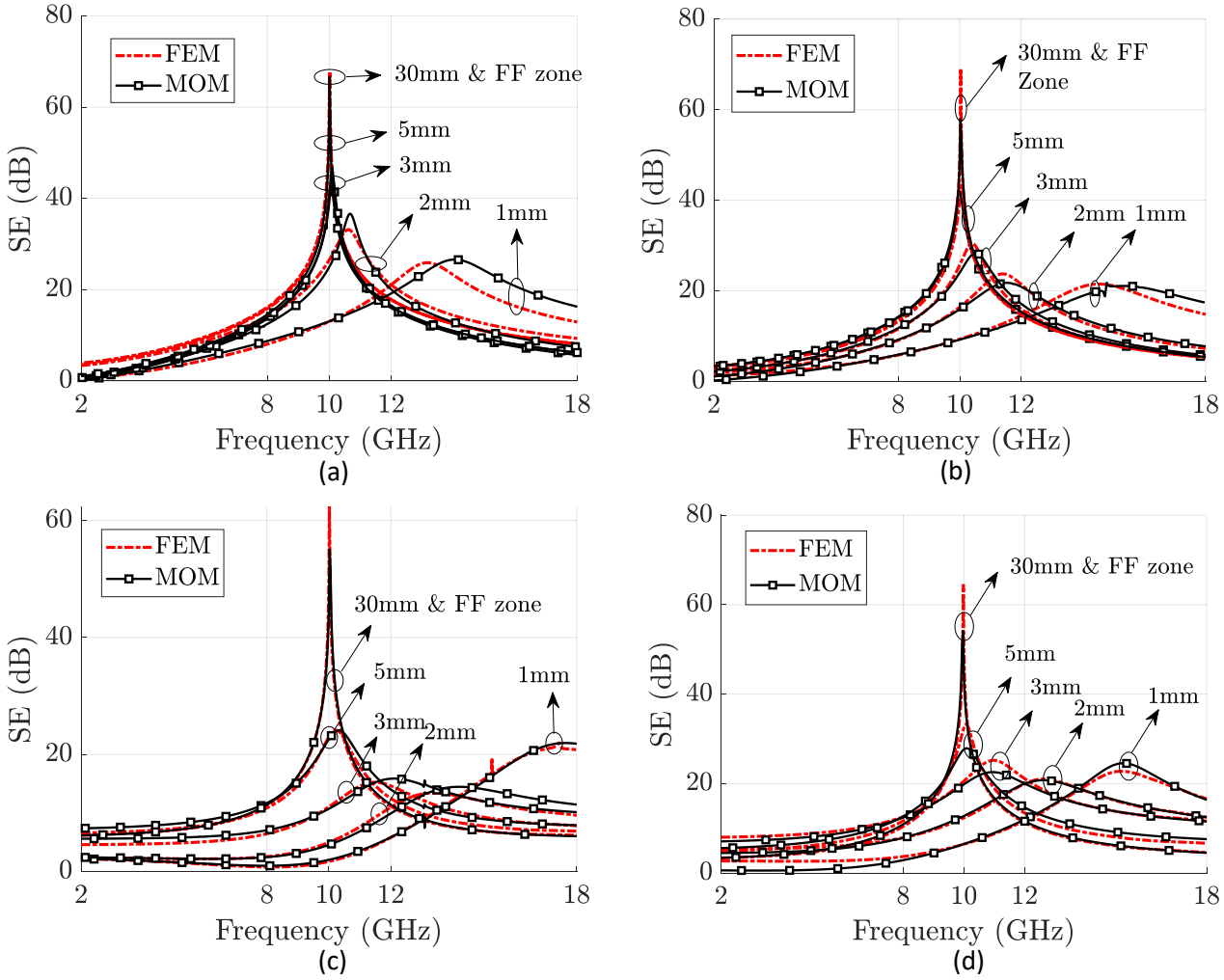

Figure 3.4. SE over frequency on marginal axis with different observation distances (NF and FF zones) [5] for (a) SL FSS, (b) CSL FSS, (c) JR FSS, (d) SRR FSS

where $\vec{\boldsymbol{E}}_{\boldsymbol{T}}$ is the transmitted electric field vector. All the structures are optimized to reject X-band transmission signals while still being transparent to other frequencies. To achieve this, a stochastic evolutionary algorithm called Particle Swarm Optimization (PSO) was used to optimize the constructive parameters of each structure, except for the line widths, which controlled the bandwidth. PSO used 30 particles with 30 iterations, resulting in 900 evaluations for each structure. Table I shows the optimized dimensions of the structures for the X-band stopband. The unit cells have a periodicity of P and an inter-element spacing of D in both the x- and y-direction. The SL structure has the smallest size, while the JR and SRR unit cells are comparably larger than SL and CSL. It is important to note that all the obtained TE results can be used for TM mode, except for SRR, which has different polarization effects for TM mode.

The numerical investigation of the shielding effectiveness (SE) provided by various structures was carried out along the central axis perpendicular to each unit cell plane. Figure 3.3 illustrates the SE changes over frequency as the observation distance, denoted as r, varies from a small fraction of the wavelength (the near-field zone) to considerable distances (the far-

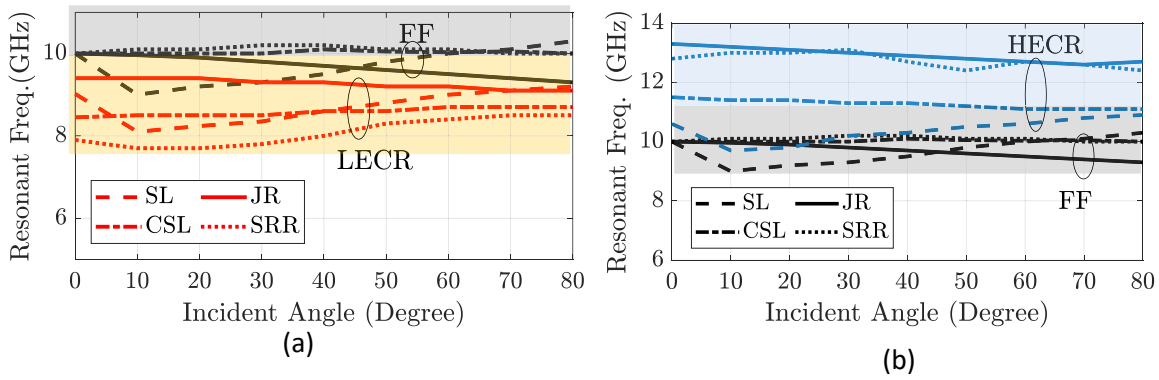

Figure 3.5. Resonant Frequency versus Incident angle [5]. (a) FF & LECR, (b) FF & HECR

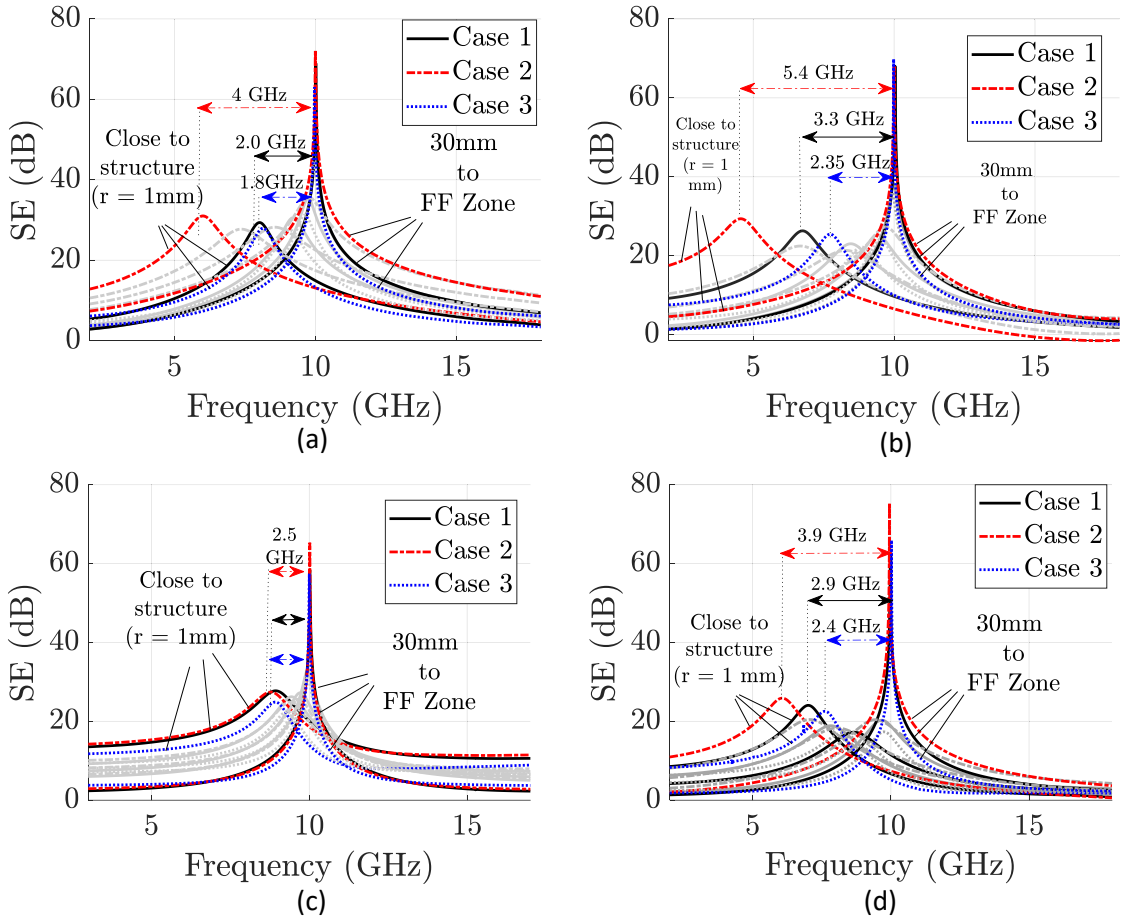

Figure 3.6. The variation of NF resonant frequency for three different cases, representing three different bandwidths [5]. Case 1 denotes the structures of Table I. Case 2 and Case 3 represent the structures with wider and narrower bandwidths. (a) SL, (b) CSL, (c) JR, (d) SRR. Gray curves show the gradual SE variation *between* 1 mm to 30 mm.

field zone). These results are obtained from two methods, MOM and FEM, which are compared for each structure. It is observed that when the observation distance becomes closer to the surface (i.e., as r decreases), the resonance frequency shifts towards lower frequencies. This indicates that the interaction is primarily with a single cell with a resonance different from the entire periodic structure when the observation point is very close to the surface. However, as the distance increases, more cells interact, leading to a shift in the resonant frequency until the

FF zone is reached, where all the periodic structures contribute. During this transition, significant degradation in SE (typically 30-40 dB) occurs, resulting in a significant deterioration in cell shielding efficiency. The NF-SE converges to the FF-SE for distances greater than one wavelength (λ=30 mm). However, the convergence rate is different for all the structures tested. For example, the resonant frequency of JR (as shown in Figure 3.3(c)) experiences a much smaller transition (about 1.6 GHz when the observation point is at r=1 mm) compared to the other structures (whose resonant frequency shift is at least 2 GHz for r=1 mm).

The transitions of the NF resonant frequency are not all towards lower frequencies. A polarization-dependent local capacitive effect is present in certain areas on the edges of the unit cell. This creates high energy concentration, resulting in an opposite NF-SE behavior. Figure 3.4 displays the SE variations versus frequency along the normal on the marginal axis. It can be concluded that in these high-concentration regions, the resonant frequency transition is towards higher frequencies. However, the same NF-SE degradation occurs in this zone. Based on Figure 3.4 (c), JR NF-SE level and resonant frequency experience a 50 dB degradation and an 8 GHz shift, respectively. This unstable feature makes JR a comparatively less reliable choice for NF shielding. One explanation for this NF behavior is that the local capacitive effect dominates in the high-concentration regions (cells' corners), while the local inductive effect dominates in the low-concentration regions (cells' centers). This leads to a shift of the transmission zero towards the upper band and lower band, respectively.

3.2.1.2 NF-SE in Local Regions (Oblique Illumination)

To investigate the effects of incident angle on the NF performance of each structure, the meta-surfaces are tested using the same procedure as in the previous section but with different azimuth illumination angles (θ). In Figure 3.5, the resonant frequency variation with respect to the incident angle is compared for both LECR and HECR, where the observation distance from the structure is 2 mm. The comparison suggests that the meta-surface performance through oblique incidences mostly depends on the observation region. For LECR, the resonant frequencies occupy a lower frequency region, whereas, for HECR, higher frequencies are blocked by the FSS, regardless of the incidence angle. The angular stability of the meta-surfaces varies depending on the area of observation (FF, LECR, or HECR) and the type of the FSS. For instance, in LECR, both JR and CSL exhibit more RF flatness over different incident angles, while CSL replicates this angular stability even in the FF region due to the U-shaped bending in the structure. [7, 100].

3.2.1.3 Effect of Dimensions on NF-SE

In order to mitigate the variation of nearfield (NF) changes with distance, the geometry and dimensions of meta-surfaces can be optimized. Since the FF resonant frequency is sensitive to the dimensions, it is reasonable to expect that dimensional changes will also affect the NF performance. The bandwidth characteristics of the structure alter with dimensional changes, as well, with thicker lines resulting in wider bandwidths. These bandwidth changes may impact

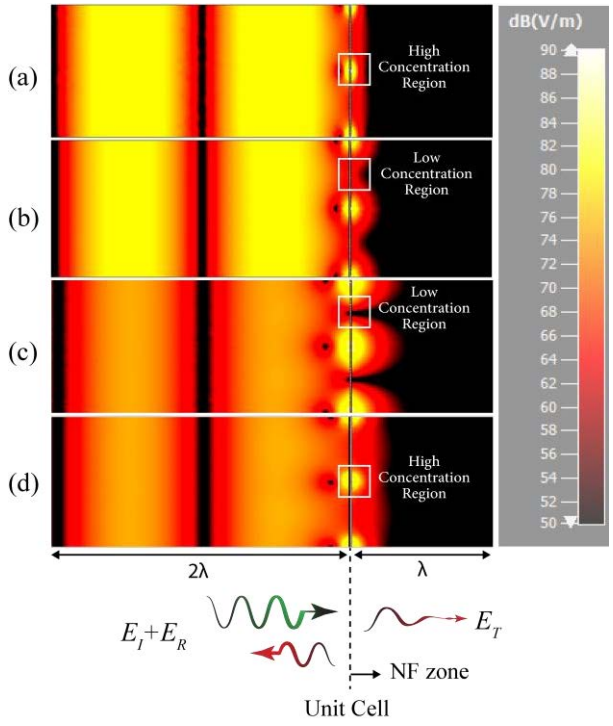

Figure 3.7. Total field distribution around the surfaces indicating the transmission of (a) SL FSS, (b) CSL FSS, (c) JR FSS, (d) SRR FSS [5].

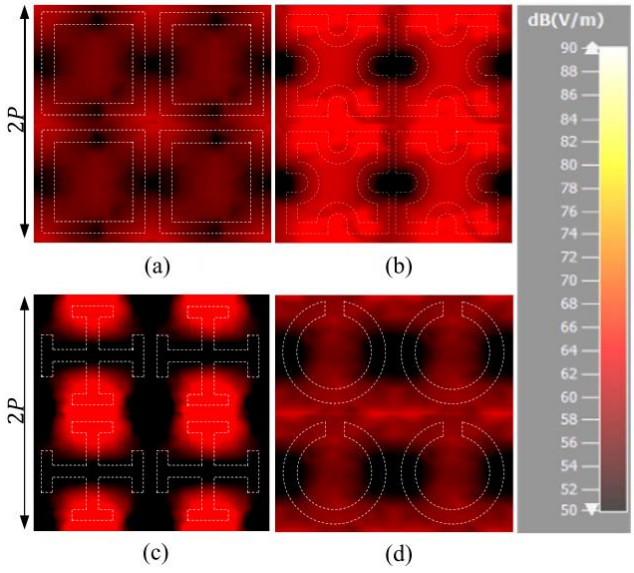

Figure 3.8. The simulated NF patterns of electric field intensity on a plane at 2 mm above the surfaces for (a) SL FSS, (b) CSL FSS, (c) JR FSS, (d) SRR FSS [5].

the sensitivity of the NF resonant frequency to the dimensions. The reason lies in the different projection areas seen by each frequency component in NF zones. To investigate the effect of dimensions on the NF behavior, the dimensions of the unit cells for SL, CSL, JR, and SRR were

modified to produce two cases with the same FF resonant frequency: Case 2 had thicker linewidths, resulting in a broader bandwidth, while Case 3 had thinner linewidths, resulting in narrower bandwidth. The nearfield effects are computed for both cases, as shown in Figure 3.6. The results demonstrate that the NF abnormalities persist even when the dimensions are changed. However, using thicker structures (wider bandwidths) increases NF abnormalities in resonant frequency shifts. This conclusion does not apply to all structures, as JR, which has an intrinsic narrow bandwidth, exhibited a more stable NF performance when different dimensions are used, as shown in Figure 3.6 (c).

A physical phenomenon can explain the findings in Figure 3.6. When the structure's thickness is increased, the fringing effect becomes wider, causing the effective electric dimension of the structure to increase. This, in turn, extends the FF zone (with a rough distance of $2D_{eff}^2/\lambda$) and elongates the NF zone. On the other hand, reducing the overall size of the structure increases the resonant frequency, which decreases the NF resonant frequency shifts. This is because as the frequency increases, the wavelength decreases, resulting in a shorter NF distance. For wearable applications with NF distances of 1-50 mm, higher frequencies may not cause practical NF issues unless extremely short-range (fraction of a millimeter) NF performance is required. Therefore, the physical justification supports the conclusion that thicker structures exhibit more NF abnormalities, whereas narrower bandwidth structures such as JR resist bandwidth changes and exhibit a more stable NF performance.

When it comes to SE level degradation, a minimal change is observed. All the unit cells tested show that an increase in bandwidth leads to a slight rise in NF-SE levels, whereas a decrease in protection occurs when the bandwidth is narrow.

3.2.1.4 NF Energy Distribution

This section demonstrates that transmission zeros can undergo a local abnormality in NF zones. The peak value of SE detects a transmission zero using NF energy/field distribution to expose the non-uniform NF behavior of different unit cells. The distribution distinguishes two fundamental regions, namely the low energy concentration region (LECR) and the high energy concentration region (HECR), based on the strength of the electric field (low and high, respectively). At the resonant frequency (10 GHz), Figure 3.7 displays a cross-section of the incident-transmission problem that allows for observing the undesirable NF leakage through the absolute value of the total electric fields. The strength of the electric field in the incident zone relies on the satisfied boundary condition on the FSS surface. Although there are minor differences in the NF distribution of the structures, the LECR and HECR are distinguishable. In Figure 3.7 (c), the JR field strength fluctuates more in the two extreme regions than in SL and SRR, which exhibit smooth attenuations in both high and low-concentration regions. Figure 3.8 compares the NF patterns of electric field intensity in a cross-section 2 mm from the FSS surface, where each figure represents four adjacent unit cells that cause a periodic local transmission zero distribution (black zones). The local transmission zeros correspond to the low-

concentration regions and have different positions for each structure. The comparison implies that although all structures share a similar periodic energy distribution pattern, each structure has a unique period, local position, and relative area of each extreme region.

3.2.1.5 NF-SE Convergence

Meta-surfaces demonstrate a correlation between their local NF and FF behaviors similar to high-impedance NF sources like a Hertzian dipole. This correlation arises due to the convergence of the NF wave impedance of NF sources to the intrinsic impedance of the medium in free space [18]. The convergence of the NF and FF behaviors in flexible FSS shields can be characterized by observing the variation of the electric NF magnitude as a function of the observation distance. The convergence can be demonstrated by monitoring the electric field strength at increasing distances from the FSS interface. Figure 3.9 illustrates the convergence of the electric field magnitude along the central normal to the unit cells. The differences in the initial values arise due to differences in the boundary conditions that must be satisfied. Despite variations in the NF strengths between different structures, the NF smoothly converges to its lowest value within one wavelength from the surface, corresponding to the FF values. Notably, while both the NF and FF zones require a high level of SE attenuation, none of the structures provide such attenuation in the NF zone identified in Figure 3.9. The convergence depth of the curves shown in Figure 3.9 depends on the maximum SE that each unit cell can provide at the center frequency. It is important to note that slight shifts in the transmission zeros may prevent the structures from performing optimally at a single frequency. However, the relatively wide bandwidth of SL mitigates the effect of these shifts and results in a higher attenuation level.

From a physical perspective, it is suggested that the NF zone experiences a transition from NF wave impedance to FF wave impedance. This phenomenon of convergence in the NF region violates the frequency selective features of FSSs. In other words, the capacity of FSSs to selectively filter specific frequencies is greatly reduced within the NF zone. As a result, because certain unwanted frequency components still exist in the NF zone, using the term "reflected component" for the absent frequency component in the FF region is inappropriate. This principle establishes the basis for the following analytical model.

3.3 NF-SE Estimation

Since NF-SE converges to FF-SE, finding an analytical solution for NF-SE without having information about FF-SE is impossible. In the following, first, the required tools to estimate FF-SE are introduced. Then, they will be used to find a model for NF estimations in single-sided FSS shields.

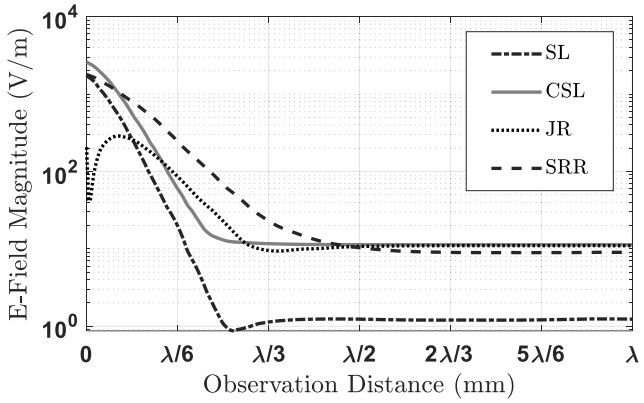

Figure 3.9. NF convergence in a local NF zone at the resonant frequency (10GHz) [5].

Table 3.2. Extracted values of L & C for SL, CSL, JR and SRR

SL		CSL		JR		SRR	
L(nH)	C(pF)	L(nH)	C(pF)	L(nH)	C(pF)	L(nH)	C(pF)
2.01	0.126	2.32	0.108	5.21	0.0486	3.89	0.0651

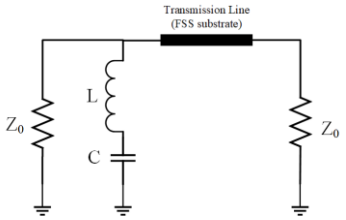

Figure 3.10. The equivalent circuit model for SL, CSL, JR and SRR [36].

3.3.1 Equivalent Circuit Model (ECM)

The NF-SE converges to the FF-SE as the observation point transitions from the NF to the FF zone. Therefore, the first step in estimating the NF behavior of an FSS is to obtain an estimate of the FF-SE. An Equivalent Circuit Model (ECM) can be a reliable FF estimation source. However, transmission line (TL) theory, a powerful tool for proposing ECMs for different electromagnetic transmitters, does not consider NF interactions. Additionally, circuit models usually fail to incorporate the complex inter-element interactions of higher-order modes when dealing with complex electromagnetic structures [46, 101]. That is why ECM is usually used to model filtering characterization of the FF behavior of unit cells. The common ECM for the structures of Figure 3.2 is depicted in Figure 3.10 as a series LC resonator. As previously mentioned, each structure contains regions with high and low energy concentrations within a single unit cell period, corresponding to capacitive and inductive components in their ECM. Note that the capacitive element, C, includes both capacitive effects of inter- and intra-element spacing $C = C_1C_2/(C_1 + C_2)$ [7]. The ultra-thin laminate in the flexible structures renders the effect inconsequential, even though the substrate can be represented as a transmission line [46, 102].

At the resonant frequency, the LC resonator demonstrates a transmission zero. The FSS FF wave impedance is

$$\hat{Z}_{FF} = j\omega L + \frac{1}{j\omega C} \tag{3.3}$$

where the transmission zero emerges at $f_r = 1/2\pi\sqrt{LC}$. The computed impedance corresponds to the FF wave impedance ($\hat{Z}_{FSS} = \hat{Z}_{FF}$) due to the circuit model's failure to account for near field effects. Simulations are conducted using Keysight Advanced Design Systems (ADS) to acquire the exact values of FF ECM components. A comprehensive study was conducted in [103] to determine the values of the circuit elements. The information regarding the achieved circuit elements of each meta-surface is reported in Table II.

3.3.2 FF-SE Model

To derive a solution for the SE of single-layer, one-sided frequency-selective shields, we address the problem outlined in Figure 3.11, similar to what is considered in Chapter II. However, in this problem, the FSS layer comprises two interfaces, which exhibit different FF impedances despite both sides of the shield having the same medium (free space). The left interface comprises periodic metallic patches, forming an uneven slab. The FF impedance, calculated via ECM, neglects the effect of the thin substrate. Therefore, it primarily determines the impedance seen through the left interface ($\hat{Z}_{FSS} = \hat{Z}_{FF}$), whereas the intrinsic impedance of the medium ($Z_H = \eta_0$) determines the impedance through a homogeneous interface. As explained in Chapter II, to obtain an exact analytical FF expression for shielding effectiveness (SE) of a uniform metallic slab, accurate results are obtained by applying appropriate boundary conditions. However, going through the time-consuming process of applying the boundary conditions for arbitrarily shaped meta-surfaces is not handy. Instead, the approximate methodology similar to what was used in Chapter II is used. Therefore, the problem depicted in Figure 3.11 is divided into three sub-problems, each involving the determination of R_{dB}, M_{dB}, and A_{dB}, respectively.

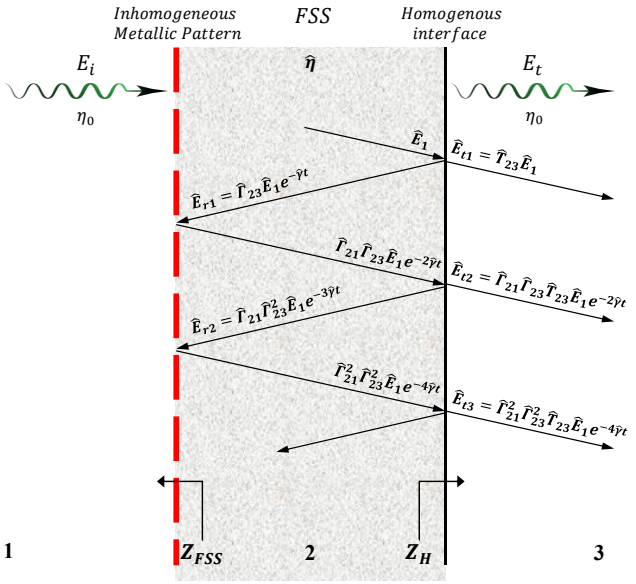

Figure 3.11. Illustration of the shielding problem with multiple reflection/transmission effect within a single layer, one-sided meta-surface [5].

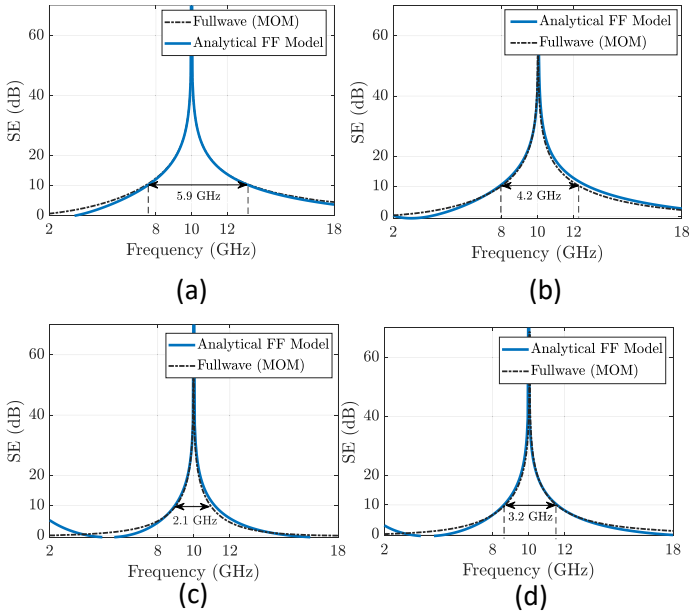

Figure 3.12. Analytical FF model verification for (a) SL, (b) CSL, (c) JR and (d) SRR [5].

Assuming no secondary reflections are occurring within the meta-surface layer, it is possible to calculate the amount of incident wave and transmitted wave by multiplying the transmission coefficients of the left and right interfaces.

$$\frac{\hat{\boldsymbol{E}}_{\boldsymbol{t_1}}}{\hat{\boldsymbol{E}}_{\boldsymbol{i}}} = K \times \frac{\hat{\boldsymbol{E}}_{\boldsymbol{t_1}}}{\hat{\boldsymbol{E}}_{\boldsymbol{1}}} \times \frac{\hat{\boldsymbol{E}}_{\boldsymbol{1}}}{\hat{\boldsymbol{E}}_{\boldsymbol{i}}} \tag{3.4}$$

$$= K \times \frac{2\hat{Z}_{FF}}{\eta_0 + \hat{Z}_{FF}} \times \frac{2\eta_0}{\eta_0 + \hat{Z}_{FF}}$$

where the constant K represents an approximation factor. To define the transmission coefficients for the first (left) and second (right) interfaces, T_{12} and T_{23}, the following definitions may be used:

$$T_{12} = \frac{2\hat{Z}_{FF}}{\eta_0 + \hat{Z}_{FF}} \tag{3.5}$$

$$\hat{T}_{23} = \frac{2\eta_0}{\eta_0 + \hat{Z}_{FF}} \tag{3.6}$$

where Z_{FF} represents the primary FF wave impedance produced by the metallic interface of the meta-surface. It should be noted that the phase shift resulting from a single transmission is disregarded, as the substrate used in wearable surfaces is extremely thin. As a result, R_{dB} can be calculated using the following formula:

$$R_{dB} = 20 \log\left(\left|\frac{\widehat{\boldsymbol{E}}_{\boldsymbol{i}}}{\widehat{\boldsymbol{E}}_{\boldsymbol{t_1}}}\right|\right) \tag{3.7}$$

$$= 20 \log\left(\left|\frac{\widehat{\boldsymbol{E}}_{\boldsymbol{i}}}{\widehat{\boldsymbol{E}}_{\boldsymbol{t_1}}}\right|\right)$$

$$= 20 \log\left(K\left|\frac{\hat{Z}_{FF}^2 + \eta_0^2 + 2\hat{Z}_{FF}\eta_0}{4\hat{Z}_{FF}\eta_0}\right|\right)$$

Substituting $\hat{Z}_{FF} = \hat{s}L + 1/\hat{s}C$ and $\hat{s} = j\omega$, (3.7) yields the transfer function below,

$$R_{dB} = 20 \log\left(\frac{K}{4}\left|\frac{(\hat{\eta} + \eta_0)(LC\hat{s}^2 + C\eta_0\hat{s} + 1)}{(LC\eta_0)\hat{s}^2 + \eta_0}\right|\right) \tag{3.8}$$

Multiple reflections and transmissions can significantly impact the accuracy of NF and FF SE calculations. In order to determine the total transmitted wave, it is necessary to calculate the sum of transmissions from the right interface, as illustrated in Figure 3.11.

$$\widehat{\boldsymbol{E}}_{\boldsymbol{t}} = \widehat{\boldsymbol{E}}_{\boldsymbol{t_1}} + \widehat{\boldsymbol{E}}_{\boldsymbol{t_2}} + \widehat{\boldsymbol{E}}_{\boldsymbol{t_3}} + \cdots \tag{3.9}$$

$$= \widehat{\boldsymbol{E}}_{\boldsymbol{t_1}}(1 + \Delta_1 + \Delta_2 + \cdots)$$

where $\widehat{\boldsymbol{E}}_{\boldsymbol{t_1}}$, $\widehat{\boldsymbol{E}}_{\boldsymbol{t_2}}$, $\widehat{\boldsymbol{E}}_{\boldsymbol{t_3}}$ and other transmitted portions are as follows

$$\widehat{\boldsymbol{E}}_{\boldsymbol{t_1}} = \frac{2\eta_0}{\eta_0 + \hat{Z}_{FF}} \widehat{\boldsymbol{E}}_{\boldsymbol{1}} \tag{3.10}$$

$$\begin{aligned} \widehat{\boldsymbol{E}}_{\boldsymbol{t_2}} &= \hat{\Gamma}_{21}\hat{\Gamma}_{23}\hat{T}_{23}\widehat{\boldsymbol{E}}_{\boldsymbol{1}}e^{-2\gamma t} = \Delta\, \widehat{\boldsymbol{E}}_{\boldsymbol{t_1}} \\ &= \frac{\hat{Z}_{FF} - \hat{\eta}}{\hat{Z}_{FF} + \hat{\eta}} \frac{\eta_0 - \hat{\eta}}{\eta_0 + \hat{\eta}} \frac{2\eta_0}{\eta_0 + \hat{Z}_{FF}} \widehat{\boldsymbol{E}}_{\boldsymbol{1}}e^{-2\gamma t} \end{aligned} \tag{3.11}$$

$$\begin{aligned} \widehat{\boldsymbol{E}}_{\boldsymbol{t_3}} &= \hat{\Gamma}_{21}^2\hat{\Gamma}_{23}^2\hat{T}_{23}\widehat{\boldsymbol{E}}_{\boldsymbol{1}}e^{-4\gamma t} = \Delta\, \widehat{\boldsymbol{E}}_{\boldsymbol{t_2}} \\ &= \left(\frac{\hat{Z}_{FF} - \hat{\eta}}{\hat{Z}_{FF} + \hat{\eta}}\right)^2 \left(\frac{\eta_0 - \hat{\eta}}{\eta_0 + \hat{\eta}}\right)^2 \frac{2\eta_0}{\eta_0 + \hat{Z}_{FF}} \widehat{\boldsymbol{E}}_{\boldsymbol{1}}e^{-4\gamma t} \end{aligned} \tag{3.12}$$

where γ represents the propagation constant and $\Delta = \hat{\Gamma}_{21}\hat{\Gamma}_{23}e^{-2\gamma t}$. The reflection coefficients at the first (left) and second (right) interfaces are denoted by $\hat{\Gamma}_{12}$ and $\hat{\Gamma}_{23}$, respectively,

$$\hat{\Gamma}_{21} = \frac{\hat{Z}_{FF} - \hat{\eta}}{\hat{Z}_{FF} + \hat{\eta}} \tag{3.13}$$

$$\hat{\Gamma}_{23} = \frac{\eta_0 - \hat{\eta}}{\eta_0 + \hat{\eta}} \tag{3.14}$$

The dominant wave impedance, denoted by $\hat{Z}_{FF}$, is the wave impedance that occurs when the wave impinges on the left interface, which consists of meta-surface metallic patches. The total transmitted electric field can be simplified as

$$\widehat{\boldsymbol{E}}_{\boldsymbol{t}} = \widehat{\boldsymbol{E}}_{\boldsymbol{t_1}}(1 + \Delta + \Delta^2 + \cdots) = \frac{\widehat{\boldsymbol{E}}_{\boldsymbol{t_1}}}{1 - \Delta} \tag{3.15}$$

which is valid for $|\Delta| < 1$. Finally, the SE can be written as

$$\begin{aligned} SE_{dB} &= 20\log\left(\left|\frac{\widehat{\boldsymbol{E}}_{\boldsymbol{i}}}{\widehat{\boldsymbol{E}}_{\boldsymbol{t}}}\right|\right) \\ &= 20\log\left(\left|\frac{\widehat{\boldsymbol{E}}_{\boldsymbol{i}}}{\widehat{\boldsymbol{E}}_{\boldsymbol{t_1}}}\right|\right) + 20\log(|1 - \Delta|) \end{aligned} \tag{3.16}$$

$$= R_{dB} + M_{dB}$$

Assuming $\hat{Z}_{FF} = \hat{s}L + 1/\hat{s}C$ while $\hat{s} = j\omega$, M_{dB} is derived as

$$\begin{aligned} M_{dB} &= 20\log(|1-\Delta|) \\ &= 20\log\left(\left|1 - \frac{\hat{Z}_{FF}-\hat{\eta}}{\hat{Z}_{FF}+\hat{\eta}}\frac{\eta_0-\hat{\eta}}{\eta_0+\hat{\eta}}e^{-2\gamma t}\right|\right) \\ &= 20log\left|1 - \frac{(\eta_0-\hat{\eta})(LC\hat{s}^2 - C\eta_0\hat{s}+1)}{(\eta_0+\hat{\eta})(LC\hat{s}^2 + C\eta_0\hat{s}+1)}e^{-2\gamma t}\right| \end{aligned} \tag{3.17}$$

The final separated derivations for reflection loss (R_{dB}), multiple transmissions (M_{dB}), and absorption loss (A_{dB}) are as follows,

$$R_{dB} = 20\log\left(K\left|\left(\frac{\eta_0+\hat{Z}_{FF}}{2\hat{Z}_{FF}}\right)\left(\frac{\eta_0+\hat{Z}_{FF}}{2\eta_0}\right)\right|\right) \tag{3.18}$$

$$M_{dB} = 20\log\left(\left|1 - \frac{\hat{Z}_{FF}-\hat{\eta}}{\hat{Z}_{FF}+\hat{\eta}}\frac{\eta_0-\hat{\eta}}{\eta_0+\hat{\eta}}e^{-j2\beta t}\right|\right) \tag{3.19}$$

$$A_{dB} = e^{\frac{t}{\delta}} \cong 0 \tag{3.20}$$

where $\eta_0, \hat{\eta}$ and $\hat{Z}_{FF}$ are the free space intrinsic impedance, the dielectric intrinsic impedance, and the FSS FF wave impedance obtained from ECM. K is set to 2 throughout the study. For the cases of ultra-thin flexible meta-surfaces, the absorption loss factor (A_{dB}) may be negligible ($A_{dB} \cong 0$). As depicted in Figures. 3.12 (a), (b), (c), and (d), the analytical model covers a bandwidth of 5.9, 4.2, 2.1, and 3.2 GHz for SL, CSL, JR, and SRR, respectively. Figure 3.12 also shows that the analytical ECM-based approach is accurate compared to the full-wave numerical method, particularly in terms of the provided 10 dB bandgap. It is worth noting that the accuracy of the approach is heavily reliant on the extracted capacitive and inductive values of the ECM model. $\hat{Z}_{FF}$, which profoundly changes with frequency, plays a dominant role in determining the reflection pole provided by the shield, as expected

3.3.3 NF SE Model

An NF approximate solution is based on the FF expression derived for single-layer, single-sided meta-surfaces. This solution predicts *extreme* SE degradation and resonant frequency transitions in the NF zone for high- and low-energy concentration regions. Chapter 2 explained that differentiation between types of sources in the NF regions is necessary to derive

the NF approximation for a homogeneous metallic sheet. However, for a meta-surface, the structure perse is the source of NF abnormalities, even when the emitting source is a uniform plane wave. Thus, the miniaturized cells act as an infinitesimal electric/magnetic NF source in the corresponding polarization, allowing the approximation of the metasurface's NF behavior as an infinite distribution of infinitesimal electric/magnetic sources. The methodology used to derive the SE of the FF sources is also applicable for NF sources, where the electric/magnetic source wave impedance always converges to the free space intrinsic impedance in the FF zone. [18]. The electric/magnetic wave impedance $\hat{Z}_{e/m}$ is repeated here for simplicity

$$\begin{cases} \hat{Z}_e = \dfrac{j/\beta_0 r + 1/(\beta_0 r)^2 - j/(\beta_0 r)^2}{j/\beta_0 r + 1/(\beta_0 r)^2}\eta_0 & \text{E-source} \\ \hat{Z}_m = -\dfrac{j/\beta_0 r + 1/(\beta_0 r)^2}{j/\beta_0 r + 1/(\beta_0 r)^2 - j/(\beta_0 r)^2}\eta_0 & \text{M-source} \end{cases} \tag{3.21}$$

where β_0 and r represent the phase constant and the spherical radial distance from the source, respectively. The wave impedance in the case of meta-surfaces may converge to the dominant FF impedance applied by the FSS. To apply the NF approximation, the meta-surface FF wave impedance in equations (3.18) and (3.19) is replaced by the following NF wave impedance

$$\hat{Z}_{NF} = \frac{\hat{Z}_{e/m}}{\eta_0} \times \hat{Z}_{FF} \tag{3.22}$$

Note that according to the NF-SE convergence, the first term, $\hat{Z}_{e/m}/\eta_0$, is supposed to converge to 1 as one moves from the proximity of the shield to the FF zone. In order to model the impedance and frequency characteristics, the electric source is used for LECR, and the magnetic source is used for HECR. This way, the wave impedance provided by the different regions could be satisfied. In the NF zone, the effective electric length varies in the high and low-concentration energy regions. In LECR, the effective electric length increases while approaching the FSS interface in the z-direction. The resonant frequency experiences a decrease, as well. In addition, the transmission zero vanishes gradually. Likewise, in HECR, the effective electric length decreases while approaching the FSS interface in the z-direction, the resonant frequency experiences an increase, and the transmission zero vanishes gradually. The following refinement must be applied in order to predict this SE behavior.

It should be noted that under the NF-SE convergence principle, the first term, $\hat{Z}_{e/m}/\eta_0$, is expected to approach one as one moves away from the shielded area and towards the FF zone. To model the impedance and frequency characteristics of the system accurately, the LECR is modeled by an electric source, while a magnetic source models the HECR. In the NF zone, the effective electric length varies in the high- and low-concentration energy regions. Specifically, in the LECR, the effective electric length increases as the FSS interface is approached in the z-direction, resulting in a decrease in the resonant frequency and a gradual disappearance of the transmission zero. Conversely, in the HECR, the effective electric length decreases as the FSS

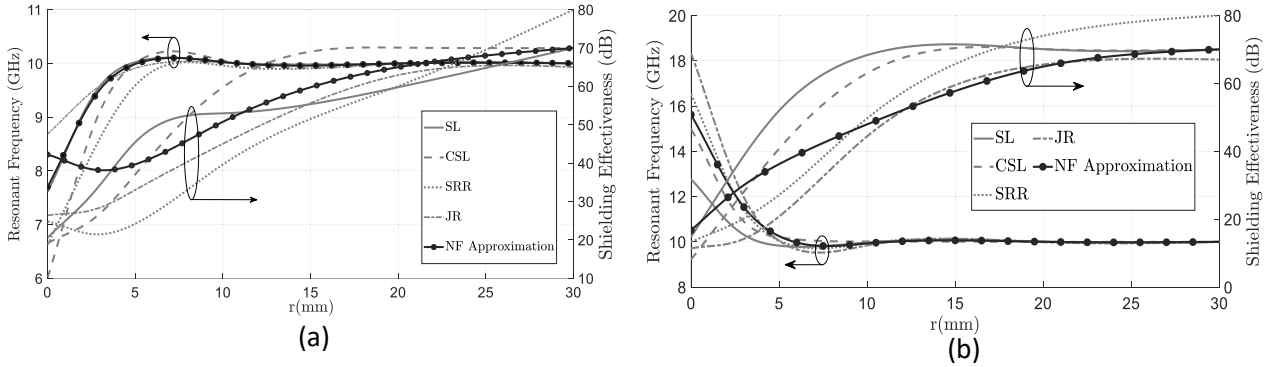

Figure 3.13. Estimated resonant frequency transition and SE degradation in resonant frequency [5]. (a) LECR (b) HECR

interface is approached in the z-direction, causing an increase in the resonant frequency and a gradual disappearance of the transmission zero. To predict this SE behavior, a refinement must be applied.

$$\omega \to b_1^{1/e^{b_2 r}}\omega - \frac{b_3}{b_4^{b_5 r}} \begin{cases} b_1 \geq 1 & LECR \\ b_1 < 1 & HECR \end{cases} \tag{3.23}$$

where b_i (i=1, 2, 3, 4, 5) are fixed factors, and r is the distance from the FSS interface in millimeters. The first term of (3.23), $b_1^{1/e^{b_2 r}}\omega$, predicts the resonant frequency shifts, whereas the second term, $b_3/b_4^{b_5 r}$, estimates the transmission zero fluctuation as r varies. Equation (3.23) is proposed as a hypothesis function for a nonlinear regression problem that needs to be solved numerically. By utilizing an iterative learning process and incorporating four training data sets (SL, CSL, JR, and SRR), the problem is solved by finding the best-fitted hypothesis function. The optimized constants $b_1 = 2.01,\ b_2 = 0.6,\ b_3 = 1e10,\ b_4 = 1.499,\ \text{and}\ b_5 = 1$ are obtained. The changes in estimated resonant frequency shifts and SE degradation for low- and high-concentration regions are presented in Figure 3.13 (a) and (b), respectively. The proposed model provides a dependable approximation for the transitions in NF resonant frequency and SE degradation.

The extreme NF response of configurations with known ECM can be evaluated using the proposed methodology that deploys both ECM and the NF wave impedance. This model is suitable only for assessing *extreme* regions of high and low energy concentration, which share similar behavior in all single-sided FSSs. However, more elaborate ECM models are required to differentiate between subtle nuances of NF behavior in different shields. Despite being a rough approximation, the provided NF behavior of the model is useful in representing the four metasurfaces' shielding performance and pole transitions. The comparison in Figure 3.13 reveals a convergence in resonant frequency as the local distance from the shield increases in the LECR and HECR regions. It is worth noting that the proposed model considers polarization as a function of ECM. When the user offers the TM ECM, it estimates TM NF behavior.

If we delve deeper into its workings, one may intuitively infer that the proposed model is sensitive to spatial positions. However, it is important to note that the model solely depends

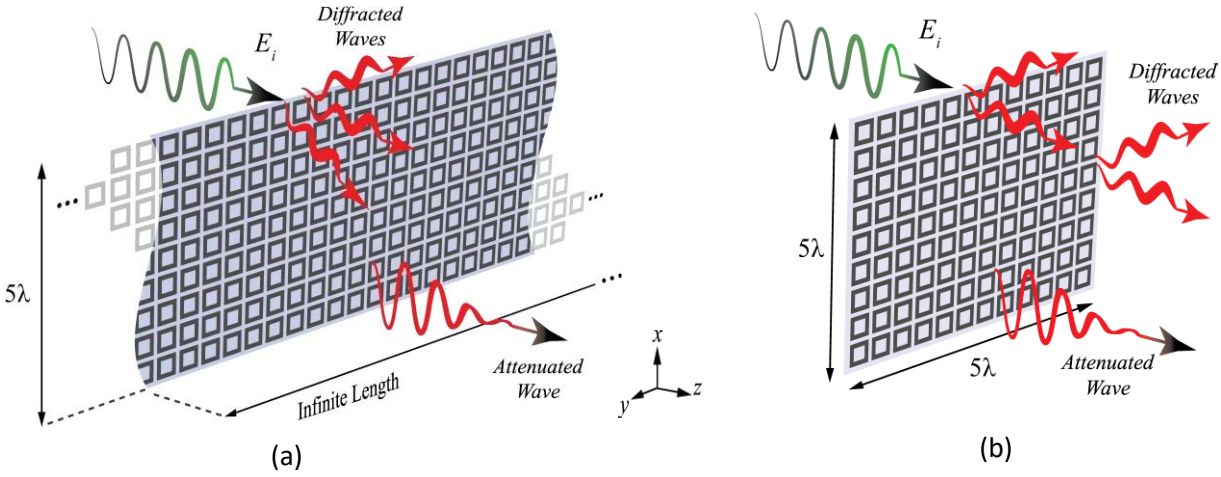

Figure 3.14. Edge Diffraction Problems [5]. (a) limited in one dimension (b) limited in two dimensions

on r, the normal distance from the interface. This is because the model has been specifically developed to estimate the behavior of LECR and HECR, which are worst-case scenarios with high abnormalities. Therefore, the model only estimates the extreme nearfield regions of LECR and HECR, not the in-between regions.

The proposed method is a fundamental engineering technique that offers a general understanding of the structure's NF performance. As implied, the NF approximation's dependence on geometry is significant. Since the performance is based on the given ECM, using a different elaborated ECM for each geometry would result in a specific nearfield effect. However, if the ECMs for the structures are very similar, they will have very similar FF characteristics with a rough estimation of relatively similar NF behavior in the extreme regions (LECR and HECR). In this scenario, the NF approximation predicts comparable nearfield effects, which can be used to represent similar structures under test, as shown in Figure 3.13. The same applies to polarization and incident angle. The ECM provided for the structures only accounts for normal incidences, meaning that we cannot use them for other oblique incidences unless the ECM performance is sensitive to the incident angle.

In addition, the provided NF model offers the opportunity to extract an NF ECM where applicable.

3.4 NF Effect of Edge Diffractions

Edge diffraction can negatively affect the performance of meta-surfaces in NF (near-field) applications. There are different scenarios of diffraction and Figure 15 shows the edge diffraction issues that have been discussed in the literature. To study the local effect of diffracted waves on NF-SE, the meta-surfaces under test are truncated in one or two directions, as illustrated in Figures. 3.14 (a) and (b). In Figure 3.14 (a), a plane wave is emitted to the surfaces, and the undesired frequency components are suppressed by the frequency selective pattern of the FSSs. However, other undesired components still diffract from the edges. The analysis of the NF

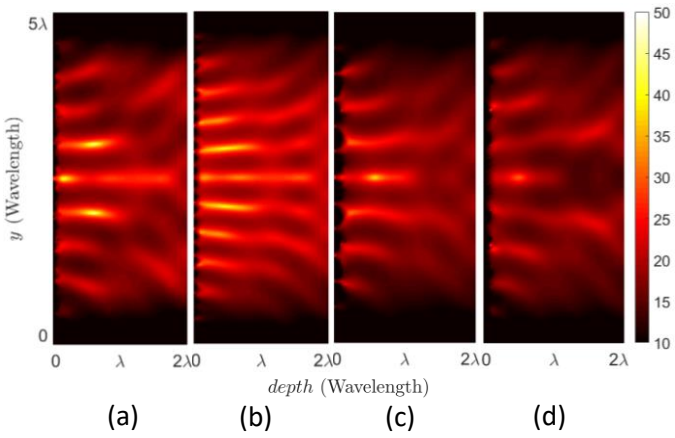

Figure 3.15. Shielding Effectiveness distribution of an infinite plane affected by Edge diffraction [5]. (a) SL, (b) CSL (c) JR, (d) SRR

reveals crucial information about the critical region, where the phase changes caused by edges may be destructive or constructive at local spots, leading the LECR and HECR to shift sporadically. Therefore, illustrating local NF-SE diffraction may not provide a reliable comparison. In Figure 3.15, the NF-SE distributions are compared at different depths (on x-constant planes in Figure 3.14 (a)). According to Figure 3.15, edge diffraction completely degrades the SE (shielding effectiveness) level on the edges of the NF region to less than 10 dB. The superiority of SL and CSL structures is noticeable in Figure 3.15 (a) and (b), respectively. This is because they are miniaturized elements with dimensions of 0.187 λ and 0.23 λ, respectively, resulting in a higher density of cells and promoting lower disturbance caused by diffracted waves. However, CSL exhibits more traces of 35 dB SE and higher SE levels, which confirms its superior resistance to 1D edge diffractions.

In Figure 3.14 (b), a $5\lambda \times 5\lambda$ shield is exposed to an incident plane wave, with diffractions from four edges. Figure 3.16 shows the levels of NF-SE through multiple y-constant cross-sections. It can be observed that diffraction at the four edges of the shield leads to significant instability in nearfield SE. Moreover, the SE level drops intensely to 10 dB and lower adjacent to the edges. At the central region of the shield, where impinging phases interact constructively, a level of 50 dB of SE is achieved. However, a distinct difference exists between the SE distribution of SL and CSL compared to JR and SRR due to the electrical size of the cells. Figures. 3.16 (a) and (b) demonstrate the ability of SL and CSL to provide an extended shielded area from NF zones located near the shield surface to the zones located at a distance of λ from the shield. However, as one moves away from the center, CSL shows a smooth area with around 20 dB of NF-SE. This relative local SE stability makes CSL more desirable than the other three case studies.

It should be noted that, due to the scattering effects of finite substances, the FF characteristic of such limited structures is expected to be entirely dominated by the wave scattered from the edges, thereby eliminating the FF-SE performance. As a result, there is a limit on placing the susceptible object near the edged shield. For the case study presented here,

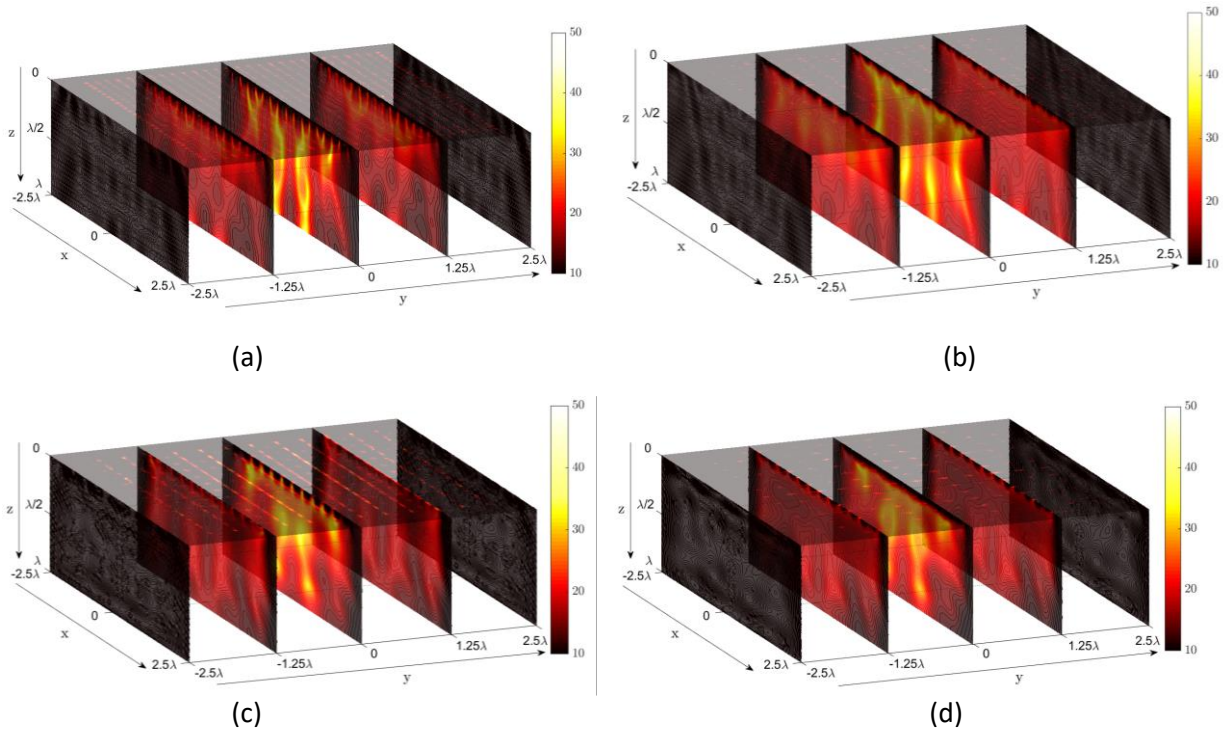

Figure 3.16. Shielding Effectiveness of a $5\lambda \times 5\lambda$ truncated shield with edge diffraction effect [5]. (a) SL (b) CSL (c) JR (d) SRR

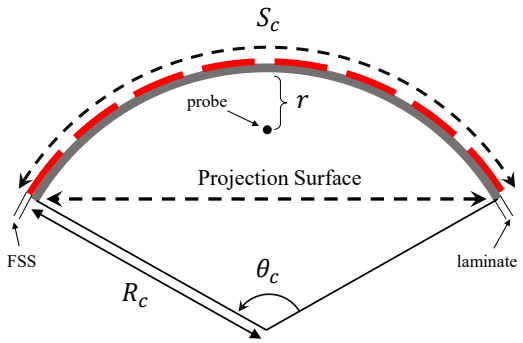

Figure 3.17. The geometry and configuration used for conformal meta-surfaces [5].

Table 3.3. Dimensions for Conformal Structures

	SL	CSL	JR	SRR
Periodicity (mm)	5.61	6.868	11.04	11.15
PL (mm)	5λ	5λ	5λ	5λ
$N = \left\lceil \frac{S_c}{P} \right\rceil \begin{cases} R_c = 20cm \\ R_c = 10cm \\ R_c = 7.5cm \end{cases}$	28 31 42	23 25 35	14 16 22	14 16 22

the maximum normal distance from the shield to provide an SE level of at least 20 dB is 72 mm (2.4λ) for SL, 96 mm (3.2λ) for CSL, 66 mm (2.2λ) for JR, and 45 mm (1.5λ) for SRR. This indicates that CSL and SL are more reliable finite-size shields.

3.5 NF Effect of Conformal Meta-surfaces

When a meta-surface is curved, it may experience changes in performance in both the NF and FF zones. The physical length of the meta-surface unit cell and the curvature radius can play a crucial role in these undesired performance changes. The curvature configuration of the conformal surfaces is illustrated in Figure 3.17, where the structure is bent in one dimension. The central angle of the arc of a circle is directly proportional to the length of the arc and inversely proportional to the curvature radius. For comparison, a 5λ projection surface is used for each conformal structure. The structures are then bent by decreasing the curvature radius. It is important to note that the length of the meta-surface array is a function of the projection length and the curvature radius, as follows:

$$S_c = \theta_c \times R_c \tag{3.24}$$

$$PL = 2R_c \sin(\frac{\theta_c}{2}) \tag{3.25}$$

Then,

$$S_c = 2R_c \sin^{-1}(\frac{PL}{2R_c}) \tag{3.26}$$

where PL is the projection length, S_c is the length of the meta-surface array, θ_c is the angle of the arc, and R_c is the curvature radius. The conformal shields' dimensions for different curvature radii are shown in Table III. As the curvature radius decreases, the number of unit cells increases, while the projection surface remains constant. To minimize the effect of edge diffraction, the edges of the structures are placed close to absorbing boundary conditions, and a tapered incident wave with reduced amplitude is used near the edges of the arc.

Figure 3.18 illustrates the cells' average NF-SE distribution for different curvature radii, which are R_c=6.66 λ, 3.33 λ, and 2.5 λ. As the curvature radius decreases, NF-SE worsens in terms of the shielded area size and the SE distribution. For the SL case, Figures. 3.18 (a), (e), and (i) show that 30-50 dB attenuation is achievable for R_c=20 cm, but it drops to 25-45 dB for R_c=10 cm and 20-40 dB for R_c=7.5 cm. Regardless of the R_c value, CSL provides higher attenuation (higher NF-SE), especially in the central region of the concave structure, as shown in Figures. 3.18 (b), (f), and (j). CSL provides an SE level of 36-61 dB for R_c=20 cm, but this value decreases to 25-47 dB for R_c=7.5 cm. However, JR has the lowest NF-SE compared to other conformal configurations. It yields a field attenuation of 17-33 dB for R_c=20 cm, 13-37 dB for R_c=10 cm, and 9-32 dB for R_c=7.5 cm, as demonstrated in Figures. 3.18 (c), (g), and (k). It is worth noting that the average SE provided by JR is closer to the lower boundary of the mentioned ranges due to the larger size of the unit cell, which leads to lower cell density within a specified area. This results in various wave incident angles on adjacent unit cells, which changes the effective interactions of the nearby cells. SRR also exhibits low performance when it comes to conformal shields. Figures. 3.18 (d), (h), and (l) demonstrate that SRR shows an

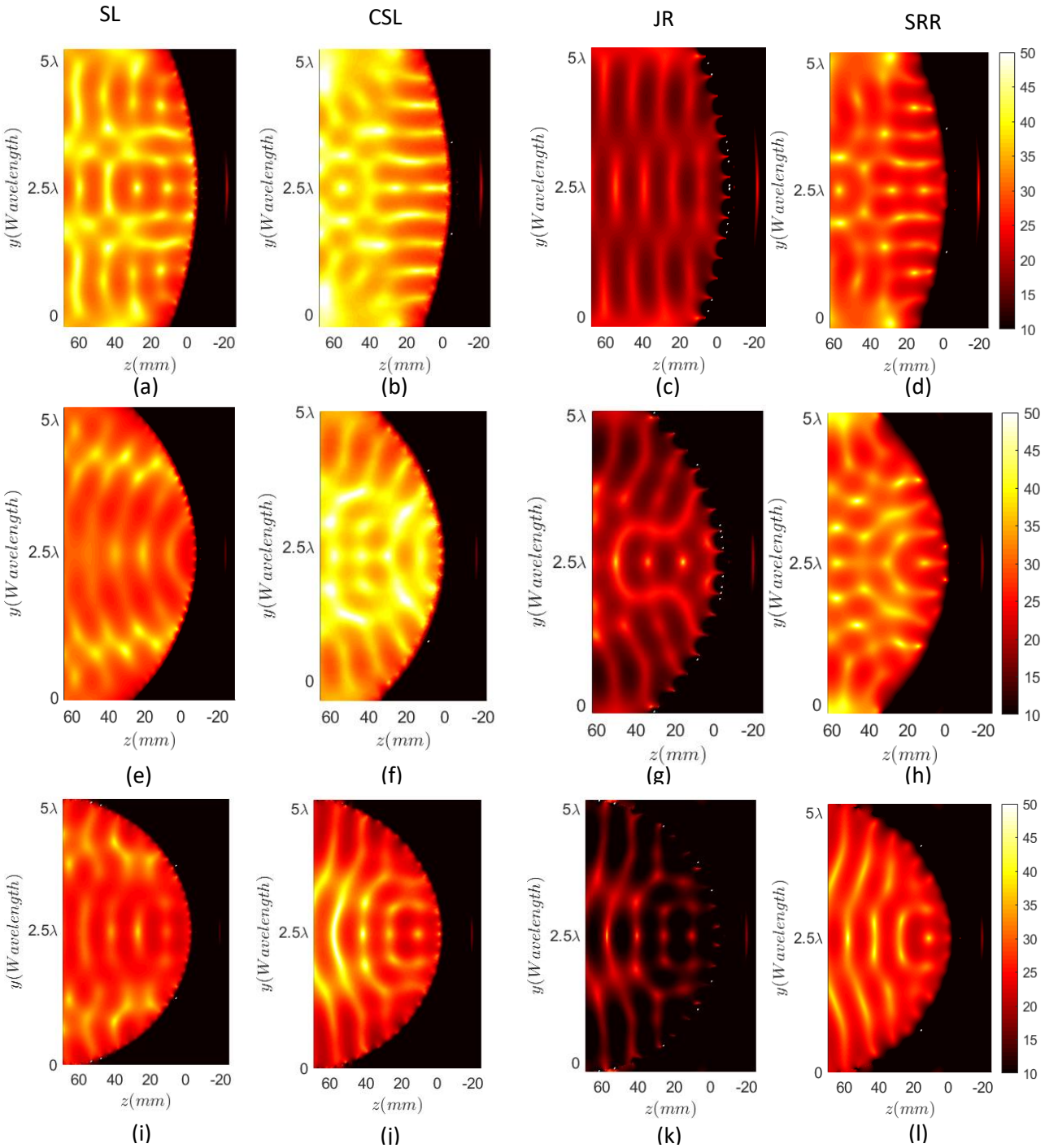

Figure 3.18. Near-field Shielding Effectiveness distribution in a conformal meta-surface (10 GHz) [5]. (a) SL (Rc = 200 mm), (b) CSL (Rc = 200 mm), (c) JR (Rc = 200 mm), (d) SRR (Rc = 200 mm), (e) SL (Rc = 100 mm), (f) CSL (Rc = 100 mm), (g) JR (Rc = 100 mm), (h) SRR (Rc = 100 mm), (i) SL (Rc = 75 mm), (j) CSL (Rc = 75 mm), (k) JR (Rc = 75 mm), (l) SRR (Rc = 75 mm),

attenuation level of 23-41 dB for R_c=200 cm, 25-45 dB for R_c=100 cm, and 20-39 dB for R_c=7.5 cm.

Figure 3.19 provides a detailed explanation of the NF-SE resonance behavior observed at five local points along the central normal of the four structures. The resonance behavior is

Table 3.4. NF Comparison Using the Developed NF Criteria

Quantity	20 dB Bandwidth	Critical Radius (Full-wave)	Critical Distance (Full-wave)
SL	24.5%	4.9cm	3.1mm
CSL	16.2%	5.1cm	4.4mm
JR	8.10%	11.8cm	5.2mm
SRR	10.2%	5.6cm	6.8mm

analyzed as the curvature radius changes from 6.6λ to 3.3λ and 2.5λ. The results indicate that compared to CSL, JR, and SRR, the square loop FSS exhibits greater stability in NF-SE, as the resonant frequency remains relatively constant at distances of 5mm or more. Additionally, the square loop FSS exhibits stable characteristics in terms of SE level at the resonant frequency. However, at specific local points, such as (r = 10, R_c = 200), (r = 30, R_c = 200), (r = 10, R_c = 100), and (r = 50, R_c = 200), dual resonance is observed due to the sensitivity of the SL unit cells to the local incident angle. In contrast, CSL is found to maintain a 20 dB bandwidth of 2 GHz for all curvature radii and produces a single 10 GHz resonance up to 50 dB for R_c=10 cm. On the other hand, JR and SRR exhibit much narrower 20 dB bandwidths of one and 1.2 GHz, respectively, which easily shifts into undesired frequency bands.

The focal axis's location in conformal structures depends on the geometry and can be found at HECR or LECR. It is theoretically established that if the number of elements in the structure is even, the focal axis will be normal to the center of unit cells, which is equivalent to LECR. Conversely, if the number of elements is odd, the normal focal axis is positioned at HECR. In terms of aperture response fidelity compared to unit cell responses, both CSL and JR structures exhibit similar performance as their unit cells. This particular feature suggests that the performance of a conformal structure on the focal axis can be predicted using the proposed analytical model.

3.6 Critical Distance and Critical Radius

SE degradation and resonant frequency transition in infinite planar shields can pose a significant security risk and must be accurately quantified. To address this issue, the critical distance (d_{cr}) can be defined as the distance at which the SE level undergoes a 20 dB decrease or the resonant frequency shifts by 10% of the desired bandwidth. For instance, the critical distance can be calculated for SL, CSL, JR, and SRR to be 3.1, 4.4, 5.2, and 6.8 mm, respectively. Therefore, SL has a smaller critical distance compared to the other structures.

In the case of the curved configuration, a critical radius (R_{cr}) can be defined as the curvature radius that provides a shielded area with an SE level of 25 dB and no more than a 10% shift in resonant frequency, which covers at least half of the total area (half-circle area

$\pi R_{cr}^2/2$). For SL, CSL, JR, and SRR, this value is calculated as 4.9 cm, 5.1 cm, 11.8 cm, and 6.2 cm, respectively. It is worth noting that the bandwidth influences the nearfield SE changes and resonant frequency shifts, and therefore, the critical radius may vary for each structure depending on the bandwidth. Table IV provides an NF comparison of the cells analyzed in this study based on the criteria.

3.7 Further Discussions

While the results presented in this study are specific to four common geometries, they can be applied more broadly to other structures due to the fundamental LECR and HECR analyses applicable to all unit cells. Some key observations that can be generalized include:

Since capacitive and inductive elements are present in all equivalent circuit models, LECR and HECR are considered local low and high capacitive effects in all meta-surfaces. The only variation between different unit cells is the spatial periodicity of the extreme regions, which causes differing densities of near-field anomalies. Therefore, designers of shields are advised to consider the behavior of cells in these two regions carefully.

NF to FF convergence is another feature that may be supported in all metasurfaces. The fact that the geometrical dimension affects the convergence rate may also be considered a general solution for controlling the NF effects of metasurfaces. As observed in this chapter, increasing bandwidth has resulted in unstable NF characteristics in all the metasurfaces under test. Thus, the NF SE of shields has to be compared with respect to the rational bandwidth of the structures. When the bandwidth is large, this loss in the NF stability might be a challenging topic for future work.

To control the near-field effects of metasurfaces, the phenomenon of NF convergence to FF can be used, and it is a common feature in all types of meta-surfaces. The geometrical dimensions and structure bandwidth influence the convergence rate. We saw that a wider bandwidth causes unstable NF characteristics in all metasurfaces tested. Therefore, comparing the near-field SE of shields should be done in relation to the rational bandwidth of the structures. The loss of NF stability at higher bandwidths is a topic that could be addressed in future works.

When subjected to bending or edge diffraction, the shielding stability of miniaturized structures can be applied to other small structures. In future studies, it would be beneficial to analyze other highly miniaturized components, such as multiple split ring resonators [104] and spiral resonators [105]. This analysis can provide greater control over localized attenuation of the near-field. The introduced critical distance and critical radius criteria are valuable tools for such investigations into the near-field.

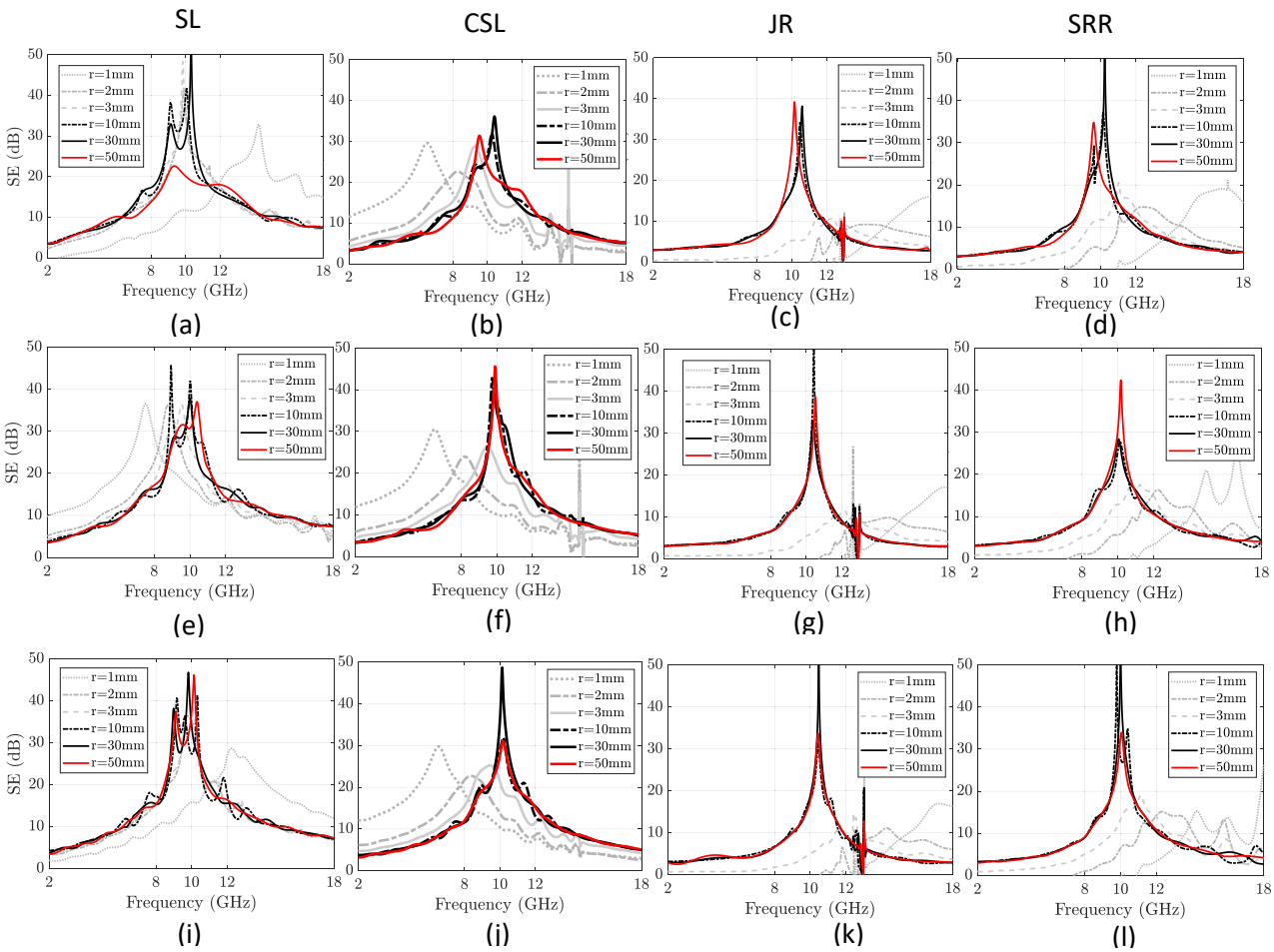

Figure 3.19. Local SE versus frequency in conformal meta-surfaces (10 GHz) [5]. (a) SL (Rc = 200 mm), (b) CSL (Rc = 200 mm), (c) JR (Rc = 200 mm), (d) SRR (Rc=200 mm), (e) SL (Rc = 100 mm), (f) CSL (Rc = 100 mm), (g) JR (Rc = 100 mm), (h) SRR (Rc = 100 mm), (i) SL (Rc = 75 mm), (j) CSL (Rc = 75 mm), (k) JR (Rc = 75 mm), (l) SRR (Rc = 75 mm),

Last but not least, our data shows that given the specific ECM model, the provided analytical method may be capable of estimating the NF performance of LECR and HECR of every single layer, single-sided FSS structure regardless of the structure's geometry.

This chapter has addressed the fundamental differences between farfield and near-field shielding performance in single-layer frequency-selective surfaces. Now that we have gained much insight into near-field abnormalities, we can explore further to find ways to reduce these nearfield malfunctions.

Chapter 4: Metasurface Design

In the previous chapter, we investigated the abnormal NF behavior of conventional bandstop metasurfaces. One remaining question is, is there any design approach that can lead to a stable NF behavior? In this chapter, we will introduce a new type of flexible bandstop frequency selective surface (FSS) that offers stable nearfield (NF) characteristics at the X-band frequency range, which was impossible with traditional FSSs analyzed in Chapter 3. The proposed structure consists of two layers of patches, with periodic convoluted square loops (CSL) on one side of a flexible substrate and periodic square loops (SL) on the other. The interaction between the patches creates a multipole resonator that operates by changing the local coupling effect between the cells on both sides, resulting in capacitive and inductive characteristics that enable spatial filtering for both nearfield and farfield. We have developed an accurate equivalent circuit model (ECM) to validate the coupling effect and have identified four operational modes with distinct behavior. We have demonstrated the structure's performance using each operational mode and have achieved an X-band NF shielding of at least 30 dB at the center frequency with a maximum 10-dB fractional bandwidth of 32%. This structure outperforms conventional shields in terms of nearfield shielding performance, which is confirmed by measurement results.

4.1 Abnormal NF Problem

So far, we have learned about the difficulties related to FSS NF performance. Chapter 3 analyses showed that while FF shielding may be effective, it does not necessarily translate to the same level of NF performance. The study also suggested that the widely used single-sided shields may have compromised performance due to the absence of NF compatibility.

Based on the findings, conventional structures do not provide sufficient nearfield stability, leading to resonant frequency fluctuations and degradation in shielding effectiveness. This degradation is fundamentally justified as frequency-selective surfaces are resonant structures with distinct nearfield and farfield zones. In the nearfield zone, most energy is stored as standing wave energy due to the imaginary wave impedance, resulting in no specific resonant frequency. In contrast, the imaginary part of the wave impedance degrades in the farfield zone, and wave power converges to the real traveling wave value. The nearfield stability varies among structures, with some providing shorter shielding convergence from nearfield to farfield zones. Although, in Chapter 3, a model was proposed to predict the instability in single-layer, one-

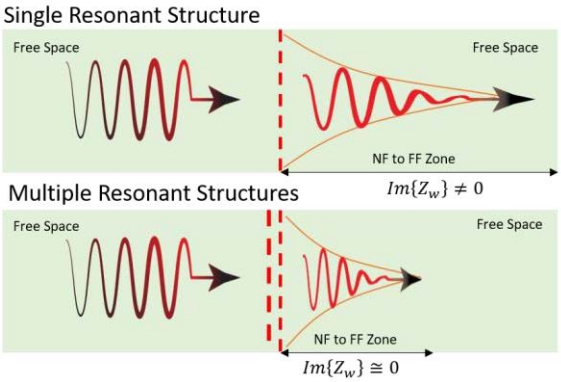

Figure 4.1. Spatially faster convergence of multi-resonant structures [6].

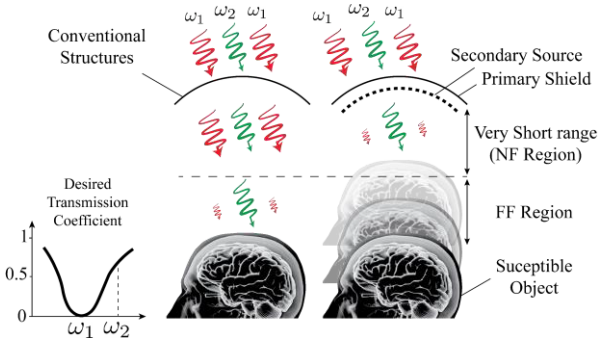

Figure 4.2. The application of two resonant sources in reducing the distance between the susceptible object and the shield [6]. The shields may be brought closer to the susceptible object with the effect of the secondary source in shortening/removing the undesired NF zone

sided structures, no structural solution has been developed to overcome these NF instabilities. As a result, using conventional unit cells in wearable shields may still result in interference, causing biological hazards or component malfunctions. On the other hand, complying with FF regulations alone is inadequate to ensure NF shield compliance. Many X-band applications require an NF range of 1-10 mm, which necessitates a design that can cause considerable loss within a small range. This specified NF range is called the reactive and radiating NF regions, where the field variations experience local instability and intense wave impedance variations [18]. The meta-surfaces currently available are not designed with NF considerations in mind. As a result, NF instability causes a significant shift in resonant frequencies and degradation in shielding effectiveness, as stated in [5].

This study focuses on the issue of shielding, which pertains to an object sensitive to specific frequency bands (X-Band) while allowing communication through other frequency bands. The problem involves an interfering or hazardous signal that could impact the object. To address this issue, it is necessary to identify two types of frequency components: those that are desired and those that are undesired. The flexible shield aims to conceal one of the undesired frequency components while permitting the passage of the other frequency component.

4.2 Multi-resonant-structure solution

This section proposes that the interaction of two resonant structures could be optimized to provide a faster nearfield to farfield convergence (faster conversion of the imaginary wave impedance to real). Figure 4.1 illustrates the conceptual difference between shields with single resonant structures and those with multiple resonant structures optimized for creating stable effects in NF zones. This methodology can be applied to other metasurface applications that require specific performance in the nearfield zone. First, the two resonant structures need to be chosen. The choice highly depends on the general performance the designer requires (bandpass, band stop, multiband). Then, each resonant structure's nearfield (NF) performance needs to be

monitored by time-domain or frequency-domain nearfield probes. The cells are then placed close to one another to observe how NF characteristics change. This response can then be optimized to analyze the level of NF improvement. Using three resonant structures might create faster NF to farfield (FF) convergence but will probably deteriorate the bandwidth, as three structures can exhibit three different electrical lengths leading to different undesired harmonics. In this case, the resulting unit cells will consist of two conducting patches mounted on two sides of a flexible laminate to provide destructive field components at the desired frequency band. The optimum interaction leads to stable NF shielding effectiveness. NF region is not removable as it is an integral part of the radiation characterization of any resonant structure. However, if the designer uses a nearby local interaction of a secondary electromagnetic source, NF stabilization could lead to a shortened NF to FF range. The NF interaction should be destructive in the NF region to create a band-stop characteristic. If the design lacks NF capabilities, there is a risk of unattenuated emissions of undesired frequency components in the NF region due to unstable transmission zeros [5]. However, they diminish in the FF, making it safe for the susceptible object to be placed in the FF region. Figure 4.2 illustrates this concept in a practical example, where a living organism (human brain) is exposed to radiation in a microwave problem. The shield is supposed to provide a filtering effect for some frequencies while it is invisible for others. Without an NF shield, the metasurface must be placed far away from the susceptible object, leading to bulky measurement facilities. While the susceptible object can be brought close to an NF-compatible shield, making the facility much more compact. We will show this is possible by designing a secondary resonant source and optimizing its mutual coupling with the primary shield.

Adding an engineered secondary source can result in faster spatial convergence of the fields in the NF region, effectively securing the NF region against undesired frequency components. This spatially faster attenuation is achieved by a faster annihilation of the imaginary part of wave impedance, as demonstrated in Figure 4.1. To create a secondary NF source, another structure is placed on the opposite side of the flexible shield, and the mutual coupling is optimized to enable the necessary interaction without interfering with the actual performance of the resonant structure. It is important to note that the secondary source may not resonate at the desired frequency, as it only contributes to NF convergence. Additionally, each resonating cell must have a secondary unit cell at the unit-cell level.

The mechanism for achieving nearfield (NF) shielding is akin to achieving NF focus using lens structures in the microwave regime. In microwave lenses, the planar distribution of cells can be optimized to achieve various responses, including NF focus, where array theory in the NF is incorporated to create nulls or amplification at different local points. However, this chapter aims to demonstrate that a similar behavior can be obtained at the cell level rather than the array level. In other words, this work suggests that having only two resonant structures is sufficient for achieving the desired response in the NF zone. Therefore, the mechanism is similar to what is observed in lens behavior using planar distributions, but the tuning factors are different and somewhat more complicated.

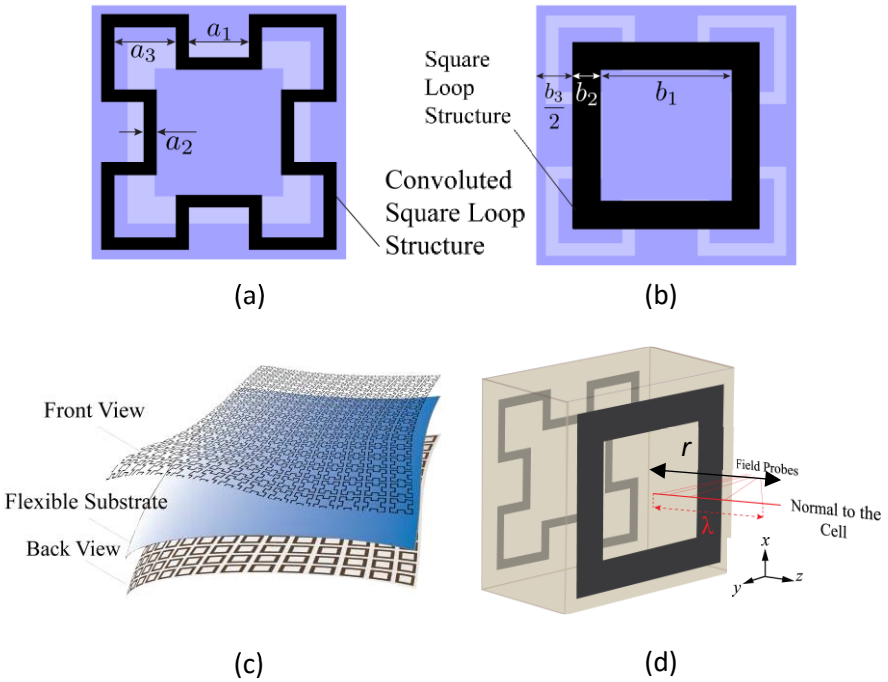

Figure 4.3. The proposed design [6], (a) Front view, Convoluted Square Loop (b) Back view, square loop structure, (c) Topology of the flexible FSS created by periodically repeating the proposed unit-cells on the two sides of a flexible laminate in two dimensions. (d) Perspective view of the cell near-field simulation setup.

Table 4.1. Dimensions of the Unit-Cell Operating at 10 GHz
(Units in Millimeter)

Parameters	Optimization Range	Optimized Dimensions
a_1	0.50-2.0	1.19
a_2	0.15-0.6	0.23
a_3	0.50-2.0	1.23
b_1	1.00-4.0	2.53
b_2	0.15-0.6	0.53
b_3	0.15-0.6	0.35

For instance, the interaction between the different parts of the two resonant structures in NF shielding can be interpreted as the interaction between the cells in array theory. The surface current distribution throughout the cell structure is interpreted as the amplitude distribution in array theory. Similarly, the surface current phase distribution is interpreted as the phase distribution in arrays. Since the interaction intensities, elements, and distances vary significantly depending on the geometry of the two resonant structures, numerical methods are the most accurate for analyzing them.

4.3 Proposed Cell and its NF Shielding Performance

For the FSS design, a Convoluted Square Loop (CSL) has been chosen as the resonating cell, while a miniaturized Square Loop (SL) is used on the backside, as depicted in Figures. 4.3(a) and 3(b), respectively. CSL is preferred in literature because it provides more polarization stability [7, 100]. A Rogers 5880 laminate with a thickness of 0.127 mm, a relative permittivity of 2.2, and a dielectric loss tangent of 0.0009 is utilized to ensure the structure's conformability. Figure 4.3(c) illustrates the topology of various parts of the proposed FSS resonator. The initial structure has been optimized as a filter with a single transmission zero at 10 GHz. Table I provides the optimized dimensions for the designed structure and the associated ranges have been chosen to guarantee the final structure's miniaturization.

To conduct a nearfield analysis, a periodic unit-cell is subjected to a plane wave that includes undesired X-band frequency components. The setup for the unit cell simulation can be seen in Figure 4 (d). The reflected and transmitted electric fields are detected and distinguished using the following fundamental relations.

$$\vec{E}_T = \vec{E}_{TOT} \tag{4.1}$$

in the transmission zone, and

$$\vec{E}_R = \vec{E}_{TOT} - \vec{E}_I \tag{4.2}$$

in the reflection zone, where $\vec{E}_R$, $\vec{E}_T$, $\vec{E}_I$, and $\vec{E}_{TOT}$ are the reflected, transmitted, incident, and total electric field vectors, respectively. Then, the effectiveness of the shield is computed by

$$SE = 20\ log \left| \frac{\chi_I}{\chi_T} \right| \tag{4.3}$$

where subscripts I and T refer to the incident and transmitted waves, respectively, and χ refers to the electric or magnetic fields.

Variations in NF-SE may occur when the probe is moved along the x or y direction due to the non-uniform concentration of energy near the structure, leading to different NF effects. It has been demonstrated that there is a periodic region of low and high energy concentration with low and high local capacitive effects. Therefore, as suggested in [5], the unit-cell performance should be monitored at both the center and edge, where the extreme effects are predominant. Figure 4.4 (a) shows the computed SE along the central normal to the unit cell, where "r" represents the observation distance from the cell. It is observed that the transmission zero demonstrates stable performance as we approach the surface. Figure 4.4(b) shows the computed SE along the normal to the surface at the unit cell's edge. Similar stable NF performance is observed in this region. The performance for the distance range of r = 30 mm to

the farfield is presented with a single solid red or blue curve, as no changes are observed. However, in both cases, a slight decrease in the depth of the transmission zero is experienced.

Figure 4.4 (c) and (d) demonstrate the NF response of a single-sided CSL proposed in [7] in two specified regions for comparison purposes. The results indicate that the single-sided FSS lacks sufficient NF stability, as stated in [5], making it unsuitable for wearable applications. Therefore, due to its unstable NF transmission zero, the CSL cannot provide the necessary shielding of 30 dB at 10 GHz within 5 mm from the surface. In contrast, the new design offers a zero dB SE at 11 GHz, creating a distinct upper shielding band, which provides greater control over the shielded spectrum. Furthermore, the co- and cross-polarized NF electric field distribution of the proposed cell and the conventional single-layer CSL are compared in Figures. 4.4 (e) and (f), respectively. The proposed cell exhibits superior field attenuation of 35 dB in the nearfield zone (within 20 mm from the structure). The co-polarized transmission is more uniform, leading to a more stable nearfield performance. Additionally, the proposed cell minimizes cross-polarized components, which may help improve signal integrity.

In order to gain further insight into the performance, a different scenario was studied and documented in [106]. The investigation focused on two harmonics, one that is desirable and the other undesired. The undesired harmonic falls within the bandgap and has a frequency of 10.5 GHz, while the desirable harmonic lies outside the bandgap and has a frequency of 14 GHz. The graph in Figure 4.5 displays the harmonic attenuations measured in dB. The proposed structure effectively shields the undesired harmonic within the critical NF zone by providing 20 dB of attenuation. Additionally, it maintains the second harmonic more effectively than the traditional CSL across the entire NF zone. On the other hand, the conventional structure provides less than 20 dB attenuation within the first 5 mm from the undesired component's structure, the first harmonic.

In Figure 4.4, it is apparent that the proposed unit cell and the CSL differ in their bandwidths, with the former appearing to have a narrow bandwidth due to the interaction between its two patches. However, the subsequent section demonstrates that tuning the corresponding equivalent circuit model can substantially eliminate this narrow bandwidth, generating both narrow and wideband characteristics with adjustable reflection zeros.

4.4 An Accurate Equivalent Circuit Model

Creating an accurate equivalent circuit model (ECM) for the proposed design can offer more insight into how the transmit-metasurface works. Additionally, it presents an opportunity to manipulate the hidden features of the design by regulating the mutual coupling, wave impedance, and the resonant frequency associated with it. To accomplish this, the reflection/transmission performance of the structure must first be analyzed using a full-wave approach. Subsequently, an equivalent schematic that considers each element is proposed based on the structure's geometry and possible coupling components. Finally, an optimization process

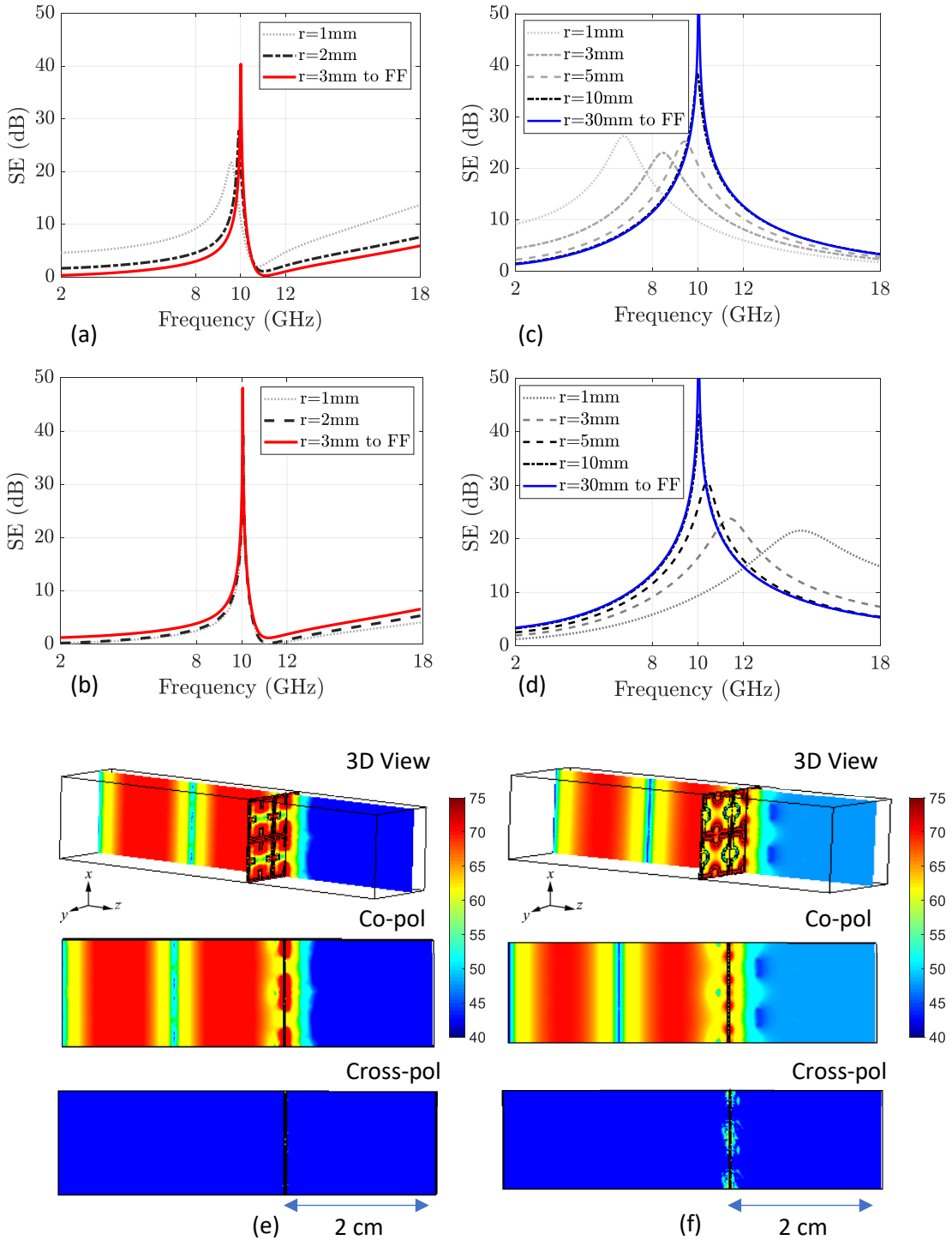

Figure 4.4. Unit cell analysis in nearfield [6], (a) NF-SE for the proposed layer along the central normal where the inductive effect is dominant, (b) NF-SE for the proposed layer along the axial normal where the capacitive effect is dominant, (c) NF-SE for for CSL along the central normal where the inductive effect is dominant, (d) NF-SE for CSL along the axial normal where the capacitive effect is dominant, (e) co- and cross- polarized field distribution for the proposed cell (10GHz) (dBv/m), (f) co- and cross- polarized field distribution for CSL (10GHz) (dBv/m).

is conducted to achieve the same reflection and transmission coefficient as the full-wave analysis by precisely determining the capacitive and inductive effects of the structure.

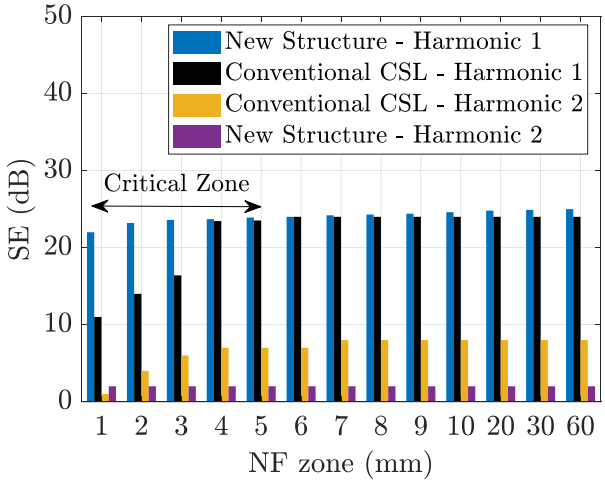

Figure 4.5. SE variations of the structures under test for two harmonics. Harmonic 1 is an undesired harmonic to be shielded while harmonic 2 is a desired component which should be preserved in NF zone.

In order to demonstrate how the two sides of the structure can result in zero transmission at 10 GHz, a detailed schematic from Figure 4.6 (a) must be utilized, incorporating the interelement mutual couplings. By utilizing electromagnetic compatibility principles [18] and transmission line theory, each line oriented in the same direction as the incident electric field introduces an inductive effect on the contributing loop and is represented as an inductor. Similarly, the adjacent metallic surfaces store energy modeled as a capacitor. The vertical branch of the SL has a mutual coupling effect on the vertical branches of the three neighboring CSLs, resulting in three mutual coupling effects of M_i (i=1,2,3). Additionally, there may be some energy stored between the two faces, which can be represented by a capacitor C_3. Notably, since the branches modeled by L_2 and L_4 have equal length, L_2 and L_4 are also equal and exhibit equal mutual coupling to $L_1 (M_1 = M_3)$.

Figure. 4.6 (b) displays the proposed circuit schematic for the tested design. The full-wave analysis results for transmission and reflection are utilized as references in a circuit simulator. Keysight Advanced Design Systems (ADS) platform is utilized for the schematic synthesis procedure, while the optimization process uses a Genetic Algorithm (GA). The schematic undergoes optimization to estimate the capacitive and inductive effects, with the resulting values being reported in Table II. It is important to note that additional inductive and capacitive effects may have been introduced based on the structure's geometry. However, their contribution is deemed insignificant during optimization, resulting in very low values. For instance, the low value for the capacitor C_3 indicates that the energy stored in the thin substrate is negligible.

Although the full-wave analysis can be utilized to verify the results, the proposed circuit from Figure 4.6 (b) can be solved to obtain the scattering matrix of FSS and the impedance characteristics (Z_{FSS}). According to the recommended process in [107], the system ABCD matrix must be determined first. Since the Figure. 4.6 (b) model incorporates the impact of both sides

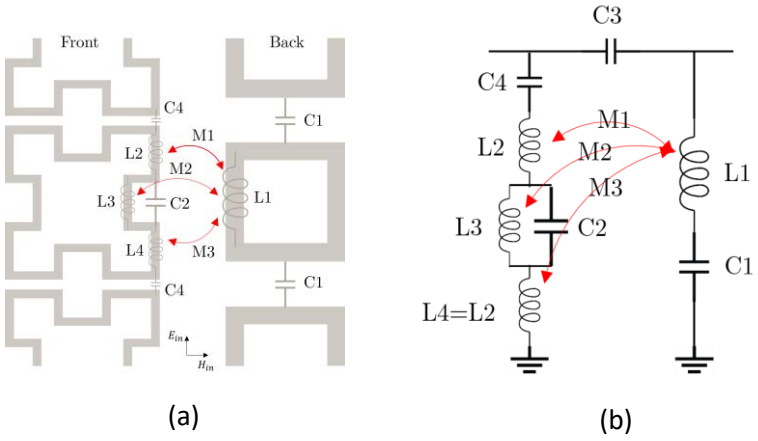

Figure 4.6. ECM for the proposed structure [6], (a) Interelement interactions and equivalent circuit elements, (b) The resulted schematic

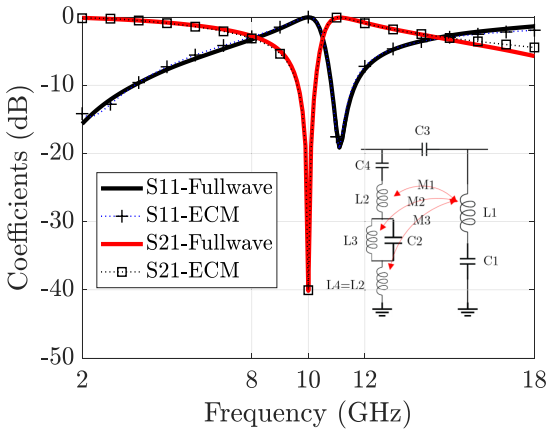

Figure 4.7. Comparison of the transmission and reflection effect of the proposed structure using the suggested ECM and full wave analysis [6].

Table 4.2. Values of Capacitors & Inductors for the proposed ECM

PARAMETERS	VALUES
L_1	26.4193 nH
L_2	7.14912 nH
L_3	22.0803 nH
L_4	7.14912 nH
C_1	0.678402 pF
C_2	0.0237627 pF
C_3	2.353e-07 pF
C_4	1.45453 pF
M_1	8.91665 nH
M_2	19.1736 nH
M_3	8.91665 nH

Table 4.3. Impedance Coefficients

Parameters	Values	Parameters	Values
A_0	0	B_0	-4.1×10^{84}
A_1	$-(1.5\times10^{77})j$	B_1	$-(1.0\times10^{75})j+7.9\times10^{76}$
A_2	5.8×10^{67}	B_2	7.5×10^{64}
A_3	$(3.2\times10^{57})j$	B_3	$(5.5\times10^{53})j-10^{57}$
A_4	-7.9×10^{45}	B_4	-1.4×10^{43}
A_5	$-(1.7\times10^{35})j$	B_5	$(1.5\times10^{27})j-5.0\times10^{35}$
A_6	-6.7×10^{18}	B_6	-6.1×10^{16}
A_7	$-(3.4\times10^{8})j$	B_7	3.4×10^{8}

of the patch and their interactions, the following ABCD matrix adequately represents the entire unit (i.e., two patches and the substrate in between).

$$\begin{bmatrix} A & B \\ C & D \end{bmatrix} = \begin{bmatrix} 1 & 0 \\ 1/Z_{FSS} & 1 \end{bmatrix} \tag{4.4}$$

where Z_{FSS} is the computed FSS impedance. One can calculate the reflection and transmission coefficient of the structure using the following equations.

$$S_{11} = \frac{AZ_0 + B - CZ_0^2 - DZ_0}{AZ_0 + B + CZ_0^2 + DZ_0} \tag{4.5}$$

$$S_{21} = \frac{2Z_0}{AZ_0 + B + CZ_0^2 + DZ_0} \tag{4.6}$$

where $Z_0 = 377$ Ohms is the free space intrinsic impedance. To determine the FSS impedance characteristics using the ECM, one may utilize frequency domain (phasor) analysis. In this approach, the mutual coupling on the front face can be represented by three controlled voltage sources of

$$v_i = j\omega M_i\ (I_i), \quad i = 1,2,3 \tag{4.7}$$

where ω is the angular frequency and I_i is the current of the involved loop. Then, four equations must be solved to determine the circuit's input impedance. However, the parametric solution of these equations results in an overly complex expression for the input impedance. Therefore, we opt to utilize the exact values of capacitance and inductance. As a result, the input impedance of the shield can be approximated as follows.

$$Z_{in}(\omega) \cong \frac{A_7\omega^7 + A_6\omega^6 + A_5\omega^5 + A_4\omega^4 + A_3\omega^2 + A_1\omega + A_0}{B_7\omega^7 + B_6\omega^6 + B_5\omega^5 + B_4\omega^4 + B_3\omega^2 + B_1\omega + B_0} \tag{4.8}$$

where the coefficients, A_i and B_i, are listed in Table III. From $Z_{in}(\omega)$ and the schematic of Figure 4.6 (b), $Z_{FSS}(\omega)$ can be calculated by,

$$\begin{aligned} Y_{in}(\omega) &= \frac{1}{Z_{in}(\omega)} \\ &= Y_{FSS}(\omega) + \frac{1}{\eta_0} \\ &= \frac{1}{Z_{FSS}(\omega)} + \frac{1}{\eta_0} \end{aligned} \tag{4.9}$$

$$Z_{FSS}(\omega) = \frac{1}{Y_{in}(\omega) - \frac{1}{\eta_0}} \tag{4.10}$$

where $\eta_0 = 120\pi$ is the intrinsic impedance of free space.

Figure 4.7 compares the analytical ECM-based response to the full-wave analysis. It is noted that a reflection zero is present near the transmission zero. However, this reflection zero does not restrict the structure's performance and helps create a sharp upper-band roll-off, which can be used to control transmission cut-offs. It should be emphasized that combining the single schematic of each side through cascading does not produce the same transmission and reflection effect, as shown in Figure 4.7, because it does not account for mutual coupling. The following section further explains the proposed design operational behaviors and associated ECM by highlighting the shield's different characteristics.

4.5 Operation Mode Analysis

4.5.1 Mode Investigation

The ECM for the proposed design offers valuable insights into the potential capabilities of the shield, which can expand its possible applications. The position of the reflection zero, its relationship with the transmission zero, and its location within the spectrum are among the important features that could be of interest. Additionally, having more control over the stopband bandwidth is another advantage from which a shield designer may benefit.

As the circuit elements of Figure. 4.6 are linked to multiple parts of the structure. Changing a single physical dimension of the unit cell can change multiple circuit elements. Therefore, analyzing the contribution of each element separately may not be directly linked to the effect of a specific physical dimension. Hence, the analysis of the elements should be purposeful and selective. For example, four distinct operation modes can be achieved by tuning the proposed ECM's mutual coupling parameters M1 and M2, as shown in Figures. 4.8 (a), (b), (c), and (d). These modes include 1) a preceding reflection zero, 2) two reflection zeros, 3) a posterior reflection zero, and 4) a wideband response without a reflection zero. Mode 1 is useful when a sharp lower band roll-off is required, while Mode 2 is beneficial for dual-band stopbands but with a narrower stopband due to surrounding reflection zeros. Mode 3 is used when an upper band threshold is needed, and Mode 4 provides wideband coverage with smooth roll-offs. These modes provide designers with greater flexibility and insight into the potential capabilities of the shield.

4.5.2 Realization of Potential Operation Modes

The aforementioned potential performances can be achieved by selecting an appropriate mutual coupling for the design, which can be controlled by changing the substrate and cell line thicknesses. However, a separate optimization process is required to utilize the four hidden features. Full-wave analysis and their NF transmission performances show that all operation modes provide a very stable NF transmission stability due to the presence of the secondary cell.

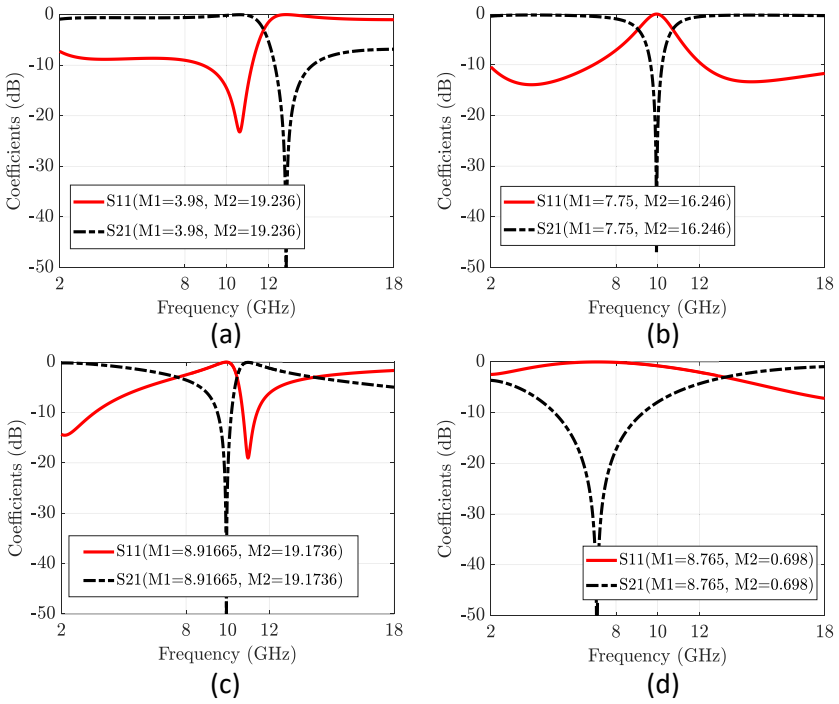

Figure 4.8. Different operation modes by adjusting the mutual couplings of the ECM [6]. (a) Mode 1: preceding reflection zero, (b) Mode 2: two reflection zeros, (c) Mode 3: posterior reflection zero, and (d) Mode 4: wideband response without reflection zero.

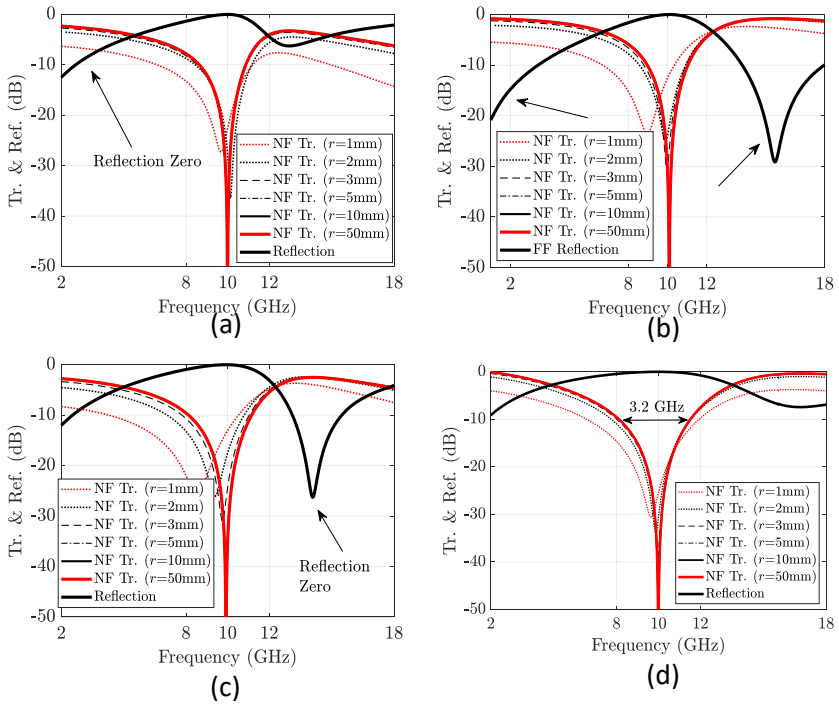

Figure 4.9. Realization of the predicted transmission (Tr.) modes using full-wave analysis and their NF performances [6]. (a) Op. Mode 1: preceding reflection zero, (b) Op. Mode 2: two reflection zeros, (c) Op. Mode 3: posterior reflection zero, and (d) Op. Mode 4: wideband response without reflection zero. Zeros are shown by arrows.

The stopband attenuation level and the resonance frequency shifts are also very stable for all

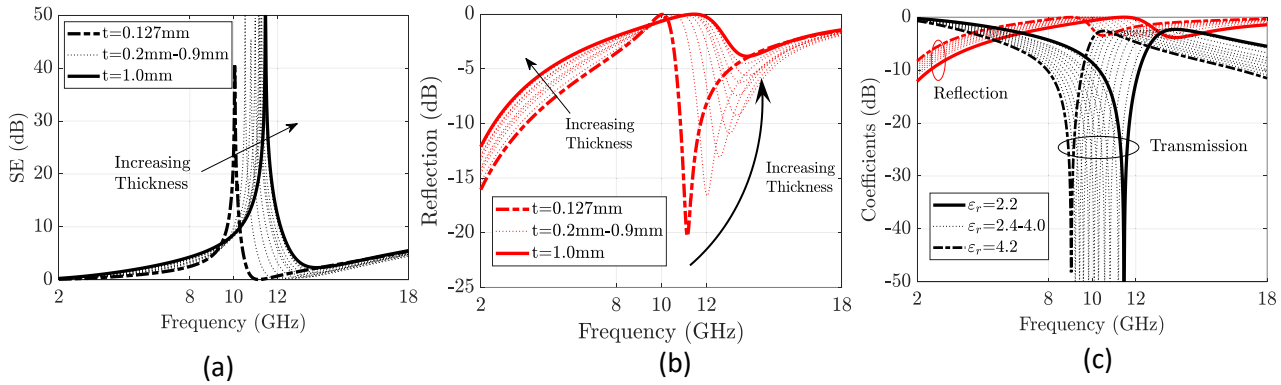

Figure 4.10. Illustration of the substrate effect on the SE and reflection zero of the surface [6]. (a) SE variation by changing the substrate thickness (b) Reflection zero variations by changing the substrate thickness, (c) SE sensitivity to the relative permittivity of the substrate

Table 4.4. Dimensions of the Structures with Different Operation Modes (Units in Millimeter)

Parameters	Op. Mode 1	Op. Mode 2	Op. Mode 3	Op. Mode 4
a_1	1.45	0.46	0.89	0.89
a_2	0.16	0.174	0.44	0.44
a_3	1.47	1.90	1.43	1.43
b_1	2.74	1.58	1.5	1.5
b_2	0.365	0.467	0.57	0.57
b_3	2.05	2.836	3.15	3.15
thickness	1.205	0.127	0.127	1.37

operation modes. Modes 1, 2, 3, and 4 provide a 10 dB fractional bandwidth of 20%, 19%, 28%, and 32%, respectively. Due to the physical limitations, obtaining strong reflection zeros is impossible. For example, obtaining a reflection zero ahead of the transmission zero is more challenging due to the structure's intrinsic limitations. The dimensions of the structures for each mode are reported in Table IV.

Chapter 3 has uncovered an unfavorable relationship between the bandwidth and the convergence of the near-field (NF) of single-sided meta-surfaces [5]. It was discovered that surfaces with broader bandwidths tend to exhibit more instability in the NF compared to those with narrower bandwidths. However, this work presents a unique characteristic in which the NF stability is independent of the structure's bandwidth and potentially its dimensions. As illustrated in Figure 4.9, the NF transmission coefficient remains constant in the NF zone, even though the modes have different bandwidths. This is attributed to the localized effect of the secondary source, resulting in faster spatial convergence of the NF fields.

4.6 Adjustable Reflection/Transmission

Certain geometric factors can influence the position, depth, and presence of reflection zeros, and controlling these characteristics can be achieved through parametric analysis. The substrate characteristics significantly impact the mutual coupling between the two sides; therefore, it is a crucial factor to consider. Figure 11 demonstrates this effect on Mode 3's transmission and reflection. Figure 4.10(a) shows that the shielded band shifts as the substrate thickness increases, and the stopband 10 dB bandwidth has increased from 0.5 GHz (5% fractional bandwidth) to 1.8 GHz (16% fractional bandwidth). Furthermore, Figure 4.10(b) indicates that the reflection zero decreases by -16 dB when the substrate is 1 mm. Thus, increasing the bandwidth leads to the elimination of the reflection zero. Another parametric analysis is conducted using a 1 mm thickness for the structure to illustrate the effect of the relative permittivity of the laminate. Figure 4.10(c) demonstrates that the frequency shift caused by the substrate thickness increase could be entirely compensated.

4.7 Shielding against High Power Radiations

This section aims to test the performance of the shield in a simulation that resembles a real-life scenario and complies with standard regulations. The aim is to identify any local characteristics of the transmitted field distribution by monitoring field patterns. The shield's performance is expected to remain unaffected when used in planar or conformal configurations for flexible applications. However, the spatial phase distribution of the transmitted waves may differ when the structure is bent due to edge diffractions and geometrical deformation, which may cause performance degradation. In [5], it has been shown that miniaturized unit cells can withstand these destructive bending effects. Mode 2 design is selected for further investigation because it has a thin laminate and a large enough bandwidth.

4.7.1 FCC criteria for microwave exposure

The Federal Communications Commission (FCC) has recognized that exposure to high levels of RF power can be hazardous due to thermal effects and has stated that exposures above 100-200 $\mathrm{mW/cm^2}$ can cause serious harm to biological tissue [108]. The following equation can be used to estimate the equivalent electric field intensity of high-power radiation [109].

$$W_{av} = \frac{1}{2} Re\{\boldsymbol{E} \times \boldsymbol{H}^*\} \ (\mathrm{W/m^2}) \tag{4.11}$$

where W_{av} represents the wave power density. The equivalent electric field intensity that satisfies the FCC regulation can be calculated using the following formula for plane waves: $|\boldsymbol{H}| = |\boldsymbol{E}|/\eta$, where η is the intrinsic impedance of free space.

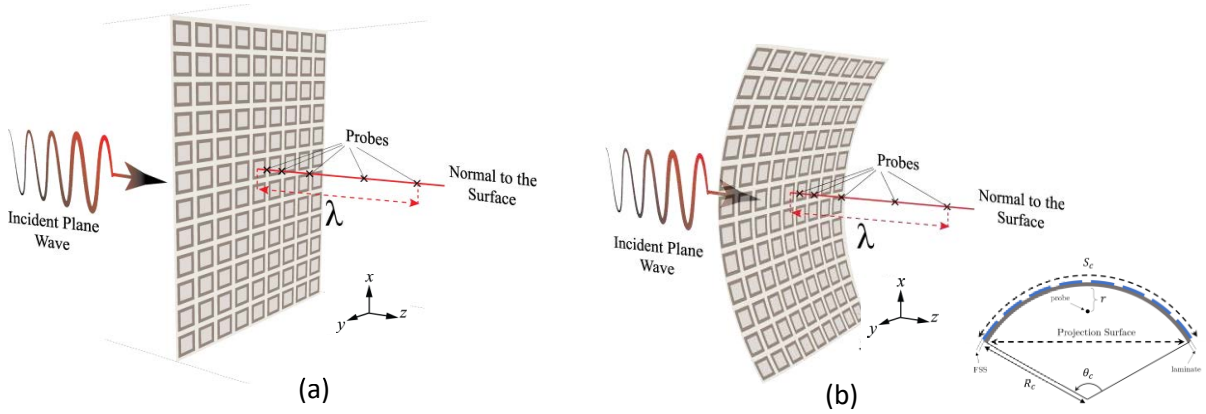

Figure 4.11. The 3D configurations used for FSS field distribution analysis [6]. (a) Planar, and (b) Conformal

$$|E| = \sqrt{2\eta W_{av}}\ (\mathrm{V/m}) \tag{4.12}$$

Therefore, in order to avoid any thermal effect, the electric field intensity must be reduced to a level that is less than 868 V/m (58.8 dBV/m).

4.7.2 Shielding performance for planar and curved surfaces

The meta-surface proposed in this study is tested in both planar and conformal configurations, as shown in Figure 4.11. The length of the shield is kept constant, while different curvature radii are used to account for various projection surfaces. The curvature radii are chosen to cover the maximum bending applicable to the human body. The projection length in the curvature is determined by the number of unit cells, unit cell length, and curvature radius, as per a specific formula.

$$PL = 2R_c \sin\left(\frac{NP}{2R_c}\right) \tag{4.13}$$

where R_c, S_c, and PL represent the curvature radius, the length of the meta-surface array, and the projection length, respectively (see Figure 4.11). P represents the unit cell length. The experiment used three projection lengths of 10λ, 9λ, and 6.6λ, consisting of 60 unit cells, as suggested by (4.13). A high-power plane wave with 75 dBV/m electric field strength is directed toward the shield, while the safe area, according to the FCC, is considered to be at 55 dB or lower intensity. The NF electric fields were monitored to compute the field distributions. The electric field intensity distribution for the planar configuration is shown in the 2D view in Figure

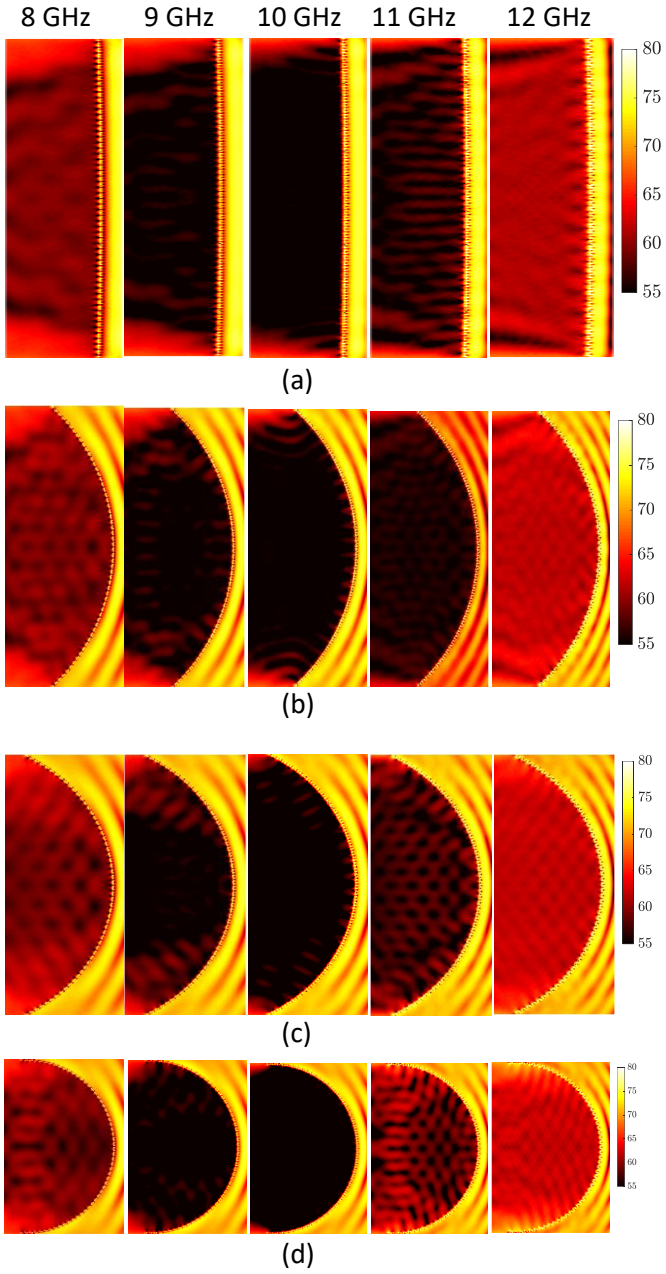

Figure 4.12. The field distribution within the shielded area [6]. (a) planar configuration, (b) conformal, $R_c = 20\text{cm}$, (c) conformal, $R_c = 15\text{cm}$, (d) conformal, $R_c = 10\text{cm}$, At center frequency, at least 20 dB SE is obtained within the majority of the shielded area.

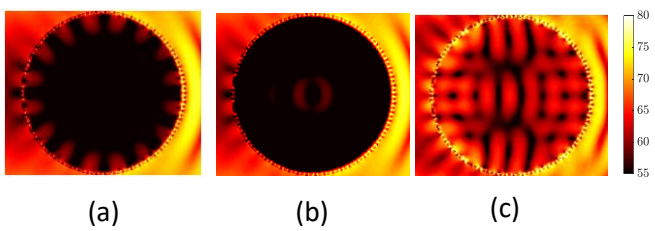

Figure 4.13. Shield's field distribution around the center frequency when rolled [6]. (a) 9 GHz, (b) 10 GHz, (c) 11 GHz.

4.12 (a), while Figures. 4.12 (b)-(d) illustrate the distribution inside the curvature for curvature

Table 4.5. NF Comparison of the Structures Reported in This Work with the Popular Structures (10 GHz)

Quantity	20 dB Bandwidth	Critical Radius	Critical Distance
Op. Mode 1	10.3%	4.9 cm	<0.033 λ
Op. Mode 2	10.1%	4.0 cm	<0.033 λ
Op. Mode 3	12.0%	3.4 cm	<0.033 λ
Op. Mode 4	13.3%	4.5 cm	<0.033 λ
SL [1]	24.5%	4.9cm	≃0.1 λ
CSL [1]	16.2%	5.1cm	≃0.146 λ
JR [1]	8.10%	11.8cm	≃0.173 λ
SRR [1]	10.2%	5.6cm	≃0.226 λ

radii of 20, 15, and 10 cm, respectively. The proposed shield provides 20 dB shielding in most of the intended area. However, at the edges of the structure, the unit cells are prevented from operating correctly due to the incident angle effect, causing a malfunction of the transmission zero provided by the shield and the unavoidable edge diffraction effect on truncated surfaces.

4.7.3 Shielding performance for closed surfaces

A shield's performance stability is essential when wrapped around an object. Shields with closed surfaces can be problematic if they are not well-designed. This is because electromagnetic leakages caused by surface imperfections or the incident angle can cause the undesired transmitted power to become trapped inside the closed surface, making it even more harmful or interfering. To analyze this effect, the surface is rolled without a susceptible object, with a 5 cm (1.66λ) curvature radius, and the electric fields inside the enclosure are monitored. Figure 4.13 shows that the proposed double-layer structure provides sufficient attenuation at the center frequency (10 GHz), even though it exhibits a maximum field intensity of 67dB at 11 GHz.

4.8 NF Efficiency Comparison

In Chapter 3, the cell's NF performance was quantified to gauge the reliability of different shields. The quantification was done based on two important criteria called "critical distance" and "critical radius." These criteria can help determine the shield's limitations without the object's presence. Critical distance is the distance from the surface at which the SE level experiences a 20-dB reduction or a 10% shift in the resonant frequency within the desired

bandwidth (whatever comes first). The critical radius is defined as the curvature radius in which the shielded area has an SE level of 25 dB and a resonant frequency shift of no more than 10%, covering at least half of the total area in curved configurations (half-circle area $\pi R_{cr}^2/2$) [5].

Table V presents a comparison of critical distance and critical radius values for four common frequency selective surfaces, namely Square Loop (SL), Convolutional Square Loop (CSL), Jerusalem (JR), and Split Ring Resonator (SRR), with the proposed schemes. The conventional structures offer a minimum distance of 0.1λ and a curvature of 4.9 cm, both associated with SL. However, the proposed scheme exhibits lower radius and distance values than SL due to their smaller size and manipulation of the secondary side to eliminate unwanted NF components. It should be noted that achieving excellent nearfield performance with the proposed surfaces comes at the cost of compromised bandwidth compared to conventional structures.

4.9 Measurements

Mode 2 is chosen for measurement because it offers physical flexibility and a relatively wideband transmission characteristic. A laminate thickness of 0.127mm is also available commercially. A flexible substrate of Rogers RT-Duroid 5880, which has a relative permittivity of 2.2 and a loss tangent of 0.0005, is chosen. However, if the substrate is embedded in a wearable shield, different substrate materials with similar electromagnetic characteristics may be selected based on the desired comfort level. The amount of attenuation is computed.

$$Attenuation_{dB} = E_{w/o}(dB) - E_w(dB) \tag{4.14}$$

where the sensed electric magnitude without and with the presence of the surface is denoted by $E_{w/o}$ and E_w, respectively. The NF probe employs an open-ended waveguide model that imitates real behavior and lessens the fields at the boundaries while magnifying the sensed fields at the center. As a result, the effective sensed area is decreased and the sensing resolution is enhanced.

4.9.1 Normal Incidences

The open-ended WR90 NF probe scans the entire surface and measures the sensed electric field for two scenarios: with and without the surface. Figure 4.14 displays the measurement configuration used for the planar structure. The surface is positioned in a window coated with absorber material and is illuminated by an X-band horn antenna. Figure 4.15 depicts the bandstop stability at different probe distances from the structure when the incidence is perpendicular. The findings match the simulation results in Figure 4.9 (b). The attenuation across the surface is demonstrated in Figure 4.16 for various probe distances, and in all cases, the minimum attenuation of 30 dB is achieved. The first noteworthy observation is the periodic pattern of attenuation, which was initially observed in [5]. The first physical interpretation of

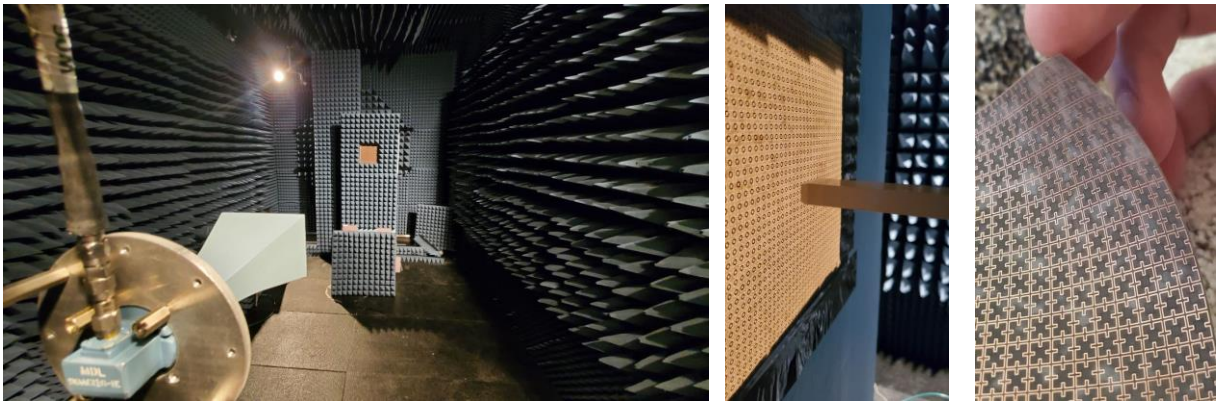

Figure 4.14. Measurement setup for planar configuration with an X-band horn radiator and NF probe [6]

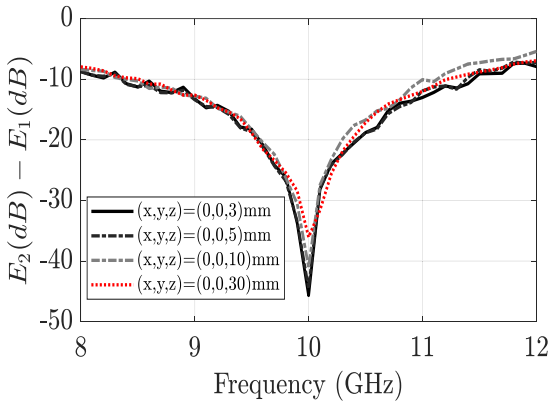

Figure 4.15. Normal Incidence measured NF attenuation vs frequency for different probe distances [6].

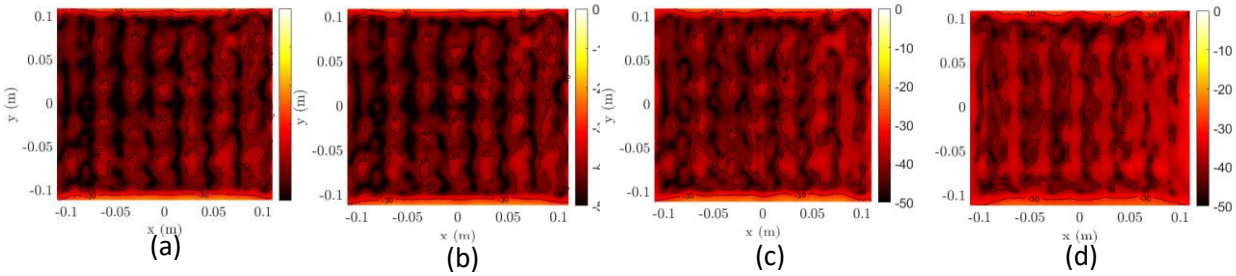

Figure 4.16. Measured field attenuation behind the shield window illuminated by plane waves (10 GHz) when the probe distance from the structure changes [6]. (a) 3 mm, (b) 5 mm, (c) 10 mm, (d) 30 mm

this behavior is the non-uniform distribution of local capacitive effects that electric and magnetic dipoles can model. Therefore, each point experiences a slightly different reactive effect that fluctuates in NF shielding. The second factor that might cause this periodic effect is the WR90 probe's scan resolution and it's mutual coupling with the shield surface.

4.9.2 Oblique Incidences

By azimuthally rotating the wall in Figure 4.14, the structure's performance is analyzed for oblique incidences. TE and TM modes were measured when the nearfield probe was kept within 1 cm from the surface. The results are shown in Figure 4.17. When the TE incident angle

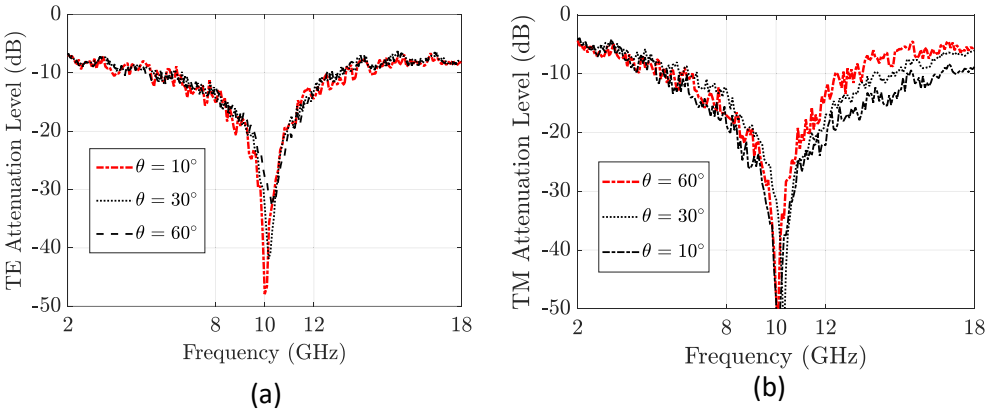

Figure 4.17. Oblique incidence *measured* NF attenuation vs frequency for probe distances under 1 cm [6]. (a) TE mode, (b) TM mode.

reaches 60 degrees, a slight deviation is observed in the resonant frequency while the 30 dB attenuation level is maintained at the center frequency. However, the overall performance is almost insensitive to the TE mode incident angle. Fig 4.17 (b) illustrates the TM mode attenuation level with different incident angles. It shares a similar performance, while high-angle incidences influence the bandwidth.

4.9.3 Conformal FSS

The flexible FSS is intended to be used near vulnerable objects, so it is essential to ensure that it can maintain stable nearfield performance when the shield is bent. This would enhance the surface's utility in conformal applications. To this end, a conformal configuration shown in Figure 4.18 has been designed. It includes a 3D-printed curved frame with a curvature radius of 20 cm. The entire structure has been embedded into absorbers to reduce edge diffraction. The nearfield response of the curved surface has been measured on the central cross-section of the surface depicted in Figure 4.18. Figure 4.19 (a) demonstrates the level of attenuation in the scanned area. Figure 4.19 (b) shows the difference between the simulation and measurement on the dB scale. The small discrepancy (up to 5 dB) may be due to a realistic nearfield probe with mutual coupling effects or the different edge diffraction effect compared to the simulation.

So far, we have investigated the questions regarding passive nearfield shielding methods using frequency-selective surfaces. We have learned how to categorize and suppress nearfield abnormalities by developing new designs. We have also learned how to estimate nearfield abnormalities in terms of resonant frequency changes and shielding effectiveness reductions. Observing edge diffraction and bending effects has helped us be cautious when designing nearfield shields. The next chapter will bring another shielding problem to the table where active shielding methods are leveraged to provide green shielding that helps reduce electromagnetic pollution.

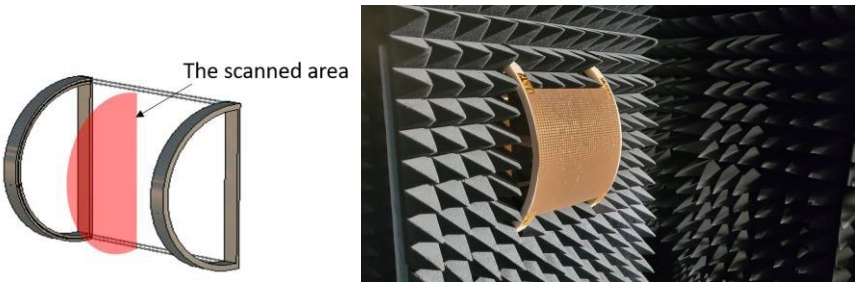

Figure 4.18. Measurement setup for conformal configuration with an X-band horn radiator and NF probe inside the curvature [6].

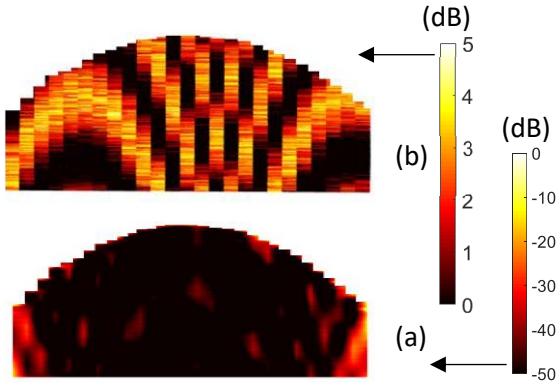

Figure 4.19. Measured field attenuation for the conformal surface. (a) electric field attenuation level (10 GHz) [6]. (b) error compared to the simulation (dB).

Chapter 5: Shielding by Space-Time Modulation

As mentioned earlier, this study has two objectives, one of which is to explore effective techniques for green shielding. This chapter will focus on space-time modulation (STM), which possesses unique nonreciprocal characteristics in wave engineering, amplification, up-conversion, and isolation. Selective shielding is an additional feature of STM media that can occur simultaneously with these other responses. For instance, it is possible to shield against a specific spectrum while maintaining the included data, transferring it to another frequency band, amplifying it, and then releasing it using STM media. However, before we can achieve our ultimate goal of green shielding, we must first develop numerical and analytical tools to accurately model and predict STM media behavior. This chapter is dedicated to this purpose, and we will propose rigorous, approximate, and numerical methods to analyze wave propagation in lossy dispersive STM media. We will examine wave dispersion, attenuation, amplification, and the solutions of electromagnetic waves in a progressively disturbed lossy medium. To obtain closed-form solutions for the dispersion relation of transverse electromagnetic waves, the second-order small perturbation approximation is employed. This method is applicable in small-perturbed lossy STM media with non-superluminal modulation. Furthermore, we will investigate the peculiar effects caused by the loss factor, the special harmonic amplification and shielding properties, and the validity of the solutions using Finite Difference Time Domain (FDTD) simulations. Finally, we will present a set of valuable conclusions, implications, and applications to shed more light on how green shielding can be achieved in a lossy STM environment.

5.1 Importance of Losses in STM Environment

Space-time modulation is a conventional but resurfaced topic that has recently experienced significant advancements and expansions [72]. Space-time modulation techniques manipulate electromagnetic waves by varying the space and time properties of the medium through which they travel. The basic rules of space-time modulation involve using a modulating signal to create variations in the electric and magnetic properties of the medium. These variations can cause the waves to be amplified, attenuated, or shifted in frequency. One important aspect of space-time modulation is that it can create nonreciprocal effects, which means that the wave's behavior depends on the direction of propagation. This property is crucial in designing devices like isolators and circulators, which allow waves to propagate in one direction. While space and time modulation have been growing independently through techniques like distributed capacitive modulation [76, 84, 110], nonuniform transmission lines [111-119], and external disturbance [76, 120], the concept of STM media has found successful applications in areas like parametric amplification [121-123], beam splitting [73], isolators [65], mixers [83], wave engineering, and nonreciprocal surfaces [66]. Space-time modulation is a

powerful tool for controlling and manipulating electromagnetic waves, and it has many applications in fields like telecommunications, sensing, and imaging.

A. L. Cullen initially studied the concept of Space-Time Modulation (STM) as a method for designing traveling-wave parametric amplifiers [124]. Later, Simon analyzed the wave equation solutions in such a medium and drew some important physical conclusions [125]. However, the existing solutions lacked sufficiency conditions and only provided an intuitive understanding of how the dominant harmonics behaved in an STM medium. A rigorous solution with arbitrary accuracy was proposed to address this issue for lossless media, where all space harmonics formed recurrence relations [126]. This approach provides a more comprehensive understanding of the behavior of EM waves in STM media and allows for precise design and analysis of STM-based devices.

The development of high-frequency wireless communication, such as 5G, poses challenges due to the attenuation and dispersion of waves in these bands, making it necessary to achieve higher efficiency. Components based on STM face limitations due to the pumping spatial period and fabrication limitations, resulting in high losses that attenuate both the pumped wave and the main signal wave, leading to poor performance. Conduction currents also contribute to energy consumption, and the propagation depth in a lossy STM medium is affected at high frequencies. Most studies on STM media focus on low-frequency microwave bands [65, 69, 71-76] and acoustic waves [77-79], and those on photonics regimes are limited to theoretical observations [70, 127-131] and lack the assumption of transition in a lossy medium. Fabricated designs have also followed this approach [65, 71, 80-84]. The practical realization of the medium has always been of interest, and considering the effects of losses, medium imperfections, and inhomogeneity of transmission lines is crucial for future designers [74]. Therefore, the theoretical and analytical analyses of the loss and dispersion effects are significant. While some research has touched upon the impact of losses in space-modulated media [111, 113, 116], it has largely been neglected in STM media due to the complexity it introduces. Previous studies had mainly focused on lossless scenarios, and even when losses were considered [126], the discussion was limited by the validity of the Weyl theorem [132], which does not hold for propagation constants with an imaginary part (i.e., loss factor). Thus, the existing solutions for the dispersion relation in lossy STM media may be unreliable, and further investigation is needed.

This chapter investigates the behavior of waves in a lossy medium with a progressive sinusoidal disturbance, considering both the medium's static conductivity and permittivity imaginary part. This realistic assumption reveals various features of wave behavior in such a medium, including the effects of the dispersion diagram in a lossy medium, the extra phase shift experienced by each harmonic, and the propagation of a specific frequency component without attenuation. The small perturbation method is used to simplify the complexities of the problem and provide closed-form solutions. The reliability and accuracy of the estimations are proven through various theoretical and computational methods. The study also provides implications for amplifying and shielding guided waves in STM media to pave the path to achieving green

shielding. The solutions are validated in the low- and high-frequency 5G bands but can be applied to other frequency bands and applications.

5.2 Progressive Disturbance in Lossy Media

5.2.1 Wave Equation in Lossy STM Media

Suppose a medium in which the relative permeability remains constant with a value of μ, but the relative permittivity, $\epsilon(t,z)$, changes in both spaces (specifically in the z-direction) and time. This type of medium is called a space-time-modulated (STM) medium. STM media share dielectric properties that vary with space and time, sinusoidally, exponentially, or with other functions. They offer many interesting applications, such as isolators [65, 81], beam splitters [73], nonreciprocal scatterers [66, 80], parametric amplifiers [126, 133], and mixers [83, 134]. The variation in permittivity is created by adjusting the local capacitive effect of the channel using an externally applied progressive disturbance, such as heat photons, X-rays, or biased varactor diodes. To create the disturbance, a specific pumping configuration can be embedded into the medium, which applies a varying voltage to the consecutive local points of the medium. Then, it is said that "the medium modified by the pump will act on the signal. Thus, the pumping can be ignored in formulating the problem" [125]. Simon related this phenomenon to the Doppler effect and justified the resulting up/down conversion [125]. The propagation, attenuation, and amplification of electromagnetic waves within a lossy STM medium with a progressive disturbance are being investigated.

It should be noted that the conductivity is assumed to be high enough to affect the modulation waves. This medium can be infinite or finite with known boundary conditions, like waveguides. Since the medium is lossy, conductive currents (J_c) are allowed to flow through it. If the pumping voltage varies sinusoidally with both space and time, the permittivity of the medium will exhibit a certain behavior.

If the pumping voltage varies sinusoidally with space and time, the time domain medium's permittivity relation can be identified as

$$\epsilon(z,t) = \epsilon_1 + \epsilon_2 \cos(\omega_1 t + k_1 z) \tag{5.1}$$

where the temporal and spatial modulation frequencies of the pump are denoted by ω_1 and k_1, respectively. The strength of modulation is indicated by the ratio of M, which is equal to the ratio of ϵ_2 to ϵ_1.

$$M = \epsilon_2/\epsilon_1 \tag{5.2}$$

The modulation factor, or velocity ratio, is another important parameter that characterizes the modulation nature. It is represented by v and defined as the ratio of the modulation phase velocity, $v_m = \omega_1/k_1$, to the phase velocity in the unperturbed medium, $v_0 = \omega/k_0$.

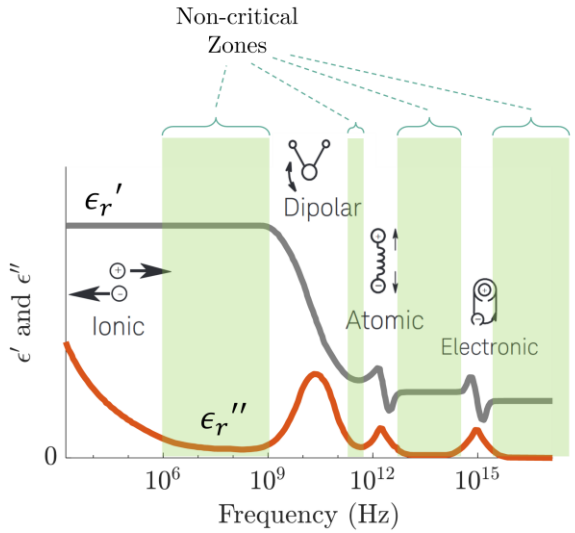

Figure 5.1. Dielectric mechanisms and the available non-critical zones that do not affect the alternating field conductivity [11]. The extension of the zones, varies with dielectric types.

$$v = \frac{v_{pump}}{v_{background}} = \frac{v_m}{v_0} \tag{5.3}$$

This ratio divides the responses into three main areas: sub-luminal (v<1), luminal (v=1), and superluminal (v>1) regions. One can imagine a superluminal case by assuming a pump wave that moves faster than the signal wave. Therefore, if both are sinusoidal waves, the state of the pump wave with a constant phase overtakes a constant phase of the signal wave.

In the frequency domain, the relative permittivity has a complex value with an imaginary component, ϵ'', which contributes to the complex permittivity ($\epsilon = \epsilon' + j\epsilon''$) in certain microwave and millimeter-wave frequencies due to dispersion. The magnitude of this component is directly proportional to the amount of dissipated energy in the material [135]. This introduces an additional conductivity factor (alternating field conductivity) to the static conductivity of the medium. However, the behavior of this factor as a function of frequency is highly dependent on the type of dielectric material. It follows a pattern influenced by multiple dielectric mechanisms, such as dipolar, atomic, and electronic. Each mechanism is associated with a cut-off frequency, also known as a critical frequency, which leads to a sudden increase in ϵ''. For instance, the atomic mechanism is typically active in the terahertz region. Figure 5.1 shows these mechanisms as reported in [136], where the imaginary part of the dielectric constant experiences a peak at each critical frequency and is near zero between the cut-off zones. Note that since the following analysis is in the time domain, we will not see the dielectric constant real or imaginary part throughout the analysis.

To commence the analysis, the issue is limited to TEM transmissions that run in the same direction as the pump. The Maxwell equations in the time domain that apply to this problem can be expressed as follows.

$$\nabla \times \vec{E} = -M_i - \frac{\partial \vec{B}}{\partial t} \tag{5.4}$$

$$\nabla \times \vec{H} = J_i + J_c + \frac{\partial \vec{D}}{\partial t} \tag{5.5}$$

$$\nabla \cdot \vec{D} = q_{ev} \tag{5.6}$$

$$\nabla \cdot \vec{B} = 0 \tag{5.7}$$

where the sources J_i and M_i denote the impressed electric and magnetic current densities, respectively. The time-dependent electric flux density is shown by $\vec{D} = \epsilon(z,t)\vec{E}$. The presence of dispersion is reflected in the effective conduction current density, $\vec{J_c} = \sigma\vec{E}$, with σ being the medium's effective conductivity. In the frequency domain, effective conductivity is the sum of the material's static conductivity (σ_s) and the alternating field conductivity ($\sigma_a = \omega\epsilon''$). Given the material's dispersion data, the following relation may be used for calculating effective conductivity.

$$\sigma \ = \omega\epsilon_0\epsilon_r tan\delta \tag{5.8}$$

Applying the curl operator on (5.4) results

$$\nabla \times \nabla \times \vec{E} = -\nabla \times M_i - \mu\frac{\partial \nabla \times \vec{H}}{\partial t} \tag{5.9}$$

Substituting (5.5) into (5.9) knowing $\nabla \times \nabla \times \vec{E} = \nabla\left(\nabla \cdot \vec{E}\right) - \nabla^2\vec{E}$ and $\vec{B} = \mu\vec{H}$,

$$\nabla\left(\nabla \cdot \vec{E}\right) - \nabla^2\vec{E} \ = -\nabla \times M_i - \mu\frac{\partial}{\partial t}[J_i + \sigma\vec{E} + \frac{\partial \vec{D}}{\partial t}] \tag{5.10}$$

$$= -\nabla \times M_i - \mu\frac{\partial J_i}{\partial t} - \mu\sigma\frac{\partial \vec{E}}{\partial t} - \mu\frac{\partial^2 \vec{D}}{\partial t^2}$$

In an isotropic medium, when the imposed external sources (J_i and M_i) are sinusoidal; their impact is reflected into $D(z,t) = \epsilon(z,t)E(z,t)$ with the permittivity of (5.1) so that they can be removed from (5.10).

$$\nabla\left(\nabla \cdot \vec{E}\right) - \nabla^2\vec{E} = -\mu\sigma\frac{\partial \vec{E}}{\partial t} - \mu\frac{\partial^2 \vec{D}}{\partial t^2} \tag{5.11}$$

Assuming an $x - polarized$ uniform plane wave and the direction of propagation of z, $\partial E_x/\partial x = \partial E_x/\partial y = E_z = E_y = 0$. Then, $\nabla \cdot \vec{E} = 0$ and (5.11) can be written as

$$\nabla^2 E_x(z,t) = \mu\sigma\frac{\partial E_x(z,t)}{\partial t} + \mu\frac{\partial^2\left(\epsilon(z,t)E_x(z,t)\right)}{\partial t^2} \tag{5.12}$$

If (5.12) is satisfied, the magnetic field is deduced from (5.5).

It was conventionally shown that in an STM medium, (5.12) is satisfied when the electric field contains numerous harmonics produced under the effect of pump temporal and spatial characteristics [125, 126, 137, 138] [139].

5.2.2 Pump and Signal Propagation Constants

The loss present affects both the modulated and signal waves. The unperturbed homogeneous medium has a complex propagation constant ($\gamma_h = \pm\sqrt{j\omega\mu(\sigma + j\omega\epsilon_1)}$) in the presence of losses. However, for a spatially and temporally inhomogeneous medium created by the pumping source, a unique propagation constant can be defined for each harmonic. This is because each spatial harmonic created by the disturbance experiences a different level of attenuation and phase change based on the local characteristics of the medium. In the case of a lossy and inhomogeneous medium with sinusoidal relative permittivity fluctuations, a complex propagation constant affecting the n^{th} harmonic can be defined as a natural multiplication of the pump propagation constant as follows.

$$\gamma_n = n\gamma_1 = n(\alpha_1 + jk_1) \tag{5.13}$$

where α_1 and γ_1 are the pump wave's base attenuation and propagation constant in the homogeneous non-modulated media. While k_1 is directly chosen by the user, α_1 depends on the physical characteristics of the pump configuration and pump angular frequency (ω_1). The Floquet representation of the modulation harmonics and the main wave in a lossy medium can be written as

$$\begin{aligned} E_x(z,t) &= P(\omega_1 t - \gamma_1 z) \\ &= E_0 e^{j\omega t - \gamma z} \sum_{n=-\infty}^{+\infty} a_n e^{n(j\omega_1 t - \gamma_1 z)} \\ &= E_0 \sum_{n=-\infty}^{+\infty} a_n e^{j[(\omega + n\omega_1)t - (k + nk_1)z]}\, e^{-(\alpha + n\alpha_1)z} \end{aligned} \tag{5.14}$$

where $\gamma = \alpha + j\beta$ is the wave propagation constant in the perturbed inhomogeneous medium. P is a periodic function that can be expanded by Fourier Series. As n increases, the value of the final term increases, which results in more attenuation for higher harmonics. The following expression can be obtained by using Equation (5.1) to extend Equation (5.12) and assuming that the plane wave is x-polarized,

$$\begin{aligned} \frac{\partial^2 E_x}{\partial z^2} = \quad & +\mu\sigma\frac{\partial E_x}{\partial t} + \mu\frac{\partial^2}{\partial t^2} \\ & +\mu\frac{\partial^2}{\partial t^2}([\epsilon_1 + \epsilon_2\cos(\omega_1 t - k_1 z)]E_x) \end{aligned} \tag{5.15}$$

Substituting (5.14) into (5.15), yields the following expression for each term.

$$\frac{\partial^2 E_x}{\partial z^2} = \frac{\partial^2}{\partial z^2}\left(E_0 \sum_{n=-\infty}^{+\infty} a_n e^{j(\omega+n\omega_1)t-(\gamma+n\gamma_1)z}\right) \tag{5.16}$$

$$= E_0 \sum_{n=-\infty}^{+\infty} a_n(\gamma+n\gamma_1)^2 e^{j(\omega+n\omega_1)t-(\gamma+n\gamma_1)z}$$

$$\mu\sigma\frac{\partial E_x}{\partial t} = +\mu\sigma E_0 \sum_{n=-\infty}^{+\infty} a_n j(\omega+n\omega_1) e^{j(\omega+n\omega_1)t-(\gamma+n\gamma_1)z} \tag{5.17}$$

$$\begin{aligned}\mu\frac{\partial^2 \mathrm{D}_x}{\partial t^2} = & +\mu E_0\epsilon_1 \sum_{n=-\infty}^{+\infty} -a_n(\omega+n\omega_1)^2 e^{j(\omega+n\omega_1)t} e^{-(\gamma+n\gamma_1)z} \\ & +\mu E_0 \frac{\epsilon_2}{2} \sum_{n=-\infty}^{+\infty} -a_n(\omega+(n+1)\omega_1)^2 e^{j(\omega+(n+1)\omega_1)t} e^{-(\gamma+(n+1)\gamma_1)z} \\ & +\mu E_0 \frac{\epsilon_2}{2} \sum_{n=-\infty}^{+\infty} -a_{n+1}(\omega+(n-1)\omega_1)^2 e^{j(\omega+(n-1)\omega_1)t} e^{-(\gamma+(n-1)\gamma_1)z}\end{aligned} \tag{5.18}$$

Reordering the second and third expressions of (5.18) by $(n+1) \to n$ and $(n-1) \to n$, respectively,

$$\begin{aligned}\mu\frac{\partial^2 \mathrm{D}_x}{\partial t^2} = & +\mu E_0\epsilon_1 \sum_{n=-\infty}^{+\infty} -a_n(\omega+n\omega_1)^2 e^{j(\omega+n\omega_1)t} e^{-(\gamma+n\gamma_1)z} \\ & +\mu E_0 \frac{\epsilon_2}{2} \sum_{n=-\infty}^{+\infty} -a_{n-1}(\omega+n\omega_1)^2 e^{j(\omega+n\omega_1)t} e^{-(\gamma+n\gamma_1)z} \\ & +\mu E_0 \frac{\epsilon_2}{2} \sum_{n=-\infty}^{+\infty} -a_{n+1}(\omega+n\omega_1)^2 e^{j(\omega+n\omega_1)t} e^{-(\gamma+n\gamma_1)z}\end{aligned} \tag{5.19}$$

Applying (5.16), (5.17), and (5.19) into (5.15) and factoring out the common terms results

$$\begin{aligned}a_n(\gamma+n\gamma_1)^2 = & +j\mu\sigma(\omega+n\omega_1)a_n \\ & -\epsilon_1\mu(\omega+n\omega_1)^2 a_n\end{aligned}$$

$$-\frac{\mu\epsilon_2}{2}(\omega+n\omega_1)^2(a_{n-1}+a_{n+1})$$

(5.20)

And finally

$$\left[\frac{(\gamma+n\gamma_1)^2+\epsilon_1\mu(\omega+n\omega_1)^2-j\mu\sigma(\omega+n\omega_1)}{\mu(\omega+n\omega_1)^2}\right]a_n+\frac{\epsilon_2}{2}(a_{n-1}+a_{n+1})=0$$

(5.21)

The following recursive relation describes the relationship between the amplitudes of different harmonic modes.

$$A_n a_n+\frac{\epsilon_2}{2}(a_{n-1}+a_{n+1})=0 \tag{5.22}$$

In this relation, $n=0$ corresponds to the fundamental wave. However, unlike the lossless cases, the amplitude A_n has a complex value.

$$A_n=\epsilon_1\left[1+\left(\frac{(\gamma+n\gamma_1)^2-j\mu\sigma(\omega+n\omega_1)}{\mu\epsilon_1(\omega+n\omega_1)^2}\right)\right], \tag{5.23}$$

which is a complex number. For verification, let us assume $\epsilon_2=0$. Since $a_n\neq 0$, the coefficient A_n should be zero. For $n=0$, $a_0\neq 0$. Then

$$\left[\epsilon_1+\left(\frac{(\gamma+n\gamma_1)^2-j\mu\sigma(\omega+n\omega_1)}{\mu(\omega+n\omega_1)^2}\right)\right]_{n=0}=\epsilon_1+\left(\frac{(\gamma)^2-j\mu\sigma(\omega)}{\mu(\omega)^2}\right)$$

$$=0 \tag{5.24}$$

and (5.24) can be reordered as

$$\gamma^2=j\mu\sigma\omega-\epsilon_1\mu\omega^2=\gamma_h^2 \tag{5.25}$$

where $\gamma_h=\pm\sqrt{j\omega\mu(\sigma+j\omega\epsilon_1)}$ is the propagation constant of a lossy homogeneous medium with the permittivity of ϵ_1. Equation (5.25) is a familiar complex dispersion relation of a lossy homogeneous medium. Opting $\sigma=0$ it yields the propagation constant of a lossless dielectric.

5.3 Small Perturbation Method (SPM)

So far, the necessary adjustments for making the problem compatible with a lossy environment have been introduced. Upon comparing the results of previous works [121, 125,

126] to Equation (5.22), only the complex expression for A_n differs. In cases where there is no loss, accurate solutions that consider all harmonics have been reported [137]. This section discusses a small perturbation approximation that considers the effect of a limited number of harmonics. This approximation simplifies the presentation of the consequences of dispersive media on the harmonics. Additionally, it highlights the effect of loss on the modulation responses, which can aid designers in making informed decisions about parameter selection. Accurate formulations and corresponding results will also be presented later for verification.

5.3.1 Dispersion Relation

Our primary objective is to analyze and interpret wave attenuation in lossy STM media. The Small Perturbation Method (SPM) can offer valuable insight into the unique characteristics of lossy STM media by providing physically interpretable expressions. To achieve this, the modulation strength (M) is assumed to be small compared to the incident wave, implying very small values of ϵ_1 (note that in practical cases, the modulation strength is small [140], $\epsilon_2/\epsilon_1 < 1$ in [137] and $\epsilon_2/\epsilon_1 \to 0$ in [72]). Consequently, when utilizing the second-order perturbation method, the amplitudes of higher harmonics for $a_n(|n| \geq 2)$ are considered insignificant. This approach requires a_n to approach zero for infinite positive values of n.

By making this assumption, we can derive the approximate conductivity-dependent dispersion curves for phase and attenuation constants by solving for the solutions of $A_n = 0$.

$$\gamma = -n\gamma_1 \pm \sqrt{j\mu\sigma(\omega + n\omega_1) - \left(k_0 + n\omega_1\sqrt{\mu\epsilon_1}\right)^2} \tag{5.26}$$

where $k_0 = \omega\sqrt{\mu\epsilon_1}$. Figure 5.2 depicts the dispersion relation of $\gamma = \alpha(f) + j\beta(f)$ for a range of harmonics while operating in luminal ($v = 1$) regions. Two cases, high ($\sigma = 5$) and moderate ($\sigma = 0.1$) conductivity materials, are compared. The modulation frequency is set to $\omega_1 = 2\pi \times 0.2GHz$, and the real and imaginary parts of the propagation constant are separated to show the impact of frequency on the attenuation and phase constants. For each value of n, the Brillouin diagram consists of a pair of curves representing an independent solution. One curve is associated with forwarding waves, and the other corresponds to backward waves. It is important to note that regions with negative frequencies and negative α correspond to where the propagation axis is reversed. However, the medium conductivity always affects the phase constant. These observations remain consistent when different modulation factors of subluminal (v<1) and superluminal (v>1) cases are used. Additionally, since the modulation strength is considered zero for this comparison, there is no power carried by the harmonics, and the figures show the potential interaction of harmonics.

Upon examining the comparisons presented in Figure 5.2, the following interpretations can be made

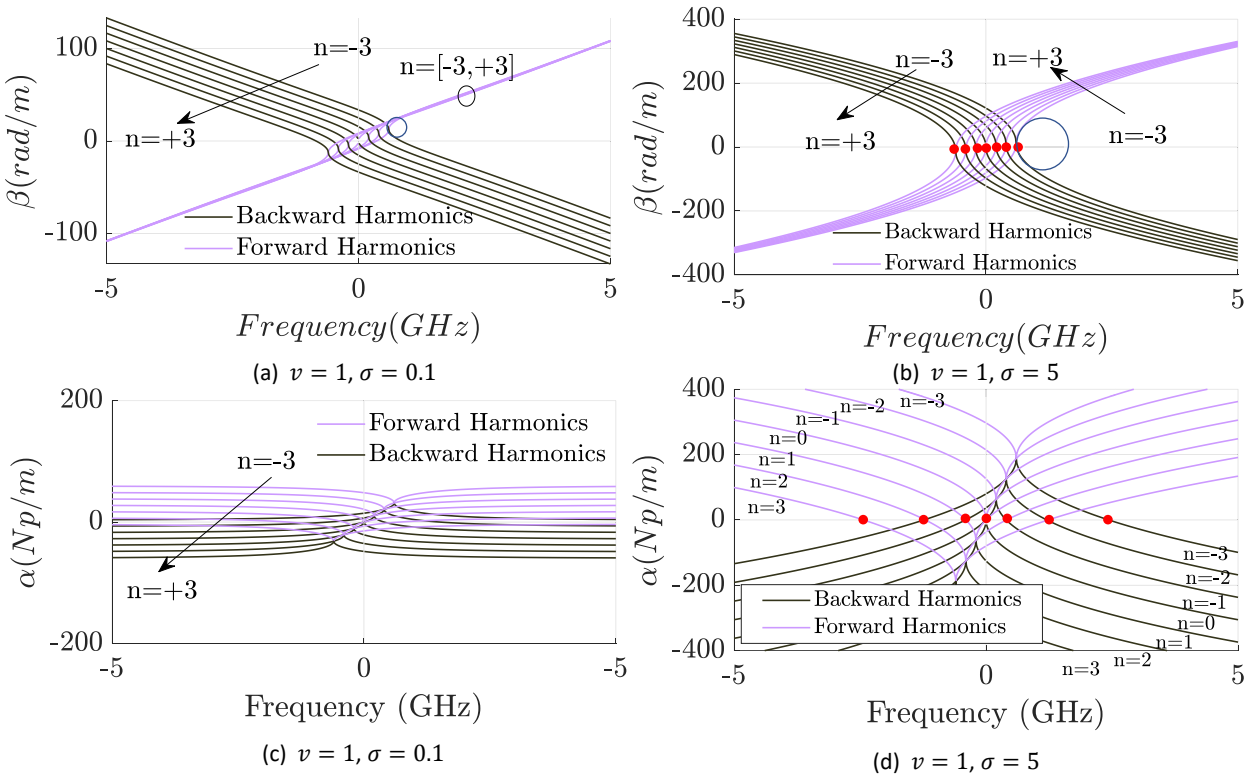

Figure 5.2. Dispersion relation for both attenuation constant and phase constant [11]

5.3.1.1 Phase Constant

The observations from Figure 5.2 suggest that the phase constant follows semi-straight lines when the medium conductivity is moderate, consistent with previous findings [137]. In low-loss dispersive environments, all forward harmonics overlap, indicating that they are almost in phase synchronism at all frequencies. However, increasing losses lead to changes in this behavior. As seen in Figure 5.2 (a) and (b), higher conductivities cause the harmonic lines to become curved. The nth forward and backward harmonics intersect when $|\omega| = |n\omega_1|$. Increasing the conductivity increases the tangential circle's radius to the parabola shown in Figure 5.2 (a) and (b). This effect causes larger separations among the forward harmonics in Figure 5.2 (b) than in the low-loss case of Figure 5.2 (a). When the conductivity is large, the forward harmonics are separated, implying weaker forward and backward waves that are considered undesirable for non-reciprocal parametric amplification. In addition, high conductivity degrades the non-reciprocity as both forward and backward harmonics are far apart (the amplifier is almost reciprocal for the high-conductivity case). Furthermore, certain frequencies can prevent the propagation of a specific harmonic while allowing others to propagate. These frequencies are marked by red dots in Figure 5.2 (b), and they can be determined by solving $Im\{\gamma_n(f)\} = 0$.

5.3.1.2 Attenuation Constant

The attenuation constant is an essential factor in determining the key features of STM media. Unlike the moderate-loss case, where each harmonic shows similar loss levels, in the high-conductivity case, each harmonic shows different loss levels, as shown in Figure 5.2(d). The loss variation with frequency for forward harmonics differs from the backward harmonics, making the attenuation non-reciprocal. This asymmetry in attenuation suggests that the negative effect on signal amplification is more significant as the harmonics experience larger spatial distances. Red dots in Figure 5.2(d) represent single operating frequencies for each harmonic where the attenuation is zero for that harmonic, while other harmonics experience some attenuation level. These points may be obtained by finding the solutions of $Re\{\gamma_n(f)\} = 0$. It should be noted that the solutions mentioned above depend highly on both operation and modulation frequencies. Changing the frequencies may affect the form of the harmonic interactions, even if the ratio, ω_1/ω, is kept constant. However, the relation provided in Equation (5.26) allows for predicting such frequency-dependent interactions.

5.3.2 Possible solutions for second-order SPM

Based on the observations from Figure 5.2 (d) and Equation (5.14), it can be inferred that the attenuation experienced by higher harmonics is greater compared to that of lower harmonics. This implies that the second-order perturbation method is more reliable in lossy media. Ignoring higher orders in Equation (5.22), we obtain a system of equations for n = 0, +1, and -1.

$$A_{n=-1}a_{-1} + \frac{\epsilon_2}{2}(a_0) = 0 \tag{5.27}$$

$$A_{n=0}a_0 + \frac{\epsilon_2}{2}(a_{-1} + a_{+1}) = 0 \tag{5.28}$$

$$A_{n=+1}a_1 + \frac{\epsilon_2}{2}(a_0) = 0 \tag{5.29}$$

The condition of having nontrivial solutions can be obtained by setting the determinant of the coefficient matrix to zero.

$$A_{n=0} - \frac{\epsilon_2^2}{4}\left[\frac{1}{A_{n=+1}} + \frac{1}{A_{n=-1}}\right] = 0 \tag{5.30}$$

that connects γ and ω to certain medium and modulation parameters, namely ω_1, k_1, and σ. By substituting the coefficients A_n into Equation (5.30) using the method outlined in Appendix A and reorganizing the Equation, the following key relation is obtained.

Table 5.1. The Parameters of the lossy STM Medium for Comparison

	Modulation Parameters		Main Signal Parameters		Medium Parameters	
	Name	Value	Name	Value	Name	Value
Rigorous	M	**0.1-0.3**	f	0-5GHz	σ	0.1-0.5
	v	0.1, 1, 4			ϵ_r	1
	f_1	0.2 GHz			μ_r	1
SPM	M	**Negligible**	f	0-5GHz	σ	0.1-0.5
	v	0.1, 1, 4			ϵ_r	1
	f_1	0.2 GHz			μ_r	1

$M = \epsilon_2/\epsilon_1$, $v = v_m/v_0$, $v_m = \omega_1/k_1$, $v_0 = \omega/k_0$

$$\left(\frac{1}{C}\right)\left(\frac{1}{Y^2-1}\right)\left[\frac{1}{1+C\left(\frac{Y+Y_1}{1+W}\right)^2 - C\left(\frac{1}{1+W}\right) - \left(\frac{1}{1+W}\right)} + \frac{1}{1+C\left(\frac{Y-Y_1}{1-W}\right)^2 - C\left(\frac{1}{1-W}\right) - \left(\frac{1}{1-W}\right)}\right] = \frac{1}{Z} \tag{5.31}$$

where $Y = \gamma/\gamma_0$, $W = \omega_1/\omega$, $Y_1 = \gamma_1/\gamma_0$ and $Z = \epsilon_2^2/4\epsilon_1^2$. The coefficient C, which is equal to $\frac{1}{\epsilon_1 \mu}\frac{\gamma_0^2}{\omega^2}$, is a complex coefficient that varies based on the medium's conductivity and operating frequency. Unlike the lossless version described in [126], the parameter Y not only changes with W but is also influenced by the operating frequency, even when W is unchanged. This characteristic results in distinct operational behavior at each frequency.

Using the dispersion solution derived from Equation (5.31), it is possible to determine the harmonic amplitudes within an amplifier or attenuator, particularly for small values of M. This has been analytically explored for lossless cases in [126]. One approach for determining the harmonic values involves using the known values of W, Y_1, Z, and C to obtain a 3rd order equation of the form $A'Y^3 + B'Y^2 + C'Y + D' = 0$, where A', B', C,' and D' depend on variables W and σ. The Equation can be solved for Y using either theoretical or numerical methods. The resulting values of Y (and potentially, γ) can then be substituted into equations (5.27)-(5.29) to establish a relationship for the three desired harmonics, a_{-1}, a_0 and a_{+1}.

5.4 Rigorous Method

A recursive formula based on computational methods is available for dispersion-less lossless problems that consider all harmonics. Developing a similarly rigorous solution for the lossy case as a validation tool would be beneficial. The system of homogeneous equations

presented in Equation (5.22) has nontrivial solutions only when the determinant equals zero. Thus, a meaningful relationship between γ and ω can be established that accounts for the effect of σ. The process of deriving the recursive dispersion relation is the same as that used for the lossless case, which was introduced in [137, 141]. By following the same procedure for lossy cases, the resulting dispersion relation obtained from this method can be expressed as:

$$D_n - \frac{1}{D_{n-1} - \frac{1}{D_{n-2} - \cdots}} - \frac{1}{D_{n+1} - \frac{1}{D_{n+2} - \cdots}} = 0 \tag{5.32}$$

where $D_n = 2A_n/\epsilon_2$ is a complex function of σ and modulation parameters.

As one might expect, the rigorous solution is difficult to interpret when considering the effect of individual constituent parameters of the medium on the behavior of STM wave harmonics. Although a computational method might be helpful, increasing the harmonics causes the order of (5.32) to rise, making it computationally demanding to obtain a reliable solution and limiting the ability to consider all harmonics. It is important to note that an optimization algorithm is required to obtain accurate solutions through an iterative process. The accuracy of this method is heavily dependent on the optimization algorithm parameters and the order of the problem. Gradient descent has traditionally been utilized to solve the lossless problem [137], while in this study, Particle Swarm Optimization (PSO) is employed to obtain solutions for multiple harmonics. In lossy media, $A_n(\gamma, \omega, \sigma)$ adopts complex values, and therefore, (5.32) is satisfied when its imaginary and real parts are both equal to zero.

Figure 5.3 compares the rigorous method and SPM for different modulation strengths (M>0) using the medium and modulation parameters specified in Table 5.1. As the modulation strength increases, the deviation between the solutions obtained by the rigorous method and SPM becomes more significant, especially when the medium disturbance increases. This is because the SPM neglects the high modulation strengths (large values of M), leading to instability in the interactions [138]. However, the SPM remains accurate in the low conductivity regions, as there are no unstable interactions for $v < 1$, regardless of the losses and frequency range. This is not the case luminal and superluminal regions where SPM shows some deviation from the accurate solutions. Additionally, the interactions tend to be more stable in lossy media, where the power carried by high harmonics is significantly attenuated. Therefore, high conductivity regions are not of concern, and the SPM becomes more accurate in predicting solution regions as the operating frequency increases in such media. Furthermore, amplification stability can be achieved in low-loss environments by adjusting the frequency, causing higher-

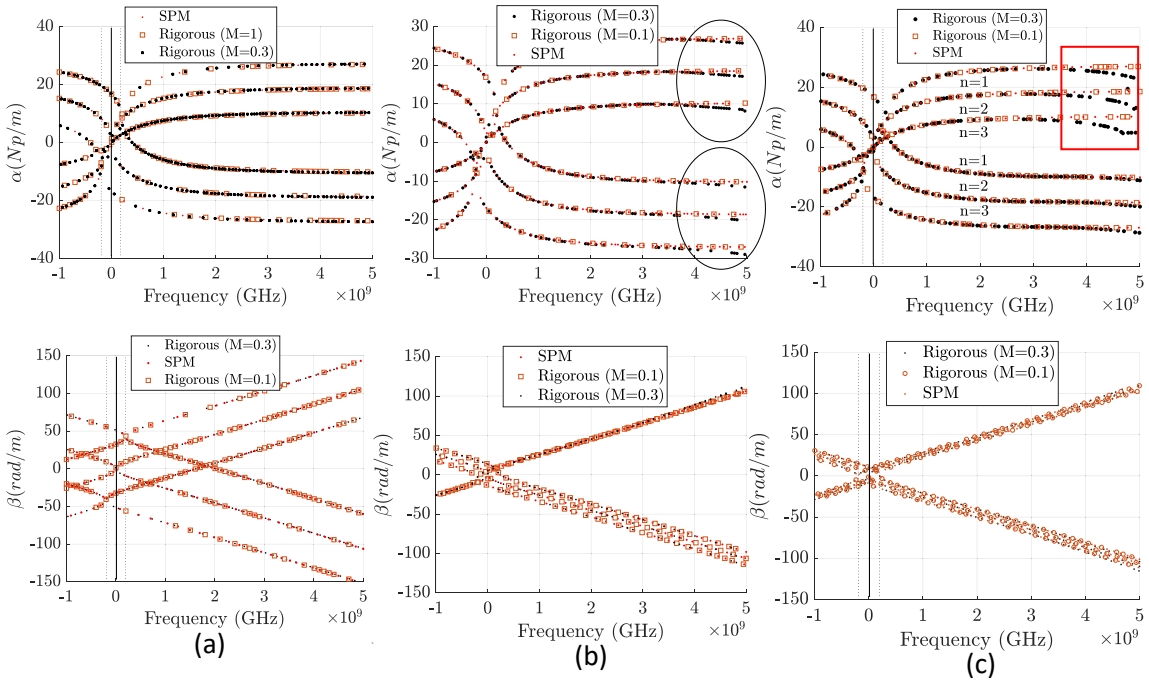

Figure 5.3. Dispersion comparison between the rigorous method and the SPM method [11]. (a) Subluminal Region, (b) Luminal Region, (c) Superluminal Region

order harmonics to experience more losses, resulting in a more stable interaction and greater accuracy of the SPM in predicting solution regions.

5.5 FDTD Method for Lossy STM Media

Although SPM and the rigorous method provided useful insights and accurate solutions for the problem, FDTD simulations can handle more complex problems. Previous studies have successfully used FDTD simulations to model finite-size zero-thickness space-time modulated Huygens' metasurfaces, where the modulation is applied to a single node surrounded by an undisturbed medium [142, 143]. FDTD formulations have recently been developed for time-varying media with zero conductivity [144]. The effect of conductivity has also been neglected in previous studies where FDTD was used to simulate STM media [66, 73].

In this section, the FDTD update equations will be modified to include the conductivity effect in STM media, making the numerical method versatile enough to handle complex STM media with non-zero thicknesses and losses.

5.5.1 Update equations for lossy STM media

When assuming an x-polarized TEM wave with an arbitrary propagation direction, Equations (5.4) and (5.5), vector equations, can be decomposed into three scalar equations for three-dimensional space. This results in the following three relations:

$$\frac{\partial H_y}{\partial t} = \frac{1}{\mu}\left(\frac{\partial E_z}{\partial x} - \frac{\partial E_x}{\partial z} - M_i\right) \tag{5.33}$$

$$\frac{\partial H_z}{\partial t} = \frac{1}{\mu}\left(\frac{\partial E_x}{\partial y} - \frac{\partial E_y}{\partial x} - M_i\right) \tag{5.34}$$

$$\frac{\partial D_x}{\partial t} = \frac{\partial H_z}{\partial y} - \frac{\partial H_y}{\partial z} - \sigma E_x - J_i \tag{5.35}$$

where according to the initial polarization assumption, $\partial E_y/\partial x = \partial E_z/\partial x = Ez = Ey = 0$. Replacing the permittivity of (5.1) with (5.35) yields

$$\frac{\partial \epsilon(z,t)}{\partial t} E_x + \epsilon(z,t)\frac{\partial E_x}{\partial t} = \frac{\partial H_z}{\partial y} - \frac{\partial H_y}{\partial z} - J_i - \sigma E_x \tag{5.36}$$

The FDTD update equations for a lossy STM medium can be obtained by using the Yee algorithm as described in [145] and applying the central difference approximation to equations (5.33), (5.34), and (5.36) at the time step of $t = n + \frac{1}{2}$.

$$H_{y,(i,j,k)}^{n+\frac{1}{2}} = H_{y,(i,j,k)}^{n-\frac{1}{2}} + C_{hye,(i,j,k)}\left(E_{x,(i,j,k+1)}^{n} - E_{x,(i,j,k)}^{n}\right) \tag{5.37}$$

$$H_{z,(i,j,k)}^{n+\frac{1}{2}} = H_{z,(i,j,k)}^{n-\frac{1}{2}} + C_{hze,(i,j,k)}\left(E_{x,(i,j+1,k)}^{n} - E_{x,(i,j,k)}^{n}\right) \tag{5.38}$$

$$\left[\frac{A}{2} + \frac{B}{\Delta t}\right] E_{x,(i,j,k)}^{n+1} = \left[\frac{B}{\Delta t} - \frac{A}{2}\right] E_{x,(i,j,k)}^{n} + \frac{H_{z,(i,j,k)}^{n+\frac{1}{2}} - H_{z,(i,j-1,k)}^{n+\frac{1}{2}}}{\Delta y} - \frac{H_{y,(i,j,k)}^{n+\frac{1}{2}} - H_{y,(i,j,k-1)}^{n+\frac{1}{2}}}{\Delta z} + -\sigma E_{x,(i,j,k)}^{n+\frac{1}{2}} - J_i \tag{5.39}$$

Replacing $E_{x,(i,j,k)}^{n+\frac{1}{2}} = \frac{E_{x,(i,j,k)}^{n+1} + E_{x,(i,j,k)}^{n}}{2}$ in (5.39) and reordering gives

$$\left[\frac{A}{2} + \frac{B}{\Delta t} + \frac{\sigma}{2}\right] E_{x,(i,j,k)}^{n+1} = \left[\frac{B}{\Delta t} - \frac{A}{2} - \frac{\sigma}{2}\right] E_{x,(i,j,k)}^{n} + \frac{H_{z,(i,j,k)}^{n+\frac{1}{2}} - H_{z,(i,j-1,k)}^{n+\frac{1}{2}}}{\Delta y} -$$

$$\frac{H_{y,(i,j,k)}^{n+\frac{1}{2}} - H_{y,(i,j,k-1)}^{n+\frac{1}{2}}}{\Delta z} - J_i \tag{5.40}$$

where A and B represent Spatio-temporal permittivity-dependent coefficients

$$A = \frac{\epsilon_{(i,j,k)}^{n+1} - \epsilon_{(i,j,k)}^{n}}{\Delta t} \tag{5.41}$$

$$B = \epsilon_{(i,j,k)}^{n+\frac{1}{2}} \cong \frac{\epsilon_{(i,j,k)}^{n+1} + \epsilon_{(i,j,k)}^{n}}{2} \tag{5.42}$$

both of which are known coefficients and are selected using a look-up table.

5.5.2 Area of Validity based on the velocity factor (v)

The STM medium illustrated in Figure 5.4 is utilized to test its accuracy, and a single-frequency planar wave illuminates it. The wave spectrum is observed using a one-dimensional STM medium probe. Different frequency bands, sub-6 GHz and mm-wave regimes, are analyzed using FDTD, rigorous, and SPM. These methods estimate the distribution and strength of the excited local harmonics. The outcomes are compared to a conventional technique that multiplies harmonic amplitudes in lossless media by a rough attenuation factor [84]. This conventional approach has been used for low-frequency applications with an estimation error of 2-3 dB. However, the comparison indicates that the error rate increases significantly at high frequencies because the conventional method does not consider wave dispersion.

5.5.2.1 Low-Frequency Region (sub-6GHz)

The experiment examines two cases with differing conductivity, a low conductivity case ($\sigma \cong 0$) and a high conductivity case ($\sigma \cong 0.1$). The relative permittivity varies sinusoidally with space and time, as shown in Figure 5.4, and is characterized by $\epsilon_{r1} = 1,\ \epsilon_{r2} = 0.1$ (M = 0.1), $\omega_1 = 2\pi \times 0.5\ GHz$. k_1 is set using velocity ratio (v). The total-field scattered-field (TFSF) region separates incident and total fields. The medium is excited by a 5 GHz TMx-polarized single-frequency sinusoidal plane wave, and a Convolutional perfectly matched layer (CPML) is used as the absorbing boundary condition. The time-domain electric field is sampled throughout the simulation, and the harmonic amplitudes and phases are calculated using a fast Fourier transform (FFT).

Figures. 5.5 (a)-(f) demonstrate the frequency domain electric field at a single central probe point (shown in Figure 5.4) compared to the rigorous, SPM, and conventional methods. The experiment confirms that the conductivity of the medium affects the interaction of harmonics, particularly in luminal and superluminal modulations. While the developed FDTD and rigorous methods can predict this effect, SPM is only valid when spatiotemporal interaction occurs to the first three harmonics, a_{-1},a_0, and a_1. On the other hand, the conventional method

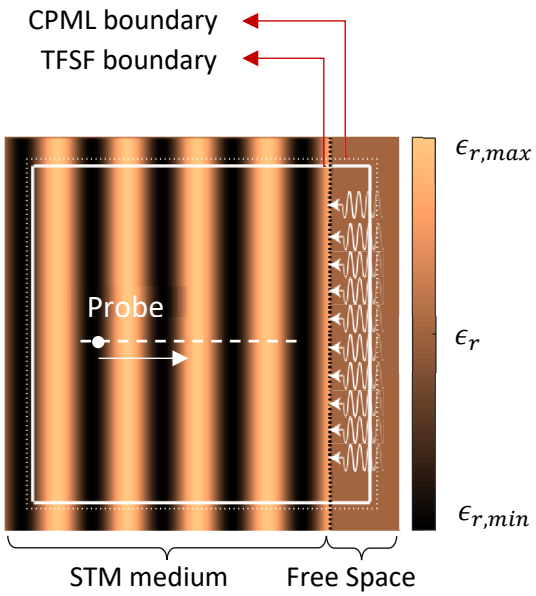

Figure 5.4. Relative permittivity distribution in a STM medium for a single time step [11]. The probe is placed at the center of the medium and can move horizontally.

predicts magnitudes with an error of approximately 2 dB. This error reflects the dispersion effect of a high-loss STM environment.

5.5.2.2 High-Frequency Region (mm-wave)

This examination assumes that the specification is similar to the sub-6GHz scenario but with the signal frequency in the millimeter-wave range. The modulated medium has characteristics by $\epsilon_{r1} = 1$, $\epsilon_{r2} = 0.01$, $\omega_1 = 2\pi \times 5\ GHz$. The modulation strength is assumed to be insignificant to avoid oscillation in the millimeter-wave range (M = 0.01). If a 60 GHz TMx-polarized single frequency sinusoidal plane wave illuminates the medium, up/down-converted harmonics are anticipated to arise at frequencies of {..., 55 GHz, 60 GHz, 65, GHz,...}. The harmonic amplitudes are evaluated utilizing the FFT method. Figures. 5.5 (g)-(i) exhibit the harmonic amplitudes in the central probe using the FDTD, rigorous, SPM, and the conventional method. The findings show that the developed methods agree, while the conventional method overestimates the outcomes because it does not consider the indispensable effect of dispersion, which is more important in the millimeter-wave region. In this case, the error reached 7 dB for each harmonic. The error remains constant for the luminal and superluminal cases of Figures. 5.5 (h) and (i), but the SPM method becomes less accurate for the superluminal case. The FDTD method agrees with the rigorous method in all situations.

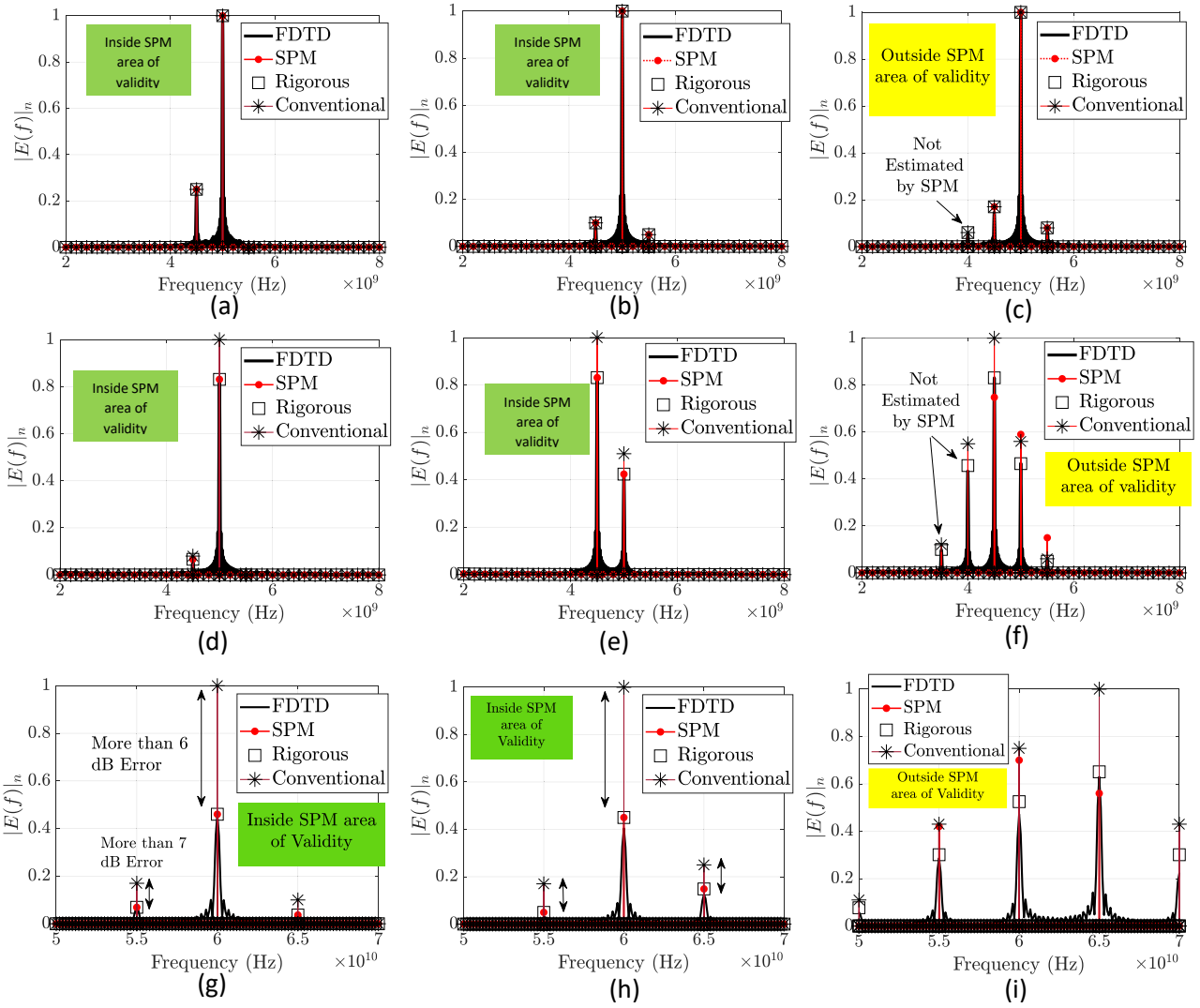

Figure 5.5. Comparisons of the FDTD, rigorous, SPM and conventional methods [11]. The harmonics are estimated by applying FFT to the time domain signal sensed in the central local probe. (a) sub-6GHz region with $v = 0.5$, $\sigma = 0$, (b) sub-6GHz region with $v = 1$, $\sigma = 0$, (c) sub-6GHz region with $v = 4$, $\sigma = 0$, (d) sub-6GHz region with $v = 0.5, \sigma = 0.1$, (e) sub-6GHz region with $v = 1, \sigma = 0.1$, (f) sub-6GHz region with $v = 4, \sigma = 0.1$. (g) mmwave region with $v = 0.5\ \sigma = 0.03$, (h) mmwave region with $v = 1\ \sigma = 0.03$, (i) mmwave region with $v = 4$, $\sigma = 0.03$,

According to the principle of energy conservation, the SPM method generates more powerful harmonics in superluminal regions. This is due to the assumption that the remaining harmonics are negligible, resulting in the energy being allocated to the main three harmonics, which leads to misleading findings for superluminal regions. However, SPM predictions are precise for liminal and subluminal regions. In other words, when the modulation strength is insufficient to distribute energy among higher harmonics and the modulation is not superluminal, the SPM method produces reliable results.

5.6 Implications for Amplification and Shielding

By validating the existing methods, we can explore other crucial characteristics related to wave propagation in lossy STM media.

5.6.1 Stability

Although this study does not distinguish between stable ($v < 1$) [137] and unstable ($v > 1$) [138] interactions, both the developed FDTD update equations and the rigorous method can estimate both types of instabilities. In either case, truncating the STM medium is the optimal approach to avoid further exposure to interact as a stable modulator. However, the investigation suggests that loss could be another useful factor in maintaining amplification in the stable region as the modulation strength increases. For example, selecting M = 1 in the luminal region may result in unstable amplification, while the same feature in a lossy medium leads to typical harmonic propagation. This idea could have an application in cases where high up-conversion is necessary and instability becomes unavoidable. The loss could be the final option that prevents the up-converter from operating unstably.

5.6.2 Simultaneous Amplification and Shielding

When the STM medium experiences losses, it is possible to amplify and shield two harmonics simultaneously. Frequency down-conversion occurs when the fundamental forward wave (n = 0) interacts with the forward harmonics with a negative number, resulting in the components of $\omega + n\omega_1$with negative values of n. Frequency up-conversion occurs when the fundamental forward wave (n = 0) interacts with the backward harmonics with a positive number. Research [146] [125] shows that frequency up/down conversion can also lead to amplification. Our observations also suggest that a lossy STM medium can be designed to amplify a specific harmonic while shielding another. This concept is illustrated in Figure 5.6, where the pump wave attenuates the main signal while mounting the amplified energy on the down-converted harmonics. This notion involves using the loss factor to shield a particular frequency while using modulation to mount energy on another frequency. One practical application of this idea is to down-convert high-power, high-frequency emissions onto lower harmonics to shield them and use the included data simultaneously.

5.6.3 The Notion of Zero-attenuation Frequencies

Let us review the concept of STM media. We inject some energy into the medium stored as a capacitive effect. It is possible to harness this energy to amplify a desired harmonic or prevent it from dissipation. This is similar to using an external DC voltage to amplify a small AC signal in electronics. In this case, the disturbed relative permittivity distribution plays a key role in efficiently propagating a specific frequency component, with both attenuation level and phase constant being important factors. For a specific harmonic, satisfying the zero attenuation

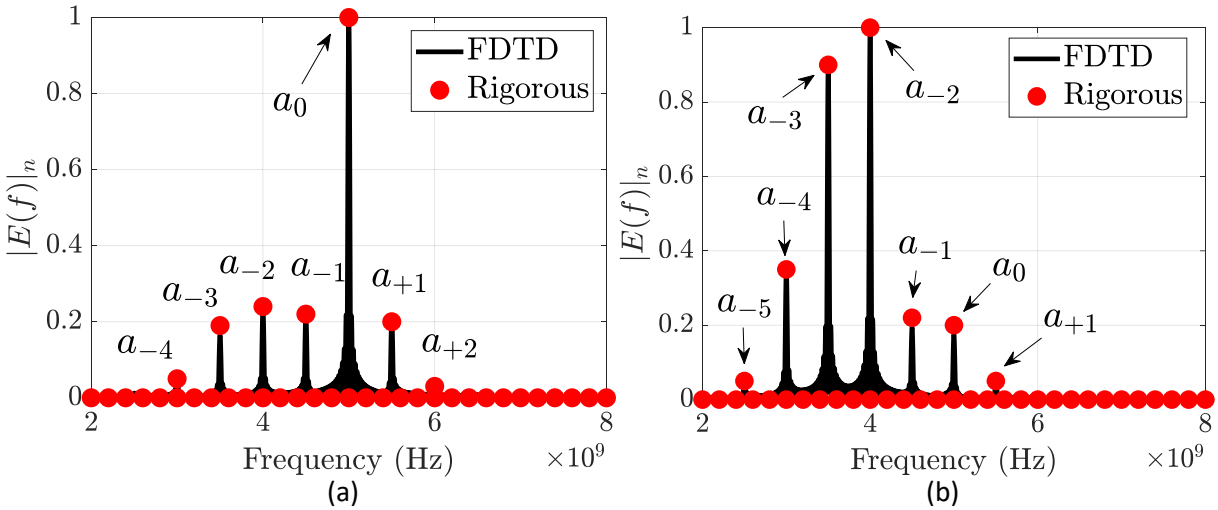

Figure 5.6. The notion of amplifying different harmonics while shielding the main 5GHz harmonic in a superluminal region (M=0.3 and v=4). This phenomenon does not happen when medium is lossless. (a) lossless medium, (b) lossy medium with $\sigma = 0.1$

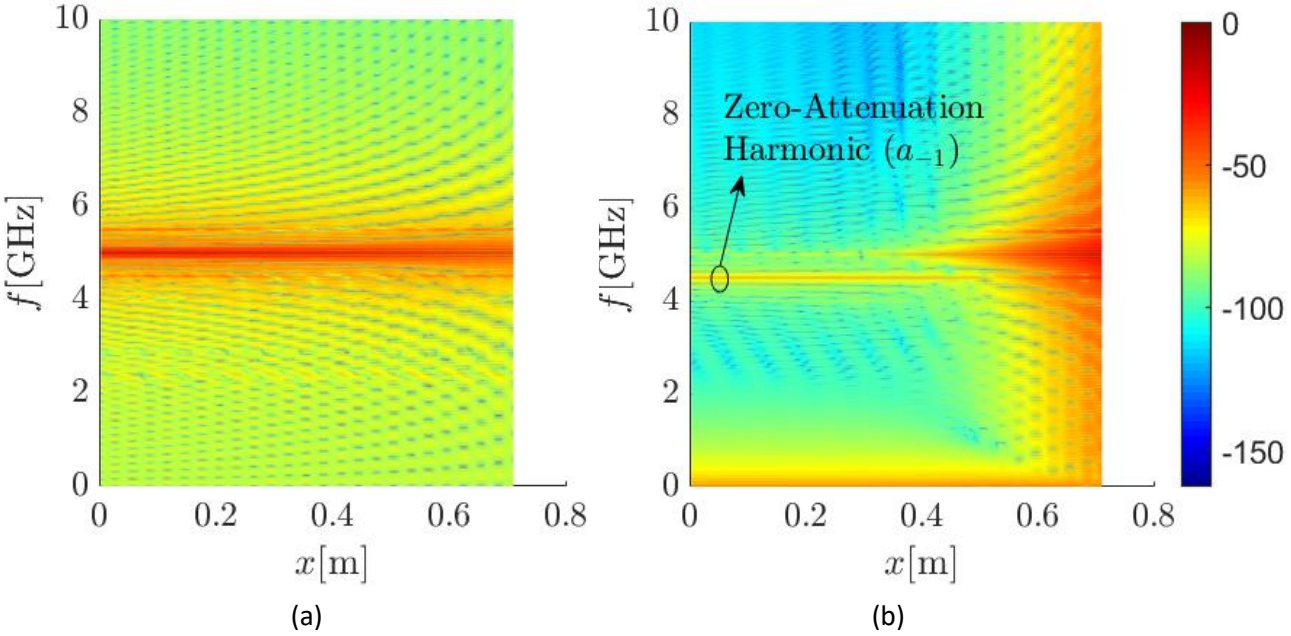

Figure 5.7. The notion of amplified and zero-attenuation frequencies in lossy environments [11] (a) Amplification in lossless STM media, and (b) Zero-Attenuation in lossy STM media.

and non-zero phase constant conditions is necessary for the endless propagation of a frequency component in a lossy medium. By numerically solving for $Re\{\gamma_n(f)\} = 0$ in Figure 5.3 with v=1, the frequency corresponding to non-zero phase constant and zero attenuation is 4.5 GHz, as confirmed by the FDTD simulation of Figure 5.7. This concept can be applied when energy needs to be transmitted through a high-loss environment with minimal exposure.

The SPM, rigorous, and numerical solutions all agree and provide reliable results compared to conventional methods. However, to minimize concerns regarding the applicability of simulations, the authors recommend minimizing possible factors that could reduce applicability during experimental procedures. These factors include the dependence of medium

permittivity on heat, the compatibility of dielectric materials with high frequencies, the spatial distance of varactor diodes, and the resulting capacitive effect. In contrast to dispersion-less cases, where behavior remains constant with a constant modulation frequency ratio (W), dispersive media exhibit different harmonic behavior at different operation frequencies due to the nonlinear relationship between the complex propagation constant and the operation frequency.

This chapter has provided us with the essential tools for exploring shielding using STM media. The following chapter will demonstrate how the features of STM media can be utilized for effective green shielding purposes.

Chapter 6: Green Shielding Methods

With the developed FDTD method for lossy STM media, we are equipped with the necessary tools to simulate wave interaction in STM media for special purposes of amplification or shielding. It was previously outlined that the conventional absorbers and FSS shields have limitations. Conventional absorbers are reliable in reducing reflection but cannot be designed for a specific frequency range, leading to data loss. On the other hand, FSSs can shield a specific frequency while not considered green shields as they reflect the undesired frequencies, making environments electromagnetically polluted. This chapter introduces a new class of shielding methods that use STM materials to manage undesired energy effectively while meeting the requirements of green shielding. An optimization-based synthesis technique is presented, resulting in four shielding methods that achieve data preservation, high shielding effectiveness of at least 20 dB, and reflection reduction of at least 10 dB (Green Shielding) through upconversion, down-conversion, diversion, and frequency distribution of the signal. These shielding methods offer diverse output signal types and directional flexibility, providing an additional advantage. The energy conservation rule enables the designer to control the propagation of certain frequency components, resulting in controlled amplified or attenuated propagation. The Finite Difference Time Domain (FDTD) Method numerical results are validated by the rigorous method. Finally, the challenges and probable methods for building a block of STM slab will also be discussed.

6.1 STM Media as Green Shields

6.1.1 Problem Overview

High-conductive materials in traditional shields reflect much energy, regardless of whether they block the entire spectrum or are frequency-selective surfaces, as seen in Figure 6.1(a). Any waves penetrating the shield significantly weaken depending on the conductor's skin depth. On the other hand, they use low-reflective materials for green shielding resulting in lower reflection, higher absorption, and lower transmission, as seen in Figure 6.1(b). While these shields contribute to providing electromagnetically clean environments, they do not have a frequency selective characteristic, which means they lose the entire spectrum. A method is needed to provide green shielding while preserving the spectrum data.

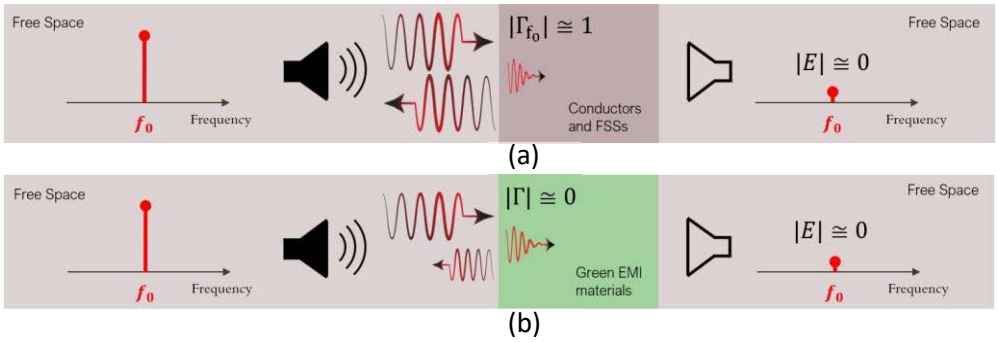

Figure 6.1. Green shielding versus conventional shielding. (a) A high-conductivity material, (b) Green shields.

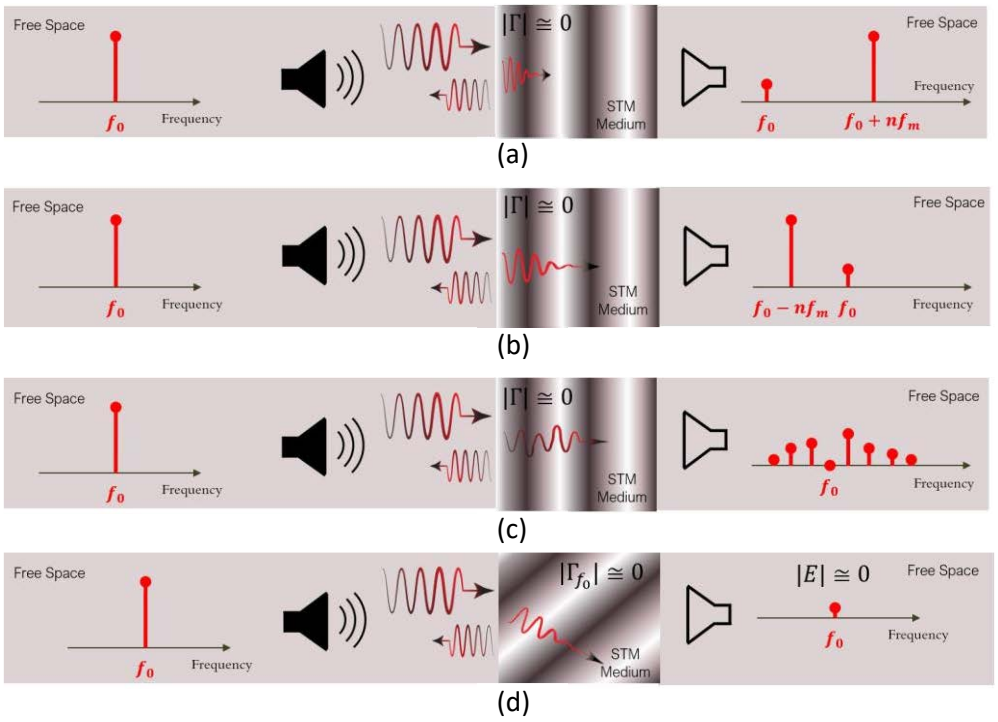

Figure 6.2. Green shielding with STM media. (a) up-conversion, (b) down-conversion, (c) Distribution, (d) Diversion

6.1.2 STM Media Solution

STM media possess several characteristics that make them a promising option for green EMI shielding. Their dielectric-based constitutive material can be lossy or lossless, and the medium's base characteristic impedance can have a fixed range (over frequency) by choosing an appropriate material. Another essential characteristic is the ability to control the medium's behavior actively. STM media can up-convert, down-convert, amplify, or attenuate the impinging spectrum, making them versatile. Figure 6.2 provides a schematic view of the green shielding mechanisms an STM medium might employ for shielding an undesired high-power frequency component. The main goal is to reduce the high-power spectrum while preserving the data included in the signal. Depending on the application, this may involve attenuating the noise, which is usually the case, or amplifying the desired spectrum. Therefore, while the

undesired frequency is shielded, the data may be transferred to other frequency bands to be extracted by demodulation.

Figure 6.2(a) represents an upconversion mechanism, where the high-power component is upconverted to a higher frequency. The other benefit is that high-frequency components are more prone to attenuation in lossy media, which means that the medium's conductivity can be chosen to ensure certain losses for the upconverted signals. When the energy is shifted to a higher frequency, the power of the undesired component drops, and losses attenuate it significantly.

Figure 6.2(b) shows a down-conversion case, where the undesired frequency is shifted to lower-frequency components. However, data loss or wave distortion may occur when the original spectrum has a wide bandwidth.

Another way to preserve data is to distribute the power over specific harmonics so that none have a high interfering amplitude, as shown in Figure 6.2(c). This shielding method has the advantage of being able to extract data from different user-defined channels. The output harmonics around f_0 are replicas of the main signal that can be collected from various channels while the main harmonic is eliminated. The bandgap between each replication can be chosen to allow the user to extract data from the desired channel/channels. The parameter associated with the bandgap is f_p or pump frequency.

Figure 6.2(d) illustrates another shielding scenario that uses a beamforming scheme to change the propagation direction. In this case, the STM medium diverts the wave direction, providing a locally shielded area. By actively controlling the direction, the user can change the direction of the waves through time while controlling the frequencies that carry the data.

6.1.3 Obtaining Minimum Reflection

Even though STM media is inhomogeneous, their interface can be treated as a homogeneous medium when the equiphase surfaces of the pump and signal waves are parallel. When a TEM incidence is assumed, the local wave impedance on the STM interface (assuming a constant z) varies with time and can be calculated as:

$$Z_w = \sqrt{\frac{j\omega\mu}{\sigma + j\omega\epsilon}} = \eta_{ct} \tag{6.1}$$

In this scenario, the instantaneous characteristic impedance of the medium at the interface, η_{ct}, is identical to the local wave impedance. The instantaneous characteristic impedance is defined by supposing the medium is homogeneous at a specific time step and incidence position. At each time step, the reflection of a plane wave when it hits the interface is related to the reflection coefficient

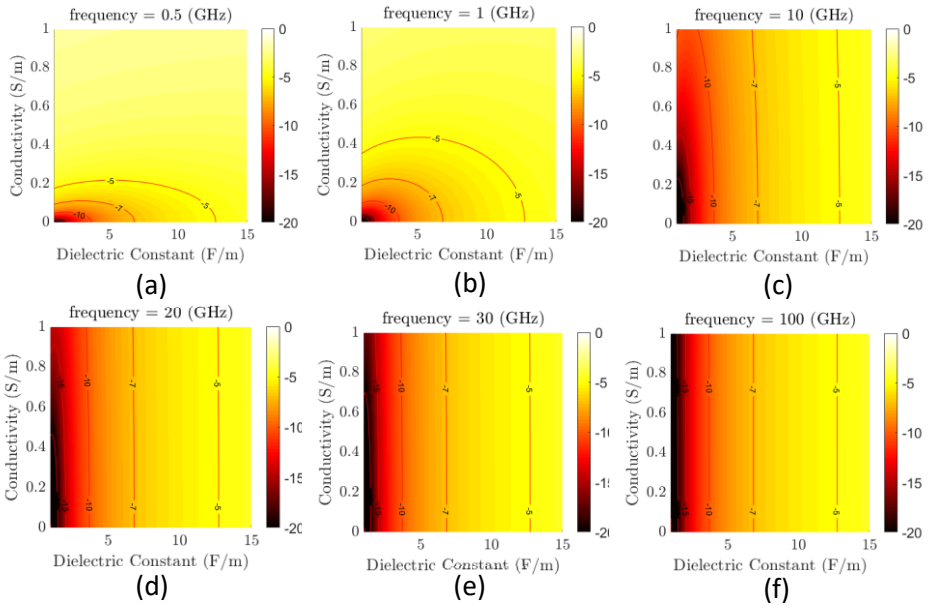

Figure 6.3. Conductivity and permittivity ranges for having minimum reflection coefficient. (a) 0.5 GHz, (b) 1 GHz, (c) 10 GHz, (d) 20 GHz, (e) 30 GHz, (f) 100 GHz.

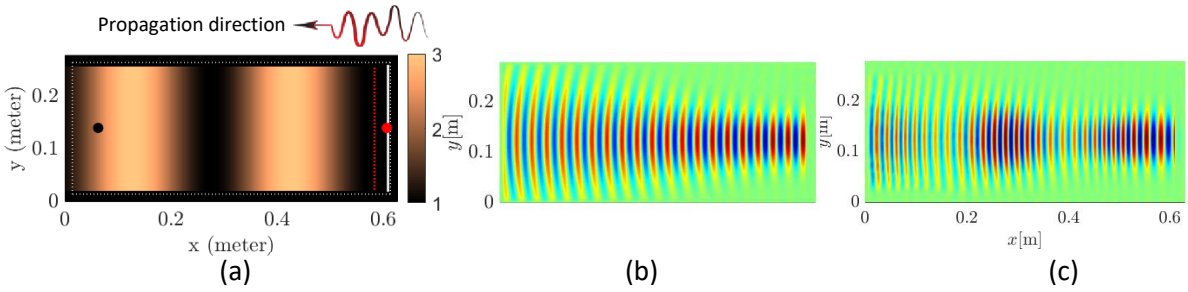

Figure 6.4. A propagation problem in a STM Medium. (a) Medium dielectric constant distribution at a single moment. (b) and (c) The propagated wave through FDTD simulation in an undisturbed and a disturbed medium at t=3.69 ns, respectively.

$$\Gamma = \frac{E_r}{E_i} = \frac{\eta - \eta_{ct}^*}{\eta + \eta_{ct}^*} \tag{6.2}$$

The value of η represents the characteristic impedance of the medium that the incident wave is traveling through. This allows designers to select a material with a minimal reflection by choosing a medium with the appropriate conductivity and relative permittivity fluctuations to minimize equation (6.2). It is critical to select the proper fluctuation as the permittivity of the STM media changes in space and time, particularly on the interface. Figure 6.3 provides the appropriate ranges for different operating frequencies. For example, if the undesired frequency component is 10 GHz, and a maximum reflection of -10 dB (less than one-tenth of the incident power) is required, then the designer must choose a material with an approximate range of relative permittivity and effective conductivity from Figure 6.3(c).

$$\epsilon'_r : 1.0 - 3.7 \tag{6.3}$$

$$\sigma: 0.0 - 0.5 \tag{6.4}$$

It is important to keep the design towards the lower end of the range in order to minimize reflections. The relative permittivity of the STM medium varies sinusoidally in both time and space, so it is crucial to ensure that the maximum range of the permittivity does not exceed the limit specified in equation (6.3) to meet the green shielding requirements. If the pump and signal wavefronts are not parallel, such as in the diversion case, (6.1) can be used in a limited area of δy where $\delta y \to 0$ (along the interface axis). This equation relates the change in the reflection coefficient to the change in the local characteristic impedance, which depends on the medium's permittivity or capacitive effect.

In the upcoming sections, the shielding mechanisms outlined in Figure 6.2 will be implemented numerically. Initially, the accuracy of the numerical method will be confirmed by comparing it with analytical solutions. Following this, a design process utilizing an optimization method will be introduced.

6.2 FDTD Model for STM Green Shield

The Finite Difference Time Domain (FDTD) is a powerful tool that can help us investigate complex STM media configurations. While the accuracy of the method must be confirmed, using the Fast Fourier Transform (FFT) to switch between time and frequency can provide insight into how the mechanisms of STM media can be utilized for green shielding. Chapter 6 contains the essential FDTD update equations for a lossy STM medium.

Figure 6.4(a) depicts a testing area designed to simulate wave behavior in an STM medium, with a luminal region excited by a 1 GHz pump wave, a 10 GHz signal wave, and a modulation strength (M) of 0.5. The medium exhibits high attenuation with a relative permittivity of 2 and a conductivity of 0.1. The FDTD solver uses a Courant factor of 0.495, 20 cells per wavelength, and a 0.0007×0.0007 m^2 cell size in a 0.6×0.25 m^2 domain. Convolutional perfectly matched layers (CPML) and total-field scattered fields (TFSF) are employed for wave absorption and reflection coefficient estimation. Figures. 6.4(b) and (c) demonstrate time-domain wave propagation in the FDTD solver, with the condensed wavelength in Figure 6.4(c) indicating up-conversion.

To validate the FDTD method used in this study, both the generated harmonics and the reflection level will be compared with the theoretical approach. The frequency domain will be used for transmission response analysis, as the signal spectrum and the relative attenuation of each harmonic are significant in transmission. However, for reflected fields, the real-time magnitude of the wave will be monitored in the time domain to ensure that the green shielding requirements are met. To examine the transmission, a single local point (indicated by a black spot in Figure 6.4(a)) will be chosen, and the wave frequency spectrum will be extracted using the Fourier transform. The estimated spectra from FDTD and the theoretical approach are compared, as shown in Figure 6.5(a). For time-domain reflection performance, two separate

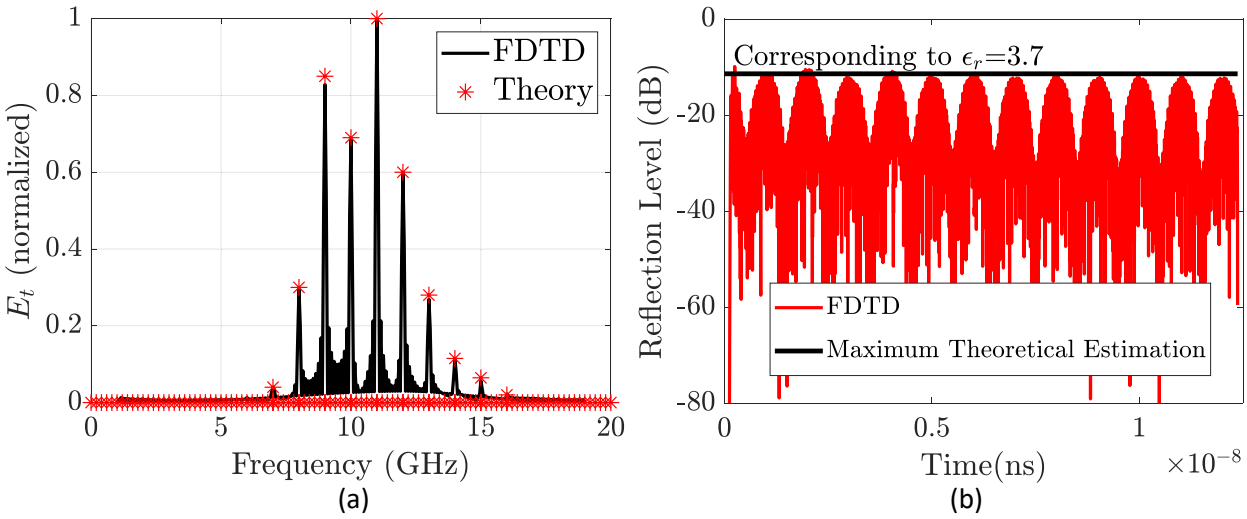

Figure 6.5. FDTD Transmission and Reflection validation. (a) Transmission, (b) Reflection.

simulations will be conducted. The first simulation will record the total wave in the time domain at a single point in the reflection zone (indicated by a red spot in Figure 6.4(a)). The second simulation will record the incident wave in the time domain in a free space medium at the same point. Due to the permittivity's real-time fluctuations within the range of 1.0-3.7, the maximum displayed reflection level corresponds to $\epsilon_r = 3.7$ and $\sigma = 0$. Assuming a maximum electric field intensity of 1 v/m for the incident field, the reflected wave is expected to range between 0 and 1 v/m, and it can be estimated by

$$\mathrm{E}_r(t) = 20\log\big(E_{tot}(t) - E_{in}(t)\big) \;\; dBv/m \tag{6.5}$$

where the total and incident electric fields sensed in the reflection zone are denoted by $E_{tot}(t)$ and $E_{in}(t)$, respectively. TFSF can also be done by separating the total and reflected waves. Figure 6.5 (b) shows the FDTD reflection level comparison with the maximum theoretical estimation. The numerical reflection performance is validated since the reflection computed by FDTD is below the maximum theoretical estimation.

6.3 Green Shield Design Procedure

Amplitude modulation can be achieved using an STM medium, which generates infinite harmonics due to its nonlinear nature. The amplification level of each harmonic is different, while the unamplified harmonics attenuate due to medium losses. Therefore, this medium can be tailored to provide shielding, as shown in Figure 6.1. However, the STM environment's performance depends on various parameters, including the modulation factor, the relative permittivity of the background and disturbance, and the effective conductivity of the medium. These parameters affect performance nonlinearly, making gaining intuition through parametric analysis challenging. A design procedure considering all resources and limitations should be followed to obtain a specified response. By utilizing FDTD and PSO, this technique determines

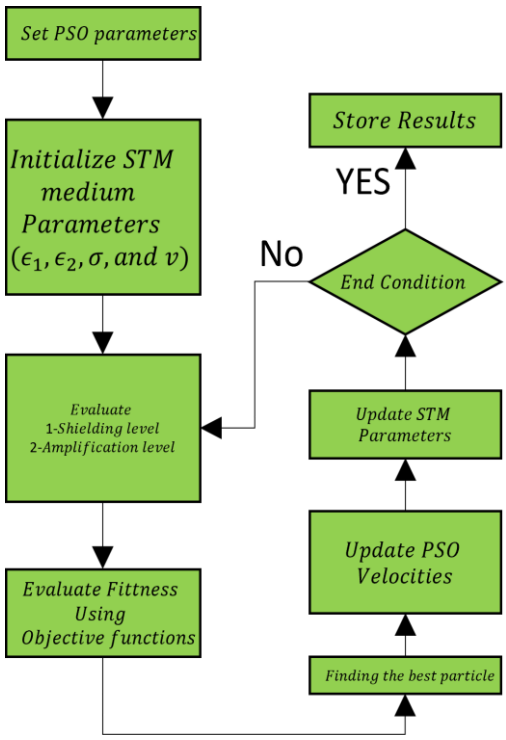

Figure 6.6. Green shielding design procedure using STM media.

the precise modulation strength or velocity ratio required to achieve a desired outcome. The optimal parameters obtained are then saved in a lookup table, enabling the user to adjust the shield to the desired mode, effectively shielding a specific harmonic while amplifying another. The procedure includes

1. Establish the numerical problem akin to the one analyzed in Figure 6.4,
2. Setting PSO parameters
3. Determining the medium conductivity and permittivity ranges depending on the desired green shielding level from (6.2).
4. Selecting the maximum achievable conductivity identified in step 3 to optimize the shielding or absorption efficiency. To account for the dispersion effect, we incorporate the impact of the alternating field conductivity on the static conductivity.
5. Obtaining the best STM parameters using an optimization technique aimed at single or multiple objectives. For instance, attenuating the interfering frequency and amplifying the desired frequencies could be viewed as two distinct objectives. Particle Swarm Optimization (PSO) was utilized in this study. It is worth noting that this process can be conducted through both theoretical and numerical approaches. However, applying this design procedure to the theoretical approach is not advisable, as the theoretical method already includes an optimization step.

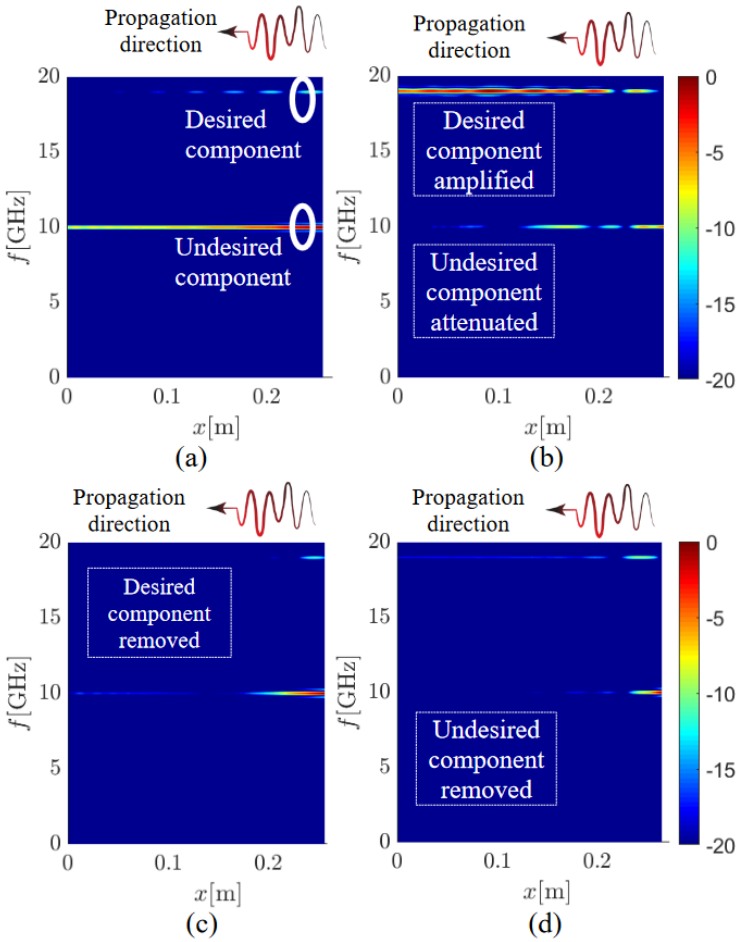

Figure 6.7. Shielding using up-conversion. (a) with unoptimized parameters ($\epsilon_1 = 1$, $\epsilon_2 = 0.3$, $\sigma = 0.03$, and $v = 1$), (b) with optimized parameters ($\epsilon_1 = 2.7$, $\epsilon_2 = 0.98$, $\sigma = 0.029$ and $v = 1.1$). (c) and (d) the effect of increasing conductivity on (a) and (b) harmonics ($\sigma = 0.1$), respectively.

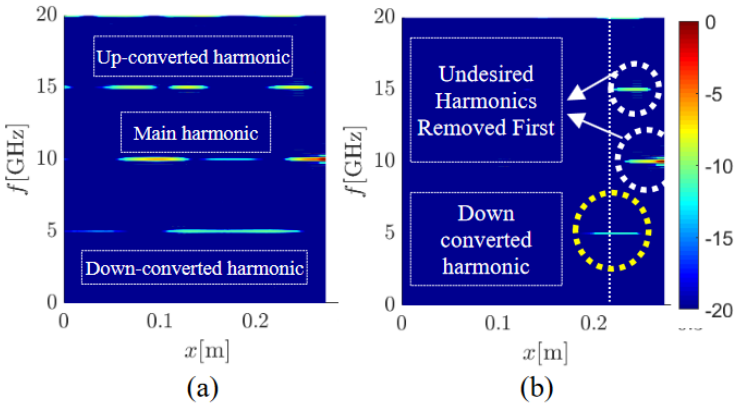

Figure 6.8. Shielding using down-conversion. (a) in a lossless medium ($\epsilon_1 = 2.3$, $\epsilon_2 = 0.98$, $\sigma = 0$ and $v = 0.9$), (b) with optimized parameters ($\epsilon_1 = 2.3$, $\epsilon_2 = 0.98$, $\sigma = 0.07$ and $v = 0.9$).

The suggested synthesis approach can achieve the intended shielding while also providing additional advantages, such as up-conversion, down-conversion, distribution, or diversion. The recursive process is depicted in Figure 6.6. It is important to note that while the focus in the

upcoming sections is on shielding a 10 GHz frequency component, the technique's effectiveness in shielding broadband noise will be examined separately.

The conversion of signals from the baseband to the passband or vice versa is called up or down-conversion, respectively. However, when an object is vulnerable to a particular frequency, up/down-conversion may serve two purposes. First, shielding the object by attenuating the undesired frequency. Second, preserving the data by shifting it to another band. This section is dedicated to customizing the properties of STM media to offer green shielding for X-band signals using up/down- conversion. It is worth noting that there are no restrictions on the thickness of the STM media at this stage. Therefore, the focus is primarily on the shield's efficiency and the reliability of the outcome.

6.4 Up-conversion

Assuming that one receiver can only receive low K-band signals (18-22 GHz), while the other is susceptible to high power X-band signals (8-12 GHz), STM media can be used to control the undesired signal level, data center frequency, and required amplification for the up-converted signal. To achieve this, the pump frequency is set to 9 GHz, which allows up-converted harmonics to be detected at various frequencies, such as 19 GHz, 28 GHz, and 37 GHz, when a 10 GHz TMx-polarized plane wave is applied to the medium. The design procedure of Figure 6.6 is then used to characterize the rest of the medium's parameters, which results in $\epsilon_1 = 2.7$, $\epsilon_2 = 0.98$, $\sigma = 0.029$ and $v = 1.1$. The attenuation level is set to 20 dB to minimize undesired harmonic signals, while the amplification level for the desired frequency band is 3 dB.

To monitor the behavior of waves in the medium, the electric field in the time domain is recorded on the line that connects the two dots, as shown in Figure 6.4(a). By applying FFT to the recorded data, the spatial-frequency map of Figure 6.7 is obtained that illustrates the movement of energy among harmonics as the wave travels between the two points. Figure 6.7(a) and (b) display two cases, one with optimal parameters and the other with non-optimal parameters ($\epsilon_1 = 1$, $\epsilon_2 = 0.3$, $\sigma = 0.03$, and $v = 1$), respectively. The optimized parameters provide a desired shielding effect for the undesired 10 GHz harmonic and a maximum amplification of 3 dB for the upconverted harmonic. Increasing conductivity can remove the desired or undesired harmonics, as shown in Figures. 6.7(c) and (d). Therefore, preserving the upconverted data requires amplifying the upconverted signal to ensure its strength is higher than the undesired signal.

When the modulation factor is less than unity for a mono-tone signal, there may not be amplified up-conversion. This is because the sub-luminal region has lower harmonic interactions compared to the luminal and superluminal regions.

6.5 Down-conversion

In 1956, J. M. Manley and H. E. Rowe analyzed the power flow into and out of a nonlinear circuit when excited by different harmonics [146]. This circuit became known as a space-time modulation equivalent circuit [147]. The analyses based on the Manley-Rowe relations show that the maximum achievable gain during down-conversion is determined by the ratio of the down-converted frequency to the main frequency. Therefore, amplifying the signal during down-conversion is not possible. From a shielding perspective, attenuating the main undesired frequency may attenuate the down-converted signal. In contrast, up-conversion and amplification can be achieved simultaneously, amplifying the up-converted signals while attenuating the down-converted ones. However, down-conversion always results in energy leakage to up-converted harmonics, as demonstrated in this section.

In order to preserve the down-converted signal while blocking the unwanted component, the optimization objectives must be adjusted. Precisely, the energy of the unwanted component should be redirected to the downconverted harmonic, which should be propagated further than the other harmonics for extraction purposes. Instead of relying on fixed values for amplification and shielding, which worked well for upconversion, the designer may aim for a specified energy difference (amplitude) between the down-converted and unwanted harmonics during optimization. This energy difference must exceed a certain threshold to attenuate the unwanted harmonic effectively.

To shield an undesired harmonic at 10 GHz, down-conversion to the sub-6GHz 5G region is employed with optimized parameters of $\epsilon_1 = 2.3$, $\epsilon_2 = 0.98$, $\sigma = 0.07$ and $v = 0.9$. The down-conversion frequency is 5 GHz, bringing the undesired 10 GHz component down to 5 GHz. The power distribution of the down- and up-converted harmonics is shown in Figures. 6.8(a) and (b), where Figure 6.8(b) demonstrates that the main undesired harmonic (10 GHz harmonic) and the upconverted harmonic (15 GHz harmonic) are eliminated. The down-converted harmonics can be collected within the next 2 cm of the structure, and if further propagation is required, an STM medium truncation can prevent wave attenuation. The white line in Figure 6.8(b) indicates a possible truncation point with a strong downconverted signal. It is observed that removing the upconverted signals is more challenging than the down-converted ones, making downconversion a worst-case scenario. Furthermore, higher modulation factors increase upconversion and make the loss factor less effective in eliminating undesired harmonics.

6.6 Distribution

An intrinsic characteristic of an STM medium is its ability to distribute the power of one frequency component among multiple harmonics, as demonstrated in Figure 6.2(c), making it an effective shielding technique when the incident power is high enough to cause interference. This distribution capability can be actively tuned to distribute power over several collectible

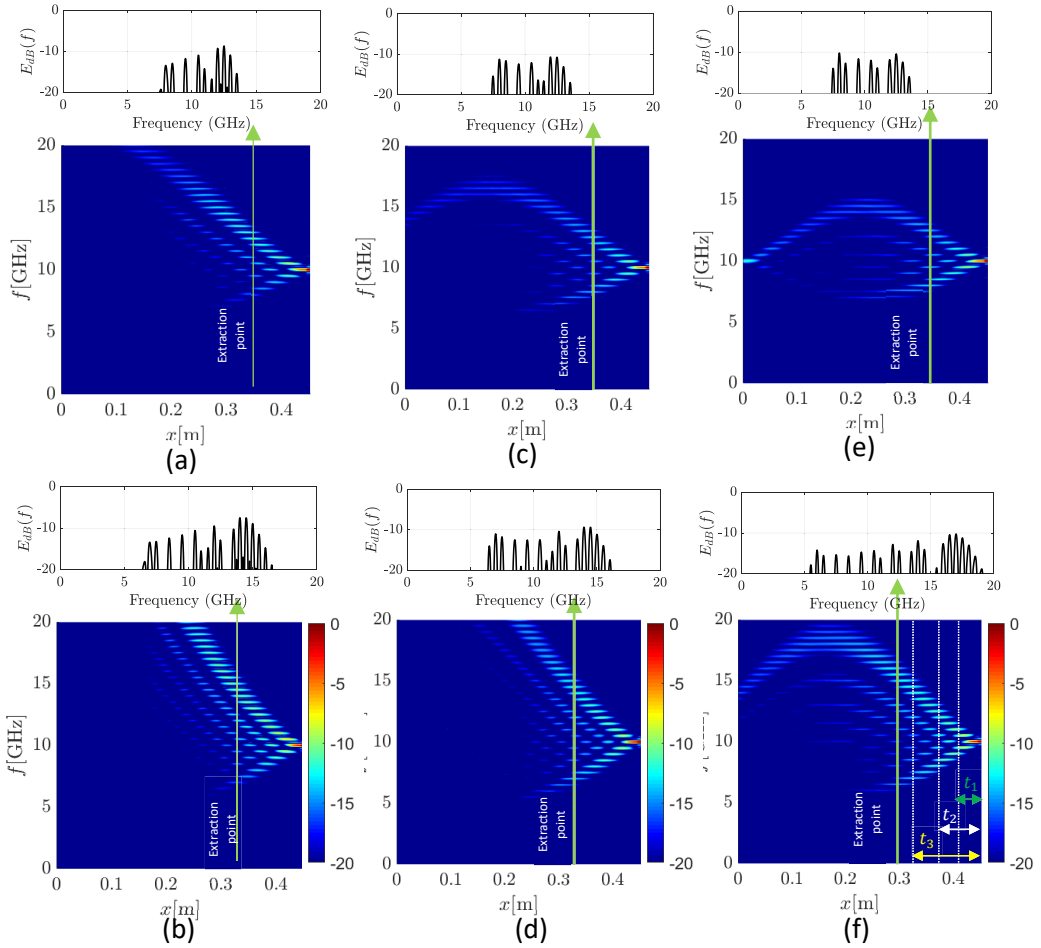

Figure 6.9. Shielding using distribution. (a) M=0.33, v=1, (b) M=0.5, v=1, (c) M=0.33, v=1.5, (d) M=0.5, v=1.5, (e) M=0.33, v=4, (f) M=0.5, v=4.

harmonics, particularly in the luminal or superluminal modulation regions where Spatiotemporal harmonic interactions are high, causing energy to shift from the undesired frequency to the upper or lower bands and remove the main harmonic. The presence of loss can help achieve the desired shielding level, but it is also achievable in lossless media, with the main harmonic either entirely removed or attenuated to a certain level. To reduce the power of the undesired 10 GHz component by at least 20 dB while exciting nearby harmonics, the critical parameters are the modulation factor and the modulation strength, which determine the degree of interaction among the nearby harmonics.

To remove the undesired frequency, it is necessary to distribute its energy level onto nearby harmonics, which can lead to significant attenuation when exposed to medium losses. The objective is to minimize the main harmonic by spreading the signal energy among the surrounding harmonics. A parametric analysis would be useful since this section covers multiple goals. The medium size used for this experiment is 0.5 × 0.1 m^2 with the same FDTD specifications as the previous cases studied in this chapter. Figure 6.9 demonstrates the shielding of a 10 GHz harmonic using the power distribution method in a lossless medium with $\epsilon_1 = 3, \epsilon_2 = 1$. The 1D plot above each figure shows the spectrum at a possible extraction point

where the 10 GHz component experiences 20 dB attenuation. The pump frequency is 0.5 GHz, and various velocity ratios (1, 1.5, and 4) and modulation strengths (0.33 and 0.5) have been employed to evaluate their effectiveness.

In all cases, the power is transferred from the primary harmonic to lower or higher harmonics, thereby eliminating the unwanted 10 GHz harmonic. It is worth noting that this shielding level was achieved in a medium that does not incur any losses. The medium conductivity is a secondary tool to create attenuation for the undesired harmonics. Another notable feature is the divergence (depicted in Figures. 6.9a, 6.9b, and 6.9d) and convergence (depicted in Figures. 6.9c, 6.9e, and 6.9f) of the excited harmonics, which is due to the periodic nature of the medium and is dependent on the relative permittivity's spatial and temporal periods. However, this characteristic is affected by modulation strength, which means that a given modulation strength has a maximum limit for up/down- conversion. Increasing the modulation strength results in the excitation of higher harmonics. Decreasing the pump frequency, increasing the modulation strength, and raising the velocity ratio all reduce the period of this frequency convergence, as illustrated in Figure 6.9. All the schemes can shield the primary 10 GHz component despite the erratic behavior in up/down-conversion. The dotted lines in Figure 6.9(f) indicate the locations where the medium can be truncated, which will be discussed in the following sections.

6.7 Diversion

As depicted in Figure 6.2 (d), there are alternative methods of shielding provided by STM media, besides simply transferring the signal energy to other harmonics. Redirecting the signal to another direction can shield local points and enable the signal data collected by a receptor located far away from the vulnerable object. This technique is particularly useful when the susceptible object remains stationary but is exposed to high-power radiation that needs to be locally diverted to a proper direction for collection. Additionally, the method can be applied to active real-time beam forming, beam splitting, and beam steering, among other out-of-scope applications, as suggested in [73].

In this section, a parametric analysis is conducted to investigate wave diversion within an STM environment under various directions of disturbance. Wave diversion occurs when the pump wavefront is not parallel to the signal wavefront, the disturbance is strong enough to trap the upconverted signals behind the moving pump wavefront, and the disturbance wave velocity predominantly affects the signal wave propagation. In practical applications, wave direction can be changed by applying the pump voltage to two sides of the medium with a phase lag. The phase lag is related to different disturbance directions. Figure 6.10 depicts the relative permittivity distribution in the medium with the pump wave direction set to 45 degrees. Figure 6.11 shows the wave's time and frequency domain propagation in three spatiotemporal regions (subluminal, luminal, and superluminal). The superluminal case is shown in Figure. 6.11 (a) is unsuitable for diversion as it fails to affect the signal wavefronts significantly. Moreover, the

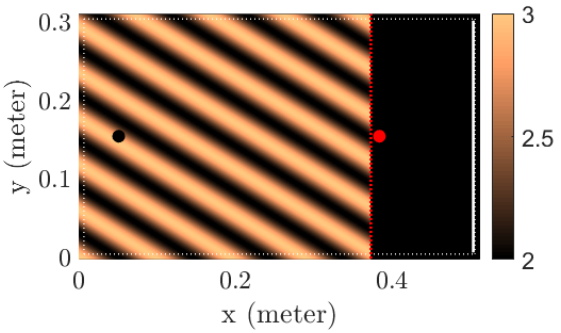

Figure 6.10. An example of relative permittivity distribution for diversion.

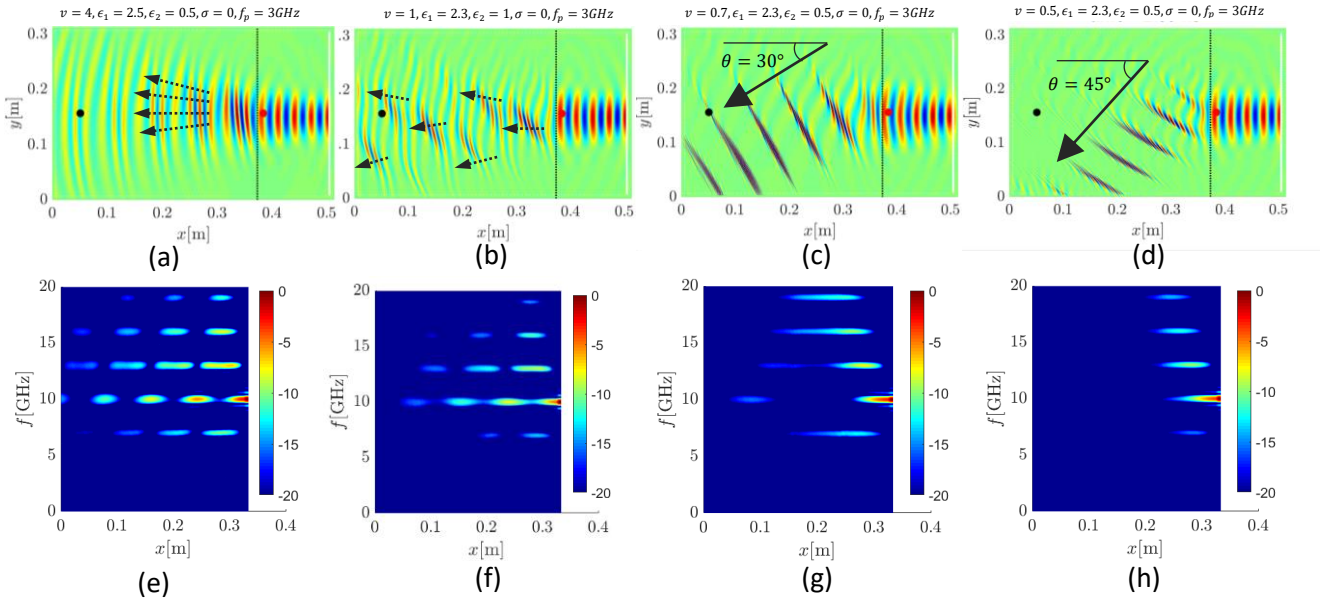

Figure 6.11. Shielding using diversion. (a) and (e) Superluminal regime with $v = 4, \epsilon_1 = 2.5, \epsilon_2 = 0.5, M = 0.2, \sigma = 0, f_p = 3GHz$, in time and frequency, respectively, (b) and (f) luminal regime with $v = 1, \epsilon_1 = 2.3, \epsilon_2 = 1, M = 0.434, \sigma = 0, f_p = 3GHz$, in time and frequency, respectively, (c) and (g) subluminal $30°$ regime with $v = 0.7, \epsilon_1 = 2.3, \epsilon_2 = 0.5, \sigma = 0, f_p = 3GHz$, in time and frequency, respectively, (d) and (h) subluminal $45°$ regime with $v = 0.5, \epsilon_1 = 2.3, \epsilon_2 = 0.5, M = 0.217, \sigma = 0, f_p = 3GHz$, in time and frequency, respectively.

luminal case shown in Figure 6.11 (b) disperses the incoming energy through several diverted wavefronts and does not focus the energy in the desired direction. On the other hand, the subluminal cases shown in Figures. 6.11 (c) and (d) exhibit promising performances in diverting the upconverted wave to $\theta = 30°$ and $\theta = 45°$, respectively. The spectrum analysis of the lossless subluminal cases in Figure 6.11 (g) and (h) explains that choosing $\theta = 45°$ removes the undesired signal and all other harmonics from the line-of-sight direction within a shorter distance.

6.8 Medium Thickness

An STM medium amplifies the upconverted signal without thickness limitations, but material truncation offers the benefit of controlling shield stability and reducing thickness. The truncation must be done appropriately to ensure the maximum required shielding effectiveness.

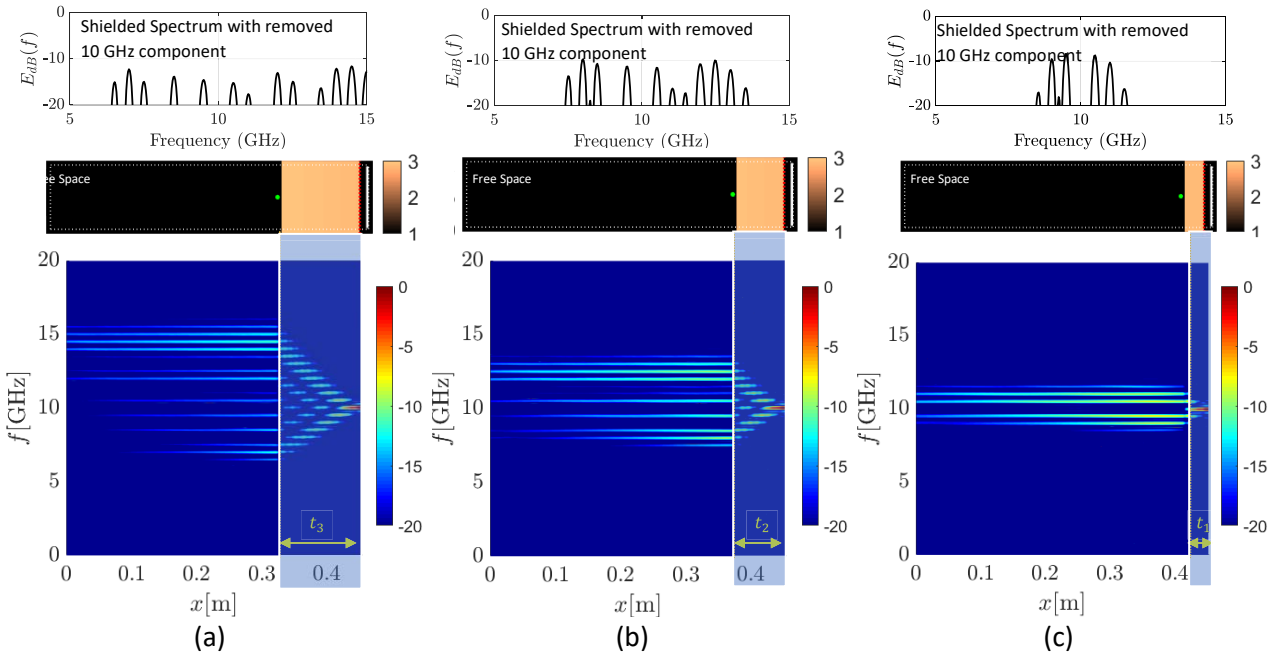

Figure 6.12. Medium truncation for power distribution purposes. (a) Thick truncation ($t_2 = 0.120m$), (b) Medium truncation ($t_2 = 0.069m$), (c) Thin truncation ($t_1 = 0.027m$).

Additionally, proper truncation can be used to control the output harmonics. Consider the distribution scenario of Figure 6.9, where the 10 GHz signal power is distributed over other harmonics. Figure 6.9 (f) illustrates the power distribution, where the main undesired 10 GHz component experiences a swing of high and low amplitudes resulting from the spatio-temporal interaction between the harmonics. The conservation of energy suggests that the incident energy should be mounted on at least one harmonic at a time (if it is not dissipated), and thus, all harmonics cannot have zero magnitudes at a single point.

According to this interpretation, Figure 6.9 (f) shows three possible truncation points represented by a dotted line. These lines are located where the magnitude of the 10 GHz harmonic is -20 dB. By truncating the medium from any of these points, no 10 GHz components will touch the interface and up-/ down-converted harmonics will be transmitted through the STM medium to free space. The resulting shielded wave spectrum through the three truncations is shown in Figure 6.12, where the 1D spectrum above each frequency-distance figure shows the wave spectrum after transmitting to free space. As a result, -20 dB attenuation is expected for the 10 GHz components. The medium truncation at t_3 results in the thickest shield shown in Figure 6.12 (a). In this medium, the energy has more time to move onto the upper and lower harmonics. In contrast, Figure 6.12 (c) shows one of the thinnest shields realized, with a thickness of t_1. When the wave has a lower interaction time in the STM medium, it can spread to the closest possible harmonics of $f_0 \pm f_p, f_0 \pm 2f_p, f_0 \pm 3f_p$. Similarly, thickness t_2 ($t_1 < t_2 < t_3$) provides an effect that can be categorized between the effects of t_1 and t_3. Increasing the pump frequency or thickness can increase the distance of the first harmonic from the main 10 GHz component. Additionally, increasing the modulation strength can increase the harmonic levels.

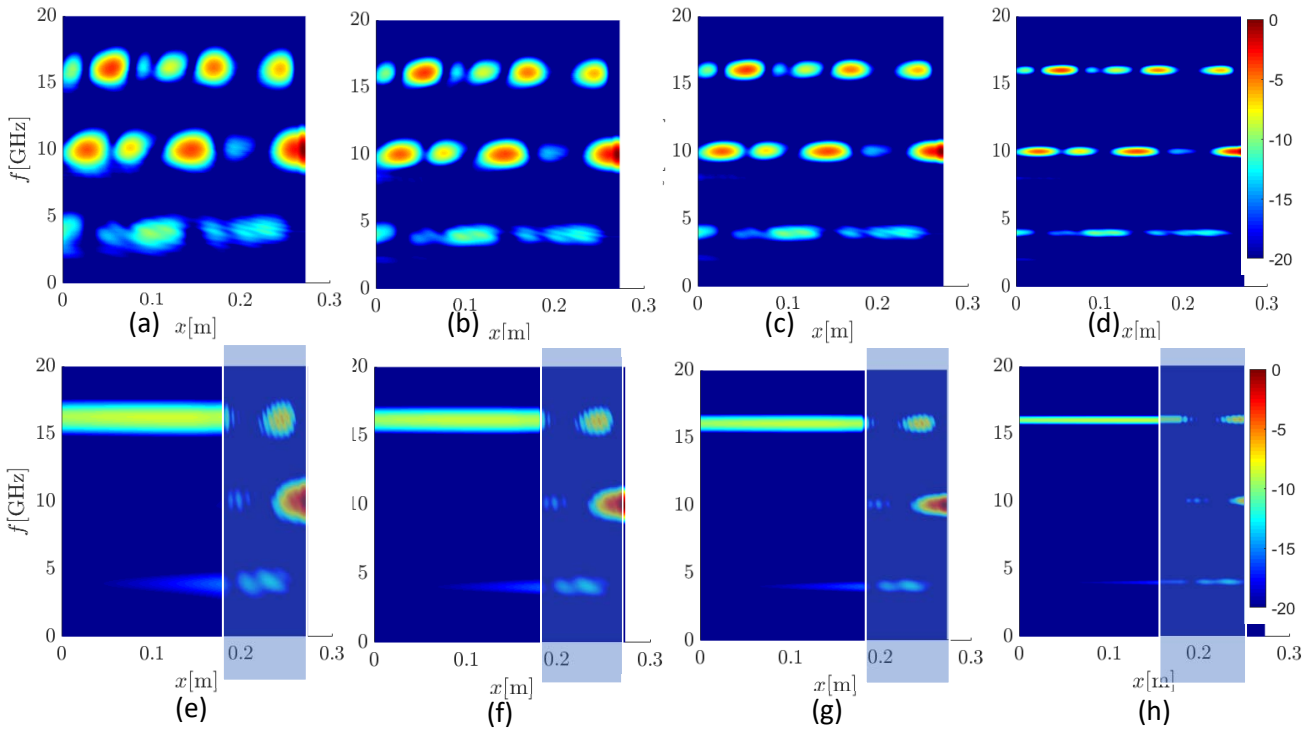

Figure 6.13. Shielding broadband noise. (a), (b), (c), and (d) synthesized STM shield for upconverting the noise with 40, 30, 20, and 10 % fractional bandwidth, respectively, (e), (f), (g), and (h) truncated slab for extracting the data at an upconverted channel corresponding to 40, 30, 20, and 10 % noise bandwidth, respectively.

Truncation is essential for up-conversion, down-conversion, and distribution. However, our simulations indicate that truncation may not have the expected effects for the diversion case. There is a fundamental reason: when the edge of a diverted wavefront, containing a range of up/downconverted harmonics, reaches the slab interface, it behaves like a point source that disperses the up/down-converted power through cylindrical waves. This goes against the primary goal of diversion. As a result, diverted signals must be extracted directly from the STM Medium.

6.9 Broadband Noise

The effectiveness of STM green shields for 10 GHz mono-tone interferences has been examined. However, it is also important to investigate the shield's performance when it is exposed to broadband noises. Thus, four samples of X-band noises with Gaussian spectrums and 20-dB fractional bandwidths of 10%, 20%, 30%, and 40% were chosen to test the STM medium's shielding capabilities. The medium's properties were $M = 0.5$ ($\epsilon_1 = 2, \epsilon_2 = 1$), $v = 0.6$ and $\sigma = 0.01$, while the up-conversion frequency was 16 GHz (pump frequency of 6 GHz).

Figures. 6.13(a)-(d) depict the potential upconversion behavior for each bandwidth in an infinite STM medium. However, we observed higher harmonic interactions in broadband cases, increasing the likelihood of instabilities. This means that instabilities may occur even in the subluminal region, which has not been previously reported. To achieve the desired upconverted spectrum, proper truncation is necessary.

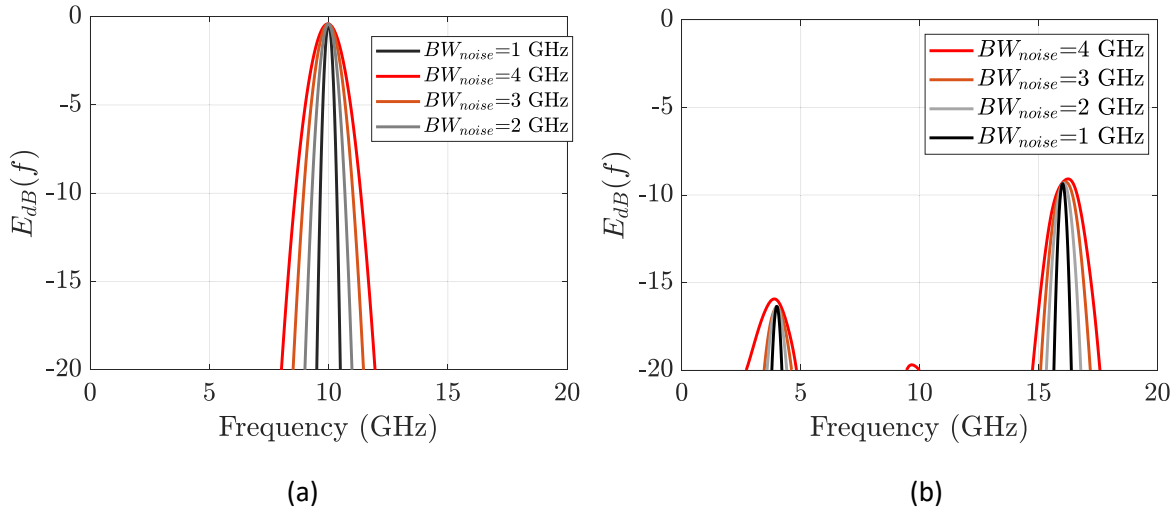

Figure 6.14. Spectrum analysis for different noise bandwidths, (a) The spectrum of the impinged noise/ undesired signal. (b) The spectrum of the received signal.

Figures. 6.13(e)-(h) demonstrate the shielding performance of the STM slabs when illuminated by different noise bandwidths. In all cases, the shield could remove the wideband noise while upconverting the data to a different Ku-band channel. The spectrum analysis in Figure 14 shows a nonlinear response that may accompany the upconversion of wideband signals. The noise with 40% fractional bandwidth experienced a slightly higher shift than the estimated noise with 10% fractional bandwidth. As the noise bandwidth increases, the upconverted/down-converted spectrum may experience a 1.2% shift compared to the expected range. Our findings suggest that this nonlinear shift is more significant when the bandwidth increases, owing to the nonlinear behavior of STM media [11].

Different sets of modulation parameters lead to specific effects on a frequency component. When one set of parameters is used for a range of frequencies, only one of the frequency components undergoes the anticipated upconversion effect. This might lead to wave distortion in the time domain. Therefore, while STM media can shield broadband noises, the reliability of the extracted upconverted/down-converted data depends on the noise bandwidth.

6.10 Building an STM Slab

A review of the recent practical investigations on STM media indicates that most are limited to low-frequency microwaves [65, 71, 80, 81, 83, 84, 148]. The general fundamental reason for this is that experimental difficulties increase exponentially with frequency while theoretical works do not have this limitation. Identifying these obstacles and technical challenges can serve as a starting point for the practical implementation of STM slabs in the future.

This section discusses the experimental limitations and challenges that working with STM media may cause. Additionally, we will explore how various engineering teams from diverse backgrounds can address these issues. The following argument will also help us differentiate

between the nature of the work done in Chapters 5 and 6 and the idea of practically realizing STM slabs by viewing them as two different problems with different natures.

The problem of fabricating STM media can be divided into two branches. STM transmission lines and STM slabs. The fabrication challenges of these two components might differ with the latter including more difficulties. STM transmission lines necessitate a one-dimensional pump configuration on a line (coplanar wave guide or microstrip line), while the STM slabs require a three-dimensional configuration to produce modulation. Although the problems addressed in this dissertation can be applied to transmission lines, the simulation goals and the shielding problems addressed lean more toward the slabs excited by a TEM plane wave. Shielding by STM slabs is mostly a radiation problem rather than a conduction one, and from an electromagnetic compatibility point of view, it is known as a radiated susceptibility/emission problem. The realization of such a project requires the contribution of different mechanics, chemistry, material, and electrical departments. This distinguishes it as a whole different project. That is why we should be aware of differentiating between the features these media can provide and how they can be realized as a homogenous STM slab. This work's primary focus is based on a theoretical approach validated by numerical results. The practical side is, by far, in its immature stage and has many gaps to be filled. Some gaps are more associated with technological difficulties than technical, practical methods.

In the following, we will provide as much helpful information as we observed during the investigation to help future researchers realize such an interesting medium. Thus, we start with an introduction to how an STM transmission line is implemented, and then we go through the conditions that need to be satisfied when it comes to homogenous STM slabs.

6.10.1 The realization of STM transmission lines:

Using varactor diodes, STM transmission lines have been widely realized [65, 71, 80, 81, 83, 84, 148]. The lines may be used as Mixers (up-and down-converters), isolators, nonreciprocal amplifiers, or attenuators. There are two commonly used configurations for realizing these components.

- First, a space-time modulated pump wave is used through linearly distributed varactor diodes mounted on a uniform transmission line.
- Second, a time-modulated pump wave (time-modulation) through linearly distributed varactor diodes mounted on a **nonuniform** transmission line (space-modulation).

Figures. 6.15 (a) and (b) illustrate the schematic of such realizations. A uniform distribution of varactor diodes is required to inject the carrier frequency as the signal wave passes the line. Conductor-backed coplanar waveguides (CPW) are ideal as varactor diodes can load them locally. Figure 6.15 (a) shows a fixed-linewidth CPW loaded by a uniform distribution of varactor diodes. The pumped wave must be modulated in space and time [84]. Figure 6.15

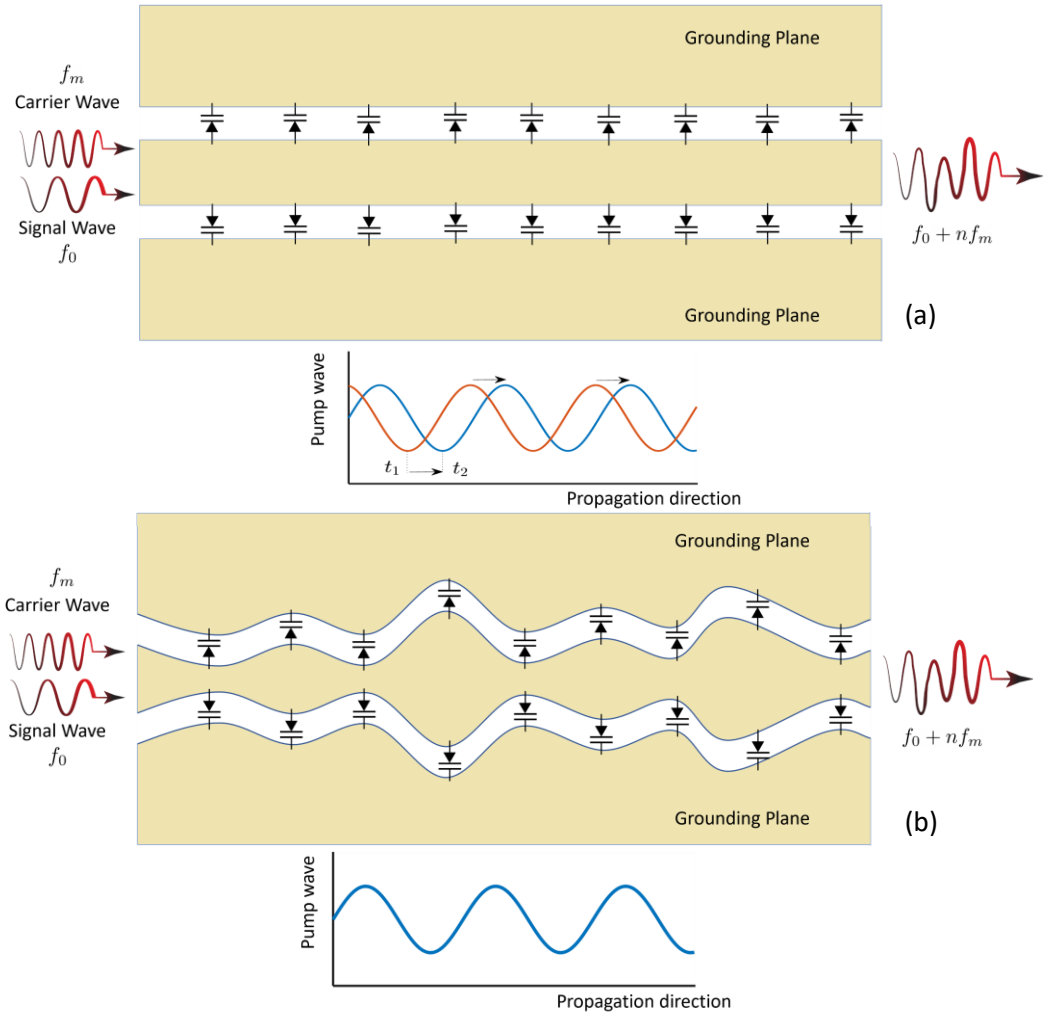

Figure 6.15. STM transmission lines. (a) Space modulated line and time mudulated wave. (b) Space-time mudulated pump wave.

(b) illustrates an idea investigated in [83], where the space modulation is created physically by varying the CPW linewidth.

The introduced configurations can be ineffective when the frequency increases. This is due to the physical size of the varactor diodes responsible for sampling the pump wave. Therefore, at least ten varactor diodes are required within a pump wavelength. For example, the size of each varactor diode in a package must not exceed 1mm for a pump wave of around 30 GHz. This constraint explains why recent research has emphasized low-frequency applications.

6.10.2 The phenomenon of local capacitive effect

Each varactor diode applies a localized capacitive effect on the areas around the mounted components. Figure 6.16 shows this physical phenomenon on the schematics of Figure 6.15. The distances between the varactor diodes should be chosen to reduce the overlapped areas. In other

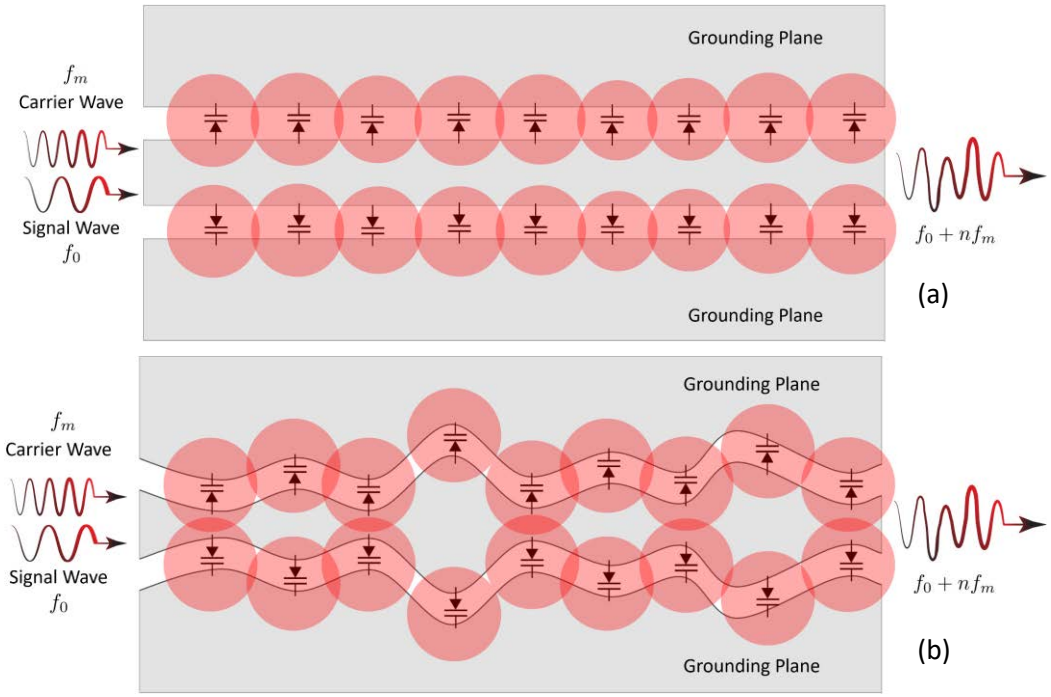

Figure 6.16. The phenomenon of local capacitive effect. (a) Space modulated line and time modulated wave. (b) Space-time modulated pump wave.

words, the overlapped areas are exposed to at least two different capacitive effects, resulting in an excessive increase in the locally induced relative permittivity of the medium. Recent works have experimented with this optimal distance [65, 71, 80, 81, 83, 84]. Failing to meet the required optimal distance can deteriorate the expected inhomogeneity and create new harmonics or distortion in time.

6.10.3 The realization of a homogeneous STM slab:

Figure 6.17 shows the three-dimensional view of the STM slab concept. Despite this STM slab's numerous benefits, the structure has three main fabrication difficulties. First, the varactor diode distances are adjusted to minimize the phenomenon of the local capacitive effect. This problem is mainly due to the higher number of surrounding varactor diodes in a three-dimensional space. Second, the connection of each diode to the next diode on the adjacent surface must have the least interaction with the transmission of the signal waves. This is because both the pump wave and signal wave share the same path, which could interfere with the signal wave. Incorporating a proper biasing network that does not interfere with the transmission of the waves is the third prominent challenge for realizing such a slab.

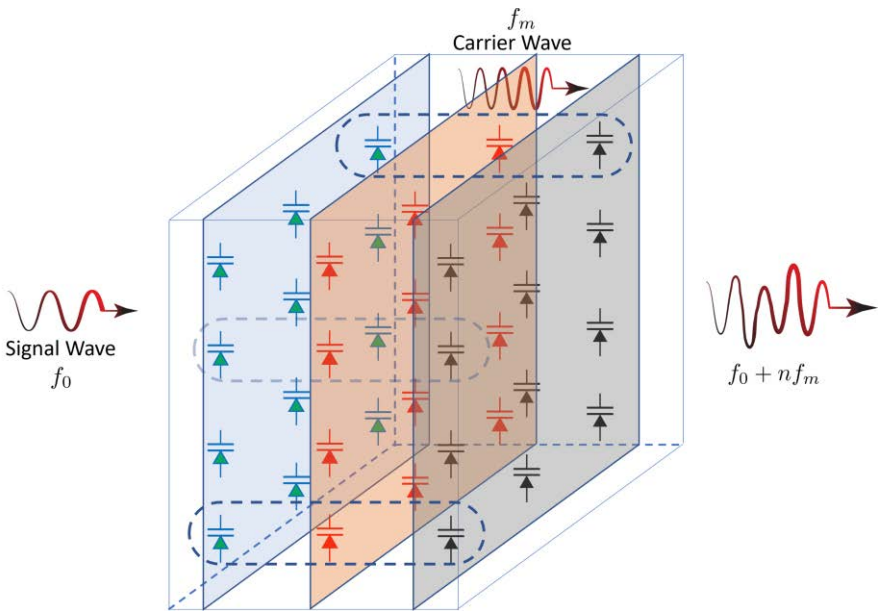

Figure 6.17. STM slabs.

6.10.4 Further Discussions

As implied, such a disturbed medium requires a special architecture and is different from merely realizing a transmission line. These difficulties soar when the frequency increases. In the millimeter-wave region, the designers may face other fabrication barriers and limitations that may halt them from further investigating the transmission lines or slabs.

This work has adopted certain measures and considerations that helped minimize the concerns regarding the method's applicability. Note that all approximation results, rigorous methods, and FDTD results agree (in their respective area of validity). However, as explained in the last chapter, this study has not settled for validating the numerical achievements by theoretical methods, which, per se, is a reliable approach. During the validation procedure of Chapter 5, a comparison with a recently validated method was added. The proposed FDTD method in this study could accurately estimate the amount of the reported practical loss. Note that the conventional method was the only estimation method available for lossy environments that failed to estimate the loss. Therefore, all the available data has been used to prove the efficiency of the proposed method (conventional method, full-wave method, rigorous method).

The challenges the designer might face when designing STM media are listed here to wrap the section up.

6.10.4.1 The radiation of the pump wave

Pump waves can be converted into leaky waves and be radiated when the substrate has a low dielectric constant. High permittivity material is recommended as these materials can store energy without creating leaky waves.

6.10.4.2 The dependency of the medium permittivity to heat:

Since the performance of semiconductor-based components varies with temperature, the designers might ensure their design operates at the recommended temperature. Otherwise, the imposed capacitive effect changes, leading to a different up/down-converted signal and higher-than-expected loss.

6.10.4.3 The quality of the dielectric materials:

The imaginary part of the permittivity changes versus frequency. In order to avoid unpredictable behavior, high-frequency compatible laminates need to be used with known dispersion effects—for instance, IsoClad high-frequency laminates offered by Rogers Corp.

6.10.4.4 The imperfection of the varactor arrays

The imperfection of the varactor arrays, especially in high frequencies: as the modulation temporal frequency increases, the spatial distance between the varactor diodes decreases. This requires appropriate technology for mounting the diodes.

6.10.4.5 The amount of capacitive overlap effect

To avoid this overlap, the area covered by each capacitor needs to be determined before fabrication. This challenging experimental issue needs to be addressed in a different project.

Last but not least, if material engineers focus on designing a new material that exhibits a sensitive refractive index to the applied capacitive or heat effect, some doors would open in the optical regime to switch active cloaking from microwave frequencies to optical regions.

Chapter 7: Achievements and Related Topics

This chapter will present the essential conclusions regarding the two main topics (Nearfield shielding and green shielding) studied in this dissertation. Next, it casts light on the remaining shielding topics regarding the perspectives for future applications of STM slabs. The potential benefits of STM media for the optics/electromagnetics community are discussed, highlighting the advantages of cloaking techniques in optics and microwave regimes. The concepts of active Cloaking and active shielding will be merged to familiarize readers with different terminologies that serve similar purposes. It turns out that the green shielding methods discussed in the previous chapter are good candidates for other similar applications. After a review of the importance of visual invisibility and scattering cancellation methods, it is explained that radar cross section (RCS) reduction could be a useful cloaking example that can be addressed using green shielding methods. Thus, we draw the reader's attention to applying green shielding methods (by STM media) in RCS reduction to shield objects from being detected by radars. This chapter is highly recommended to those who want to investigate the applications of metamaterials and, specifically, STM media as a topic for their future academic research.

7.1 Dissertation Achievements

The contribution of this dissertation to the advancement of knowledge is divided into two branches: nearfield shielding and green shielding. Two chapters were dedicated to the nearfield shielding problem, and the green shielding concept was addressed in two chapters. The last chapter was added to give the readers some perspective about the potential applications of STM media for active shielding in other domains. The achievements of this dissertation are categorized based on answering four essential shielding questions listed below.

7.1.1 NF Shielding Achievements

Two essential problems regarding NF shielding were addressed. First, the following questions were outlined in Chapter 3. “What are the differences between NF and FF shielding? How can we predict the NF performance of an FSS shield?” Four commonly used metasurfaces with X-band bandstop responses were compared to answer these questions. To show how nearfield response exhibits different characteristics compared to farfield response, electric field distributions, resonant frequency shifts, shielding effectiveness degradation, dimension effects, edge diffraction effects, and bending effects were analyzed in both nearfield and farfield zones. It was observed that although the studied FSSs had similar far-field shielding performance, they exhibited different nearfield behavior. The reader gained insights into the low- and high-energy concentration regions of the FSS and how the resonant frequency of the FSS changes in these

regions. An analytical model based on the equivalent circuit model (ECM) was proposed to predict the near- and far-field shielding effectiveness (SE) for single-sided, single-layer FSSs. The farfield response was modeled by substituting the medium's intrinsic impedance with the FSS surface impedance obtained from ECM, and using this impedance to find a slab's shielding effectiveness. The NF behavior of cells was also modeled by an approximate method that uses a novel inhomogeneous nearfield surface impedance to substitute for the intrinsic impedance of the medium.

The study also reveals that NF transmission instability increases with increasing cell bandwidth. Miniaturized elements, such as square-loop (SL) and convolutional square-loop (CSL), demonstrated more resistance to NF-SE degradation when exposed to edge diffraction or when used in conformal structures. Critical radius and critical distance were defined as criteria for practical nearfield shielding applications. SL and CSL showed critical radii of 4.9 cm and 5.1 cm, respectively, while the measures were 11.8 cm and 5.6 cm for JR and SRR. Critical distances of 3.1 mm and 4.4 mm for SL and CSL were obtained, while the measures for JR and SRR were 5.2 mm and 6.8 mm, respectively. Therefore, SL and CSL also showed faster NF to FF convergence over Jerusalem cross (JR) and split-ring resonator (SRR). Stability in resonant frequency, longer trusted regions, less sensitivity to bending, and higher NF-SE level were the other upsides of SL and CSL compared to JR and SRR. This investigation shed light on the specifications and considerations necessary for dealing with NF abnormalities in flexible ultra-thin frequency selective surfaces.

The second question addressed in Chapter 4 is, "How can we design a shield with stable NF characteristics? Alternatively, how can we reduce the distance between shields and susceptible objects without experiencing NF instabilities?" For this purpose, a new miniaturized, flexible frequency selective surface was proposed to shield the X-band interferences in nearfield (NF) and far-field (FF) zones. The NF stability is obtained by optimizing the mutual coupling between two resonant structures. The design performance has been analyzed using an accurate equivalent circuit model that includes the mutual coupling and substrate effects. The model accuracy is validated by comparing it with full-wave analysis, and a parametric study is conducted to address the narrowband characteristics of the proposed structure. The final structure shows superior NF stability with a critical radius of 3.4 cm and a critical distance of less than 0.03λ. This improved performance is because of the optimal interaction of resonant surfaces for removing NF components. Some other benefits of the proposed design include better control of reflection and transmission zeros, adjustable resonant frequency, and enhanced bandwidth. The shield's performance has been analyzed for curved or wearable configurations, where minimal degradation around center frequency was obtained. The results show that the proposed shield is reliable within a distance of λ from the susceptible object and is a promising candidate for wearable applications where the separation distance between the shield and the object is less than $\lambda/6$ (5 mm for 10 GHz).

7.1.2 Green Shielding Achievements

Two essential questions have been answered regarding green shielding techniques using STM media. First, what features do STM media have that enable them for green shielding applications? Intending to provide the tools for green shielding analysis, Chapter 5 examines the behavior of waves in a lossy STM medium, specifically looking at dispersion, amplification, and attenuation. Various methods for wave propagation in lossy STM media, including approximate, rigorous, and numerical-based FDTD solutions, have been introduced and compared. The small perturbation method (SPM) was used to obtain simplified closed-form solutions for the wave dispersion diagram. The areas of validity for these solutions in both high-loss, sub-6GHz regions, and millimeter-wave regions were thoroughly discussed. The SPM method provided fast solutions for low-disturbed lossy media, while the FDTD formulation provided reliable solutions for any strength of sinusoidal disturbance in lossy media. The results showed that the dispersion curves were influenced by medium conductivity, operation frequency, and modulation spatial and temporal frequencies. The FDTD results are 2-7 dB more accurate than conventional methods that do not consider medium dispersion. After being equipped with advanced tools for dealing with STM media, a range of implications and applications were introduced that showcase the advantages of STM media for green shielding applications. These include insights on reciprocity, stability, down/up-conversion, and zero-attenuation frequencies. For instance, it was shown that it is possible to tune STM media in a way that one harmonic experiences zero phase constant (no propagation). Therefore, the user can block/shield one harmonic. At the same time, achieving a zero attenuation constant for another harmonic is possible, which leads to a simultaneous amplification and shielding feature. These insights will be used to design green shields with special features.

The second question was how to design a green shield with minimized reflection and amplification/up-conversion/distribution/diversion of the desired harmonic while the undesired harmonic is absorbed. With the developed tools from Chapter 5, Chapter 6 investigates modern green shielding methods that use STM media. Four shielding mechanisms of up conversion, down conversion, distribution, and diversion were introduced to reduce transmission and reflections of undesired spectrums efficiently. A design procedure that links PSO to FDTD was introduced. The medium's permittivity and conductivity must not exceed a certain amount to minimize reflection. Despite obtaining at least 20 dB SE, -10 dB reflection, and at least 3 dB gain, it turns out that every mechanism has its advantages and features. Up-conversion amplifies the desired harmonics that can be used for data collection, while down-conversion collects data without amplification using the proposed design procedure. Power distribution reduces harmonic excitation levels and removes the main undesired harmonic. The STM medium also allows for redirecting wave propagation, known as diversion. Since the medium produces harmonics in a spatio-temporal manner, truncating the medium allows for choosing the harmonics that need to propagate without further attenuation. Further investigations showed that the media could be used even for broadband noises. The analyses indicate that although realizing an STM medium

is still in the preliminary stages, the selectivity characteristic and the diversity of solutions make it a superior choice for shielding than conventional green shields.

In the rest of the dissertation, several essential perspectives have been introduced for future researchers, highlighting the potential benefits that STM media can provide for cloaking applications in optical and microwave regions. The concepts of shielding and Cloaking are merged, and various cloaking techniques (e.g., transformation optics to achieve invisibility cloaks) are introduced, some of which are only suitable for microwave frequency applications. A discussion is provided that explores the usefulness of green shielding methods for cloaking purposes. The usefulness of STM shielding methods is further investigated for cloaking techniques in RCS reduction. Simulation results provide an optimistic perspective on the usefulness of the green shielding STM method in cloaking applications.

7.2 Cloaking: From Invisibility Cloaks to Microwave Cloaks

Cloaking generally means hiding or making something imperceptible, but the interpretation of Cloaking can vary extensively depending on the field or application. In computer science, the term cloaking is frequently linked to concealing content from search engines with the intent of manipulating search results, and this practice is commonly referred to as search engine cloaking. In physics, Cloaking is defined as using metamaterials to deflect light waves around an object, making it invisible. This field has been the focus of research lately and has the potential for military, medical, and other applications. Even different frequency ranges have given the term "cloaking" slightly different meanings. For instance, Cloaking in optical regions is used for different applications than microwave regimes. In biology, Cloaking can signify diverse mechanisms that animals employ to disguise themselves from predators or prey. For instance, some animals have developed camouflage patterns that help them blend in with their surroundings, while others can generate toxins or emit unpleasant odors in self-defense.

Despite having a similar concept, the term cloaking has diverse meanings and applications in different fields, and comprehending the context used is critical to understanding its implications fully. In the following, we will review Cloaking and invisibility in optics and microwave regimes, highlighting their differences and similarities with shielding techniques. We will then explore merging STM shielding methods with cloaking techniques. The discussion starts with visual invisibility and will be extended to different means of invisibility and cloaking methods.

7.2.1 Invisibility Cloak

Invisibility could have different realizations and applications in different frequency ranges. However, as humans, we are more intrigued by visual invisibility in the visible light

region, that is to say, SHIELDING HUMANS/OBJECTS FROM BEING SEEN. When exploring around space-time modulation and its applications in shielding starts, understanding the features of changing wave direction through transmission, being non-reciprocal, absorbing and up/down-converting EM waves, the possibility to control the wave amplification, and the fact that this can be a real-time interaction, is attractive enough to make the reader think about this seemingly farfetched dream. If one is looking for a solution to this human dream, this section can help one gain a pervasive knowledge of where science has stood by this date and how the STM technique has the potential to provide certain levels of invisibility. Before we jump into the visible light region, it should be noted that switching from microwave frequencies (300 MHz to 300 GHz [149]) to visible light spectrum (400 THz to 700 THz) for visual invisibility will be a reckless transition without being equipped with proper fundamental knowledge about the critical limitations, conditions, and approximations in the optical regime. Therefore, this section discusses invisibility in different frequency regimes to highlight each regime's challenges and recent progress. In addition, we need to clarify how an invisibility cloak operates and what we can physically expect from it in different frequency regimes. In other words, we need to discover what portion of the fiction can come true. Can physical limitations allow a surface to hide an object perfectly? The theoretical answer is yes. The practical answer is not yet. The motivating answer is that some levels of invisibility and camouflaging are practically possible.

7.2.2 A review of the cloaking methods

At this stage, one might wonder if invisibility results from zero forward scattering/diffraction from the object. While this condition will be discussed in this chapter, we will show that there is a difference between visual invisibility and invisibility against microwave sensors/radars. In addition, it will be elaborated that perfect visual invisibility in the optical region is far more subtle than scattering cancellation.

Several seemingly different mechanisms for hiding objects (visually or from a Radar perspective) have recently been investigated [150, 151]. Some are still in microwave and millimeter wave regions, while others are theoretically efficient for visible regions. However, as of the date, the available methods can be categorized into three dominant mechanisms based on the visual/behavioral effects they cause. One mechanism involves providing perfect minimal-disturbance transmissions of electromagnetic waves that result in perfect invisibility (theoretically). The second focuses on scattering cancellation mechanisms that lead to radar invisibility and black visual effects. The third one provides partial invisibility using altered laws of reflection and refraction.

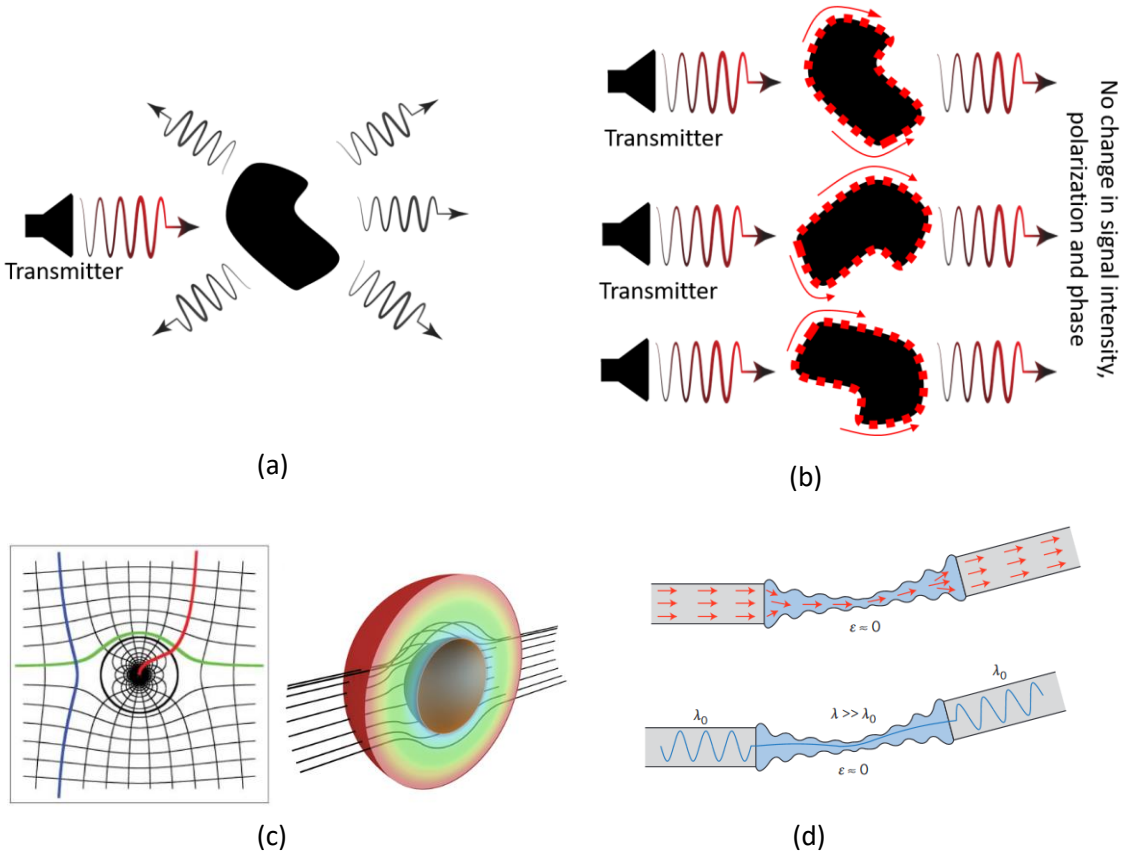

Figure 7.1. The concept of perfect transmission. (a) Scattering from an arbitrary object (b) Perfect invisibility condition for a cloaked object (c) A 2D and 3D representation of operation mechanism for optical conformal mapping [152],[153], (d) The schematic effect of near-zero refractive index materials on changing the direction and wavelength of light [155].

7.2.2.1 Based on Perfect/Engineered Transmission

One category is based on transformation optics [152, 153] and conformal mapping [154]. It focuses on embedding zero-index and/or transparent materials in optimal geometries in a way that instead of transmission or reflection, power flow experiences wavelength stretches, diversions, and bending effects toward the cloak surface and passes around the target without any collision/interaction with the target [155]. This minimum interaction with light rays provides the invisibility condition shown in Fig 8.1 (a) and (b). As a result, the shield/cloak can replace the human body with the background view due to no light interaction with the cloaked object. The concept of transformation optics is shown in Figures. 8.1 (c). In practice, this means that the cloak should be able to let the background reflected waves go through it from one side and guide them to the other side of the shield, and finally recombine them as plane waves (not dispersed rays) in precisely the same direction as they have entered the cloak, where the observer is located. As Fermat's principle shows [156], light rays use the shortest optical paths in media with a constant refractive index ($n = \sqrt{\epsilon_r \mu_r}$). If the refractive index of the material experiences a spatial variation, the shortest paths are curved rather than straight, which results in a variation in the light ray direction. As a result of Fermat's principle, one way to create a shorter path for light is to increase the speed of propagation ($v = c/n$) by creating a curved path that

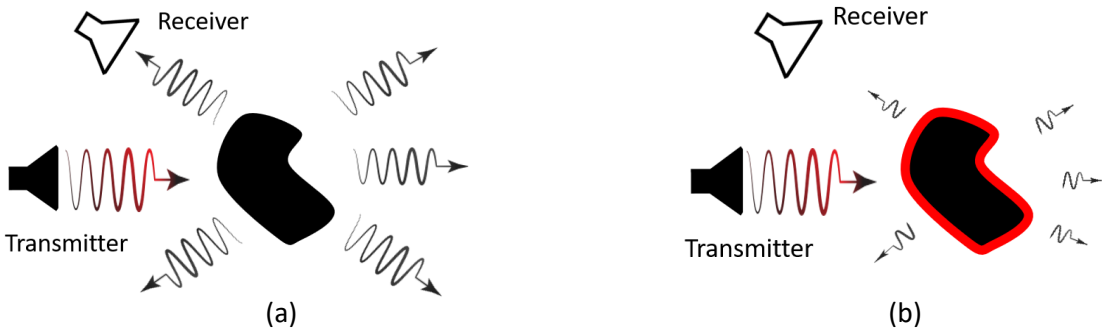

Figure 7.2. The general concept of perfect absorption or scattering cancellation for achieving invisibility/ Camouflage. (a) Scattering from an arbitrary object (b) Reduced scattering due to the presence of a cloak

has a refractive index between 0 and 1 (the reader may learn about the possibility of making such a metamaterial by reading about near-zero refractive index [157-159] and negative refractive index [160-162] materials). Figure 7.1 (d) illustrates this concept where the guided wavelength ($\lambda_g = \lambda_0/\epsilon_{ff}$) is stretched inside the near-zero refractive index material. A similar concept can be seen when the radio wave direction bends when it passes the ionosphere (the refractive index is less than one). Thermally modulated carbon nanotubes seem to produce a similar effect [163]. The other way to create the curved path is to enter the light into a dense material with a higher refractive index and then create a curved path with a lower refractive index so the light rays can be bent. It is implied that the performance of such a shield is highly dependent on the geometrical form of the cloak. Altering the cloak geometry might change the direction of the output light rays. For instance, it may be unable to redirect the background waves to the observer's eyes when the observer is moving. Therefore, even if the whole concept is realized, it might be specific to one incident and observation angle. In this case, if the observant move, what will be seen is a portion of background which might not be a perfect match with the rest of the background (a shifted view of background). In addition, this method comes with some other theoretical impossibilities and fabrication challenges, such as the need to inhomogeneous and anisotropic distribution of ϵ and μ [164], the losses involved for extreme material constitutive parameters [165], bandwidth limitation due to the requirement to superluminal wave propagation [166, 167]. They also explain why most works that follow this cloaking mechanism are limited to solid and bulky materials highly dependent on the observer's location or the light incident angle. This static characteristic prevents the shield from performing well when the surface is dynamically deformed. Illusive Cloaking merges the concepts of complementary media and transformation optics to obtain transparency independent of the object's geometry [168-170]. Recently, an investigation has suggested that using fast-light media cloaks, also known as tachyonic cloaks, might be a better choice regarding bandwidth, independence to the incident angle, and phase challenges [171]. In addition, using quasi-conformal mapping techniques, also known as carpet cloaking, might result in more fabrication simplicity while lacking perfect invisibility [172-174]. Another technique that falls into the first category uses perfectly matched transmission line networks [175-178] to transmit the incident

signal with zero reflection and minimize phase disruptions [175]. It also enables having a broadband characteristic that does not require superluminal propagation [179]. The transmission-line-based cloak network must be fully embedded into/around the object, making the cloak bulky [180, 181]. Another challenge with this method is the transmission losses imposed in the optical region. This explains why this method has mainly been applied to microwave and millimeter-wave domains. Using metamaterials in microwave regions provides the possibility of fabricating and experimentally validating the cloaking performance [182]. As of today, while no proven experimental approach provides perfect transmission and ray reconstruction for all incident light angles, discovering new approaches to engineer and control electromagnetic waves has brought a new surge of hope to this field [66, 68].

7.2.2.2 Based on Perfect Absorption

The second dominant category for achieving invisibility/camouflage is scattering cancellation methods, where a preferably thin shell wraps the object to absorb/cancel out the dominant scattering components. Figure 7.2 illustrates this concept. When no visible light is scattered from an object, the object looks black, which could be a good goal for camouflage but not perfect invisibility. In microwave region, however, it means that there will be no reflection to be detected by a microwave sensor/Radar. Therefore, this method provides invisibility against radar detection (invisibility in microwave regime) while creating black visual effects for visible light. Also, the cancellation mechanisms might differ for the cases where the object size is not much larger than the operation wavelength (usually the case for radar detections) compared to the cases where target dimensions are much higher than the wavelength (the case for visual invisibility) [183-186]. Conventional absorbing-based cloaking methods that use metal fibers, carbon, and ceramic materials to provide perfect wave absorption are still reliable for absorption purposes [187]. Sensor cloaking [188-190], RCS reduction [191, 192], and mutual coupling cancellation are the other similar applications of this broad absorption-based cloaking methodology that highly incorporate metasurfaces [193, 194] and plasmonic metamaterials [195-200]. In [201], for instance, the possibility of scattering cancellation is analytically investigated when plasmonic metamaterials coat the spherical target with negative ϵ_r. It shows that there are some parametric conditions that result in negligible scattering cross section. Metasurfaces have been designed to provide such an effect in microwave frequencies [202, 203]. The idea of surface/mantle cloaking was another attempt, closely correlated with metasurfaces, to simplify the volumetric properties of metamaterials used for scattering cancellation [204]. Multilayered structures are designed to diminish dominant scattered modes where multiple scattering terms must be removed [205-207]. Since increasing the electrical length of objects dramatically increases the scattering modes, this approach may become complex for these specific sizes [205, 208].

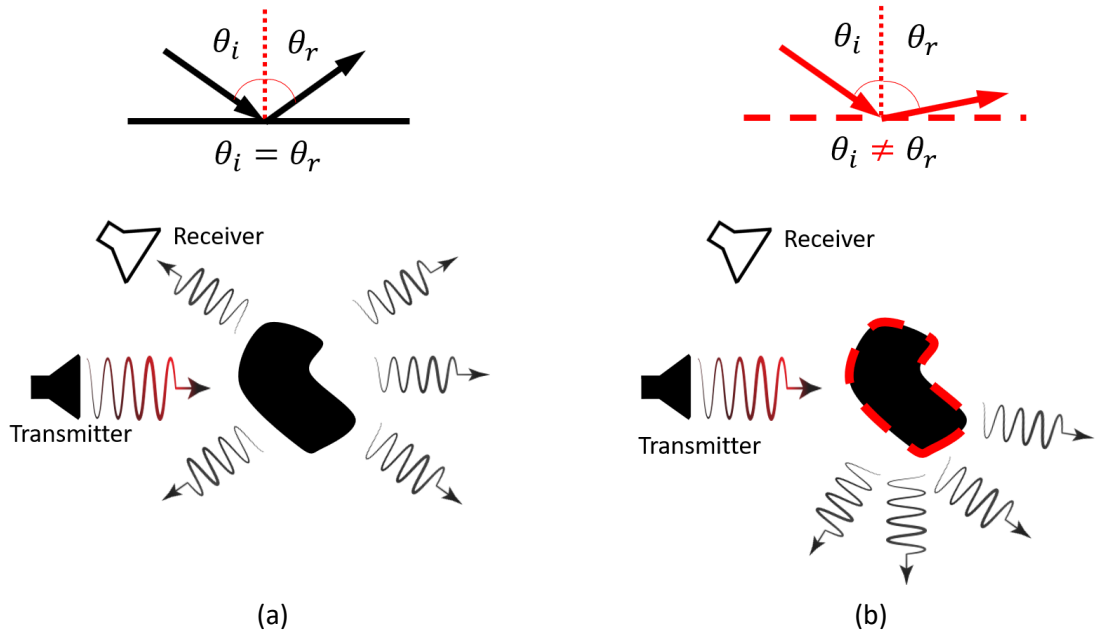

Figure 7.3. The general concept of Snel's Law Violation (abnormal reflections). (a) Scattering from an arbitrary object (b) abnormal scattering due to the presence of a metasurface

7.2.2.3 Based on Snel's Law Violation (abnormal reflections)

The third general methodology that can benefit camouflage (not perfect invisibility) is when the cloak violates generalized laws of reflection and refraction by creating an abrupt phase discontinuity on the order of wavelength [209, 210]. This passive method allows the designing of the desired light beam using an array of metallic metasurfaces [211]. The concept is shown in Figure 7.3. Physically speaking, if a dynamic cloak consists of several patches that reflect light beams, only part of them reach the observer's eyes, creating a certain level of confusion/ invisibility. For the static cases, the cloak boundary condition can be perfectly manipulated so that perfect invisibility happens. Augmented-reality technology is another highly correlated terminology with abnormal reflection methodology [212]. Retro-reflective materials are one product of this technology that can potentially create abnormal reflections.

7.2.2.4 Criticisms/ Discussion

Reviewing the abovementioned approaches, one can understand that applying cloaking techniques suitable for visual invisibility does not necessarily lead to the desired outcome for achieving invisibility in other applications and frequency ranges. This is because invisibility/cloaking has different meanings in different applications. For instance, while transformation optics can lead to visual invisibility, it cannot provide invisibility against radars in the microwave regimes realized by zero backward/forward scattering.

Second, it should be noted that realizing many of the abovementioned techniques, even in microwaves and millimeter-wave regions, is accompanied by technological limitations. For

instance, applying the theoretical achievements to a microscopic scale of the order of 40-70 nm ($\lambda_0/10$) is one of the challenges optical designers are dealing with. Therefore, another criticism about the methods and studies presented in optical frequencies is that they are limited to theoretical analysis without experimental verifications/ practical solutions.

Third, because of the electromagnetic nature of visible light, it is understandable that achieving invisibility in lower frequencies will be a great step for achieving similar results in the visible region. However, since objects' scattering characteristics differ with the object's electrical size, another severe criticism about the available works in the optical region is the requirement of electrically large objects. Thus, even the available numerical methods have to be limited due to computational burden (See [196, 199] for an example). Although many of the cloaking techniques in microwave frequencies are for Radar applications, the same criticism is valid for microwave cloaking techniques that provide a groundwork for optical regions. Therefore, the cloaking techniques in microwave frequencies cannot be applied to visible regions unless the electrical size of the examined object is large.

7.2.3 Reconfigurable/ intelligent Cloaking

7.2.3.1 Incorporating Active Metasurfaces

There are proven studies based upon "the uniqueness of the inverse-scattering problem for waves" that explain why *perfect* visual invisibility might not be physically achievable [213, 214]. In fact, none of the abovementioned passive approaches has provided perfect visual invisibility for all incident angles and polarizations within a nonzero bandwidth [150, 151, 215]. This explains why dynamic objects cannot be cloaked using passive approaches. As recently as 2016, an investigation unveiled the fundamental physical limitations and impossibilities of passive Cloaking [215], from which the interest in active Cloaking may be fueled. Considering the delicate wave engineering required to guide, divert, and in some cases, absorb the dynamic incidences, the unique features of active cloaking sound essential despite all the physical barriers for active Cloaking in optical regions. Reconfigurable and intelligent Cloaking are two closely related topics that are being experimentally investigated in microwave regime. Metasurfaces provide interesting features to be used for this purpose. The mechanism is usually based upon using variable capacitors (e.g., varactor diodes) controlled by a bias voltage to change the cloak's local boundary condition. Machine learning algorithms may be used to predict the required local boundary condition (and the associated parameters) for the specific desired response (transmission, absorption, or reflection) [216]. In other words, the cloak needs to be self-adaptive in order to be able to create dynamic boundary conditions for dynamic incidences. Therefore, different AI methodologies, such as classification, recognition, prediction, and optimization, can provide the required parameters for dynamic responses [217-220].

7.2.3.2 How can STM media help create an Invisibility Cloak?

As elaborated earlier, the mechanisms used for achieving invisibility against radars/ sensors differ from those used for visual invisibility. The former uses perfect absorption methods (scattering cancellation), while the latter deals with perfect transmission techniques (e.g., transformation optics). It was also noted that the most promising way to ensure a microwave regime technique can be applied to optical frequencies is to monitor its usefulness for electrically large objects. The key features of STM media can be leveraged for different cloaking methods, including perfect transmission, perfect absorption, and abnormal reflections. Diversion, up/down conversion, or absorption create different visual effects for optical applications and cloaking in other frequency ranges. Here, some physical insights will be provided for the reader.

The diversion and distribution features can be combined to create a curved wave path that guides the incident wave toward the desired direction. The distribution technique showed that it is possible to recombine the upconverted harmonics to reconstruct the main signal, which is an important goal in transformation optics.

The diversion feature could also be useful for Snell's law violation purposes (abnormal reflections). The implementation and realization seem to be simpler and independent from diode distribution. This is because there should not be a uniform distribution of capacitive effects for achieving random wave reflection. In addition, there will be no need for a sinusoidal pump wave as a random function will cause abnormal reflections. Visually, this will cause the object to blend into the background. From a radar perspective, this creates a stealth object that has the potential to be hidden from being detected.

The absorption and nonreciprocal features are great candidates for achieving scattering cancellation purposes. The incident wave could be effectively absorbed into the object in a microwave regime. While the reflection will be minimized, the transmitted data into the object (an aircraft, for example) can still be recovered and used. The unique feature of nonreciprocity does not allow the transmitted wave to escape from the cloaked object. The object behaves as a black hole!

Since the general usefulness of STM media still needs to be discovered, as a reasonable research methodology, focusing on microwave region cloaking enables us to set aside the technical difficulties in the optical region (where fabrication is of concern). This approach also helps identify which of the three introduced methodologies STM technology can play a role in. Working on electrically large structures can be considered the next step to generalize the conclusion into optical frequencies. Therefore, the next section will be dedicated to using STM media in one specific cloaking technique for RCS reduction.

7.3 RCS Reduction by STM Media

Radar cross-section (RCS) reduction, is a technique used to minimize the detectability of an object by reducing the amount of electromagnetic energy reflected in the radar. RCS reduction can increase the stealthiness of aircraft, ships, and other vehicles, making them less vulnerable to detection by enemy radars. Geometry shaping, using absorbing materials and plasma, and passive and active cancellations are well-known methods for this purpose, which involve using unique structures that manipulate the incident electromagnetic waves to reduce their scattering from the object [221].

Active RCS cancellation is an emerging research field with numerous applications in military and civilian domains. Active RCS cancellation removes the structure RCS and Antenna mode RCS [222]. Moreover, RCS reduction can also improve the accuracy and range of radar systems by reducing interference from background clutter.

This section will be dedicated to this topic and explore the possibility of using STM media. After a brief introduction to the underlying principles of the RCS concept, we will use FDTD simulations to show some of the advantages of STM coats for RCS reduction purposes. Additionally, we will discuss the potential scenarios and configurations that might lead to promising results in reducing object backward/forward scattering.

7.3.1 RCS Concept

Echoarea or radar cross section is a metric that quantifies the amount of energy scattered in a particular direction when an incoming wave illuminates a target. As described in [135], it is "the area intercepting the amount of power that, when scattered isotropically, produces at the receiver a density equal to the density scattered by the actual target." According to the IEEE Dictionary of Electrical and Electronics terms [223], RCS is defined as "a measure of reflective strength of a target defined as 4π times the ratio of the power per unit solid angle scattered in a specified direction to the power per unit area in a plane wave incident on the scatterer from a specified direction." To eliminate the impact of the distance between the target and the illumination source, RCS is normalized to the power density of the incident wave at the target location. This normalization eliminates the influence of the transmitter power level and distance on the RCS value as the illuminating wave attenuates due to inverse square spherical spreading. RCS describes the target's properties and is not influenced by the transmitter power, receiver sensitivity, or the distance between the transmitter and receiver. The following definitions calculate the two-dimensional RCS (scattering width) and three-dimensional RCS from scattered and incident electric fields.

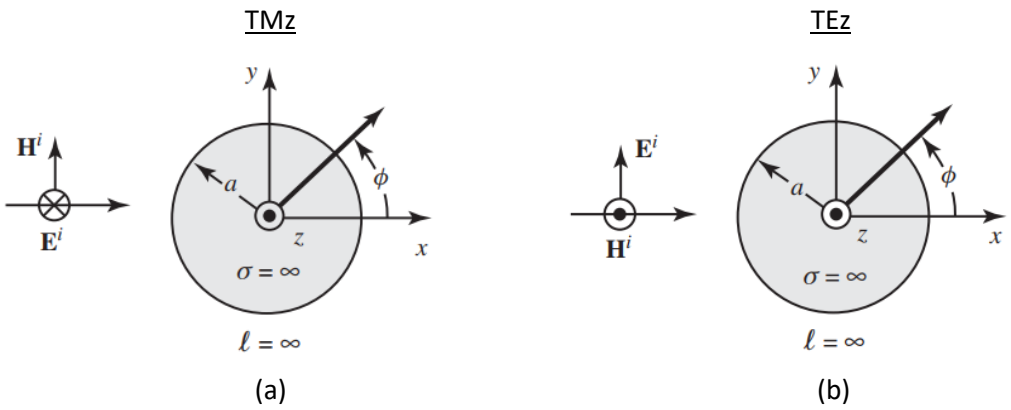

Figure 7.4. Plane wave incident on an infinite cylinder [135]. (a) TMz, (b) TEz.

$$\sigma_{3D}(RCS) = \begin{cases} \lim\limits_{r\to\infty}\left[4\pi r^2 \dfrac{P_s}{P_i}\right] \\ \lim\limits_{r\to\infty}\left[4\pi r^2 \dfrac{|E_s|^2}{|E_i|^2}\right] \end{cases} (sm) \tag{7.1}$$

$$\sigma_{2D}(Scattering\ Width) = \begin{cases} \lim\limits_{\rho\to\infty}\left[4\pi\rho \dfrac{P_s}{P_i}\right] \\ \lim\limits_{\rho\to\infty}\left[4\pi\rho \dfrac{|E_s|^2}{|E_i|^2}\right] \end{cases} (m) \tag{7.2}$$

Fundamentally, RCS is the ratio between the scattered and incident power densities multiplied by a factor with a square meter unit. Thus, the RCS unit (in the 3D case) is a square meter that implies the represented scattered area of the scatterer (not necessarily the physical size of the scatterer). Since the RCS value changes with the observation angle, three RCS types are of higher interest: monostatic or backscatter, forward scattering, and bistatic scattering/RCS.

RCS is also a function of transmitter polarization, receiver polarization, the angular orientation of the scatterer, scatterer geometry, material composition, and frequency. To address RCS dependency on polarization, the *scattering polarization matrix* needs to be used as follows:

$$E_s = \bar{S}E_i \tag{7.3}$$

which relates the incident (E_i) and scattered (E_s) electric fields. If we decompose the incident and scattered electric fields into two independent polarizations, e.g., 1 and 2, (7.3) yields

$$\begin{bmatrix} E_s^1 \\ E_s^2 \end{bmatrix} = \begin{bmatrix} S_{11} & S_{12} \\ S_{21} & S_{22} \end{bmatrix} \begin{bmatrix} E_i^1 \\ E_i^2 \end{bmatrix} \tag{7.4}$$

where the complex S_{ii} components can be found using the scattering relation of (7.1) as

$$S_{ii} = \frac{\sqrt{\sigma_{ii}}}{r\sqrt{4\pi}} \tag{7.5}$$

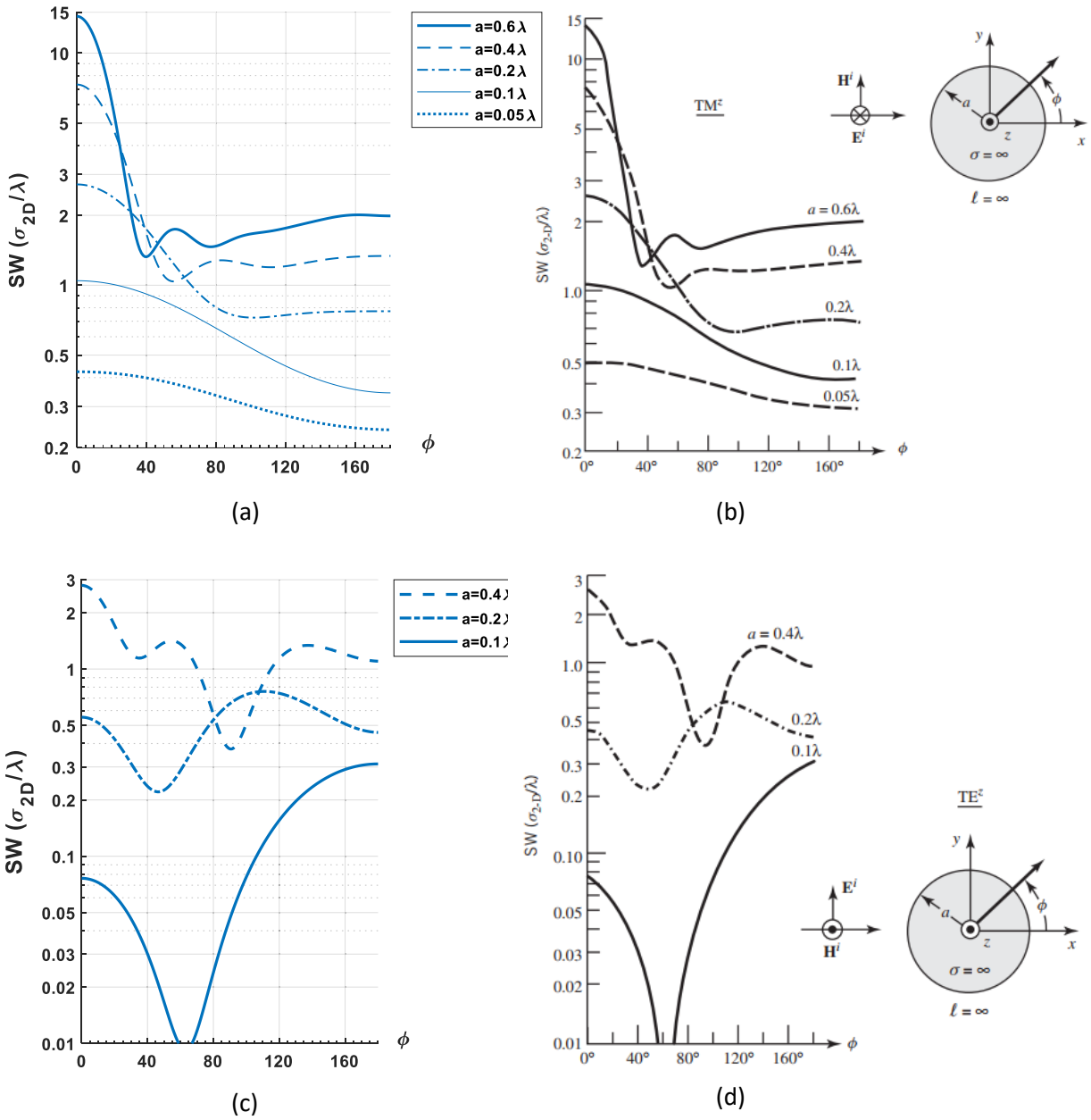

Figure 7.5. Bistatic scattering width (SW) of a circular cylinder. (a) FDTD TMz, (b) Theoretical TMz [77], (c) FDTD TEz, (d) Theoretical TEz [135]

Vertical/horizontal linear polarization, x/y linear polarization, co/cross-polar polarization, left-/right- hand circular polarization, θ/ϕ polarization are the two independent/orthogonal polarizations. For the vertical/horizontal polarization, (7.4) is written as

$$\begin{bmatrix} E_s^v \\ E_s^h \end{bmatrix} = \begin{bmatrix} S_{vv} & S_{vh} \\ S_{hv} & S_{hh} \end{bmatrix} \begin{bmatrix} E_v^1 \\ E_h^2 \end{bmatrix} \tag{7.6}$$

while circular polarization

$$\begin{bmatrix} E_s^{lc} \\ E_s^{rc} \end{bmatrix} = \begin{bmatrix} S_{lc,lc} & S_{lc,rc} \\ S_{rc,lc} & S_{rc,rc} \end{bmatrix} \begin{bmatrix} E_v^{lc} \\ E_h^{rc} \end{bmatrix} \tag{7.7}$$

Moreover, having only one scattering polarization matrix is sufficient to find the other types. For instance, the following relation transforms the v/h scattering polarization matrix to the lc/rc matrix.

$$\begin{bmatrix} E_s^{lc} \\ E_s^{rc} \end{bmatrix} = \frac{1}{2} \begin{bmatrix} 1 & -j \\ 1 & +j \end{bmatrix} \begin{bmatrix} S_{vv} & S_{vh} \\ S_{hv} & S_{hh} \end{bmatrix} \begin{bmatrix} 1 & 1 \\ -j & +j \end{bmatrix} \tag{7.8}$$

7.3.2 FDTD Validation for RCS Estimation

Before finding the effect of STM coats on a target's RCS, we need to be equipped with the necessary numerical tools for this purpose. In [145], all the required steps to find the RCS of a two- or three-dimensional object using the FDTD method have been provided. Therefore, we settle for a brief description of how FDTD estimates various types of RCS. For simplicity, we consider the two-dimensional case. Since RCS is a measure in large distances ($r \to \infty$), it is necessary to determine the radiation or scattered fields in a region distant from the antenna or scatterer (farfield region). In order to find the scattered power in the farfield zone, nearfield to farfield (NTFF) transformation techniques with surface equivalent theorem [224] are used. Therefore, first, an imaginary surface that surrounds the scatterer is chosen. The electric and magnetic fields inside the surface are used to determine the equivalent currents of $\vec{J}$ and $\vec{M}$ on the surface. Then, the auxiliary vector potentials of $\vec{A}$ and $\vec{F}$ are calculated to compute the radiated fields in farfield zone.

For validation, the scattering width of an infinite conducting cylinder will be investigated as shown in Figure 7.4. The 2D bistatic RCS when the cylinder is impinged by uniform TMz and TEz plane waves are calculated using FDTD. In [135], the scattering for the same problem was found theoretically using a modal technique. Figure 7.5 shows the FDTD and theoretical results for comparison where four radii of a =0.05λ ,0.1 λ, 0.2 λ, 0.4 λ, 0.6 λ are used. The FDTD results are highly accurate compared to the theoretical method in [135].

7.3.3 STM Coating

This section will conduct a similar test to find a metallic object's 2D bistatic RCS (scattering width) when different coating materials, including STM media, are used. The study helps identify the characteristics of STM coating for RCS reduction purposes. Assume an infinite conducting square that is illuminated by a uniform plane wave. The 2D problem is identical to a 3D problem where the scatterer is a rectangular prism extending to infinity along the z-axis. Figure 7.6 illustrates the configuration where the object is illuminated by a TMz uniform plane wave with and without STM coating.

The idea of STM coating for RCS reduction arises from Chapter 6's achievements, where STM media showed promising effects in reducing the secondary reflections from surfaces. The

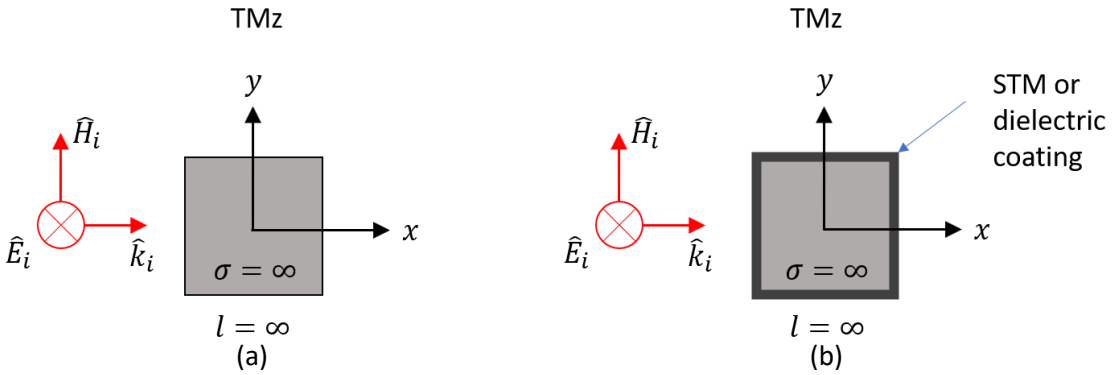

Figure 7.6. TMz plane wave incident on an infinite rectangular prism. (a) without coating, (b) with coating.

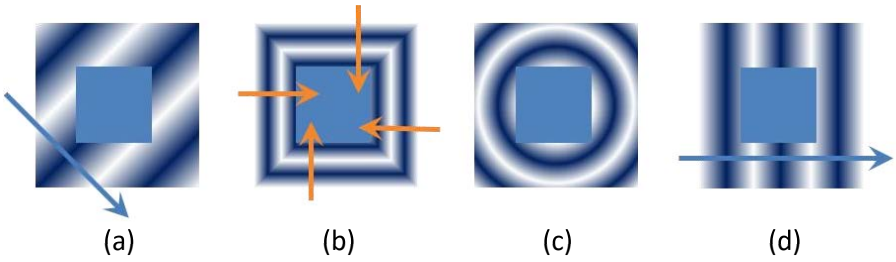

Figure 7.7. An infinite rectangular prism covered by a layer of STM coating with different disturbance distributions.

mechanism and design procedure behind RCS reduction using STM media are the same mechanisms used for green shielding purposes (Minimum reflection, transmission attenuation of the undesired harmonic, and the amplification of the desired harmonic). The reflection reduction capability may absorb the electromagnetic waves scattered from an object. Then, the media is optimized to attenuate the main harmonic. The amplification of the desired harmonic depends highly on the designer and their goals. The minimization of the main harmonic reflections does not guarantee the scattering removal. If the STM media is designed to transfer the energy to other harmonics, transmitting these harmonics through the coating layer might cause reflections from the conducting object. These secondary reflections may be minimized by choosing a proper pump direction, as shown in Figure 7.7 and a proper medium conductivity. This implies that the object will not show any reflective effects, which will cause RCS to drop.

STM coating can be applied in different configurations, each providing a specific response that can be analyzed separately. Figure 7.7 illustrates the possible configurations that include a variety of pump wave directions (disturbance distribution). The modulation parameters and STM medium thickness are the other factors that can be considered in a design procedure for

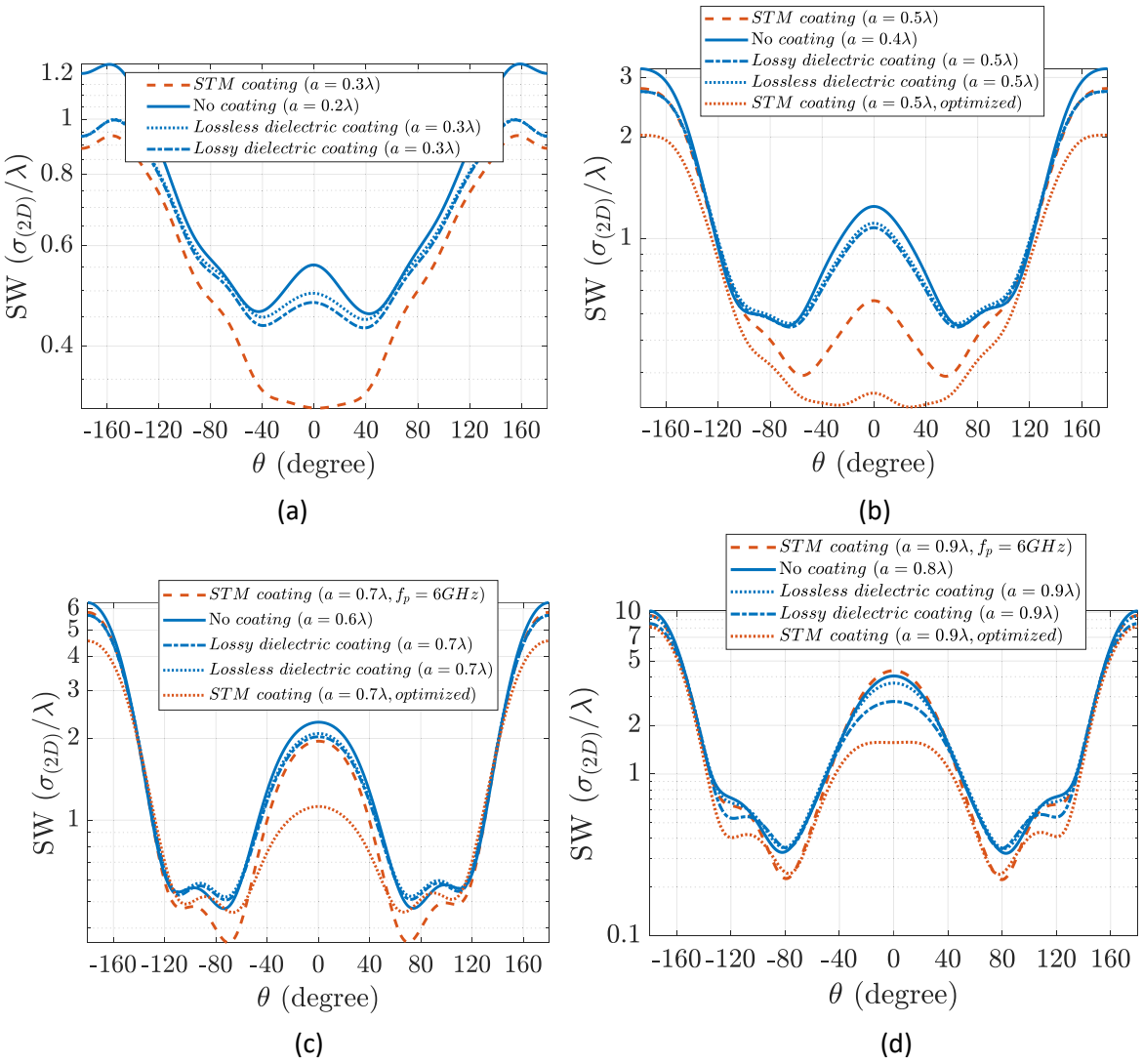

Figure 7.8. Bistatic scattering width (SW) of an infinite rectangular prism (TMz) for different side lengths (denoted by a) and various coatings. (a) $a = 0.2\lambda$, (b) $a = 0.4\lambda$, (c) $a = 0.6\lambda$, (d) $a = 0.8\lambda$.

achieving a specific response. This section uses the configuration of Figure 7.7 (d) with the permittivity and conductivity ranges specified in Chapter 6 for green shielding purposes. A similar design procedure minimizes both the transmission and reflection, leading to increased absorption.

In Figure 7.8, the computed bistatic scattering widths are compared when the object is coated by a 0.1λ thickness of the lossless dielectric, lossy dielectric, and STM media. The procedure is repeated for several side lengths of the 2D cube. It is observed that STM media was able to reduce the bistatic RCS, specifically the forward scattering. The smaller the object is, the more forward scatter reduction is observed compared to the other coatings. The modulation parameters were optimized using the same green shielding design procedure introduced in Chapter 6 (Figure. 6.6). The unoptimized STM may cause even higher forward

scattering when the object is electrically large. This observation is seen in Figure 7.8 (d), where the unoptimized STM coating causes a slightly higher forward scatter value.

This test reveals that STM media can be further investigated for similar purposes of RCS reduction, Cloaking, and shielding. The coating response to TEz mode illumination could be left as a task for those interested in this topic for future research. Changing the direction of the applied pump wave might be a crucial factor in RCS reduction as it impacts the direction of the signal wave. This might be an interesting topic for future investigation. Active Cloaking using the space-time modulation concept might provide much more distinctive advantages. However, how this traveling capacitive effect can be applied to a slab is a fabrication challenge that can also be studied shortly.

References

[1] S. Geetha, K. Satheesh Kumar, C. R. Rao, M. Vijayan, and D. Trivedi, "EMI shielding: Methods and materials—A review," *Journal of Applied Polymer Science,* vol. 112, no. 4, pp. 2073-2086, 2009.

[2] A. Kausar, I. Rafique, and B. Muhammad, "Electromagnetic interference shielding of polymer/nanodiamond, polymer/carbon nanotube, and polymer/nanodiamond–carbon nanotube nanobifiller composite: a review," *Polymer-Plastics Technology and Engineering,* vol. 56, no. 4, pp. 347-363, 2017.

[3] T. Zaremba, A. R. Jakobsen, M. Søgaard, A. M. Thøgersen, and S. Riahi, "Radiotherapy in patients with pacemakers and implantable cardioverter defibrillators: a literature review," *Europace,* vol. 18, no. 4, pp. 479-491, 2016.

[4] A. Li, S. Singh, and D. Sievenpiper, "Metasurfaces and their applications," *Nanophotonics,* vol. 7, no. 6, pp. 989-1011, 2018.

[5] A. Darvish, and A. A. Kishk, "Near-field shielding analysis of single-sided flexible metasurface stopband TE: Comparative approach," *IEEE Transactions on Antennas and Propagation,* vol. 69, no. 1, pp. 239-253, 2020.

[6] A. Darvish, and A. A. Kishk, "X-Band Nearfield Shielding Metasurface With Adjustable Reflection/Transmission Zeroes," *IEEE Transactions on Electromagnetic Compatibility*, 2022.

[7] M. Nauman, R. Saleem, A. K. Rashid, and M. F. Shafique, "A miniaturized flexible frequency selective surface for X-band applications," *IEEE Transactions on Electromagnetic Compatibility,* vol. 58, no. 2, pp. 419-428, 2016.

[8] T. S. Kumar, and K. Vinoy, "A Miniaturized Angularly Stable FSS for Shielding GSM 0.9, 1.8, and Wi-Fi 2.4 GHz Bands," *IEEE Transactions on Electromagnetic Compatibility,* vol. 63, no. 5, pp. 1605-1608, 2021.

[9] X.-X. Wang, J.-C. Shu, W.-Q. Cao, M. Zhang, J. Yuan, and M.-S. Cao, "Eco-mimetic nanoarchitecture for green EMI shielding," *Chemical Engineering Journal,* vol. 369, pp. 1068-1077, 2019.

[10] D.-Q. Zhang, T.-T. Liu, J.-C. Shu, S. Liang, X.-X. Wang, J.-Y. Cheng, H. Wang, and M.-S. Cao, "Self-assembly construction of WS2–rGO architecture with green EMI shielding," *ACS Applied Materials & Interfaces,* vol. 11, no. 30, pp. 26807-26816, 2019.

[11] A. Darvish, and A. A. Kishk, "Space-Time Modulation in Lossy Dispersive Media and the Implications for Amplification and Shielding," *IEEE Transactions on Microwave Theory and Techniques*, 2022.

[12] W. Yin, H. Zhang, T. Zhong, and X. Min, "A novel compact dual-band frequency selective surface for GSM shielding by utilizing a 2.5-dimensional structure," *IEEE Transactions on Electromagnetic Compatibility,* vol. 60, no. 6, pp. 2057-2060, 2018.

[13] U. Rafique, S. A. Ali, M. T. Afzal, and M. Abdin, "Bandstop filter design for GSM shielding using frequency selective surfaces," *International Journal of Electrical and Computer Engineering,* vol. 2, no. 6, pp. 846, 2012.

[14] A. A. Dewani, S. G. O'Keefe, D. V. Thiel, and A. Galehdar, "Window RF shielding film using printed FSS," *IEEE Transactions on Antennas and Propagation,* vol. 66, no. 2, pp. 790-796, 2017.

[15] S. Ünaldı, S. Cimen, G. Çakır, and U. E. Ayten, "A novel dual-band ultrathin FSS with closely settled frequency response," *IEEE Antennas and Wireless Propagation Letters,* vol. 16, pp. 1381-1384, 2016.

[16] M. Safari, C. Shafai, and L. Shafai, "X-band tunable frequency selective surface using MEMS capacitive loads," *IEEE Transactions on Antennas and Propagation,* vol. 63, no. 3, pp. 1014-1021, 2014.

[17] X. Jia, Y. Li, B. Shen, and W. Zheng, "Evaluation, fabrication and dynamic performance regulation of green EMI-shielding materials with low reflectivity: A review," *Composites Part B: Engineering*, pp. 109652, 2022.

[18] C. R. Paul, *Introduction to Electromagnetic Compatibility*: Wiley, 2006.

[19] E. Degrave, B. Meeusen, A. R. Grivegnée, M. Boniol, and P. Autier, “Causes of death among Belgian professional military radar operators: A 37-year retrospective cohort study,” *International Journal of Cancer,* vol. 124, no. 4, pp. 945-951, 2009.

[20] V. Garaj-Vrhovac, G. Gajski, S. Pažanin, A. Šarolić, A.-M. Domijan, D. Flajs, and M. Peraica, “Assessment of cytogenetic damage and oxidative stress in personnel occupationally exposed to the pulsed microwave radiation of marine radar equipment,” *International Journal of Hygiene Environmental Health,* vol. 214, no. 1, pp. 59-65, 2011.

[21] R. Paulraj, and J. Behari, “Biochemical changes in rat brain exposed to low intensity 9.9 GHz microwave radiation,” *Cell biochemistry biophysics,* vol. 63, no. 1, pp. 97-102, 2012.

[22] O. J. Møllerløkken, and B. E. Moen, “Is fertility reduced among men exposed to radiofrequency fields in the Norwegian Navy?,” *Bioelectromagnetics: Journal of the Bioelectromagnetics Society, The Society for Physical Regulation in Biology and Medicine, The European Bioelectromagnetics Association,* vol. 29, no. 5, pp. 345-352, 2008.

[23] V. Garaj-Vrhovac, and V. Oreščanin, “Assessment of DNA sensitivity in peripheral blood leukocytes after occupational exposure to microwave radiation: the alkaline comet assay and chromatid breakage assay,” *Cell Biology and Toxicology,* vol. 25, pp. 33-43, 2009.

[24] O. Johansson, “Disturbance of the immune system by electromagnetic fields—A potentially underlying cause for cellular damage and tissue repair reduction which could lead to disease and impairment,” *Pathophysiology,* vol. 16, no. 2-3, pp. 157-177, 2009.

[25] C. Zhang, Y. Zhang, Z. Li, and Y. Gao, “Effects of fetal microwave radiation exposure on offspring behavior in mice,” *Journal of Radiation Research,* vol. 56, no. 2, pp. 261-268, 2014.

[26] G. Pandey, H. Singh, P. Bharti, A. Pandey, and M. Meshram, “High gain Vivaldi antenna for radar and microwave imaging applications,” *International Journal of Signal Processing Systems,* vol. 3, no. 1, pp. 35-39, 2015.

[27] A. Sharma, K. K. Kesari, V. K. Saxena, and R. Sisodia, “Ten gigahertz microwave radiation impairs spatial memory, enzymes activity, and histopathology of developing mice brain,” *Molecular and Cellular Biochemistry,* vol. 435, pp. 1-13, 2017.

[28] S. Verma, G. K. Keshri, M. Sharma, K. V. Mani, S. Karmakar, S. Chauhan, and A. Gupta, "X-Band Microwave Radiation Induced Biological Effects in Rats Skin: Plausible Role of Heat Shock Proteins." pp. 175-177.

[29] M. H. Al-Saleh, and U. Sundararaj, “X-band EMI shielding mechanisms and shielding effectiveness of high structure carbon black/polypropylene composites,” *Journal of Physics D: Applied Physics,* vol. 46, no. 3, pp. 035304, 2012.

[30] S. Dhawan, N. Singh, and S. Venkatachalam, “Shielding behaviour of conducting polymer-coated fabrics in X-band, W-band and radio frequency range,” *Synthetic Metals,* vol. 129, no. 3, pp. 261-267, 2002.

[31] M. Han, X. Yin, H. Wu, Z. Hou, C. Song, X. Li, L. Zhang, and L. Cheng, “Ti3C2 MXenes with modified surface for high-performance electromagnetic absorption and shielding in the X-band,” *ACS Applied Materials & Interfaces,* vol. 8, no. 32, pp. 21011-21019, 2016.

[32] Z. Wang, R. Wei, and X. Liu, “Fluffy and ordered graphene multilayer films with improved electromagnetic interference shielding over X-band,” *ACS Applied Materials & Interfaces,* vol. 9, no. 27, pp. 22408-22419, 2017.

[33] K. C. B. Naidu, and W. Madhuri, “Microwave processed bulk and nano NiMg ferrites: a comparative study on X-band electromagnetic interference shielding properties,” *Materials Chemistry and Physics,* vol. 187, pp. 164-176, 2017.

[34] K. Jagatheesan, A. Ramasamy, A. Das, and A. Basu, “Electromagnetic shielding behaviour of conductive filler composites and conductive fabrics–a review,” 2014.

[35] D. Jiang, V. Murugadoss, Y. Wang, J. Lin, T. Ding, Z. Wang, Q. Shao, C. Wang, H. Liu, and N. Lu, “Electromagnetic interference shielding polymers and nanocomposites-a review,” *Polymer Reviews,* vol. 59, no. 2, pp. 280-337, 2019.

[36] S. Maity, and A. Chatterjee, "Conductive polymer-based electro-conductive textile composites for electromagnetic interference shielding: A review," *Journal of Industrial Textiles,* vol. 47, no. 8, pp. 2228-2252, 2018.

[37] A. K. Singh, A. Shishkin, T. Koppel, and N. Gupta, "A review of porous lightweight composite materials for electromagnetic interference shielding," *Composites Part B: Engineering,* vol. 149, pp. 188-197, 2018.

[38] Z. Jia, M. Zhang, B. Liu, F. Wang, G. Wei, and Z. Su, "Graphene Foams for Electromagnetic Interference Shielding: A Review," *ACS Applied Nano Materials,* vol. 3, no. 7, pp. 6140-6155, 2020.

[39] A. Iqbal, P. Sambyal, and C. M. Koo, "2D MXenes for electromagnetic shielding: a review," *Advanced Functional Materials,* vol. 30, no. 47, pp. 2000883, 2020.

[40] R. Kumar, S. Sahoo, E. Joanni, R. K. Singh, W. K. Tan, K. K. Kar, and A. Matsuda, "Recent progress on carbon-based composite materials for microwave electromagnetic interference shielding," *Carbon,* vol. 177, pp. 304-331, 2021.

[41] M. Wang, X.-H. Tang, J.-H. Cai, H. Wu, J.-B. Shen, and S.-Y. Guo, "Construction, mechanism and prospective of conductive polymer composites with multiple interfaces for electromagnetic interference shielding: a review," *Carbon,* vol. 177, pp. 377-402, 2021.

[42] P. Song, B. Liu, H. Qiu, X. Shi, D. Cao, and J. Gu, "MXenes for polymer matrix electromagnetic interference shielding composites: A review," *Composites Communications,* vol. 24, pp. 100653, 2021.

[43] N. Wu, Q. Hu, R. Wei, X. Mai, N. Naik, D. Pan, Z. Guo, and Z. Shi, "Review on the electromagnetic interference shielding properties of carbon based materials and their novel composites: Recent progress, challenges and prospects," *Carbon,* vol. 176, pp. 88-105, 2021.

[44] H. Guo, Y. Chen, Y. Li, W. Zhou, W. Xu, L. Pang, X. Fan, and S. Jiang, "Electrospun fibrous materials and their applications for electromagnetic interference shielding: A review," *Composites Part A: Applied Science and Manufacturing,* vol. 143, pp. 106309, 2021.

[45] Y. Yang, H. Zhou, X.-H. Wang, and Y. Mi, "Low-pass frequency selective surface with wideband high-stop response for shipboard radar," *Journal of Electromagnetic Waves and Applications,* vol. 27, no. 1, pp. 117-122, 2013.

[46] K. Sarabandi, and N. Behdad, "A frequency selective surface with miniaturized elements," *IEEE Transactions on Antennas and Propagation,* vol. 55, no. 5, pp. 1239-1245, 2007.

[47] N. Behdad, "A second-order band-pass frequency selective surface using nonresonant subwavelength periodic structures," *Microwave and Optical Technology Letters,* vol. 50, no. 6, pp. 1639-1643, 2008.

[48] T.-K. Wu, "Four-band frequency selective surface with double-square-loop patch elements," *IEEE Transactions on Antennas and Propagation,* vol. 42, no. 12, pp. 1659-1663, 1994.

[49] S. Ghosh, and S. Lim, "Fluidically reconfigurable multifunctional frequency-selective surface with miniaturization characteristic," *IEEE Transactions on Microwave Theory and Techniques,* vol. 66, no. 8, pp. 3857-3865, 2018.

[50] T.-K. Wu, and S.-W. Lee, "Multiband frequency selective surface with multiring patch elements," *IEEE Transactions on Antennas and Propagation,* vol. 42, no. 11, pp. 1484-1490, 1994.

[51] E. F. Sundarsingh, and V. S. Ramalingam, "Mechanically reconfigurable frequency selective surface for RF shielding in indoor wireless environment," *IEEE Transactions on Electromagnetic Compatibility,* vol. 62, no. 6, pp. 2643-2646, 2020.

[52] R. Sivasamy, L. Murugasamy, M. Kanagasabai, E. F. Sundarsingh, and M. G. N. Alsath, "A low-profile paper substrate-based dual-band FSS for GSM shielding," *IEEE Transactions on Electromagnetic Compatibility,* vol. 58, no. 2, pp. 611-614, 2016.

[53] I. S. Syed, Y. Ranga, L. Matekovits, K. P. Esselle, and S. G. Hay, "A single-layer frequency-selective surface for ultrawideband electromagnetic shielding," *IEEE Transactions on Electromagnetic Compatibility,* vol. 56, no. 6, pp. 1404-1411, 2014.

[54] R. Sivasamy, B. Moorthy, M. Kanagasabai, V. R. Samsingh, and M. G. N. Alsath, "A wideband frequency tunable FSS for electromagnetic shielding applications," *IEEE Transactions on Electromagnetic Compatibility,* vol. 60, no. 1, pp. 280-283, 2017.

[55] A. Zhang, and R. Yang, "Anomalous birefringence through metasurface-based cavities with linear-to-circular polarization conversion," *Physical Review B,* vol. 100, no. 24, pp. 245421, 2019.

[56] M. Mantash, A. Kesavan, T. A. J. I. A. Denidni, and W. P. Letters, "Beam-tilting endfire antenna using a single-layer FSS for 5G communication networks," *IEEE Antennas and Wireless Propagation Letters*, vol. 17, no. 1, pp. 29-33, 2017.

[57] F. Bayatpur, and K. Sarabandi, "Multipole spatial filters using metamaterial-based miniaturized-element frequency-selective surfaces," *IEEE Transactions on Microwave Theory and Techniques,* vol. 56, no. 12, pp. 2742-2747, 2008.

[58] C.-N. Chiu, C.-H. Kuo, and M.-S. Lin, "Bandpass shielding enclosure design using multipole-slot arrays for modern portable digital devices," *IEEE Transactions on Electromagnetic Compatibility,* vol. 50, no. 4, pp. 895-904, 2008.

[59] S. Hashemi, and A. Abdolali, "Room shielding with frequency-selective surfaces for electromagnetic health application," *International Journal of Microwave and Wireless Technologies,* vol. 9, no. 2, pp. 291, 2017.

[60] S. Ghosh, and K. V. Srivastava, "Broadband polarization-insensitive tunable frequency selective surface for wideband shielding," *IEEE Transactions on Electromagnetic Compatibility,* vol. 60, no. 1, pp. 166-172, 2017.

[61] D. Li, T.-W. Li, E.-P. Li, and Y.-J. Zhang, "A 2.5-D angularly stable frequency selective surface using via-based structure for 5G EMI shielding," *IEEE Transactions on Electromagnetic Compatibility,* vol. 60, no. 3, pp. 768-775, 2018.

[62] S. Yang, P. Liu, M. Yang, Q. Wang, J. Song, and L. Dong, "From flexible and stretchable meta-atom to metamaterial: A wearable microwave meta-skin with tunable frequency selective and cloaking effects," *Scientific Reports,* vol. 6, pp. 21921, 2016.

[63] P. Gurrala, S. Oren, P. Liu, J. Song, and L. Dong, "Fully conformal square-patch frequency-selective surface toward wearable electromagnetic shielding," *IEEE Antennas and Wireless Propagation Letters,* vol. 16, pp. 2602-2605, 2017.

[64] M. Bilal, R. Saleem, Q. H. Abbasi, B. Kasi, and M. F. Shafique, "Miniaturized and flexible FSS-based EM shields for conformal applications," *IEEE Transactions on Electromagnetic Compatibility,* vol. 62, no. 5, pp. 1703-1710, 2020.

[65] S. Taravati, "Self-biased broadband magnet-free linear isolator based on one-way space-time coherency," *Physical Review B,* vol. 96, no. 23, pp. 235150, 2017.

[66] S. Taravati, and A. A. Kishk, "Advanced wave engineering via obliquely illuminated space-time-modulated slab," *IEEE Transactions on Antennas and Propagation,* vol. 67, no. 1, pp. 270-281, 2018.

[67] T. W. Ebbesen, H. J. Lezec, H. Ghaemi, T. Thio, and P. A. Wolff, "Extraordinary optical transmission through sub-wavelength hole arrays," *Nature,* vol. 391, no. 6668, pp. 667-669, 1998.

[68] J. B. Pendry, D. Schurig, and D. R. Smith, "Controlling electromagnetic fields," *Science,* vol. 312, no. 5781, pp. 1780-1782, 2006.

[69] P. Celli, and S. Gonella, "Low-frequency spatial wave manipulation via phononic crystals with relaxed cell symmetry," *Journal of Applied Physics,* vol. 115, no. 10, pp. 103502, 2014.

[70] M. M. Salary, S. Jafar-Zanjani, and H. Mosallaei, "Electrically tunable harmonics in time-modulated metasurfaces for wavefront engineering," *New Journal of Physics,* vol. 20, no. 12, pp. 123023, 2018.

[71] S. Taravati, and C. Caloz, "Mixer-duplexer-antenna leaky-wave system based on periodic space-time modulation," *IEEE Transactions on Antennas and Propagation,* vol. 65, no. 2, pp. 442-452, 2016.

[72] S. Taravati, and A. A. Kishk, "Space-Time Modulation: Principles and Applications," *IEEE Microwave Magazine,* vol. 21, no. 4, pp. 30-56, 2020.

[73] S. Taravati, and A. A. Kishk, "Dynamic modulation yields one-way beam splitting," *Physical Review B,* vol. 99, no. 7, pp. 075101, 2019.

[74] S. Taravati, "Giant linear nonreciprocity, zero reflection, and zero band gap in equilibrated space-time-varying media," *Physical Review Applied,* vol. 9, no. 6, pp. 064012, 2018.

[75] N. A. Estep, D. L. Sounas, J. Soric, and A. Alù, "Magnetic-free non-reciprocity and isolation based on parametrically modulated coupled-resonator loops," *Nature Physics,* vol. 10, no. 12, pp. 923-927, 2014.

[76] J. R. Reyes-Ayona, and P. Halevi, "Electromagnetic wave propagation in an externally modulated low-pass transmission line," *IEEE Transactions on Microwave Theory and Techniques,* vol. 64, no. 11, pp. 3449-3459, 2016.

[77] M. B. Zanjani, A. R. Davoyan, A. M. Mahmoud, N. Engheta, and J. R. Lukes, "One-way phonon isolation in acoustic waveguides," *Applied Physics Letters,* vol. 104, no. 8, pp. 081905, 2014.

[78] C. Shen, X. Zhu, J. Li, and S. A. Cummer, "Nonreciprocal acoustic transmission in space-time modulated coupled resonators," *Physical Review B,* vol. 100, no. 5, pp. 054302, 2019.

[79] X. Zhu, J. Li, C. Shen, G. Zhang, S. A. Cummer, and L. Li, "Tunable unidirectional compact acoustic amplifier via space-time modulated membranes," *Physical Review B,* vol. 102, no. 2, pp. 024309, 2020.

[80] S. Taravati, N. Chamanara, and C. Caloz, "Nonreciprocal electromagnetic scattering from a periodically space-time modulated slab and application to a quasisonic isolator," *Physical Review B,* vol. 96, no. 16, pp. 165144, 2017.

[81] N. Chamanara, S. Taravati, Z.-L. Deck-Léger, and C. Caloz, "Optical isolation based on space-time engineered asymmetric photonic band gaps," *Physical Review B,* vol. 96, no. 15, pp. 155409, 2017.

[82] Z. Wu, and A. Grbic, "A transparent, time-modulated metasurface." *2018 12th International Congress on Artificial Materials for Novel Wave Phenomena (Metamaterials).* IEEE, pp. 439-441.

[83] S. Taravati, "Aperiodic space-time modulation for pure frequency mixing," *Physical Review B,* vol. 97, no. 11, pp. 115131, 2018.

[84] S. Qin, Q. Xu, and Y. E. Wang, "Nonreciprocal components with distributedly modulated capacitors," *IEEE Transactions on Microwave Theory and Techniques,* vol. 62, no. 10, pp. 2260-2272, 2014.

[85] L. Hasselgren, and J. Luomi, "Geometrical aspects of magnetic shielding at extremely low frequencies," *IEEE Transactions on Electromagnetic Compatibility,* vol. 37, no. 3, pp. 409-420, 1995.

[86] P. R. Bannister, "Further notes for predicting shielding effectiveness for the plane shield case," *IEEE Transactions on Electromagnetic Compatibility*, no. 2, pp. 50-53, 1969.

[87] P. R. Bannister, "New theoretical expressions for predicting shielding effectiveness for the plane shield case," *IEEE Transactions on Electromagnetic Compatibility*, no. 1, pp. 2-7, 1968.

[88] R. G. Olsen, M. Istenic, and P. Zunko, "On simple methods for calculating ELF shielding of infinite planar shields," *IEEE Transactions on Electromagnetic Compatibility,* vol. 45, no. 3, pp. 538-547, 2003.

[89] M. H. Oktem, and B. Saka, "Design of multilayered cylindrical shields using a genetic algorithm," *IEEE Transactions on Electromagnetic Compatibility,* vol. 43, no. 2, pp. 170-176, 2001.

[90] O. J. Møllerløkken, B. E. Moen, The Society for Physical Regulation in Biology, and T. E. B. A. Medicine, "Is fertility reduced among men exposed to radiofrequency fields in the Norwegian Navy?," *Bioelectromagnetics: Journal of the Bioelectromagnetics Society, The Society for Physical Regulation in Biology and Medicine, The European Bioelectromagnetics Association,* vol. 29, no. 5, pp. 345-352, 2008.

[91] V. Garaj-Vrhovac, V. J. Oreščanin, and toxicology, "Assessment of DNA sensitivity in peripheral blood leukocytes after occupational exposure to microwave radiation: the alkaline comet assay and chromatid breakage assay," *Cell Biology and Toxicology,* vol. 25, no. 1, pp. 33-43, 2009.

[92] E. Degrave, B. Meeusen, A. R. Grivegnée, M. Boniol, and P. J. Autier, "Causes of death among Belgian professional military radar operators: A 37-year retrospective cohort study," *International Journal of Cancer*, vol. 124, no. 4, pp. 945-951, 2009.

[93] O. Johansson, "Disturbance of the immune system by electromagnetic fields—A potentially underlying cause for cellular damage and tissue repair reduction which could lead to disease and impairment," *Pathophysiology,* vol. 16, no. 2-3, pp. 157-177, 2009.

[94] V. Garaj-Vrhovac, G. Gajski, S. Pažanin, A. Šarolić, A.-M. Domijan, D. Flajs, M. Peraica, and E. Health, "Assessment of cytogenetic damage and oxidative stress in personnel occupationally exposed to the pulsed microwave radiation of marine radar equipment," *International Journal of Hygiene and Environmental Health*, vol. 214, no. 1, pp. 59-65, 2011.

[95] R. Paulraj, J. Behari, and Biophysics, "Biochemical Changes in Rat Brain Exposed to Low Intensity 9.9 GHz Microwave Radiation," *Cell Biochemistry and Biophysics,* vol. 63, no. 1, pp. 97-102, May 01, 2012.

[96] S. Singh, K. V. Mani, and N. Kapoor, "Effect of occupational EMF exposure from radar at two different frequency bands on plasma melatonin and serotonin levels," *International Journal of Radiation Biology*, vol. 91, no. 5, pp. 426-434, 2015.

[97] A. Sharma, K. K. Kesari, V. K. Saxena, R. J. Sisodia, and C. Biochemistry, "Ten gigahertz microwave radiation impairs spatial memory, enzymes activity, and histopathology of developing mice brain," *Molecular and Cellular Biochemistry,* vol. 435, no. 1, pp. 1-13, November 01, 2017.

[98] R. Langley, and A. Drinkwater, "Improved empirical model for the Jerusalem cross." *IEE Proceedings H (Microwaves, Optics and Antennas),* vol. 129, no. 1, pp. 1-6, 1982.

[99] A. E. Yilmaz, and M. J. Kuzuoglu, "Design of the Square Loop Frequency Selective Surfaces with Particle Swarm Optimization via the Equivalent Circuit Model," *Radioengineering,* vol. 18, no. 2, 2009.

[100] E. A. Parker, "Convoluted array elements and reduced size unit cells for frequency-selective surfaces." *IEE Proceedings H-Microwaves, Antennas and Propagation*. vol. 138. no. 1. IET, 1991.

[101] M. Haghzadeh, and A. Akyurtlu, "All-printed, flexible, reconfigurable frequency selective surfaces," *Journal of Applied Physics,* vol. 120, no. 18, pp. 184901, 2016.

[102] B. Monacelli, J. B. Pryor, B. A. Munk, D. Kotter, G. Boreman, and Propagation, "Infrared frequency selective surface based on circuit-analog square loop design," *IEEE Transactions on Antennas and Propagation,* vol. 53, no. 2, pp. 745-752, 2005.

[103] F. Costa, A. Monorchio, G. Manara, and P. Magazine, "Efficient analysis of frequency-selective surfaces by a simple equivalent-circuit model," *IEEE Antennas and Propagation Magazine,* vol. 54, no. 4, pp. 35-48, 2012.

[104] F. Bilotti, A. Toscano, and L. Vegni, "Design of spiral and multiple split-ring resonators for the realization of miniaturized metamaterial samples," *IEEE Transactions on Antennas and Propagation,* vol. 55, no. 8, pp. 2258-2267, 2007.

[105] Q. Chen, D. Sang, M. Guo, and Y. Fu, "Miniaturized frequency-selective rasorber with a wide transmission band using circular spiral resonator," *IEEE Transactions on Antennas and Propagation,* vol. 67, no. 2, pp. 1045-1052, 2018.

[106] A. Darvish, and A. A. Kishk, "Novel Miniaturized Wearable Frequency Selective Surface Design for Stable Nearfield Band-stop Characterization." *2020 IEEE USNC-CNC-URSI North American Radio Science Meeting (Joint with AP-S Symposium)*, pp. 179-180. IEEE, 2020.

[107] F. Costa, A. Monorchio, and G. Manara, "An overview of equivalent circuit modeling techniques of frequency selective surfaces and metasurfaces," *Appl. Comput. Electromagn. Soc. J.,* vol. 29, no. 12, pp. 960-976, 2014.

[108] E. Fields, R. F. Cleveland, and J. L. Ulcek, "Questions and answers about biological effects and potential hazards of radiofrequency electromagnetic fields." *Standards Development Branch, Allocations and Standards Division, Office of Engineering and Technology, Federal Communications Commission*, 1999.

[109] C. A. Balanis, *Antenna theory: analysis and design*: John Wiley & Sons, 2016.

[110] K. Lu, "An efficient method for analysis of arbitrary nonuniform transmission lines," *IEEE Transactions on Microwave Theory and Techniques,* vol. 45, no. 1, pp. 9-14, 1997.

[111] M. H. Eghlidi, K. Mehrany, and B. Rashidian, "Analytical approach for analysis of nonuniform lossy/lossless transmission lines and tapered microstrips," *IEEE Transactions on Microwave Theory and Techniques,* vol. 54, no. 12, pp. 4122-4129, 2006.

[112] D. Kuznetsov, "Efficient circuit simulation of nonuniform transmission lines," *IEEE Transactions on Microwave Theory and Techniques,* vol. 46, no. 5, pp. 546-550, 1998.

[113] N. Boulejfen, A. B. Kouki, and F. M. Ghannouchi, “Frequency-and time-domain analyses of nonuniform lossy coupled transmission lines with linear and nonlinear terminations,” *IEEE Transactions on Microwave Theory and Techniques,* vol. 48, no. 3, pp. 367-379, 2000.

[114] A. Cheldavi, “Exact analysis of coupled nonuniform transmission lines with exponential power law characteristic impedance,” *IEEE Transactions on Microwave Theory and Techniques,* vol. 49, no. 1, pp. 197-199, 2001.

[115] S. M. H. Javadzadeh, Z. Mardy, K. Mehrany, F. Farzaneh, and M. Fardmanesh, “Fast and efficient analysis of transmission lines with arbitrary nonuniformities of sub-wavelength scale,” *IEEE Transactions on Microwave Theory and Techniques,* vol. 60, no. 8, pp. 2378-2384, 2012.

[116] P. Rulikowski, and J. Barrett, “Ultra-wideband pulse shaping using lossy and dispersive nonuniform transmission lines,” *IEEE Transactions on Microwave Theory and Techniques,* vol. 59, no. 10, pp. 2431-2440, 2011.

[117] F. Lindqvist, T. Magesacher, A. Fertner, P. Ödling, and P. O. Börjesson, “Estimation of nonhomogeneous and multi-section twisted-pair transmission-line parameters,” *IEEE Transactions on Microwave Theory and Techniques,* vol. 63, no. 11, pp. 3568-3578, 2015.

[118] J. Kimionis, A. Collado, M. M. Tentzeris, and A. Georgiadis, “Octave and decade printed UWB rectifiers based on nonuniform transmission lines for energy harvesting,” *IEEE Transactions on Microwave Theory and Techniques,* vol. 65, no. 11, pp. 4326-4334, 2017.

[119] M. S. Nikoo, S. M.-A. Hashemi, and F. Farzaneh, “Theoretical analysis of RF pulse termination in nonlinear transmission lines,” *IEEE Transactions on Microwave Theory and Techniques,* vol. 66, no. 11, pp. 4757-4764, 2018.

[120] H. Kim, A. B. Kozyrev, A. Karbassi, and D. W. van Der Weide, “Compact left-handed transmission line as a linear phase–voltage modulator and efficient harmonic generator,” *IEEE Transactions on Microwave Theory and Techniques,* vol. 55, no. 3, pp. 571-578, 2007.

[121] E. Cassedy, “Temporal instabilities in traveling-wave parametric amplifiers (correspondence),” *IRE Transactions on Microwave Theory and Techniques,* vol. 10, no. 1, pp. 86-87, 1962.

[122] M. Charbonneau-Lefort, B. Afeyan, and M. Fejer, “Optical parametric amplifiers using nonuniform quasi-phase-matched gratings. II. Space-time evolution of light pulses,” *JOSA B,* vol. 25, no. 5, pp. 680-697, 2008.

[123] S. Taravati, and C. Caloz, "Space-time modulated nonreciprocal mixing, amplifying and scanning leaky-wave antenna system." *2015 IEEE International Symposium on Antennas and Propagation & USNC/URSI National Radio Science Meeting*. IEEE, pp. 639-640, 2015.

[124] A. Cullen, “A travelling-wave parametric amplifier,” *Nature,* vol. 181, no. 4605, pp. 332-332, 1958.

[125] J.-C. Simon, “Action of a progressive disturbance on a guided electromagnetic wave,” *IRE Transactions on Microwave Theory and Techniques,* vol. 8, no. 1, pp. 18-29, 1960.

[126] A. Oliner, and A. Hessel, “Wave propagation in a medium with a progressive sinusoidal disturbance,” *IRE Transactions on Microwave Theory and Techniques,* vol. 9, no. 4, pp. 337-343, 1961.

[127] P. Dong, S. F. Preble, J. T. Robinson, S. Manipatruni, and M. Lipson, “Inducing photonic transitions between discrete modes in a silicon optical microcavity,” *Physical Review Letters,* vol. 100, no. 3, pp. 033904, 2008.

[128] Z. Yu, and S. Fan, “Complete optical isolation created by indirect interband photonic transitions,” *Nature Photonics,* vol. 3, no. 2, pp. 91-94, 2009.

[129] H. Lira, Z. Yu, S. Fan, and M. Lipson, “Electrically driven nonreciprocity induced by interband photonic transition on a silicon chip,” *Physical Review Letters,* vol. 109, no. 3, pp. 033901, 2012.

[130] M. M. Salary, S. Jafar-Zanjani, and H. Mosallaei, “Time-varying metamaterials based on graphene-wrapped microwires: Modeling and potential applications,” *Physical Review B,* vol. 97, no. 11, pp. 115421, 2018.

[131] D. Ramaccia, D. L. Sounas, A. Alù, F. Bilotti, and A. Toscano, "Nonreciprocity in antenna radiation induced by space-time varying metamaterial cloaks," *IEEE Antennas and Wireless Propagation Letters,* vol. 17, no. 11, pp. 1968-1972, 2018.

[132] F. Riesz, and B. S. iVagy, *Functional Analysis*, p.^pp. 367: Frederick Ungar Co.,, 1955.

[133] H. Hsu, "Backward traveling-wave parametric amplifiers." pp. 91-92.

[134] S. Taravati, and G. V. Eleftheriades, "Space-time medium functions as a perfect antenna-mixer-amplifier transceiver," *Physical Review Applied,* vol. 14, no. 5, pp. 054017, 2020.

[135] C. A. Balanis, *Advanced Engineering Electromagnetics*: John Wiley & Sons, 2012.

[136] Keysight, and Technologies, *Basics of measuring the dielectric properties of materials,* Application Note, 2017.

[137] E. Cassedy, and A. Oliner, "Dispersion relations in time-space periodic media: Part I—Stable interactions," *Proceedings of the IEEE,* vol. 51, no. 10, pp. 1342-1359, 1963.

[138] E. Cassedy, "Dispersion relations in time-space periodic media part II—Unstable interactions," *Proceedings of the IEEE,* vol. 55, no. 7, pp. 1154-1168, 1967.

[139] J. C. Slater, "Interaction of waves in crystals," *Reviews of Modern Physics,* vol. 30, no. 1, pp. 197, 1958.

[140] G. Roe, and M. Boyd, "Parametric energy conversion in distributed systems," *Proceedings of the IRE,* vol. 47, no. 7, pp. 1213-1218, 1959.

[141] A. Oliner, and A. Hessel, "Guided waves on sinusoidally-modulated reactance surfaces," *IRE Transactions on Antennas and Propagation,* vol. 7, no. 5, pp. 201-208, 1959.

[142] M. Cryan, I. Craddock, and C. Railton, "Finite difference time domain (FDTD) modelling of losses and group velocity below the light-line in photonic crystal structures." *International Symposium on Photonic and Electromagnetic Crystal Structures (PECS-VI),* 2005.

[143] Y. Vahabzadeh, N. Chamanara, and C. Caloz, "Generalized sheet transition condition FDTD simulation of metasurface," *IEEE Transactions on Antennas and Propagation,* vol. 66, no. 1, pp. 271-280, 2017.

[144] X. Liu, and D. A. McNamara, "The use of the FDTD method for electromagnetic analysis in the presence of indepedently time-varying media," *International Journal of Infrared and Millimeter Waves,* vol. 28, no. 9, pp. 759-778, 2007.

[145] A. Z. Elsherbeni, and V. Demir, *The finite-difference time-domain method for electromagnetics with MATLAB simulations*: The Institution of Engineering and Technology, 2016.

[146] J. Manley, and H. Rowe, "Some general properties of nonlinear elements-Part I. General energy relations," *Proceedings of the IRE,* vol. 44, no. 7, pp. 904-913, 1956.

[147] B. R. Gray, "Design of RF and microwave parametric amplifiers and power upconverters," Georgia Institute of Technology, 2012.

[148] D. Ramaccia, D. L. Sounas, A. Alù, A. Toscano, and F. Bilotti, "Phase-induced frequency conversion and doppler effect with time-modulated metasurfaces," *IEEE Transactions on Antennas and Propagation,* vol. 68, no. 3, pp. 1607-1617, 2019.

[149] R. T. Hitchcock, *Radio-frequency and microwave radiation*: AIHA, 2004.

[150] C. Qian, and H. Chen, "A perspective on the next generation of invisibility cloaks—Intelligent cloaks," *Applied Physics Letters,* vol. 118, no. 18, pp. 180501, 2021.

[151] S. Vellucci, A. Monti, M. Barbuto, A. Toscano, and F. Bilotti, "Progress and perspective on advanced cloaking metasurfaces: from invisibility to intelligent antennas," *EPJ Applied Metamaterials,* vol. 8, pp. 7, 2021.

[152] U. Leonhardt, "To invisibility and beyond," *Nature,* vol. 471, no. 7338, pp. 292-293, 2011.

[153] B. Zhang, "Electrodynamics of transformation-based invisibility cloaking," *Light: Science & Applications,* vol. 1, no. 10, pp. e32-e32, 2012.

[154] U. Leonhardt, "Optical conformal mapping," *Science,* vol. 312, no. 5781, pp. 1777-1780, 2006.

[155] H. Chu, Q. Li, B. Liu, J. Luo, S. Sun, Z. H. Hang, L. Zhou, and Y. Lai, "A hybrid invisibility cloak based on integration of transparent metasurfaces and zero-index materials," *Light: Science & Applications,* vol. 7, no. 1, pp. 1-8, 2018.

[156] M. Born, and E. Wolf, *Principles of optics: electromagnetic theory of propagation, interference and diffraction of light*: Elsevier, 2013.

[157] I. Liberal, and N. Engheta, "Near-zero refractive index photonics," *Nature Photonics,* vol. 11, no. 3, pp. 149-158, 2017.

[158] T. J. Cui, D. R. Smith, and R. Liu, *Metamaterials*: Springer, 2010.

[159] A. K. Sarychev, and V. M. Shalaev, *Electrodynamics of metamaterials*: World Scientific, 2007.

[160] C. M. Soukoulis, S. Linden, and M. Wegener, "Negative refractive index at optical wavelengths," *Science,* vol. 315, no. 5808, pp. 47-49, 2007.

[161] V. Veselago, "Electrodynamics of media with simultaneously negative electric permittivity and magnetic permeability," *Advances in Electromagnetics of Complex Media and Metamaterials*, pp. 83-97: Springer, 2002.

[162] G. V. Eleftheriades, and K. G. Balmain, *Negative-refraction metamaterials: fundamental principles and applications*: John Wiley & Sons, 2005.

[163] A. E. Aliev, Y. N. Gartstein, and R. H. Baughman, "Mirage effect from thermally modulated transparent carbon nanotube sheets," *Nanotechnology,* vol. 22, no. 43, pp. 435704, 2011.

[164] Z. Ruan, M. Yan, C. W. Neff, and M. Qiu, "Ideal cylindrical cloak: perfect but sensitive to tiny perturbations," *Physical Review Letters,* vol. 99, no. 11, pp. 113903, 2007.

[165] J. S. Toll, "Causality and the dispersion relation: logical foundations," *Physical Review,* vol. 104, no. 6, pp. 1760, 1956.

[166] J. Perczel, T. Tyc, and U. Leonhardt, "Invisibility cloaking without superluminal propagation," *New Journal of Physics,* vol. 13, no. 8, pp. 083007, 2011.

[167] P. Alitalo, H. Kettunen, and S. Tretyakov, "Cloaking a metal object from an electromagnetic pulse: a comparison between various cloaking techniques," *Journal of Applied Physics,* vol. 107, no. 3, pp. 034905, 2010.

[168] Y. Lai, H. Chen, Z.-Q. Zhang, and C. T. Chan, "Complementary media invisibility cloak that cloaks objects at a distance outside the cloaking shell," *Physical Review Letters,* vol. 102, no. 9, pp. 093901, 2009.

[169] Y. Lai, J. Ng, H. Chen, D. Han, J. Xiao, Z.-Q. Zhang, and C. T. Chan, "Illusion optics: the optical transformation of an object into another object," *Physical Review Letters,* vol. 102, no. 25, pp. 253902, 2009.

[170] A. Vozianova, V. Gill, and M. Khodzitsky, "Illusion optics: The optical transformation of an object location." *2016 10th International Congress on Advanced Electromagnetic Materials in Microwaves and Optics (METAMATERIALS)*. IEEE, pp. 115-117, 2016.

[171] K. Tsakmakidis, O. Reshef, E. Almpanis, G. Zouros, E. Mohammadi, D. Saadat, F. Sohrabi, N. Fahimi-Kashani, D. Etezadi, and R. Boyd, "Ultrabroadband 3D invisibility with fast-light cloaks," *Nature Communications,* vol. 10, no. 1, pp. 1-7, 2019.

[172] J. Li, and J. B. Pendry, "Hiding under the carpet: a new strategy for cloaking," *Physical Review Letters,* vol. 101, no. 20, pp. 203901, 2008.

[173] R. Liu, C. Ji, J. Mock, J. Chin, T. Cui, and D. Smith, "Broadband ground-plane cloak," *Science,* vol. 323, no. 5912, pp. 366-369, 2009.

[174] T. Ergin, N. Stenger, P. Brenner, J. B. Pendry, and M. Wegener, "Three-dimensional invisibility cloak at optical wavelengths," *Science,* vol. 328, no. 5976, pp. 337-339, 2010.

[175] P. Alitalo, O. Luukkonen, L. Jylha, J. Venermo, and S. A. Tretyakov, "Transmission-line networks cloaking objects from electromagnetic fields," *IEEE Transactions on Antennas and Propagation,* vol. 56, no. 2, pp. 416-424, 2008.

[176] P. Alitalo, C. A. Valagiannopoulos, and S. A. Tretyakov, "Simple cloak for antenna blockage reduction." *IEEE International Symposium on Antennas and Propagation (APSURSI)*. IEEE, pp. 669-672, 2011.

[177] P. Alitalo, S. Ranvier, J. Vehmas, and S. Tretyakov, "A microwave transmission-line network guiding electromagnetic fields through a dense array of metallic objects," *Metamaterials,* vol. 2, no. 4, pp. 206-212, 2008.

[178] P. Alitalo, F. Bongard, J.-F. Zürcher, J. Mosig, and S. Tretyakov, "Experimental verification of broadband cloaking using a volumetric cloak composed of periodically stacked cylindrical transmission-line networks," *Applied Physics Letters,* vol. 94, no. 1, pp. 014103, 2009.

[179] S. Tretyakov, P. Alitalo, O. Luukkonen, and C. Simovski, "Broadband electromagnetic cloaking of long cylindrical objects," *Physical Review Letters,* vol. 103, no. 10, pp. 103905, 2009.

[180] J. Vehmas, P. Alitalo, and S. Tretyakov, "Experimental demonstration of antenna blockage reduction with a transmission-line cloak," *IET Microwaves, Antennas & Propagation,* vol. 6, no. 7, pp. 830-834, 2012.

[181] J. Vehmas, P. Alitalo, and S. A. Tretyakov, "Transmission-line cloak as an antenna," *IEEE Antennas and Wireless Propagation Letters,* vol. 10, pp. 1594-1597, 2011.

[182] D. Rainwater, A. Kerkhoff, K. Melin, J. Soric, G. Moreno, and A. Alù, "Experimental verification of three-dimensional plasmonic cloaking in free-space," *New Journal of Physics,* vol. 14, no. 1, pp. 013054, 2012.

[183] C. F. Bohren, and D. R. Huffman, *Absorption and scattering of light by small particles*: John Wiley & Sons, 2008.

[184] A. Alù, and N. Engheta, "Theory and potentials of multi-layered plasmonic covers for multi-frequency cloaking," *New Journal of Physics,* vol. 10, no. 11, pp. 115036, 2008.

[185] J. C. Soric, A. Monti, A. Toscano, F. Bilotti, and A. Alù, "Multiband and wideband bilayer mantle cloaks," *IEEE Transactions on Antennas and Propagation,* vol. 63, no. 7, pp. 3235-3240, 2015.

[186] C. A. Valagiannopoulos, P. Alitalo, and S. A. Tretyakov, "On the minimal scattering response of PEC cylinders in a dielectric cloak," *IEEE Antennas and Wireless Propagation Letters,* vol. 13, pp. 403-406, 2014.

[187] Q. Li, Z. Zhang, L. Qi, Q. Liao, Z. Kang, and Y. Zhang, "Toward the application of high frequency electromagnetic wave absorption by carbon nanostructures," *Advanced Science,* vol. 6, no. 8, pp. 1801057, 2019.

[188] A. Alù, and N. Engheta, "Cloaking a sensor," *Physical Review Letters,* vol. 102, no. 23, pp. 233901, 2009.

[189] A. Alù, and N. Engheta, "Cloaking a receiving antenna or a sensor with plasmonic metamaterials," *Metamaterials,* vol. 4, no. 2-3, pp. 153-159, 2010.

[190] R. Fleury, J. Soric, and A. Alù, "Physical bounds on absorption and scattering for cloaked sensors," *Physical Review B,* vol. 89, no. 4, pp. 045122, 2014.

[191] C. Zhang, J. Yang, W. Cao, W. Yuan, J. Ke, L. Yang, Q. Cheng, and T. Cui, "Transparently curved metamaterial with broadband millimeter wave absorption," *Photonics Research,* vol. 7, no. 4, pp. 478-485, 2019.

[192] H. Lv, Z. Yang, H. Xu, L. Wang, and R. Wu, "An electrical switch-driven flexible electromagnetic absorber," *Advanced Functional Materials,* vol. 30, no. 4, pp. 1907251, 2020.

[193] B. Edwards, A. Alù, M. G. Silveirinha, and N. Engheta, "Experimental verification of plasmonic cloaking at microwave frequencies with metamaterials," *Physical Review Letters,* vol. 103, no. 15, pp. 153901, 2009.

[194] P.-Y. Chen, and A. Alu, "Mantle cloaking using thin patterned metasurfaces," *Physical Review B,* vol. 84, no. 20, pp. 205110, 2011.

[195] A. Alu, and N. Engheta, "Plasmonic materials in transparency and cloaking problems: mechanism, robustness, and physical insights," *Optics Express,* vol. 15, no. 6, pp. 3318-3332, 2007.

[196] A. Alù, and N. Engheta, "Multifrequency optical invisibility cloak with layered plasmonic shells," *Physical Review Letters,* vol. 100, no. 11, pp. 113901, 2008.

[197] S. Tricarico, F. Bilotti, A. Alù, and L. Vegni, "Plasmonic cloaking for irregular objects with anisotropic scattering properties," *Physical Review E,* vol. 81, no. 2, pp. 026602, 2010.

[198] A. Alu, D. Rainwater, and A. Kerkhoff, "Plasmonic cloaking of cylinders: finite length, oblique illumination and cross-polarization coupling," *New Journal of Physics,* vol. 12, no. 10, pp. 103028, 2010.

[199] F. Bilotti, S. Tricarico, and L. Vegni, "Plasmonic metamaterial cloaking at optical frequencies," *IEEE Transactions on Nanotechnology,* vol. 9, no. 1, pp. 55-61, 2009.

[200] M. Fruhnert, A. Monti, I. Fernandez-Corbaton, A. Alù, A. Toscano, F. Bilotti, and C. Rockstuhl, "Tunable scattering cancellation cloak with plasmonic ellipsoids in the visible," *Physical Review B,* vol. 93, no. 24, pp. 245127, 2016.

[201] A. Alù, and N. Engheta, "Achieving transparency with plasmonic and metamaterial coatings," *Physical Review E,* vol. 72, no. 1, pp. 016623, 2005.

[202] A. Edalati, and K. Sarabandi, "Wideband, wide angle, polarization independent RCS reduction using nonabsorptive miniaturized-element frequency selective surfaces," *IEEE Transactions on Antennas and Propagation,* vol. 62, no. 2, pp. 747-754, 2013.

[203] A. Y. Modi, C. A. Balanis, C. R. Birtcher, and H. N. Shaman, "New class of RCS-reduction metasurfaces based on scattering cancellation using array theory," *IEEE Transactions on Antennas and Propagation,* vol. 67, no. 1, pp. 298-308, 2018.

[204] A. Alù, "Mantle cloak: Invisibility induced by a surface," *Physical Review B,* vol. 80, no. 24, pp. 245115, 2009.

[205] A. Monti, L. Tenuti, G. Oliveri, A. Alù, A. Massa, A. Toscano, and F. Bilotti, "Design of multi-layer mantle cloaks." *2014 8th International Congress on Advanced Electromagnetic Materials in Microwaves and Optics*, pp. 214-216, 2014.

[206] L. Tenuti, G. Oliveri, A. Monti, F. Bilotti, A. Toscano, and A. Massa, "Design of mantle cloaks through a System-by-Design approach." *2016 10th European Conference on Antennas and Propagation (EuCAP)*, pp. 1-3, 2016.

[207] H. Younesiraad, M. Bemani, and S. Nikmehr, "Scattering suppression and cloak for electrically large objects using cylindrical metasurface based on monolayer and multilayer mantle cloak approach," *IET Microwaves, Antennas & Propagation,* vol. 13, no. 3, pp. 278-285, 2019.

[208] A. Alù, and N. Engheta, "Effects of size and frequency dispersion in plasmonic cloaking," *Physical Review E,* vol. 78, no. 4, pp. 045602, 2008.

[209] N. Yu, P. Genevet, M. A. Kats, F. Aieta, J.-P. Tetienne, F. Capasso, and Z. Gaburro, "Light propagation with phase discontinuities: generalized laws of reflection and refraction," *Science,* vol. 334, no. 6054, pp. 333-337, 2011.

[210] J. Zhang, Z. Lei Mei, W. Ru Zhang, F. Yang, and T. Jun Cui, "An ultrathin directional carpet cloak based on generalized Snell's law," *Applied Physics Letters,* vol. 103, no. 15, pp. 151115, 2013.

[211] L. Jiang, B. Fang, Z. Yan, H. Gan, C. Li, M. Zhang, Z. Hong, and X. Jing, "Bandwidth-enhanced carpet cloak by using a phase-gradient metasurface with a multilayer unit cell in terahertz range," *Optics Communications,* vol. 471, pp. 125827, 2020.

[212] J. Carmigniani, B. Furht, M. Anisetti, P. Ceravolo, E. Damiani, and M. Ivkovic, "Augmented reality technologies, systems and applications," *Multimedia Tools and Applications,* vol. 51, pp. 341-377, 2011.

[213] E. Wolf, and T. Habashy, "Invisible bodies and uniqueness of the inverse scattering problem," *Journal of Modern Optics,* vol. 40, no. 5, pp. 785-792, 1993.

[214] A. I. Nachman, "Reconstructions from boundary measurements," *Annals of Mathematics,* vol. 128, no. 3, pp. 531-576, 1988.

[215] F. Monticone, and A. Alù, "Invisibility exposed: physical bounds on passive cloaking," *Optica,* vol. 3, no. 7, pp. 718-724, 2016.

[216] C. Qian, B. Zheng, Y. Shen, L. Jing, E. Li, L. Shen, and H. Chen, "Deep-learning-enabled self-adaptive microwave cloak without human intervention," *Nature Photonics,* vol. 14, no. 6, pp. 383-390, 2020.

[217] Z. Liu, D. Zhu, S. P. Rodrigues, K.-T. Lee, and W. Cai, "Generative model for the inverse design of metasurfaces," *Nano Letters,* vol. 18, no. 10, pp. 6570-6576, 2018.

[218] W. Ma, F. Cheng, and Y. Liu, "Deep-learning-enabled on-demand design of chiral metamaterials," *ACS Nano,* vol. 12, no. 6, pp. 6326-6334, 2018.

[219] W. Ma, Z. Liu, Z. A. Kudyshev, A. Boltasseva, W. Cai, and Y. Liu, "Deep learning for the design of photonic structures," *Nature Photonics,* vol. 15, no. 2, pp. 77-90, 2021.

[220] J. Peurifoy, Y. Shen, L. Jing, Y. Yang, F. Cano-Renteria, B. G. DeLacy, J. D. Joannopoulos, M. Tegmark, and M. Soljačić, "Nanophotonic particle simulation and inverse design using artificial neural networks," *Science Advances,* vol. 4, no. 6, pp. eaar4206, 2018.

[221] E. F. Knott, J. F. Schaeffer, and M. T. Tulley, *Radar cross section*: SciTech Publishing, 2004.

[222] H. Singh, and R. M. Jha, *Active radar cross section reduction*: Cambridge University Press, 2015.

[223] J. Radatz, *The IEEE standard dictionary of electrical and electronics terms*: IEEE Standards Office, 1997.

[224] R. Paknys, *Applied frequency-domain electromagnetics*: John Wiley & Sons, 2016.

Appendix A

Replacing A_n coefficients into (5.30) gives the following relation

$$\left(\epsilon_1+\frac{\gamma^2-j\mu\sigma\omega}{\mu\omega^2}\right)-\frac{\epsilon_2^2/4}{\epsilon_1+\left(\frac{(\gamma+\gamma_1)^2-j\mu\sigma(\omega+\omega_1)}{\mu(\omega+\omega_1)^2}\right)}-\frac{\epsilon_2^2/4}{\epsilon_1+\left(\frac{(\gamma-\gamma_1)^2-j\mu\sigma(\omega-\omega_1)}{\mu(\omega-\omega_1)^2}\right)}=0 \tag{A-1}$$

Factoring out ω and ϵ_1,

$$\left(1+\frac{\gamma^2-j\mu\sigma\omega}{\epsilon_1\mu\omega^2}\right)-\frac{\epsilon_2^2/4\epsilon_1^2}{1+\left(\frac{(\gamma+\gamma_1)^2-j\mu\sigma\omega\left(1+\frac{\omega_1}{\omega}\right)}{\epsilon_1\mu\omega^2\left(1+\frac{\omega_1}{\omega}\right)^2}\right)}-\frac{\epsilon_2^2/4\epsilon_1^2}{1+\left(\frac{(\gamma-\gamma_1)^2-j\mu\sigma\omega\left(1-\frac{\omega_1}{\omega}\right)}{\epsilon_1\mu\omega^2\left(1-\frac{\omega_1}{\omega}\right)^2}\right)}=0 \tag{A-2}$$

Then, $j\mu\sigma\omega-\epsilon_1\mu\omega^2$ is replaced by the propagation constant of lossy unmodulated homogeneous media, γ_0^2.

$$\left(1+\frac{\gamma^2-(\gamma_0^2+\epsilon_1\mu\omega^2)}{\epsilon_1\mu\omega^2}\right)-\frac{\epsilon_2^2/4\epsilon_1^2}{1+\left(\frac{(\gamma+\gamma_1)^2-(\gamma_0^2+\epsilon_1\mu\omega^2)\left(1+\frac{\omega_1}{\omega}\right)}{\epsilon_1\mu\omega^2\left(1+\frac{\omega_1}{\omega}\right)^2}\right)}-\frac{\epsilon_2^2/4\epsilon_1^2}{1+\left(\frac{(\gamma-\gamma_1)^2-(\gamma_0^2+\epsilon_1\mu\omega^2)\left(1-\frac{\omega_1}{\omega}\right)}{\epsilon_1\mu\omega^2\left(1-\frac{\omega_1}{\omega}\right)^2}\right)}=0 \tag{A-3}$$

And re-arranging to have γ/γ_0 and γ_1/γ_0 terms

$$\frac{1}{\epsilon_1\mu}\frac{\gamma_0^2}{\omega^2}\left(\frac{\gamma^2}{\gamma_0^2}-1\right)-\frac{\epsilon_2^2/4\epsilon_1^2}{1+\left(\frac{1}{\epsilon_1\mu}\frac{\gamma_0^2}{\omega^2}\right)\left(\frac{\left(\frac{\gamma}{\gamma_0}+\frac{\gamma_1}{\gamma_0}\right)^2-\left(1+\frac{\epsilon_1\mu\omega^2}{\gamma_0^2}\right)\left(1+\frac{\omega_1}{\omega}\right)}{\left(1+\frac{\omega_1}{\omega}\right)^2}\right)}$$
$$-\frac{\epsilon_2^2/4\epsilon_1^2}{1+\left(\frac{1}{\epsilon_1\mu}\frac{\gamma_0^2}{\omega^2}\right)\left(\frac{\left(\frac{\gamma}{\gamma_0}-\frac{\gamma_1}{\gamma_0}\right)^2-\left(1+\frac{\epsilon_1\mu\omega^2}{\gamma_0^2}\right)\left(1-\frac{\omega_1}{\omega}\right)}{\left(1-\frac{\omega_1}{\omega}\right)^2}\right)}=0$$

(A-4)

Letting $\gamma/\gamma_0 = Y$, $\omega_1/\omega = W$, $\gamma_1/\gamma_0 = Y_1$ and $\epsilon_2^2/4\epsilon_1^2 = Z$, the following function of the form of $Z = f(Y, W)$ is obtained

$$\left(\frac{1}{C}\right)\left(\frac{1}{Y^2-1}\right)\left[\frac{1}{1+C\left(\frac{(Y+Y_1)^2-(1+1/C)(1+W)}{(1+W)^2}\right)}\right.$$
$$\left.+\frac{1}{1+C\left(\frac{(Y-Y_1)^2-(1+1/C)(1-W)}{(1-W)^2}\right)}\right]=\frac{1}{Z}$$

(A-5)

where $C=\frac{1}{\epsilon_1\mu}\frac{\gamma_0^2}{\omega^2}$ is a function of operating frequency and the conductivity of the medium. If (A-5) is expanded in the following form,

$$\left(\frac{1}{C}\right)\left(\frac{1}{Y^2-1}\right)\left[\frac{1}{1+C\left(\frac{Y+Y_1}{1+W}\right)^2-C\left(\frac{1}{1+W}\right)-\left(\frac{1}{1+W}\right)}\right.$$
$$\left.+\frac{1}{1+C\left(\frac{Y-Y_1}{1-W}\right)^2-C\left(\frac{1}{1-W}\right)-\left(\frac{1}{1-W}\right)}\right]=\frac{1}{Z}$$

(A-6)

Removing the loss effect would lead to $C=-1$, and the same *lossless* dispersion relation results reported in [125]. Thus, (A-5) is verified.